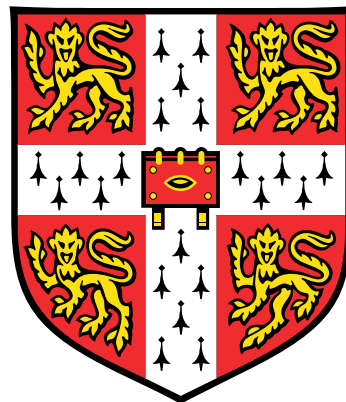


Numerical simulations of instabilities in general relativity



Markus Kunesch

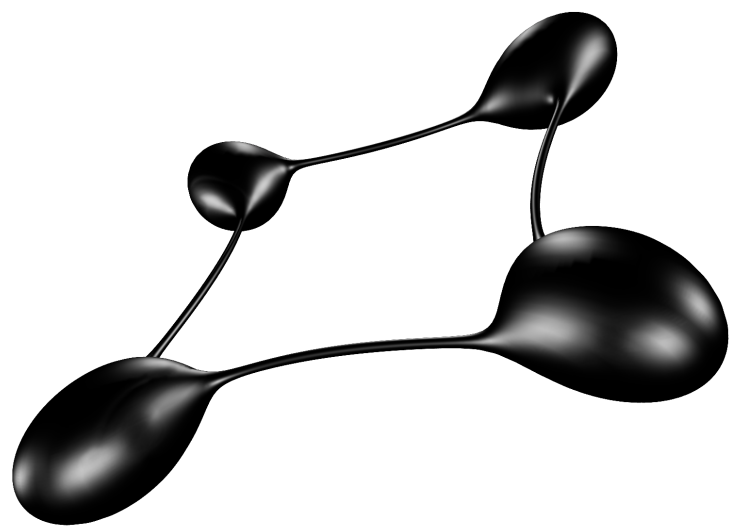
Supervisor: Dr Pau Figueras

Department of Applied Mathematics and Theoretical Physics
University of Cambridge

This dissertation is submitted for the degree of
Doctor of Philosophy

King's College

September 2018



Declaration

This dissertation is the result of my own work and includes nothing which is the outcome of work done in collaboration except as declared in the Preface and specified in the text.

It is not substantially the same as any that I have submitted, or, is being concurrently submitted for a degree or diploma or other qualification at the University of Cambridge or any other University or similar institution except as declared in the Preface and specified in the text.

I further state that no substantial part of my dissertation has already been submitted, or, is being concurrently submitted for any such degree, diploma or other qualification at the University of Cambridge or any other University or similar institution except as declared in the Preface and specified in the text.

This dissertation does not exceed the prescribed word limit for the relevant Degree Committee.

Markus Kunesch
September 2018

Acknowledgements

I am deeply indebted to my supervisor, Pau Figueras, for his encouragement, guidance, and support every step along the way, and for creating such a stimulating, collaborative, and enjoyable research environment. Furthermore, I am extremely grateful to my co-supervisor, Ulrich Sperhake, on whose advice, support, and insight I could rely throughout my PhD. I would also like to thank my examiners, Vitor Cardoso and Harvey Reall, for their valuable comments and suggestions.

I was tremendously lucky to have Saran Tunyasuvunakool as fellow PhD student and would like to thank him for his knowledge, advice, and friendship, and for coming up with methods for finding apparent horizons that no human was meant to find. Furthermore, I am deeply grateful to Hans Bantilan for many interesting discussions and for his kindness, humour, and relentless enthusiasm. Finally, I would like to thank Rodrigo Panosso Macedo for the enjoyable collaboration on Myers-Perry black holes in my final year.

It has been an immense privilege for me to be part of the GRCHOMBO team. I particularly want to thank Eugene Lim for bringing me on board and for his advice and encouragement throughout the years, and Katy Clough for the truly enjoyable and fruitful collaboration. Furthermore, I would like to thank Alejandro Duran, Juha Jäykkä, and Kacper Kornet for countless interesting discussions and for their help with the more technical parts of my work. I would also like to express my deepest gratitude to my friends and colleagues at DAMTP and QMUL, among others Benjamin Wallisch, Chandrima Ganguly, Charlotte Kirchhoff-Lukat, Chris Moore, Davide Gerosa, Dejan Gajic, Giuseppe Papallo, Helvi Witek, Joe Keir, Michalis Agathos, and Will Cook.

I am grateful to all my friends in Cambridge for making my time here so wonderful. I would particularly like to thank Ben, Chandrima, Catherine, Kate, and Marlis for their encouragement and support while I was writing this thesis and for bringing so many moments of delight into what otherwise might have been a stressful time. Finally, I would like to express my deepest gratitude to my whole family for their unconditional love, their unwavering support, and for always being there for me.

My PhD was funded by an STFC studentship initially and by the European Research Council Grant No. ERC-2014-StG 639022-NewNGR in my final year. Furthermore, I received funding from the European Union’s Horizon 2020 research and innovation programme under the Marie Skłodowska-Curie Grant agreement No. 690904. I am very grateful for the financial support for conference trips from King’s College Cambridge and the Department of Applied Mathematics and Theoretical Physics and would like to thank Perimeter Institute and my host and collaborator Luis Lehner for the hospitality while I was working on Myers-Perry black holes.

The simulations presented in this thesis were carried out on the following supercomputers:

- The COSMOS Shared Memory system at DAMTP, University of Cambridge, operated on behalf of the STFC DiRAC HPC Facility. This system is funded by BIS National E-infrastructure capital Grant No. ST/ J005673/1 and STFC Grants No. ST/H008586/1, No. ST/K00333X/1.
- MareNostrum III and MareNostrum IV at the Barcelona Supercomputing Centre through the grants FI-2016-3-0006 and PRACE Tier-0 PPFPWG respectively.
- Stampede and Stampede2 at the Texas Advanced Computing Center, University of Texas at Austin, through the NSF-XSEDE grant No. PHY-090003 and an allocation provided by Intel for their Parallel Computing Centres.
- SuperMike-II at Louisiana State University under allocation NUMREL06.
- Cartesius, SURFsara, in the Netherlands through the PRACE DECI grant NRBA.

I would also like to thank the above institutions for the technical support they provided. Furthermore, I would like to thank Intel for providing computer resources and support through the Intel Parallel Computing Centre at the University of Cambridge and the centre’s principal investigator, Paul Shellard.

Abstract

General relativity, one of the pillars of our understanding of the universe, has been a remarkably successful theory. It has stood the test of time for more than 100 years and has passed all experimental tests so far. Most recently, the LIGO collaboration made the first-ever direct detection of gravitational waves, confirming a long-standing prediction of general relativity. Despite this, several fundamental mathematical questions remain unanswered, many of which relate to the global existence and the stability of solutions to Einstein's equations. This thesis presents our efforts to use numerical relativity to investigate some of these questions.

We present a complete picture of the end points of black ring instabilities in five dimensions. Fat rings collapse to Myers-Perry black holes. For intermediate rings, we discover a previously unknown instability that stretches the ring without changing its thickness and causes it to collapse to a Myers-Perry black hole. Most importantly, however, we find that for very thin rings, the Gregory-Laflamme instability dominates and causes the ring to break. This provides the first concrete evidence that in higher dimensions, the weak cosmic censorship conjecture may be violated even in asymptotically flat spacetimes.

For Myers-Perry black holes, we investigate instabilities in five and six dimensions. In six dimensions, we demonstrate that both axisymmetric and non-axisymmetric instabilities can cause the black hole to pinch off, and we study the approach to the naked singularity in detail.

Another question that has attracted intense interest recently is the instability of anti-de Sitter space. In this thesis, we explore how breaking spherical symmetry in gravitational collapse in anti-de Sitter space affects black hole formation.

These findings were made possible by our new open source general relativity code, GRCHOMBO, whose adaptive mesh capabilities allow accurate simulations of phenomena in which new length scales are produced dynamically. In this thesis, we describe GRCHOMBO in detail, and analyse its performance on the latest supercomputers. Furthermore, we outline numerical advances that were necessary for simulating higher dimensional black holes stably and efficiently.

Research overview

This thesis includes research that was published in the following peer-reviewed journal articles:

- [1] Bantilan, H., Figueras, P., Kunesch, M., & Romatschke, P. (2017). Non-Spherically Symmetric Collapse in Asymptotically AdS Spacetimes. *Physical Review Letters*, 119 (19), 191103.
- [2] Figueras, P., Kunesch, M., Lehner, L., & Tunyasuvunakool, S. (2017). End Point of the Ultraspinning Instability and Violation of Cosmic Censorship. *Physical Review Letters*, 118(15), 151103.
- [3] Figueras, P., Kunesch, M., & Tunyasuvunakool, S. (2016). End point of black ring instabilities and the weak cosmic censorship conjecture. *Physical Review Letters* (Editors' suggestion), 116(7), 071102.
- [4] Cook, W. G., Figueras, P., Kunesch, M., Sperhake, U., & Tunyasuvunakool, S. (2016). Dimensional reduction in numerical relativity: Modified Cartoon formalism and regularization. *International Journal of Modern Physics D*, 25(09), 1641013.
- [5] Clough, K., Figueras, P., Finkel, H., Kunesch, M., Lim, E. A., & Tunyasuvunakool, S. (2015). GRChombo: Numerical relativity with adaptive mesh refinement. *Classical and Quantum Gravity*, 32(24), 245011.

It also includes a significant amount of unpublished results, which will be published in the near future. Furthermore, I am one of the core developers of GRCHOMBO, a new open-source numerical relativity code. GRCHOMBO was made public earlier this year and is available under the 3-clause BSD license at www.grchombo.org.

As part of my PhD, I have also co-supervised three undergraduate summer interns and have made contributions to science outreach events, including a Pint of Science talk in 2016.

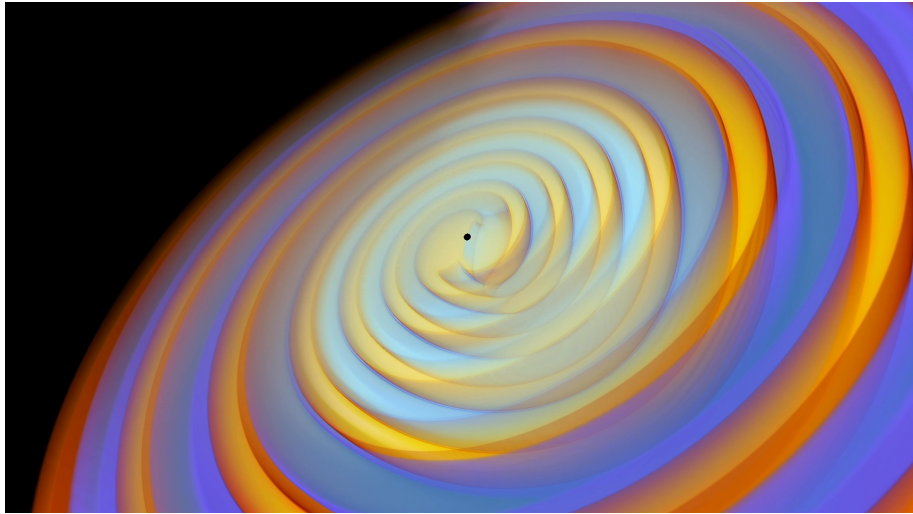


Fig. 1 Volume rendering of the gravitational waves from a binary black hole merger simulated with GRChombo.

Furthermore, I have collaborated with Intel on a visualisation of the gravitational waves from a binary black hole merger, the first-ever direct volume rendering of adaptive mesh data. The video was accepted and presented at ISC High Performance 2016. Fig. 1 shows a snapshot from the simulation.¹

¹The full video is available at <https://youtu.be/XItUV3n5IzQ>.

Table of contents

Abstract	ix
Research overview	xi
1 Introduction	1
1.1 Weak Cosmic Censorship Conjecture	4
1.2 Higher dimensional black holes	6
1.3 Numerical relativity background	9
1.3.1 ADM, BSSN, and CCZ4	10
1.3.2 Gauge choice in BSSN and CCZ4	15
1.3.3 Initial data for the puncture gauge	20
1.3.4 Generalised harmonic coordinates	21
1.3.5 Comparison of formalisms	24
2 GRCHOMBO	25
2.1 Introduction	25
2.1.1 High performance computing architecture and techniques	27
2.2 Numerical details	29
2.2.1 Adaptive mesh refinement	30
2.2.2 Tagging criteria	34
2.2.3 Boundary conditions	34

2.2.4	Parallelism	36
2.3	Testing correctness and accuracy	37
2.3.1	Software tests	37
2.3.2	Physical tests	38
2.4	Scaling tests	41
2.4.1	Results	42
2.4.2	Results on Knights Landing	45
2.4.3	Performance summary and outlook	46
2.5	Design of GRCHOMBO	47
2.5.1	Looping over cells	49
2.5.2	Vectorisation	51
2.5.3	Tensor algebra and expression templates	52
2.6	Conclusion	53
2.7	Appendix	54
2.7.1	Strong scaling for black rings	54
2.7.2	Strong scaling with different box sizes	54
3	Numerical methods for higher dimensions	57
3.1	Introduction	57
3.2	Gauge conditions	58
3.3	Singularity diffusion	60
3.4	Modified Cartoon Method	63
3.4.1	Introduction	63
3.4.2	Modified cartoon method for $SO(2)$ symmetry	66
3.4.3	Modified cartoon method for $SO(N > 2)$ symmetry	69
3.4.4	Boundary conditions and regularisation	72
3.5	Appendix A: Tensor components for $SO(N > 2)$	74
3.6	Appendix B: Regularisation terms	74

4 End point of black ring instabilities	77
4.1 Introduction	77
4.2 Numerical methods	80
4.2.1 Initial data	82
4.2.2 Gauge conditions and singularity treatment	84
4.3 Analysis methods	86
4.3.1 Wave analysis	86
4.3.2 Apparent horizons	87
4.4 Results	89
4.4.1 Very fat rings	89
4.4.2 Intermediate rings	90
4.4.3 Very thin rings	93
4.5 Discussion and outlook	97
4.6 Appendix A: Behaviour of the $m = 1$ mode	100
4.7 Appendix B: Numerical tests	100
5 End point of Myers-Perry instabilities	103
5.1 Introduction	104
5.1.1 (In-)stability of Myers-Perry black holes	105
5.1.2 6D phase diagram and bumpy black holes	107
5.2 Stability in 5D	108
5.2.1 Numerical methods	109
5.2.2 Results	110
5.3 Instabilities in 6D	111
5.3.1 Numerical methods	111
5.3.2 Analysis methods	114
5.3.3 Results: Ultraspinning instability	117
5.3.4 Results: Non-axisymmetric instabilities	126

5.3.5	Discussion	130
5.4	Appendix: Numerical tests	131
6	Implications for Weak Cosmic Censorship	135
6.1	Bifurcation process	137
7	Numerical simulations in AdS	139
7.1	Introduction	139
7.1.1	Stability of AdS	140
7.2	Numerical methods in AdS	142
7.3	Asymptotically AdS spacetimes in GRCHOMBO	144
7.4	Non-spherically symmetric collapse	145
7.4.1	Numerical Scheme	145
7.4.2	Results	147
7.4.3	Discussion	151
7.4.4	Appendix: Convergence tests	152
8	Summary	155
References		159

Chapter 1

Introduction

It is undeniable that Einstein’s equation,

$$G_{ab} + \Lambda g_{ab} = 8\pi T_{ab}, \quad (1.1)$$

is one of the most elegant equations ever written down by mankind. It is truly remarkable that all gravitational interactions in the universe, from an apple falling off a tree to the violent merger of two supermassive black holes, from the behaviour of planets in our solar system to the expansion of the whole universe, can be described by one geometric equation relating the curvature of spacetime to the matter content. General relativity has been tested with remarkable accuracy [6] and has prevailed to this day. These tests entered a completely new era recently, when the LIGO collaboration made the first-ever direct detection of gravitational waves [7, 8], confirming a long-standing prediction of general relativity. The gravitational waves originated from the merger of two black holes 1.3 billion light years away. Since then, LIGO has made several more detections [9–13], not only of coalescing black holes, but also of a neutron star binary. Due to improvements in sensitivity, we can expect a flurry of further detections in the years to come, allowing us to put ever-stronger constraints on our theory of gravity.

It is intuitive that it is hard to analyse the mathematical properties of a non-linear equation that is capable of giving rise to such a rich structure of solutions with such complex behaviour. Indeed, even though general relativity is now more than 100 years old, many mathematical questions remain unanswered. For example, we do not know whether singularities must always be hidden inside black holes or whether they can be “naked” and visible to far-away observers. This question is the subject of the *Weak Cosmic Censorship Conjecture*. Loosely, it postulates that there cannot be naked singularities (the precise form will be discussed later

in this chapter). The Weak Cosmic Censorship Conjecture has important implications for the predictive power of general relativity: if it is true, then for an observer outside of the black hole general relativity can always predict the future.

Another important question is that of the linear and non-linear stability of solutions to Einstein's equations. For example, we still have no mathematical proof that the exterior of the Kerr solution [14] that describes the black holes in our universe, including the ones involved in the mergers observed by LIGO, is non-linearly stable. There are several mathematical studies that suggest that this is the case [15–18] although there are also indications that there may be non-trivial behaviour very close to extremality [19–21]. In higher dimensions, however, we know that black holes can be unstable [22–31, 3, 32], for example when they become very thin, as is the case in the Gregory-Laflamme (GL) instability of black strings [22], or they rotate sufficiently rapidly, as is the case in the ultraspinning instability [23] and the bar-mode instability [26, 27] of Myers-Perry black holes. These instabilities have implications far beyond the study of higher dimensional black holes: there are hints from numerical simulations [33, 3, 2] that black hole instabilities may lead to violations of Weak Cosmic Censorship.

Another spacetime whose (in-)stability has attracted a lot of attention recently is anti-de Sitter (AdS) space. One reason for this is that as the maximally symmetric solution to Einstein's equations (1.1) with a negative cosmological constant, it is as fundamental mathematically as Minkowski or de-Sitter space, whose stability has been established in Ref. [34] and Refs. [35, 36] respectively. Another reason is that AdS space features in the AdS/CFT correspondence [37–39], which allows us to elucidate the behaviour of certain strongly coupled field theories by studying classical gravity in asymptotically AdS space in one dimension higher.

While all these questions are ultimately mathematical and will hopefully be answered with a precise theorem and a rigorous mathematical proof, they can all benefit from numerical work to inform the mathematical efforts and to provide numerical evidence while a proof is still outstanding. For example, the numerical simulations of scalar field collapse in $4D$ [40] and simulations of unstable black strings in $5D$ [33] have important implications for the Weak Cosmic Censorship Conjecture. Since the latter work is very important for this thesis, we will review it in detail later in this chapter. In AdS space in $D \geq 4$, numerical simulations [41–43] demonstrated that scalar field configurations with arbitrarily small amplitude can lead to the formation of a black hole after multiple reflections off the AdS boundary. This behaviour had been conjectured by Refs. [44, 45], but could not be addressed rigorously until very recently for Einstein-null dust in Refs. [46, 47].

In this thesis, we report on numerical simulations that explore instabilities of asymptotically flat black holes in $5D$ and $6D$ in the non-linear regime, and we examine the implications for the Weak Cosmic Censorship Conjecture and the topology of higher dimensional black holes. Furthermore, we study how breaking spherical symmetry affects the collapse of scalar field configurations in AdS space in order to gain insight into the non-linear stability of AdS space without symmetry assumptions. To enable these simulations, and several other numerical studies in the fields of cosmology and astrophysics [5, 48–53], we developed a new open source general relativity code GRCHOMBO [5]¹. GRCHOMBO is a multi-purpose numerical relativity code whose main distinctive feature is very flexible adaptive mesh refinement. This allows us to resolve the new length scales that are generated during instabilities accurately.

This thesis is organised as follows: in the remainder of this chapter, we give a high-level overview of the background material that is relevant for the thesis as a whole. In particular, we summarise what is known about higher dimensional black holes, the Gregory-Laflamme instability, and its implications for the Weak Cosmic Censorship Conjecture. Furthermore, we explain the necessary numerical relativity background. More detailed and specific introductions are provided at the beginning of all the other chapters of this thesis.

In chapter 2, we present the GRCHOMBO code [5, 54], explain its current design, and present the latest accuracy and performance tests. Significant work has been put into optimising GRCHOMBO to make it run faster on the latest architecture and this section will give a brief overview of these efforts. In chapter 3, we present advances and adjustments we had to make to current numerical relativity methods in order to simulate higher dimensional spacetimes stably and efficiently. This includes dimensional reduction techniques, a new singularity treatment, and adapted gauge conditions which we developed for Refs. [3, 2].

In chapter 4, we give a complete picture of instabilities of black rings [55], black holes of toroidal topology. We investigate the whole parameter range, from very fat to very thin black rings, and present evidence that very thin black rings pinch off. In chapter 5, we present our work on axisymmetric instabilities of Myers-Perry black holes in $6D$ [2], which cause the black hole to be torn apart by its rotation. Since this setting is much cheaper than black rings, we can study the approach to pinch off of the horizon in more detail. Furthermore, we present unpublished results on the non-linear stability of Myers-Perry black holes in $5D$ and non-axisymmetric instabilities in $6D$. In chapter 6, we examine the implications of our work on black rings and Myers-Perry black holes for the Weak Cosmic Censorship Conjecture.

¹GRCHOMBO is available under BSD-3 license at www.grchombo.org or directly from GitHub at <https://github.com/GRChombo/>.

In chapter 7, we present our results on non-axisymmetric scalar field collapse in AdS space [1] and outline recent work to allow the simulation of AdS space with GRCHOMBO. Finally, we summarise both our asymptotically flat and asymptotically AdS results in chapter 8.

1.1 Weak Cosmic Censorship Conjecture

Local well-posedness of Einstein’s equations was established in Ref. [56]. This result was given a more global flavour in Refs. [57, 58], which proved the existence of a unique maximal globally hyperbolic Cauchy development. However, it is obvious that Einstein’s equations cannot be globally well-posed, at least not in the sense of the completeness of all causal geodesics. For example, an observer falling into a Schwarzschild black hole will hit a singularity in finite proper time. Thus, global existence of solutions cannot hold. However, to date no generic example of a singularity outside of a black hole has been found. Since no information can escape a black hole, it may, therefore, be possible to formulate a global existence result for the spacetime outside of black holes. This is precisely what is captured by the *Weak Cosmic Censorship Conjecture* [59–62]:

Conjecture 1 (Weak Cosmic Censorship Conjecture). *The maximal Cauchy development of generic, asymptotically flat, geodesically complete initial data possesses a complete future null infinity.*

This is a very elegant statement, as it reduces the question of whether singularities arise outside black holes to a very concrete statement about the completeness of future null infinity. The rationale behind this formulation is that, by definition, every point outside of a black hole region is in the causal past of future null infinity. Thus, if there were a singularity outside of a black hole region, future null infinity could not be complete.

The formation of a singularity is an indication that general relativity is no longer applicable and that quantum gravity effects have become important. From a physical point of view, we are most interested in whether starting from initial data that can be described completely by classical general relativity, quantum gravity effects are guaranteed to be restricted to black hole regions so that they remain hidden from far-away observers. While the Weak Cosmic Censorship Conjecture is a necessary condition for this to be the case, it is not sufficient. In particular, the curvature could grow without bound inside the causal past of future null infinity, and only become singular on the event horizon so that future null infinity could still be complete. While this may seem like a corner case, the work presented in this thesis and in Refs. [33, 3, 2, 63, 64] suggests that it is very important as it can arise generically

in higher dimensions and in AdS space. For example, in chapters 4 and 5 of this thesis, we present strong numerical evidence that curvature scalars in the causal past of future null infinity can become arbitrarily large in higher dimensions. However, since numerical relativity simulations do not typically cover future null infinity or track the event horizon,² it is much less clear whether future null infinity is incomplete. This will be discussed in detail in chapter 6, where, armed with the numerical results from the simulations of black rings and Myers-Perry black holes, we will try to make the implications of Refs. [33, 3, 2] for the Weak Cosmic Censorship Conjecture more precise.

In the last forty years, there have been several numerical and mathematical attempts to find counterexamples to the Weak Cosmic Censorship Conjecture. Refs. [40, 67–69] studied spherically symmetric scalar field distributions, which collapse to black holes when their initial amplitude is sufficiently large. The results indicated that a naked singularity is formed exactly at the threshold of black hole formation. The same system was studied very recently without symmetry assumptions by Refs. [70, 48]. The problem with this setting is that the initial conditions are not generic: to produce a singularity, the initial amplitude has to be tuned precisely to its critical value. Christodoulou [71] showed mathematically that naked singularities can be formed in the collapse of inhomogeneous dust clouds. However, the assumption that the matter is dust, i.e. completely pressureless, makes this scenario unphysical or non-generic.

In AdS spacetimes, Ref. [63] presented strong evidence that regions of arbitrarily large curvature are not always hidden inside black holes, even in 4D. Recently, an analysis of stationary vacuum solutions in Ref. [64] suggested that this may happen even in vacuum and the authors are working to confirm this with fully non-linear numerical evolution. In AdS spacetimes, the boundary conditions play an important role. Therefore, it is likely that the AdS version of the Weak Cosmic Censorship Conjecture will have to be augmented with precise assumptions on what constitutes “reasonable” boundary conditions.

For the purpose of this thesis, the most important set of potential counterexamples to Weak Cosmic Censorship comes from the instability of black p -branes [72–74, 33, 75] and black holes which capture the behaviour of black p -branes. We will review this in detail in the next section.

Finally, we mention that there is a related but independent conjecture, the Strong Cosmic Censorship Conjecture, which is related to the global uniqueness of solutions. The Strong Cosmic Censorship Conjecture has been studied extensively in mathematical general relativity (e.g. in Refs. [68, 76–84]) and with numerical methods in Ref. [85]. Since this often

²See Refs. [65, 66] for two exceptions.

involves the study of black hole interiors, it lends itself much less well to numerical relativity simulations than the Weak Cosmic Censorship Conjecture.

1.2 Higher dimensional black holes

A very intriguing feature of Einstein's equations is that they generalise straightforwardly to any number of dimensions. This has motivated extensive research into whether a higher dimensional theory could unify general relativity and quantum field theory. These efforts were started by Kaluza [86] and Klein [87], who attempted to unify general relativity and electromagnetism, and continue today for example in the form of string theory and M-theory. Furthermore, the study of black holes in $5D$ is also motivated by the gauge-gravity duality [37–39], albeit in asymptotically AdS spacetimes. Progress in higher dimensions may also aid our efforts to understand the behaviour of solutions to Einstein's equations in $4D$. For example, since the Weak Cosmic Censorship Conjecture can be formulated in any number of dimensions, studying it in $D > 4$ will likely also improve our understanding of the $4D$ case.

Einstein's equations in higher dimensions lead to a much richer structure of solutions than in $4D$. We have already mentioned that black holes in higher dimensions can undergo instabilities, while their $4D$ counterparts are widely believed to be stable [15–18]. However, this is not the only way in which higher dimensional black holes exhibit richer behaviour: for example, while the horizon cross-sections of stationary black holes in $4D$ always have spherical topology [88], known results on higher dimensional black holes are much less restrictive [89, 90] and there is even an explicit example of a black hole with toroidal topology: the *black ring* [55]. Furthermore, while in $4D$ a stationary black hole solution is uniquely defined by its mass and angular momentum, we will see in chapter 4 that this is not the case in higher dimensions. Finally, in higher dimensions several black holes can be in equilibrium and form a stationary multi-black hole solution [91–94].

In the remainder of this section, we will briefly introduce the most important black hole solutions in higher dimensions. The simplest asymptotically flat black hole solution in higher dimensions is the Schwarzschild-Tangherlini solution [95], the higher dimensional generalisation of the Schwarzschild metric

$$ds^2 = - \left[1 - \left(\frac{r_H}{r} \right)^{D-3} \right] dt^2 + \frac{dr^2}{1 - \left(\frac{r_H}{r} \right)^{D-3}} + r^2 d\Omega_{D-2}^2. \quad (1.2)$$

This solution can be extended to include angular momentum in each of the $\lfloor (D-1)/2 \rfloor$ possible rotation planes [96]. The result is called the Myers-Perry black hole after the authors of Ref. [96] and is the higher dimensional analogue of the Kerr solution [14]. In addition to this, a stationary black hole solution with toroidal topology is known, the black ring. Remarkably, in $5D$ this solution was first found analytically [55]. Thereafter, black rings in $D = 6$ and 7 were constructed numerically in Refs. [97, 98]. We will examine black rings and Myers-Perry black holes in much more detail in chapters 4 and 5 respectively.

In spacetimes with compact extra dimensions, the simplest black holes are black p -branes, whose behaviour is very important for this thesis so we review them in more detail here. A black p -brane in D dimensions is the direct product of a $(D-p)$ -dimensional Schwarzschild-Tangherlini black hole with p -dimensional flat space. This leads to the metric [99]

$$ds^2 = ds_{\text{Schw.}(D-p)}^2 + \sum_{i=1}^p dx^i dx^i. \quad (1.3)$$

A black 1-brane is also called a *black string*. To make the entropy of the horizon finite, the flat directions are typically periodically identified, $x^i \sim x^i + L$. Black p -branes are very interesting mathematically for two reasons: firstly, they provided the first explicit evidence that black holes in higher dimensions can be unstable: when $L \gtrsim r_H$, where r_H is the horizon radius, black p -branes become unstable to the *Gregory-Laflamme* (GL) instability [72]. Secondly, the instability of black strings may lead to arbitrarily large curvature in the causal past of future null infinity or even a violation of the Weak Cosmic Censorship Conjecture.

The discovery of the GL instability initiated an intense search for possible end points. Gregory and Laflamme themselves conjectured in Ref. [72] that the instability would cause black strings to pinch off into a sequence of localised black holes since the latter have higher entropy than the original unstable uniform black string. This conjecture was cast into doubt when Ref. [100] showed that for a black string the horizon cannot reach zero size in a finite amount of affine parameter on the event horizon. Instead, the authors conjectured the existence of a family of non-uniform black strings that would be the end state of the GL instability. Such non-uniform black strings were indeed found [101, 102], but in $D < 14$ their entropy is lower than that of the uniform black string so that they could not possibly be the end point of the GL instability. A possible solution to this dilemma was presented in Refs. [74, 103], which argued that even if a pinch-off cannot be reached within finite affine parameter on the horizon, it could still happen in finite asymptotic time.³

³Ref. [103] attributes this idea to R. M. Wald.

Initially, fully non-linear numerical simulations of black strings [73, 74] were inconclusive since they could not follow the instability for long enough to be able to draw any conclusions about the end point. Finally, in 2010 Ref. [33] reported results of numerical simulations that allowed the authors to observe a pattern that strongly favoured the pinch off scenario: they showed that the GL instability gives rise to a sequence of spherical black holes connected by black string segments that are much thinner than the original black string. These string segments subsequently undergo the GL instability themselves and give rise to a new generation of localised black holes connected by even thinner black strings. Due to this self-similar structure, the time to pinch-off as measured by an asymptotic observer is just the sum of a geometric series and therefore finite. Ref. [33] also pointed out a similarity to the evolution of the Rayleigh-Plateau instability of fluid columns, whose connection to the GL instability had already been explored in Ref. [104]. In particular, they find that the thickness of the black string segments roughly follows a scaling law $r_H \propto t_c - t$, where t_c is the pinch-off time.

Thus, there is overwhelming numerical evidence that the horizon radius of black strings reaches zero size in finite asymptotic time. However, in a strongly asymptotically predictable spacetime, black hole regions cannot smoothly bifurcate [88]. Therefore, the simulations in Ref. [33] strongly suggest that a singularity is formed in the process of the black string pinching off. However, it may only be the event horizon that becomes singular; the spacetime outside the event horizon could remain smooth throughout and future null infinity could remain complete so that the precise statement of the Weak Cosmic Censorship Conjecture is not violated. However, even if this is the case, regions of arbitrarily large curvature scalars become visible at future null infinity suggesting that classical general relativity may no longer be sufficient. We will discuss this in more detail in chapter 6.

Since black p -branes have p compact directions, they are not asymptotically flat so that the black string spacetime could never be a counterexample to the Weak Cosmic Censorship Conjecture in its strict setting. However, there are asymptotically flat black holes in higher dimensions which, in certain regimes, mimic the behaviour of black p -branes. In this thesis, we will investigate two such black holes, black rings in $5D$ and Myers-Perry black holes in $6D$. This will allow us to study the role of asymptotic flatness in the Weak Cosmic Censorship Conjecture and, more concretely, whether the suggested counterexample to the Weak Cosmic Censorship Conjecture for black strings in Ref. [33] can be extended to asymptotically flat spacetimes.

1.3 Numerical relativity background

Even though a remarkably large number of analytic solutions to Einstein’s equations have been found, the study of general relativity in its full generality, without symmetry assumptions and with time dependence, requires approximations or numerical solutions. Attempts to solve Einstein’s equations on computers go back more than fifty years [105]. Despite this, the holy grail of numerical relativity, the simulation of an entire, non-axisymmetric binary black hole merger, remained elusive until very recently: in 2005, Pretorius [106] achieved the first-ever numerical evolution of a binary black hole spacetime with more than one orbit before merger. This was made possible partly by the rapid increase in the available computational power and partly by significant progress in the development of well-posed and stable evolution formalisms.

One of the challenges of numerical relativity is the gauge freedom in Einstein’s equations; they only fix the geometry of the spacetime uniquely, not the metric components, which depend on the coordinate system. To have any hope of constructing numerical solutions, we first have to choose a coordinate system in which the PDEs resulting from Einstein’s equations can be expressed in a way that makes them locally well-posed. We know that this is possible due to the proof of the local well-posedness of Einstein’s equations in Ref. [56], which used harmonic coordinates, $\nabla^\alpha \nabla_\alpha x^\mu = 0$. However, stable numerical evolution requires considerably more complicated formalisms. In this chapter, we present the most common ones: *Generalised Harmonic Coordinates* (GHCs) with constraint damping, the *Baumgarte-Shapiro-Shibata-Nakamura* (BSSN) formalism, and a close relative of BSSN called *Conformal Covariant Z4* (CCZ4) formalism. A useful necessary and sufficient algebraic criterion for local well-posedness is *strong hyperbolicity* [107–109]. Loosely, it requires that the principal part, the matrix of coefficients of the highest derivative terms, has real eigenvalues and is diagonalisable.^{4,5}

Despite the significant progress in numerical relativity methods in the last 20 years, there is no silver bullet that can solve Einstein’s equations numerically in all settings. The optimal choice of formalism depends heavily on the particular application and every new setting requires a lengthy exploration of the gauge parameter space and sometimes even completely new tricks. Therefore, in our treatment of BSSN/CCZ4 and GHCs, we try to include as much

⁴If only the first of these two requirements is satisfied, the system is called *weakly hyperbolic* and is not well-posed, not even locally.

⁵Since the author gave a detailed and more rigorous review of hyperbolicity and ellipticity of PDEs, including a proof of the strong hyperbolicity of the BSSN system, in an essay that he submitted for an MMath degree at the University of Cambridge, this information is not included here. The interested reader is referred to Refs. [110, 107].

intuition about why the formalisms work and what advantages and disadvantages they have. This will help us justify our choice of formalism in subsequent chapters and will motivate the improvements we had to make in order to be able to simulate higher dimensional spacetimes (chapter 3).

Finally, we mention that there is a related branch of numerical relativity, which we do not cover in this thesis: the numerical construction of stationary solutions to Einstein’s equations. In this setting, coordinate choices similar to GHCs are used to recast Einstein’s equations as an elliptic system of PDEs. This was studied in great detail in Refs. [111–116].

1.3.1 ADM, BSSN, and CCZ4

BSSN and CCZ4 are two very similar evolution systems that are based on the ADM formalism, which was proposed by Arnowitt, Deser, and Misner in 1959 [117]. To derive the ADM equations, we have to assume that we can pick a global time coordinate, t . This makes it possible to slice the spacetime into constant- t hypersurfaces Σ_t , which are all spacelike, and to write the D -dimensional spacetime metric as

$$ds^2 = -(\alpha^2 - \beta^i \beta_i) dt^2 + 2\beta_i dx^i dt + \gamma_{ij} dx^i dx^j, \quad (1.4)$$

where γ_{ij} is the induced metric on Σ_t , α is called the lapse function, and β is called the shift. This procedure of separating out the time coordinate is called the $d + 1$ split, where d is the number of spatial dimensions. As we will analyse in detail in the next section, lapse and shift define the coordinate system in formalisms based on the $d + 1$ split.

It is natural to choose the components of the spatial metric on the hypersurface, γ_{ij} , as evolution variables, but since Einstein’s equations are a set of second order PDEs, we also need information about their time derivative. A geometrically appealing way of specifying this information is through the extrinsic curvature of Σ_t , which is related to the Lie-derivative in the direction normal to the slice by

$$K_{ij} = -\frac{1}{2} \mathcal{L}_n \gamma_{ij}, \quad (1.5)$$

where n is the unit normal to the slice, $n = -\alpha dt$. In the ADM formalism, we evolve the quantities γ_{ij} and K_{ij} . In practice, the gauge functions α and β^i are also treated as evolution variables, whose evolution equations we are free to specify arbitrarily (although finding equations that lead to stable numerical evolution is not easy as we will discuss in the next section).

To reformulate Einstein's equations in terms of the evolution variables γ_{ij} and K_{ij} , we take all possible projections of Einstein's equations onto the normal vector n and onto the slice [110]. For the latter, we use the projection operator

$$\perp_b^a = \delta_b^a + n^a n_b. \quad (1.6)$$

To do this, let us first calculate all non-zero projections of the Riemann tensor. Projecting onto the slice in all indices yields *Gauss' equation*

$$\perp_a^e \perp_b^f \perp_c^g \perp_d^h R_{efgh} = \mathcal{R}_{abcd} + K_{ac}K_{bd} + K_{ad}K_{bc}, \quad (1.7)$$

where \mathcal{R}_{abcd} is the Riemann tensor of the spatial hypersurface Σ_t . Projecting three indices onto the hypersurface and one onto the normal vector leads to the *Codazzi equation*

$$\perp_a^e \perp_b^f \perp_c^g n^h R_{efgh} = -\mathcal{D}_a K_{bc} + \mathcal{D}_b K_{ac}, \quad (1.8)$$

where \mathcal{D}_a is the covariant derivative associated to the spatial metric γ , which can be shown to be equal to the projection of the spacetime covariant derivative onto the slice. Finally, projecting onto the normal vector twice and onto the slice twice yields

$$\perp_a^e n^f \perp_b^g n^h R_{efgh} = \mathcal{L}_n K_{ab} + K_{ac} K^c_b + \frac{1}{\alpha} \mathcal{D}_a \mathcal{D}_b \alpha. \quad (1.9)$$

All other projections either vanish or are related to the equations above through symmetries of the Riemann tensor.

Using the above projections of the Riemann tensor, we can calculate the possible projections of Einstein's equations. To do this, let us first introduce the following variables for the various projections of the Energy-Momentum tensor

$$\rho = T_{ab} n^a n^b, \quad j_a = -\perp_a^b T_{bc} n^c, \quad S_{ab} = \perp_a^c \perp_b^d T_{cd}. \quad (1.10)$$

Projecting onto the unit normal twice and using Gauss' equation (1.7) yields

$$\mathcal{R} - K_{ab} K^{ab} + K^2 = 16\pi\rho, \quad (1.11)$$

where K is the trace of the extrinsic curvature. Furthermore, by projecting one index of Einstein's equations onto the slice and one onto the unit normal and using the Codazzi

equation (1.8) we find

$$\mathcal{D}_c K^c{}_a - \mathcal{D}_a K = 8\pi j_a. \quad (1.12)$$

Neither of the above equations contain any information about the time derivative of the initial data and do not, therefore, form evolution equations for γ_{ij} and K_{ij} . Instead, they are constraint equations that have to be satisfied by the data on every constant-time slice. Equation (1.11) is called the *Hamiltonian constraint*, while (1.12) is called the *Momentum constraint*. If the constraints are satisfied by the initial data, they remain satisfied throughout the whole evolution, at least in the continuum limit. In practice, numerical errors always lead to constraint violating modes. Monitoring and minimising these constraint violations in order to check and improve the accuracy of simulations is one of the most important tasks in numerical relativity.

Finally, projecting Einstein's equations onto the slice on both indices and using (1.7) and (1.8) gives an evolution equation for the extrinsic curvature

$$\mathcal{L}_n K_{ab} = -\frac{1}{\alpha} \mathcal{D}_a \mathcal{D}_b \alpha + \mathcal{R}_{ab} + K K_{ab} - 2 K_{ac} K^c{}_b + 8\pi \left[\frac{S-\rho}{d-1} \gamma_{ab} - S_{ab} \right]. \quad (1.13)$$

Together with the constraint equations, this is all the information we can obtain from Einstein's equations and, indeed, all the information we need since the evolution equation for γ_{ij} follows directly from the definition of the extrinsic curvature (1.5). The only remaining step is to rewrite $\mathcal{L}_n K_{ab}$ and $\mathcal{L}_n \gamma_{ab}$ in terms of the basis vectors ∂_t and ∂_i . Thus, we obtain the ADM evolution equations

$$\begin{aligned} \partial_t \gamma_{ij} &= -2\alpha K_{ij} + \mathcal{L}_\beta \gamma_{ij}, \\ \partial_t K_{ij} &= \mathcal{L}_\beta K_{ij} - \mathcal{D}_i \mathcal{D}_j \alpha + \alpha (\mathcal{R}_{ij} + K K_{ij} - 2 K_{im} K^m{}_j) \\ &\quad + 8\pi \alpha \left(\frac{S-\rho}{d-1} \gamma_{ij} - S_{ij} \right). \end{aligned} \quad (1.14)$$

By itself, the ADM formalism is of limited use for numerical relativity, since in the general setting without symmetry assumptions it is not well-posed, not even locally. However, it is possible to modify the evolution variables in such a way as to make the equations well-posed. A particularly stable reformulation of ADM is called BSSN. It was suggested in Refs. [118, 119] and implemented and tested systematically in Ref. [120]. BSSN introduces four modifications to the ADM equations:

1. Instead of evolving the spatial metric directly, we evolve a conformal factor, χ , and a conformal metric $\tilde{\gamma}_{ij}$, which has unit determinant,

$$\chi = (\det \gamma)^{-\frac{1}{d}} \quad \text{and} \quad \tilde{\gamma}_{ij} = \chi \gamma_{ij}. \quad (1.15)$$

This important modification allows us to absorb divergences in $\tilde{\gamma}$: as $\tilde{\gamma}$ tends to infinity, χ simply tends to zero.

2. Instead of the extrinsic curvature, we evolve its trace, $K = K^i_i$, and the conformally rescaled trace-free part $\tilde{A}_{ij} = \chi K_{ij}^{\text{TF}}$.
3. We introduce new evolution variables corresponding to the contracted conformal connection functions $\tilde{\Gamma}^i = \tilde{\gamma}^{mn} \tilde{\Gamma}_{mn}^i$. The motivation behind this change is that in their original form, the ADM equations contain second spatial derivatives of the metric in the form of derivatives $\partial_j \tilde{\Gamma}^i$, which spoil the strong hyperbolicity and thus the local well-posedness of the ADM system. By promoting $\tilde{\Gamma}^i$ to evolution variables, we can replace the offending second derivatives of the metric with first derivatives of the evolved conformal connection functions.
4. Finally, we add multiples of the momentum constraint to eliminate derivatives of the extrinsic curvature in the evolution equation of $\tilde{\Gamma}^i$ and multiples of the Hamiltonian constraint to eliminate the Ricci scalar from the evolution equation of K .

It can be shown [110] that the BSSN formalism, i.e. the ADM formalism with the above modifications, is strongly hyperbolic and thus locally well-posed. This is a minimum requirement for stable simulations, but it is by no means sufficient. In practice, BSSN has been found to be very stable in astrophysical settings such as binary black hole mergers and is one of the most widely used formalisms in numerical relativity.

For most of the numerical results presented in this thesis, we have used a refinement of the BSSN system that is called *Conformal Covariant Z4* (CCZ4) system and was proposed in Refs. [121–124]. The problem with BSSN is that violations of the Hamiltonian constraint do not decay and do not propagate out of the computational domain. While this is a substantial improvement over ADM, which often exhibits rapid growth of the Hamiltonian constraint, it is not ideal as constraint violations can accumulate over time and may eventually spoil the simulation. To solve this problem, Ref. [121, 122] added new propagating degrees of freedom, Z^a , to the trace-reversed Einstein equations

$$R_{ab} + 2 \nabla_{(a} Z_{b)} - \kappa_1 [2 n_{(a} Z_{b)} - (1 + \kappa_2) g_{ab} n^c Z_c] = 8\pi \left(T_{ab} - \frac{1}{D-2} g_{ab} T \right), \quad (1.16)$$

where κ_1 and κ_2 are arbitrary parameters. With this modification of Einstein's equations, the Hamiltonian and Momentum constraints become evolution equations for Z^0 and Z_i respectively. If Z^a vanishes initially, then in the continuum limit it will remain zero throughout the whole evolution so that Einstein's equations are recovered in (1.16). However, if numerical errors lead to constraint violations and, thus, non-zero Z^a , these constraint violations can propagate and leave the numerical grid (assuming that this is allowed by the boundary conditions). Furthermore, the terms proportional to κ_1 and κ_2 can be shown to damp constraint violating modes as long as $\kappa_1 > 0$ and $\kappa_2 > -1$ [122].

The use of constraint damping terms is crucial in our work for several reasons: firstly, the adaptive mesh refinement that is required to make our simulations feasible constantly introduces constraint violations at the boundaries between refinement levels. Without constraint damping, this can significantly impact the simulation. Secondly, since small constraint violations are damped away before any significant physical evolution takes place, we can excite various instabilities of the spacetime with small constraint violating perturbations without the need for an initial data solver. Finally, for simulations in AdS space (chapter 7), where numerical errors cannot propagate out of the computational domain, constraint damping terms are essential for long-term accuracy.

The derivation of the CCZ4 equations follows exactly the same procedure as the derivation of the BSSN equations but starting from (1.16) instead of Einstein's equations. That is, we perform the $d + 1$ split, derive the modified ADM equations, and conformally rescale the variables similarly to the BSSN formalism. The crucial difference is that in CCZ4 we have the additional degrees of freedom Z^a . These are not evolved directly; instead, we define new evolution variables Θ and $\hat{\Gamma}^i$ through

$$\Theta = -n_a Z^a \quad \text{and} \quad \hat{\Gamma}^i = 2\gamma^{ij} Z_j + \tilde{\Gamma}^i. \quad (1.17)$$

The former represents the propagating degree of freedom corresponding to the Hamiltonian constraint; the latter replaces the evolved conformal connection functions of BSSN, and gives them a new meaning as propagating degrees of freedom corresponding to the momentum constraint. Thus, the somewhat ad-hoc step of promoting $\tilde{\Gamma}^i$ to an evolution variable in BSSN happens naturally in CCZ4 through the introduction of the evolution variable $\hat{\Gamma}^i$. For constraint-preserving initial data, $\Theta = 0$ and $\hat{\Gamma}^i = \tilde{\Gamma}^i$ initially.

The result of the procedure - the CCZ4 formalism - is displayed in Box 1. It is important to note that in the evolution equations we never need to evaluate the Ricci tensor on its own: it always appears in the combination $\mathcal{R}_{ij} + 2\mathcal{D}_{(i} Z_{j)}$. In this combination, derivatives of the

conformal connection function that would spoil the well-posedness cancel out. Instead, we are left with first derivatives of the evolution variable $\hat{\Gamma}^i$.

The extra parameter κ_3 in (1.23) was introduced in Ref. [123] due to stability problems when simulating black hole spacetimes. However, Ref. [124] showed that if one replaces κ_1 by κ_1/α one can make the covariant choice $\kappa_3 = 1$ while still retaining stability. The rationale behind this redefinition is that the constraint damping terms are multiplied by $\alpha\kappa_1$ and so the replacement prevents the damping terms from being switched off inside the black hole where the lapse is usually close to zero as we will see in the next section.

1.3.2 Gauge choice in BSSN and CCZ4

One of the biggest challenges in numerical relativity is the choice of coordinates. On the one hand, the coordinate system can ruin numerical simulations if it develops singularities. On the other hand, we can use the gauge freedom to our advantage when simulating black holes: since the coordinate system specifies which locations on the manifold a point on the numerical grid corresponds to, we can avoid simulating regions close to a physical singularity by a clever choice of coordinates. One of the main advantages of the $d+1$ split, and therefore the BSSN and CCZ4 formalisms, is that it allows very intuitive control over the coordinate system through the choice of lapse and shift.

To study this, let us first define the language that we will use more precisely: we will talk about the location and movement of grid points in the spacetime. By this we mean the locations in the spacetime that correspond to the grid points of our numerical domain. More precisely, if (t, x^i) is a grid point and we have a chart ϕ that maps points on the manifold to the numerical domain, then we refer to $\phi^{-1}(t, x^i)$ as the location of the grid point on the manifold. Since ϕ has a unique inverse, this language is not ambiguous.

Furthermore, we introduce the concept of a *normal observer*, an observer who moves normal to the slice with velocity n . Normal observers describe how constant-time slices evolve, but do not follow the motion of grid points parallel to the slice. While we care most about grid points, the motion of normal observers is usually easier to analyse and often gives us enough information: if the slice itself does not intersect a black hole singularity, no grid point can have reached it. The rate of change of coordinate time along the worldline of a normal observer is $dt/d\tau = \alpha^{-1}$. This gives us a useful interpretation of the lapse: it determines how much the spatial slice moves in the manifold as t is increased, as measured by the proper time of normal observers. If the lapse tends to zero, the slice does not evolve as t is increased.

Box 1: CCZ4 formalism

$$\partial_t \chi = \frac{2\chi}{d} \left(\alpha K - \partial_k \beta^k \right) + \beta^k \partial_k \chi, \quad (1.18)$$

$$\partial_t \tilde{\gamma}_{ij} = -2\alpha \tilde{A}_{ij} + 2\tilde{\gamma}_{k(i} \partial_{j)} \beta^k - \frac{2}{d} \tilde{\gamma}_{ij} \partial_k \beta^k + \beta^k \partial_k \tilde{\gamma}_{ij}, \quad (1.19)$$

$$\begin{aligned} \partial_t \tilde{A}_{ij} = & \chi \left[-\mathcal{D}_i \mathcal{D}_j \alpha + \alpha \left(\mathcal{R}_{ij} + 2\mathcal{D}_{(i} Z_{j)} - 8\pi \alpha S_{ij} \right) \right]^{\text{TF}} + \alpha \tilde{A}_{ij} (K - 2\Theta) \\ & - 2\alpha \tilde{A}_{il} \tilde{A}^l_j + 2\tilde{A}_{k(i} \partial_{j)} \beta^k - \frac{2}{d} \tilde{A}_{ij} \partial_k \beta^k + \beta^k \partial_k \tilde{A}_{ij}, \end{aligned} \quad (1.20)$$

$$\begin{aligned} \partial_t \Theta = & \frac{1}{2} \alpha \left(\mathcal{R} + 2\mathcal{D}_i Z^i - \tilde{A}_{ij} \tilde{A}^{ij} + \frac{d-1}{d} K^2 - 2\Theta K \right) - Z^i \partial_i \alpha \\ & + \beta^k \partial_k \Theta - \frac{1}{2} \alpha \kappa_1 (D + (d-1)\kappa_2) \Theta - 8\pi \alpha \rho, \end{aligned} \quad (1.21)$$

$$\begin{aligned} \partial_t K = & 2(\partial_t \Theta - \beta^k \partial_k \Theta) + \alpha \left(\tilde{A}_{ij} \tilde{A}^{ij} + \frac{1}{d} K^2 \right) - \mathcal{D}^i \mathcal{D}_i \alpha + \kappa_1 \alpha (1 - \kappa_2) \Theta \\ & + 2Z^i \partial_i \alpha + \beta^k \partial_k K + 4\pi \alpha (S + \rho), \end{aligned} \quad (1.22)$$

$$\begin{aligned} \partial_t \hat{\Gamma}^i = & -2\tilde{A}^{ij} \partial_j \alpha + 2\alpha \left(\tilde{\Gamma}_{jk}^i \tilde{A}^{jk} - \frac{d-1}{d} \tilde{\gamma}^{ij} \partial_j K - \frac{d}{2} \tilde{A}^{ij} \frac{\partial_j \chi}{\chi} \right) \\ & + \beta^k \partial_k \hat{\Gamma}^i + \tilde{\gamma}^{jk} \partial_j \partial_k \beta^i + \frac{d-2}{d} \tilde{\gamma}^{ij} \partial_j \partial_k \beta^k \\ & + \frac{2}{d} \tilde{\Gamma}^i \partial_k \beta^k - \tilde{\Gamma}^k \partial_k \beta^i + 2\kappa_3 \left(\frac{2}{d} \tilde{\gamma}^{ij} Z_j \partial_k \beta^k - \tilde{\gamma}^{jk} Z_j \partial_k \beta^i \right) \\ & + 2\tilde{\gamma}^{ij} \left(\alpha \partial_j \Theta - \Theta \partial_j \alpha - \frac{2}{d} \alpha K Z_j \right) - 2\alpha \kappa_1 \tilde{\gamma}^{ij} Z_j - 16\pi \alpha \tilde{\gamma}^{ij} j_j, \end{aligned} \quad (1.23)$$

The combination $\mathcal{R}_{ij} + 2\mathcal{D}_{(i} Z_{j)}$ is calculated using

$$\begin{aligned} \mathcal{R}_{ij} + 2\mathcal{D}_{(i} Z_{j)} = & -\frac{1}{2} \tilde{\gamma}^{mn} \partial_m \partial_n \tilde{\gamma}_{ij} + \tilde{\gamma}^{mn} \left[2\tilde{\Gamma}_{m(i}^k \tilde{\Gamma}_{j)kn} + \tilde{\Gamma}_{im}^k \tilde{\Gamma}_{kjn} \right] \\ & + \tilde{\gamma}_{m(i} \partial_{j)} \hat{\Gamma}^m + \tilde{\Gamma}^m \tilde{\Gamma}_{(ij)m} + \frac{D-3}{2\chi} \left(\tilde{D}_i \tilde{D}_j \chi - \frac{1}{2\chi} \partial_i \chi \partial_j \chi \right) \\ & + \frac{1}{2\chi} \tilde{\gamma}_{ij} \left[\tilde{\gamma}^{mn} \tilde{D}_m \tilde{D}_n \chi - \frac{D-1}{2\chi} \tilde{\gamma}^{mn} \partial_m \chi \partial_n \chi \right] \end{aligned} \quad (1.24)$$

In the BSSN/CCZ4 notation the Hamiltonian and Momentum constraints are

$$\mathcal{H} = R + \frac{d-1}{d} K^2 - \tilde{A}_{ij} \tilde{A}^{ij} - 16\pi \rho = 0, \quad (1.25)$$

$$\mathcal{M}_i = \tilde{\gamma}^{jl} \partial_j \tilde{A}_{li} + \tilde{\Gamma}^k \tilde{A}_{ki} - \frac{d-1}{d} \partial_i K - \frac{d}{2} \frac{\partial_j \chi}{\chi} \tilde{A}^j_i - 8\pi j_i = 0. \quad (1.26)$$

The worldline of grid points has tangent vector ∂_t , which can be written in terms of lapse and shift using (1.4)

$$\frac{\partial}{\partial t} = \alpha n + \beta^i \frac{\partial}{\partial x^i}. \quad (1.27)$$

Thus, the shift controls the speed at which grid points move parallel to the slice. It is important to stress that grid points do not have to follow physically allowed paths; they may even move faster than the speed of light.⁶ Indeed, this is necessary for black hole simulations in order to prevent grid points from falling further into the black hole.

From (1.27) we can immediately deduce that the simplest possible slicing condition, $\alpha = 1$, is not a good choice for numerical evolution. If $\alpha = 1$, then a quick calculation [110] shows that $n^a \nabla_a n^b = 0$, so that normal observers move on geodesics. Since in general relativity geodesics often focus, this makes the slicing condition prone to the formation of coordinate singularities. For black hole spacetimes, it causes spatial slices to intersect the singularity in finite coordinate time. While in theory it might be possible to find a shift condition that constantly moves grid points to parts of the slice that have not reached the singularity yet, in practice this would be very hard to achieve in a stable manner. To find a more promising condition, let us consider the change of the volume element along the wordline of grid points

$$\frac{\partial_t \sqrt{\gamma}}{\sqrt{\gamma}} = -\alpha K + \mathcal{D}_i \beta^i. \quad (1.28)$$

If we can keep the right hand side of this equation close to zero, we can ensure that volume elements do not shrink to zero size, suggesting the the slice does not reach the singularity. This explains why *maximal slicing* [125], defined by $K = 0$, is a very stable slicing condition as long as the shift condition ensures that the second term in (1.28) does not become very negative. Maximal slicing is achieved by choosing initial data that satisfy $K = 0$ and solving the equation $\partial_t K = 0$ for the lapse in every time step. However, this involves solving an elliptic equation at every step, which is very expensive. Instead, we use a hyperbolic slicing condition called 1 + log slicing [126, 127]

$$\partial_t \alpha = -2\alpha K. \quad (1.29)$$

With this condition, when K is large and volume elements decrease rapidly, the lapse collapses to zero. This in turn stops the slice from evolving in that region of the spacetime so that it

⁶This is the reason for why in this thesis we refrain from using the term *coordinate observers*, which is sometimes used in literature. The term “observer” is misleading as it implies that the motion is physical.

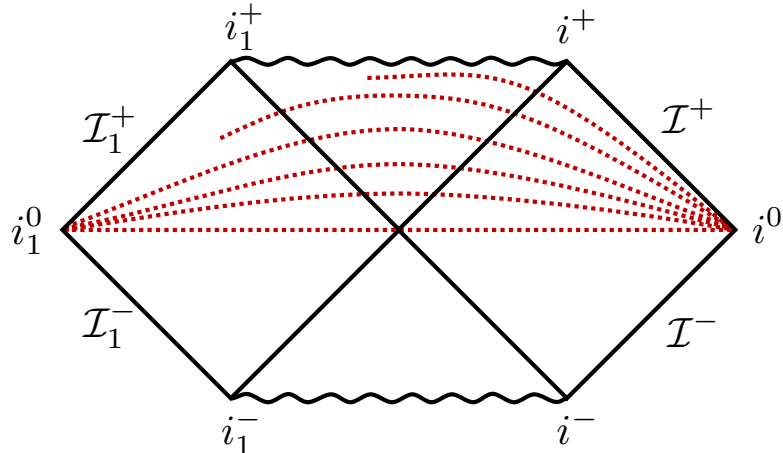


Fig. 1.1 Sketch of the evolution of constant-time slices with puncture gauge, starting from isotropic coordinates, based on numerical data presented in Ref. [128]. The slice itself always stays connected to the other asymptotically flat end, but the grid points are pushed along the slice towards future infinity by the Gamma-driver shift condition. Thus, after a while the other asymptotically flat end is no longer covered by the numerical grid.

does not reach the singularity. For CCZ4, K is typically replaced by $K - 2\Theta$ in (1.29). This does not change the equations in the continuum limit but is used for consistency with BSSN. In the latter, we subtract multiples of the Hamiltonian constraint in the evolution equation for K , which in CCZ4 corresponds to subtracting 2Θ .

The existence of singularity avoiding gauges for BSSN and CCZ4 is a considerable advantage. It means that if we start with initial data that do not contain a physical singularity, such as the Schwarzschild black hole written in isotropic coordinates, we can evolve in time without ever having to worry about the black hole singularity. Fig. 1.1 shows the evolution of constant- t hypersurfaces with $1 + \log$ slicing and the Gamma-driver shift condition (which will be discussed below) in a Penrose diagram. The gauge allows us to simulate the whole future of the event horizon without the slices ever reaching the singularity.

Since the lapse has to tend to zero inside a black hole to prevent the slice from reaching the singularity, it is important that this region of small lapse moves with the black hole. In simulations of binary black hole spacetimes, we therefore add an advection term $\beta^i \partial_i \alpha$ to (1.29). If the shift is non-zero, this term allows regions of small α to propagate across the grid. For most simulations in this thesis, we will use the CCZ4 version of $1 + \log$ slicing with an advection term

$$\partial_t \alpha = -2\alpha(K - 2\Theta) + \beta^i \partial_i \alpha. \quad (1.30)$$

The $1 + \log$ slicing condition ensures that spatial slices never reach the black hole singularity, but this is not sufficient for a successful simulation. The reason for this is simple: as we evolve forward in time, more and more grid points move along the slice into the black hole where the evolution is frozen due to the singularity avoiding slicing condition. Thus, the horizon expands in the numerical domain until all grid points are inside the black hole. Furthermore, the distance between grid points increases as they fall into the black hole, causing rapid growth of the radial metric components. This effect is called *slice stretching*.

Both these problems can be solved by using a superluminal outward-pointing shift that prevents grid points from falling towards the black hole. Currently, the most popular way of achieving this is by the so called *Gamma-driver* shift condition

$$\partial_t \beta^i = FB^i, \quad \partial_t B^i = \partial_t \hat{\Gamma}^i - \eta B^i, \quad (1.31)$$

where B^i is a new auxiliary evolution variable and F and η are parameters that we can specify freely. The action of the Gamma-driver is clearly visible in Fig. 1.1: even though constant- t slices remain attached to both spatial infinities throughout the evolution, grid points on the left are pushed towards i^+ so that after a while the numerical grid no longer covers the other asymptotically flat end.

To obtain a rough estimate of suitable values for the gauge parameters, we note that the choice of F affects the speed of propagation of gauge modes [129]. It is helpful for numerical stability to require the longitudinal part of gauge modes to travel at the speed of light in the asymptotically flat region. This fixes [130]

$$F = \frac{D-1}{2(D-2)}. \quad (1.32)$$

The parameter η determines the timescale over which unwanted oscillations of the shift should be damped. This is usually estimated by dimensional analysis so that $\eta \approx M^{-1/(D-3)}$. These choices for F and η are only rules of thumb and have to be adapted slightly in non-standard settings. However, it is usually not possible to change η and F by more than an order of magnitude without preventing the Gamma-driver from performing its task effectively. Thus, finding a suitable value for η becomes challenging for simulations of black holes with multiple length scales such as very thin rings. We will discuss a solution to this problem in chapter 3.

The success of the Gamma-driver relies on the shift vector becoming superluminal inside the black hole horizon. This is not a problem per se since it is only a gauge effect, but it can cause numerical instabilities. These instabilities can be avoided by using stencils that

are lopsided in the direction that the shift points in [110]. The need for one-sided stencils is a very inconvenient side-effect of singularity avoiding gauges as calculating the additional derivatives takes a noticeable amount of the run time and the necessary code is hard to optimise. We will discuss how this problem is addressed in GRCHOMBO in section 2.5.

The choice of $1 + \log$ slicing, together with the Gamma-driver shift condition, was essential for the successful simulation of binary black hole mergers with BSSN [131, 132] and has become the most widely used gauge condition for BSSN and CCZ4. Since it allows the evolution inside black holes to be frozen and to move these frozen regions across the numerical grid, it is often called the *moving puncture gauge*.

1.3.3 Initial data for the puncture gauge

To be able to use the puncture gauge in black hole simulations, the initial data must not contain any physical singularities. For the Schwarzschild-Tangherlini black hole, this can be achieved by using isotropic coordinates, in which the metric reads

$$ds^2 = - \left(\frac{4\rho^{D-3} - r_0^{D-3}}{4\rho^{D-3} + r_0^{D-3}} \right)^2 dt^2 + \left(1 + \frac{r_0^{D-3}}{4\rho^{D-3}} \right)^{\frac{4}{D-3}} (d\rho^2 + \rho^2 d\Omega_{D-2}^2), \quad (1.33)$$

where r_0 is the Schwarzschild radius of the black hole. These coordinates cover two copies of the exterior of the black hole and do not contain a physical singularity, only a coordinate singularity at $\rho = 0$. In BSSN variables and Cartesian coordinates, (1.33) becomes

$$\chi = \left(\frac{4\rho^{D-3}}{4\rho^{D-3} + r_0^{D-3}} \right)^{\frac{4}{D-3}}, \quad \tilde{\gamma}_{ij} = \delta_{ij}, \quad \tilde{\Gamma}^i = 0, \quad \tilde{A}_{ij} = 0, \quad K = 0. \quad (1.34)$$

This demonstrates the power of the conformal split in BSSN: even though the metric has a coordinate singularity at $\rho = 0$, the BSSN variables are all completely well-behaved and the conformal factor χ smoothly tends to zero. For the few divisions by χ in the evolution variables in Box 1, we can introduce a small cut-off on χ . Since this only needs to be done for at most one grid point deep inside the horizon, it does not affect the evolution elsewhere.

The metric (1.34) leads to the analytic initial gauge

$$\alpha = \frac{4\rho^{D-3} - r_0^{D-3}}{4\rho^{D-3} + r_0^{D-3}}, \quad \beta^i = 0. \quad (1.35)$$

The analytic lapse becomes zero at the bifurcation $(D - 2)$ -sphere and subsequently changes sign in the other asymptotically flat end. This is clearly unsuitable for numerical evolution: it is undesirable to freeze the evolution on the horizon - the region we are most interested in - and it is impossible to evolve backwards in time in the other asymptotically flat end. However, since the lapse is only a gauge variable, we can prescribe any function of our choice. Since 1 + log slicing causes the lapse to tend to zero at the puncture to prevent the slice from falling into the black hole singularity, we can minimise gauge adjustment by choosing an initial lapse that is already zero there. A popular choice is the *pre-collapsed lapse* [132, 129]

$$\alpha = \chi^{\frac{D-3}{2}}, \quad (1.36)$$

where we have chosen the exponent so that the pre-collapsed lapse has the same leading order behaviour as the analytic lapse

$$\chi^{\frac{D-3}{2}} = 1 - \frac{r_H^{D-3}}{2\rho^{D-3}} + O\left(\frac{r_H^{2D-6}}{\rho^{2D-6}}\right) = \alpha_{\text{analytic}}. \quad (1.37)$$

Somewhat surprisingly, the puncture method is so robust that it also leads to stable evolution if we choose initial data that contain a physical singularity, as long as we smooth out the singularity using the turduckening method [133, 134]. In the turduckening method of order p , a singular function is capped off such that it is C^p at the edge of the turduckened region. For example, to turducken the function $1/r$ inside the region $r < r_t$ we replace r by

$$\begin{aligned} \max(r_t, r) & \quad 0^{\text{th}} \text{ order,} \\ \max\left(\frac{1}{2}r_t + \frac{1}{2}\frac{r^2}{r_t}, r\right) & \quad 1^{\text{st}} \text{ order,} \end{aligned} \quad (1.38)$$

and similarly for higher orders.

1.3.4 Generalised harmonic coordinates

Any numerical relativity algorithm is based on two fundamental choices: the evolution variables, and the coordinate system, i.e. the functions $x^\mu(p)$ that map points p on the manifold to the computational domain. Assuming that we can pick a global time coordinate, $x^0 = t$, the most intuitive choice of evolution variables would be the metric components, $g_{\mu\nu}$, and their time derivatives, $\partial_t g_{\mu\nu}$. Written in terms of metric components, Einstein's

equations in trace-reversed form are

$$\begin{aligned} R_{\mu\nu} &= -\frac{1}{2}g^{\alpha\beta}\partial_\beta\partial_\alpha g_{\mu\nu} - \partial_\beta g_{\alpha(\mu}\partial_{\nu)}g^{\alpha\beta} - \Gamma_{\beta\mu}^\alpha\Gamma_{\alpha\nu}^\beta + g_{\lambda(\mu}\nabla_{\nu)}\Gamma^\lambda \\ &= 8\pi\left(T_{\mu\nu} - \frac{T}{D-2}g_{\mu\nu}\right). \end{aligned} \quad (1.39)$$

The only term that prevents these equations from being manifestly strongly hyperbolic is the term involving derivatives of the contracted Christoffel symbols. To eliminate this term, we use *generalised harmonic coordinates* (GHCs)

$$\nabla^\alpha\nabla_\alpha x^\mu = -g^{\alpha\beta}\Gamma_{\alpha\beta}^\mu = -\Gamma^\mu \equiv H^\mu, \quad (1.40)$$

where $H^\mu(x^\nu)$ is an arbitrary function. With GHCs, we can replace the offending derivatives by $\nabla_{(\mu}H_{\nu)}$ so that Einstein's equations become

$$\begin{aligned} &-\frac{1}{2}g^{\alpha\beta}\partial_\beta\partial_\alpha g_{\mu\nu} - \partial_\beta g_{\alpha(\mu}\partial_{\nu)}g^{\alpha\beta} - \partial_{(\mu}H_{\nu)} + H_\alpha\Gamma_{\mu\nu}^\alpha - \Gamma_{\beta\mu}^\alpha\Gamma_{\alpha\nu}^\beta \\ &= 8\pi\left(T_{\mu\nu} + \frac{T}{D-2}g_{\mu\nu}\right). \end{aligned} \quad (1.41)$$

This is a non-linear wave equation and therefore manifestly strongly hyperbolic⁷. Harmonic coordinates ($H^\mu = 0$) were already used by Ref. [56] in the first proof of well-posedness of Einstein's equations. However, in numerical relativity non-zero H^μ are necessary to allow some control over the gauge.

GHCs introduce a new coordinate constraint given by

$$C^\mu = H^\mu + \Gamma^\mu = 0. \quad (1.42)$$

If this constraint is satisfied initially, the Bianchi identity implies that it will be satisfied for all time in the continuum limit. However, in early attempts with GHCs, numerical errors led to large violations of the coordinate constraints that spoiled the simulations. This problem can be solved with exactly the same constraint damping mechanism that is used for CCZ4: instead of solving Einstein's equations, we solve the modified Einstein's equations (1.16) with additional degrees of freedom $Z^\mu = -C^\mu$ representing the constraints [122]. This leads to the widely used GHC formalism with constraint damping in Box 2.

⁷It even satisfies the stronger criterion of *symmetric hyperbolicity*, which also requires that the principal symbol is hermitian or becomes hermitian when multiplied by a suitable positive definite hermitian matrix [107–109].

Box 2: GHC formalism with constraint damping:

$$\begin{aligned} & -\frac{1}{2}g^{\alpha\beta}\partial_\beta\partial_\alpha g_{\mu\nu} - \partial_\beta g_{\alpha(\mu}\partial_{\nu)}g^{\alpha\beta} - \partial_{(\mu}H_{\nu)} + H_\alpha\Gamma_{\mu\nu}^\alpha - \Gamma_{\beta\mu}^\alpha\Gamma_{\alpha\nu}^\beta \\ & - \kappa_1(2n_{(\mu}C_{\nu)} - (1 + \kappa_2)g_{\mu\nu}n^\alpha C_\alpha) = 8\pi\left(T_{\mu\nu} + \frac{T}{D-2}g_{\mu\nu}\right), \end{aligned} \quad (1.43)$$

with constraint equations $C^\mu = H^\mu + \Gamma^\mu = 0$.

With GHCs, the coordinates can only be controlled through the choice of gauge source functions H^μ and the stability of the method depends heavily on this choice. For example, a time evolution code based on (1.43) must assume that $x^0 = t$ remains the timelike coordinate throughout the whole evolution and gauge source functions must ensure that this is indeed the case. Furthermore, they must prevent the formation of coordinate singularities in the domain. The choice of source functions has been studied much less than the choice of gauge in the $d+1$ split. Despite this, stable evolution with GHCs has been achieved in many settings. Most importantly, the first-ever simulation of a binary black hole merger by Pretorius [106] was carried out with GHCs. More recently, GHCs have also been used in higher dimensions for studying black strings [33] and in AdS [135, 136].

Even though one can transfer some of the experience with gauge choices in BSSN and CCZ4 by expressing the gauge source functions in terms of ADM variables, it has so far not been possible to find source functions that prevent grid points from falling into the black hole singularity. As a result, black hole simulations with GHCs require *excision*. The principle of excision is simple: since in the continuum limit no information can escape the black hole, one can excise a small region around the singularity from the computational domain. If the resolution is high enough, the errors that are incurred at the excision boundary do not affect the region outside the black hole.

An implementation of excision requires three steps: first, we have to find the apparent horizon to know how large the excision region can be and what shape it should have. Thereafter, we excise a suitable region and ensure that all points close to the excision boundary use appropriate one-sided stencils. Finally, as the black hole moves across the numerical grid, we have to move the excision region too, repopulating grid points that are no longer excised by extrapolating from nearby points. On top of this, we have to find a choice of gauge source functions, dissipation, and damping parameters that keeps the numerical evolution close to the excision surface stable.

1.3.5 Comparison of formalisms

We finish the discussion of GHCs with a comparison to BSSN/CCZ4. Both formalisms are very commonly used in numerical relativity; which one is preferable depends heavily on the application, the accuracy and performance requirements, and what numerical infrastructure is in place already.

Considering only the evolution equations, the GHC formalism is much simpler than BSSN and CCZ4. As a result, it is easier to write, maintain, and debug GHC code. This is also an advantage from a performance point of view: not only do the evolution equations require fewer operations per right hand side evaluation, they are also easier for the compiler to optimise. BSSN and CCZ4 require very lengthy calculations and the need for lopsided stencils in the calculation of advection derivatives harms the performance further. The simplicity of the GHC formalism also makes it much easier to adapt the code to new settings. This is one of the reasons for why evolution in AdS has been possible with GHCs [135, 136], but has not yet been achieved with BSSN or CCZ4.

The GHC formalism also has a much simpler mathematical structure than BSSN and CCZ4: the principal terms in the evolution system (1.43) are just a wave operator. This makes it much easier to use implicit integration schemes or spectral methods so that GHCs are ideal when very high accuracy is required. An example of this is the Spectral Einstein Code (SpEC) [137], which was used to produce the majority of numerical relativity waveforms for LIGO [138].

The main disadvantage of GHCs is that they allow a less intuitive control over the gauge than BSSN and CCZ4. This makes it harder to prevent coordinate singularities and is the reason for why no singularity-avoiding gauge condition has been found for GHCs to date. As a result, simulations of black hole spacetimes require excision. For most applications, excision is very hard to implement and means that one cannot use publicly available PDE solvers out of the box. Excision is especially difficult for higher dimensional black holes such as black rings and Myers-Perry black holes, which can take on very complicated shapes when they become unstable. This makes it hard to implement an apparent horizon finder that converges reliably and means that we would have to use a very complicated excision region. Excision is also bad for performance. The main reason for this is that in order to be able to excise correctly, we have to find the apparent horizon often. This can be very costly, especially when the apparent horizon finder needs many steps to converge.

Chapter 2

GRCHOMBO

This chapter presents the GRCHOMBO code, analyses its accuracy and performance, and explains its current design.

Sections 2.2 and 2.3 are based on the co-authored publication Ref. [5]. The performance tests in section 2.4 were carried out by myself with useful comments and advice from A. Duran, K. Kornet, and J. Jäykkä. I devised the current design of GRCHOMBO (section 2.5) in collaboration with S. Tunyasuvunakool and implemented large parts of the current code. GRCHOMBO is a truly collaborative effort and I am very thankful to the whole collaboration and especially K. Clough for many valuable discussions and their contributions to the code.

2.1 Introduction

In this chapter, we present GRCHOMBO, a new open-source, multi-purpose general relativity code. GRCHOMBO was first released in the code paper Ref. [5] and was made public earlier this year¹. When it was first released, GRCHOMBO was developed by six researchers at three institutions and had just over 4000 lines of code, almost all of which were contained in two files. By now, it is developed and used by around fifteen researchers at six institutions and comprises just under 20,000 lines of code in approximately 150 files. Since its first release, GRCHOMBO has led to eight publications, three of which are presented in this thesis.

GRCHOMBO is by far not the only numerical relativity code. The most famous alternatives include *SPeC* [137] and the *Einstein toolkit* [139]. *SPeC* uses the *GHC* formalism and spectral methods and is the ideal choice for producing highly accurate gravitational wave templates

¹GRCHOMBO is available at www.grchombo.org or directly on GitHub at www.github.com/GRChombo.

for LIGO. The Einstein toolkit is the most commonly used code for BSSN evolution and includes moving box refinement and some adaptive mesh support. In addition to this, a plethora of other open- and closed-source numerical relativity codes exist [140].

With GRCHOMBO, we do not try to compete with SPeC, the ideal tool for gravitational wave templates, or the Einstein toolkit. Instead, we aim to open up new avenues of research in numerical relativity by enabling a wide range of problems in cosmology, higher dimensional black holes, and AdS/CFT to be tackled easily and with feasible computational requirements. As a result, the defining features of GRCHOMBO are a very flexible design which allows the simulation of a large variety of problems with BSSN, CCZ4, and GHCs, good performance and scalability on the latest architectures, and fully adaptive mesh refinement, which we explain below.

Almost all problems in general relativity require codes to be able to resolve wildly varying length-scales accurately. In astrophysical simulations for example, the black hole has to be resolved accurately, while the size of the computational domain has to be at least 100 times larger to allow accurate gravitational wave extraction and to ensure that the boundary conditions do not spoil the results. Covering the whole domain with one very fine grid would be completely unfeasible. As a result, numerical relativity codes must be able to selectively increase the resolution in regions of interest. This is called *mesh refinement*. The simplest mesh refinement strategy is *moving box refinement*, where the resolution is increased in a few disjoint rectangular regions, whose size often has to be specified in advance. Another common strategy is *adaptive mesh refinement*, in which the user specifies a criterion to determine regions in which the resolution should be increased. In practice, all adaptive mesh refinement algorithms have to refine additional cells, partly for efficiency reasons and partly because of built-in restrictions on the shape and topology of refined regions. In this thesis, we call an implementation that can refine regions of arbitrary shape and topology *fully adaptive mesh refinement*.

The best choice of mesh refinement algorithm depends on the particular application. For binary black hole mergers, moving box refinement is sufficient since typically no new length scales are created dynamically and the shape of the refinement regions does not have to be changed frequently. Problems beyond astrophysics, such as the study of instabilities in general relativity, require fully adaptive mesh refinement due to the emergence of new length scales in regions of complicated shape and topology. These are precisely the kinds of problems we want to be able to tackle with GRCHOMBO. For this reason, GRCHOMBO is built on top of the CHOMBO libraries [141], which allow fully adaptive mesh refinement.

To ensure that GRCHOMBO runs efficiently on the latest architectures and that it is flexible enough for the future, we have completely redesigned and rewritten the code since the publication of the code paper Ref. [5]. While we have ensured that the physical results remain the same, the performance and scaling have improved significantly. In this chapter, we present the new overhauled design and explain why the changes we have made should make GRCHOMBO more future-proof and easier to use.

The remainder of this chapter is structured as follows: in section 2.2, we present the details of the numerical implementation in GRCHOMBO. In section 2.3, we present the tests that we carried out to demonstrate that GRCHOMBO produces accurate results and we explain how we ensure that we do not introduce bugs as we amend and improve the code. In section 2.4, we present the most thorough performance tests of GRCHOMBO to date on both Intel Xeon and Intel Xeon Phi processors. This information is crucial for future compute grant applications and helps users maximise the performance of GRCHOMBO on their supercomputer. Finally, in section 2.5 we give a brief overview of the design of GRCHOMBO to show how the latest performance tweaks were achieved in the code and what steps we have taken to make GRCHOMBO easy to use.

2.1.1 High performance computing architecture and techniques

Since the publication of the GRCHOMBO code paper [5], supercomputing hardware has undergone significant changes that made it necessary to redesign large parts of GRCHOMBO. Table 2.1 shows the specifications of the processor we used for scaling tests in Ref. [5] three years ago in comparison to two recent processors which we will use for our latest scaling tests in section 2.4. The data are indicative of the wider trend: there has been no significant increase, or in some cases even a decrease, in the core frequency in the last ten years [142]. The reason for this is that architectures with higher frequency are less energy efficient. As a result, an entirely serial program runs no faster or in some cases slower on more modern architectures.

Instead, processors have seen a substantial increase in core count. Intel's Knights Landing processor even uses up to 70 cores, but with significantly reduced frequency. There has also been a significant increase in the *Single Instruction, Multiple Data* (SIMD) width, the amount of data a single instruction can be applied to at the same time. In short: modern processors do not execute instructions faster than the processors from five or even ten years ago, they only execute more instructions in parallel and can apply the same instructions to more numbers at a time. To harness the improvements in hardware, the program needs to use

Code name Number	Nehalem EX X7542	Sandy Bridge E5-2670	Knights Landing 7250	Skylake 8160
Year	2010	2012	2016	2017
Cores	6	8	68	24
SIMD width [64 bit]	2	4	8	8
Base freq. [GHz]	2.7	2.6	1.4	2.1
Turbo freq. [GHz]	2.8	3.3	1.6	3.7
TDP [W]	130	115	215	150
Launch price [\$]	2000	1500	2400	4700

Table 2.1 Technical specifications of the Nehalem and Sandy Bridge processors we used for the scaling tests in Ref. [5] and the Knights Landing and Skylake processors used for the tests in this thesis. Details were taken from Ref. [143].

all these available layers of parallelism at all times. This is not easy, however, and old code often has to be improved significantly before any of the benefits of modern architecture are noticeable. This is particularly true for Knights Landing, which due to its significantly lower core frequency is much less forgiving of badly parallelised code.

Given the major differences in design between different processors, one cannot directly compare their performance. For example, it is not fair to compare the runtime of a simulation on one 68-core Knights-Landing processor to that on one 24-core Skylake processor. One of the best ways of achieving a fair comparison is to consider the performance at fixed electricity usage, i.e. the *performance per watt*. Calculating or measuring the exact electricity usage is complicated, but as a very crude estimate, one can assume that the amount of electricity a processor uses is roughly proportional to its *thermal design power* (TDP), which specifies the maximum amount of heat it may generate. We will use the TDP in section 2.4 to compare the performance of GRCHOMBO on Knights Landing and Skylake.

In modern supercomputers, thousands or even tens of thousands of processors are connected with a fast network so that they can run tasks in parallel and communicate information. Each *compute node* of this network contains one or several *sockets* for processors, which share the resources in the node. Most commonly, the communication between nodes is managed using the *Message Passing Interface* (MPI). When using MPI, many *processes*, instances of a program, are launched across the supercomputer and MPI is used to communicate information between them.

Due to the large number of cores on modern processors, there is a lot of parallelism available within a node. One way of exploiting this parallelism is to assign more than one MPI process to a node or even one MPI process per core. However, this approach is often not ideal as MPI

is designed for situations where a process keeps all its data locally and communicates with other processors to exchange data. Within a node, this is not necessary since the memory in a node is usually shared. As a result, cores can access all data directly and there is no need for communication. Instead, the main challenge is to ensure that cores never manipulate the same data at the same time since this can lead to incorrect results. There are several programming models that allow this intra-node parallelism to be organised. We use *Open Multi-Processing* (OpenMP). To make matters more complicated, on modern processors it is often beneficial to use more than one OpenMP *thread*, units of parallelism in OpenMP, per core. This allows the core to use its resources more effectively: for example, while one thread is waiting for data from memory, another thread can perform calculations.

The choice of how many MPI processes should be assigned to each node and how many OpenMP threads one should assign to each core can have a significant impact on the runtime of the program. Unfortunately, there are very few general rules on what the optimal choice is, as this heavily depends on the program and the architecture it is running on. One of the aims of the performance tests in section 2.4 is to give GRCHOMBO users guidance on what the most ideal setup is for GRCHOMBO.

2.2 Numerical details

Both CCZ4 and GHCs can be reduced to a set of coupled PDEs that are first order in time and up to second order in space. GRCHOMBO integrates these PDEs in time by taking discrete time steps using the explicit 4th order Runge-Kutta scheme. The spatial directions are discretised on a cell-centred grid. This choice is uncommon for vacuum numerical relativity codes, which usually use node-centred grids as they make the exchange of information between refinement levels easier. However, GRCHOMBO is built on top of CHOMBO, which was designed with fluid dynamics applications in mind, where cell-centred grids together with flux conservation across cell boundaries are more common. Currently, GRCHOMBO uses fourth order finite difference stencils by default, but it is designed to make it easy to replace the stencils.

The choice of an explicit numerical integration scheme introduces an upper bound on the ratio of the size of the time step to the grid spacing, the so-called *Courant factor*. This upper bound is given by the Courant–Friedrichs–Lowy (CFL) condition [144], which for the PDEs

in numerical relativity is

$$\frac{\Delta t}{\Delta x} \leq C_{\max}, \quad (2.1)$$

where C_{\max} is the maximum stable Courant factor, which depends on the characteristic speed of the equations and the integration method. The Courant condition requires us to reduce the size of the time step proportionally to the spatial resolution. In practice, the maximum stable Courant factor is not derived theoretically in numerical relativity, but by experimentation. This is possible since once the Courant factor is small enough to allow stable evolution, any further reduction typically does not change the results.

In any finite difference scheme, errors can arise from the appearance of spurious high frequency modes, with wavelength of the order of magnitude of the grid spacing. This is especially true for adaptive mesh refinement codes, for which errors are introduced by the interpolation at level boundaries and during the regridding process. To damp these high frequency modes, we use Kreiss-Oliger dissipation [145, 110] for all evolution variables. For N^{th} -order Kreiss-Oliger dissipation, the time derivative of an evolution variable ϕ is modified to

$$\partial_t \phi(t, x^i) \rightarrow \partial_t \phi(t, x^i) + \frac{(-1)^N \sigma}{2^{2N} \Delta x} \sum_i \Delta_i^{2N} \phi(t, x^i) \quad (2.2)$$

where Δx is the grid spacing, σ is a parameter controlling the strength of the dissipation, and Δ_i^{2N} is the centred difference operator of order $2N$ in the direction x^i . For example,

$$\Delta_i^6 \phi = \phi_{-3\Delta x_i} - 6\phi_{-2\Delta x_i} + 15\phi_{-\Delta x_i} - 20\phi + 15\phi_{\Delta x_i} - 6\phi_{2\Delta x_i} + \phi_{3\Delta x_i}, \quad (2.3)$$

where $\phi_{n\Delta x_i}$ is $\phi(t, x^i)$ offset by $n\Delta x$ in direction i , i.e. $\phi_{n\Delta x_i} = \phi(t, x^i + n\delta_i^j \Delta x)$. It can be shown [145], that the modification of $\partial_t \phi$ in (2.2) vanishes with $O(\Delta x^{2N-1})$ as the continuum limit is approached. Since GRCHOMBO uses fourth order stencils by default, we therefore use $N = 3$ Kreiss-Oliger dissipation to preserve the order of our method.

2.2.1 Adaptive mesh refinement

GRCHOMBO uses CHOMBO's adaptive mesh refinement implementation, which is based on the Berger-Rigoutsos mesh refinement algorithm [146]. The Berger-Rigoutsos algorithm is block-structured, meaning that the code refines the mesh by overlaying regions which require

higher resolution with boxes of grid cells with smaller grid spacing. The allowed boxes are constrained by the following two conditions:

1. *Proper nesting*: a box on the l^{th} refinement level must not touch level $(l - 2)$ directly; there must be at least one level $(l - 1)$ grid cell between them.
2. *Proper refinement*: a box on level l must not refine parts of a level $(l - 1)$ grid cell; it must refine it completely or not at all.

Furthermore, the user can specify a minimum and maximum box size. This is very important for performance and will be discussed in more detail in section 2.4. The two conditions above do not restrict the shape and topology of the refinement areas substantially. This is one of the advantages of GRCHOMBO and the reason for why the code works so well for simulations of black rings: the finest levels can have toroidal topology. Fig. 2.1 shows an example of the mesh setup for a very thin black ring during the highly dynamic stages of the evolution.

To be able to take derivatives at the edge of a box, we add additional cells, so-called *ghost cells*, on all sides of the box. These ghost cells are not evolved in time. Instead, they get filled with values from valid cells, cells that are not ghost cells, as follows: if a ghost cell overlaps with valid cells of a box on the same level, it is filled with the data from this valid cell. If it does not overlap with a grid cell on the same level, it is filled using fourth order interpolation from cells on the next coarser level, which must cover the same region because of the proper nesting condition. Ghost cells outside the computational domain are filled using the boundary conditions (see section 2.2.3).

Due to the Courant condition, the time step on each level has to be scaled with the resolution. To achieve this, we use a procedure called subcycling, which is sketched in Fig. 2.2. We start with a time step on the coarsest level. Thereafter, whenever level l has advanced by one step, level $l + 1$ takes time steps with its smaller Courant factor until it reaches the same time as level l . Once level $l + 1$ has reached the same time as level l , their data are synchronised by averaging fine data to the coarser level. After this averaging has happened, the step on level l is declared finished, meaning that its data can be averaged to level $l - 1$ if appropriate.

Whenever a level takes its second subcycling step, there is no coarser level data available for the same time so that it is not possible to fill ghost cells using interpolation in space only. CHOMBO solves this problem using the method proposed in Ref. [147]: as the coarser level takes a time step, it constructs a time interpolation polynomial from its Runge-Kutta substeps. These polynomials can later be used to fill ghost cells on the finer level using appropriate interpolation in space and time.

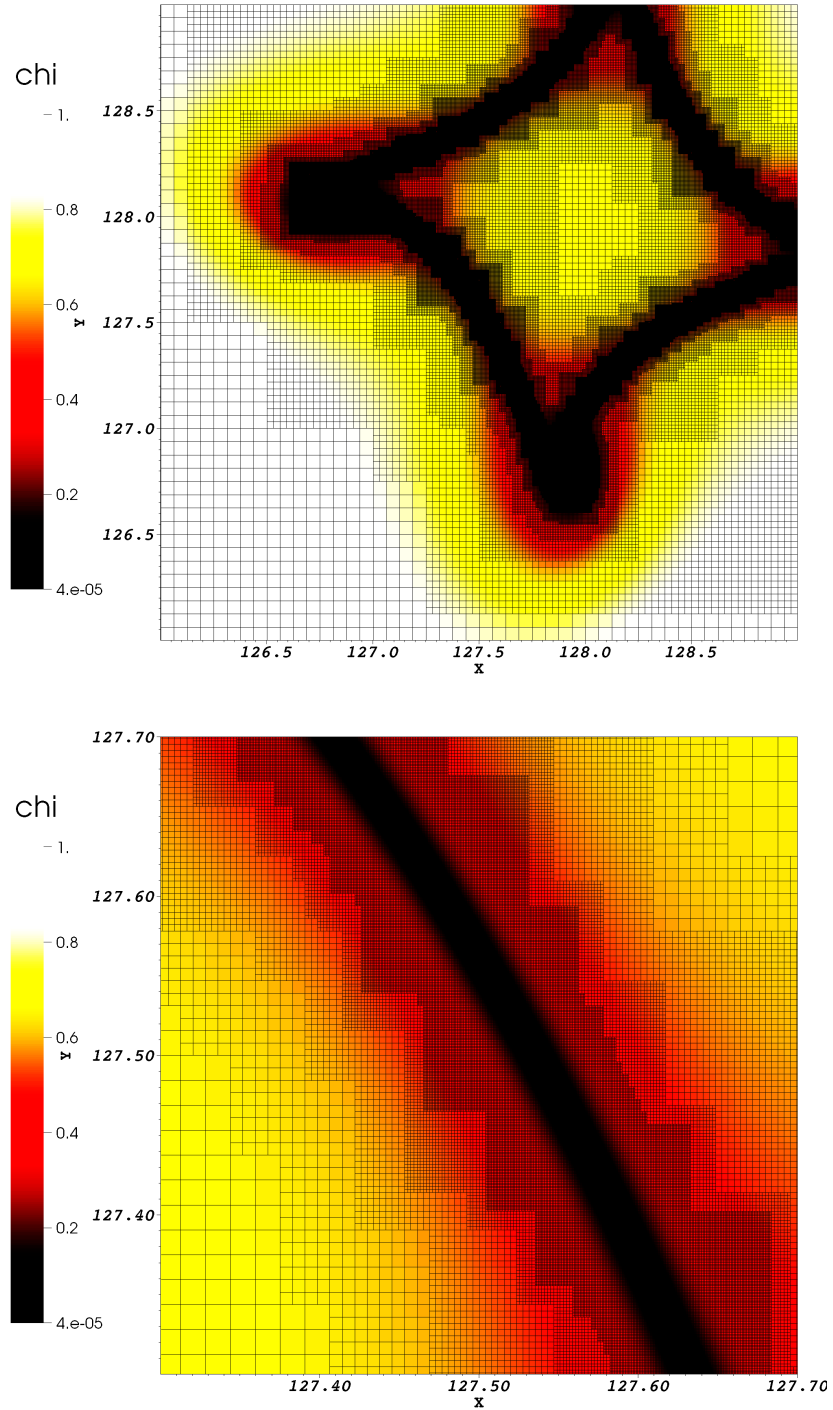


Fig. 2.1 Grid setup for a very thin black ring in the highly dynamic stages of the evolution. The bottom picture is a zoom of the picture on the top. The apparent horizon is located roughly at the $\chi = 0.2$ contour, i.e. it covers the black region in the plot. GRCHOMBO is able to adapt the grid to the toroidal topology of the black hole.

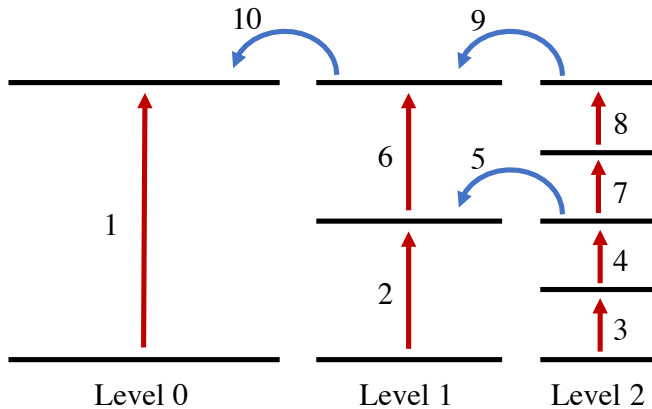


Fig. 2.2 Illustration of the subcycling procedure in GRChombo. The numbers indicate the order in which the operations are performed.

An important requirement in high performance computing is that programs must save checkpoint files at regular intervals which can be used to restart the execution. Checkpoint files ensure that the simulation does not have to be repeated in its entirety if it is terminated because of some problem with the supercomputer. Furthermore, most supercomputers do not allow programs to run for more than a few days. Since the simulations in this thesis took weeks or even months to run, they had to be stopped and restarted from a checkpoint file many times.

CHOMBO allows writing a checkpoint file whenever all levels are synchronised in time, for example before step 1 or after step 10 in Fig. 2.2. This checkpoint file stores all data and the box layout so that the simulation can be restarted without any information being lost. However, writing checkpoint files whenever all levels are synchronised is not enough for our purposes: simulating instabilities in general relativity requires very deep mesh hierarchies due to the small length scales that get produced during the instability. For example, for the simulations of the ultraspinning instability of Myers-Perry black holes in chapter 5 we used up to 22 levels. With a refinement ratio of 2, this implies that for each step on the coarsest level the finest level must take $2^{21} \approx 2$ million steps. As a result, as the simulation is running, the levels might only be synchronised in time once a month so that CHOMBO's checkpoints are written too rarely.

To solve this problem, we augmented CHOMBO's checkpointing capabilities to allow writing checkpoint files even when levels are not synchronised in time, i.e. after all of the ten steps in Fig. 2.2. This is done as follows: as level l writes its data to the checkpoint file, it also checks whether level $l + 1$ has already evolved to the same point in time. If it has not, level l also stores the coefficients of the time interpolating polynomial that is used to fill ghost cells

on the finer level to the checkpoint file. To restart from a checkpoint file, we first read in all the data and interpolating polynomials. Thereafter, we scan through all levels starting from the finest. Whenever a level has not evolved to the same point in time as the next coarser level, we take time steps until it has caught up, performing any necessary subcycling steps. In this process, we ensure that the coarse averaging procedure is done precisely once and in exactly the order that is specified in Fig. 2.2.

2.2.2 Tagging criteria

In order for CHOMBO to set up the mesh hierarchy, we must provide it with a set of “tagged” cells whose resolution we deem to be too low. There are many different ways of specifying tagging criteria, and we often use a combination of them. While it would be most intuitive to base the refinement on some measure of the numerical error, we found that this often leads to very irregular refinement regions, which cause larger numerical errors. Instead, we base the refinement on combinations of evolution variables that capture the geometry of the solution well. In our simulations, we found a tagging criterion based on the gradient of χ^{-1} to be most reliable. More concretely, we tag a cell if

$$\frac{\Delta x \sqrt{\delta^{ij} \partial_i \chi \partial_j \chi}}{\chi^2} > \sigma_\chi, \quad (2.4)$$

where σ_χ is a custom refinement threshold, and Δx is the grid spacing. The refinement in Fig. 2.1 was done using the above criterion. For rapidly rotating black holes, we usually combine (2.4) with a refinement criterion based on

$$\Delta x \sqrt{\delta_{ij} \tilde{\Gamma}^i \tilde{\Gamma}^j} > \sigma_{\tilde{\Gamma}}. \quad (2.5)$$

As we will discuss in more detail in chapter 3, $\tilde{\Gamma}$ is large in the initial data for rotating black holes but later decays due to our gauge conditions. In these cases, (2.5) captures the regions that need higher resolution better than (2.4) before gauge adjustment. Finally, whenever we want to extract gravitational waves, we add a tagging criterion that tags cells if the distance to the black hole is smaller than the wave extraction radius and the resolution is lower than the desired resolution at the extraction point.

2.2.3 Boundary conditions

In GRCHOMBO, boundary conditions can be specified in the following three ways:

- by modifying the evolution equations for cells close to the boundary,
- by filling ghost cells outside the computational domain,
- by using different stencils close to the boundary.

Which of the above methods is most appropriate and most efficient depends on the type of boundary condition that is used. Below, we discuss the most important boundary conditions and how they are implemented in GRCHOMBO.

Periodic. The simplest and most efficient way of implementing periodic boundary conditions is to fill ghost cells that are outside the domain with valid cells from the same refinement level on the other side of the domain.

Sommerfeld. A very common condition in numerical relativity is the Sommerfeld boundary condition [129], which ensures that outgoing waves do not get reflected back into the computational domain. To this end, we modify the evolution equations close to the boundary to

$$\partial_t \phi = -\frac{x^i}{r} \partial_i \phi - \frac{\phi - \phi_0}{r}, \quad (2.6)$$

where ϕ represents any evolution variable and ϕ_0 is the desired value on the boundary which we typically take to be Minkowski space.

Parity. When using the modified Cartoon method for dimensional reduction (chapter 3), we must enforce even or odd parity on the Cartoon axis. This is achieved most efficiently by filling the ghost cells outside the boundary by even or odd extrapolation of the data inside the domain. This means that the right hand side calculation remains completely unchanged and the same differentiation stencils are used everywhere in the domain.

Dirichlet. For evolution in AdS, we have to prescribe Dirichlet boundary conditions given by the metric on the boundary of AdS. However, since GRCHOMBO is cell-centred, there is no grid point at the boundary. We therefore, modify differentiation stencils close to the boundary to imitate a grid point with a fixed value on the boundary. We will discuss the details of this in chapter 7.

Due to GRCHOMBO's adaptive mesh refinement, it is sometimes computationally feasible to make the coarsest level so large that the boundary is not in causal contact with the region of interest throughout the entire simulation. In this case, the boundary conditions do not affect the results in the region of interest and we often use periodic or Dirichlet boundary

conditions as they are simple and computationally cheap. This approach is not uncommon and was used for example in Ref. [33].

2.2.4 Parallelism

As outlined in the introduction, programs may run no faster or even slower on more modern architecture unless they use all layers of parallelism: all available compute nodes, all cores, more than one hardware thread if appropriate, and SIMD instructions wherever possible. In this section we outline how these layers of parallelism are achieved in GRCHOMBO on an abstract level. The implementation will be presented in section 2.5.

A block-structured adaptive mesh refinement algorithm, such as the one used in CHOMBO, lends itself very well to parallelisation with MPI because boxes can be distributed among MPI processes easily. Since the boxes are augmented with ghost cells, each process can perform all calculations, including numerical derivatives, independently. After each time step, the values of ghost cells needs to be updated with valid or interpolated data. In most cases, these data reside on a different process and are, therefore, communicated with MPI. To ensure that the workload of each process is approximately equal, even with strongly varying box sizes, we use CHOMBO’s load balancing algorithm, which distributes boxes such that all MPI processes are assigned roughly the same number of cells. CHOMBO also allows loading and writing files in parallel using the HDF5 libraries [148].

The need to communicate ghost information puts a lower bound on the box size that can feasibly be used. As the box size is decreased, the ratio of valid cells to ghost cells becomes worse, so that we incur a larger communication cost per valid cell. In our experiments with GRCHOMBO we found that the maximum feasible ratio of ghost cells to valid cells is reached at a box size of approximately 8^3 cells. This puts an upper bound on the number of boxes a typical simulation can have, and thus the number of MPI processes that can be used efficiently: we can use at most as many processes as we have boxes, otherwise some processes are not assigned any work.

Since almost all operations in GRCHOMBO are done on a cell-by-cell basis, we can create an additional layer of parallelism by threading the loops over cells in a box using OpenMP. For operations like the interpolation of ghost cells at mesh boundaries, where the same operation is repeated for each evolution variable, we can also include the loop over evolution variables in the threading. While the MPI parallelism was largely already present in CHOMBO, significant work was still needed on the threading to ensure that there are no bottlenecks that slow down the execution. The hybrid MPI/OpenMP parallelism enables us to use fewer

processes per node while still using the resources in the node efficiently. This in turn allows us to use more nodes before running out of boxes for all MPI processes. We will see an example of this behaviour in section 2.4.

Finally, to make use of the wide SIMD unit on modern CPUs, we pack up several cells into a vector and subsequently use SIMD instructions to operate on the whole vector at once. This process is called *vectorisation*.

2.3 Testing correctness and accuracy

One of the most important aspects of numerical relativity is to ensure that the code is correct and gives accurate results. These two requirements are very different. The former relates to the code itself: all parts should perform their intended tasks as advertised. The latter relates to physics and numerical analysis: if the code performs its task correctly, it should give a good estimate of the physical results. Therefore, we carry out two categories of tests: software tests, which ensure that the code is correct, and physical tests, which ensure that the results the code produces are a good description of the physical behaviour.

2.3.1 Software tests

Since GRCHOMBO, like most numerical relativity codes, is tens of thousands of lines long, the only way to avoid bugs is by having tests for as much of the codebase as possible. Currently, GRCHOMBO includes three different types of tests:

- **Unit and integration tests.** These tests check very specific parts of GRCHOMBO or a few parts in combination on fabricated input.
- **Evolution equations.** In this type of test we set up initial data consisting of fourth order polynomials with random coefficients and evaluate the BSSN and CCZ4 right hand sides with the current version of GRCHOMBO and an old version. This ensures that as we modify and improve the code, we do not introduce bugs in the calculation of the right hand side, including the derivative calculation and the loop over the cells in a level.
- **Full evolutions.** Starting from the same random initial data as above but now with several levels of refinement, we take two full time steps including subcycling and ghost interpolation. After the first step, we save a checkpoint file and restart from the same

file. We perform this procedure with the current version of the GRCHOMBO code and an old version, which we trust to be correct, and compare the values in the checkpoint files after the second step. This is a very powerful test as it can pick up bugs in almost all components of the code, including checkpointing and restarting. The disadvantage is that it is more expensive to run and that it is harder to pin down the source of the problem if the test fails.

The first two types of tests can be executed automatically and are checked for every new contribution to the public version of the code. Currently, tests of type 3 have to be executed manually, but we plan to make them automatic in a future release of the code.

2.3.2 Physical tests

A bug-free code that works completely as intended may still give inaccurate or wrong results. Even for setups that have been studied in a lot of detail before, there are a lot of seemingly minor choices that can affect the accuracy of the results, such as how the grid is set up, how information is communicated between levels, how the time interpolation at level boundaries works, and how often algebraic constraints such as $\tilde{A}^i{}_i = 0$ are enforced.

For this reason, before applying the code to new problems, we tested GRCHOMBO in a number of standard settings, where there are published results on the performance and accuracy we can expect from a numerical relativity code based on BSSN and CCZ4. These tests are listed below. The first four of them are called *Apples with Apples* tests [149].²

- **Robust stability.** Minkowski space is slightly perturbed by adding small random noise to the initial data and evolving it in time. GRCHOMBO passes this test: as required, the constraint violations decrease when CCZ4 is used and remain constant with BSSN.
- **Linear wave.** A gravitational wave is evolved numerically. The amplitude ($A = 10^{-8}$) is chosen so small that the evolution is effectively linear and the results can be compared to the analytic solution of the linearised Einstein equations. Since GRCHOMBO uses a fourth order stencil, it performs very well in this test with deviations from the analytically calculated metric components of order 10^{-12} after 1000 periods.
- **Gauge wave.** A gauge wave is evolved across a periodic domain repeatedly. Lapse and shift have to be chosen so as to keep the shape of the gauge wave intact at an

²By now, the Apples with Apples tests are somewhat outdated and have been surpassed by tests of the accuracy of black hole simulations. Despite this, they provide very simple and well-documented first tests and include settings which are tough to simulate.

analytical level. The commonly used $1 + \log$ slicing would quickly eradicate these gauge oscillations. Numerical relativity codes based on BSSN fare really badly in this test and crash after a few dozen crossing times [149]. However, CCZ4 was designed to pass this test as it suppresses Hamiltonian constraint violations [123]. GRCHOMBO displays exactly this behaviour.

- **Gowdy Wave.** This test compares numerical results against an analytic solution for a gravitational wave propagating in a strongly curved expanding or collapsing universe. This is a very tough setting: in the expanding case, errors are usually amplified causing the code to crash, in the contracting case the code stops agreeing with the analytic solution as the singularity is approached. While GRCHOMBO is no exception to this, fourth order convergence is retained for approximately 1000 light crossing times with CCZ4.
- **Single black hole spacetimes.** We evolve a Schwarzschild black hole for $10,000M$, a Kerr black hole with spin $J/M = 0.2$ for $200M$ and a boosted black hole for $200M$. We check that the constraint violations do not grow, and that the ADM mass and linear and angular momentum remain constant.

The most important test for any numerical relativity code is to check the accuracy and convergence of the gravitational wave signal from a black hole merger. To this end, we simulate the head-on collision of two black holes of mass $0.5M$, initially a distance of $10M$ apart, at three different resolutions. All runs had 8 refinement levels in total, with a refinement ratio of 2. The coarsest resolution run had a grid spacing of $4M$ on the coarsest and $0.03125M$ on the finest level. For the two higher resolution runs, we increased the resolution by factors of $\sqrt{2}$. The results for the real part of the $l = 2, m = 0$ of $r\psi_4$, where r is the extraction radius, are shown in Fig. 2.3 in a plot versus $t_{\text{ret}} = t - r$. The initial burst of radiation is unphysical and is a property of our initial data, which consist of two superimposed static black holes. With the exception of the time range $20 \lesssim t_{\text{ret}}/M \lesssim 40$, where there is little physical wave signal, we consistently see convergence between third and fourth order. This is expected, since we use fourth order spatial discretisation but the interpolation at mesh boundaries reduces the order slightly.

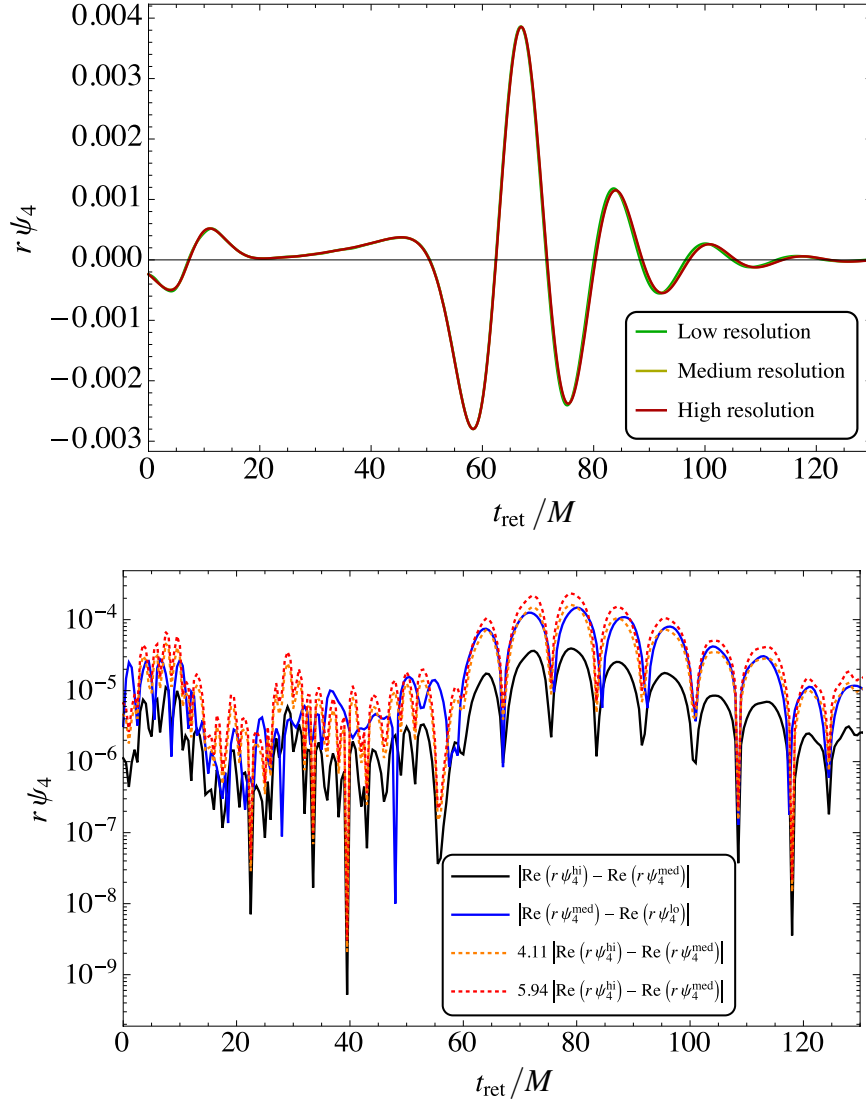


Fig. 2.3 Convergence test for head-on collisions of two black holes. *Top:* Real part of the $l = 2, m = 0$ mode of $r\Psi_4$ extracted at a radius of $60M$. *Bottom:* Difference in the results for different resolutions. The dashed orange and red lines represent third and fourth order convergence respectively.

It is important to stress that the above tests only ensure that the core components of GRCHOMBO are reliable in the standard settings. They give no guarantee that the code is accurate for new applications and with new methods. As a result, it is necessary to perform new numerical tests for every application. We will present the appropriate tests for all the results presented in this thesis in the appendices to chapters 4, 5, and 7. The upside of this is that by now, the most convincing evidence for the accuracy of GRCHOMBO does not come from the tests presented above, but from those in Refs. [3, 2, 5, 48–52], which applied GRCHOMBO in considerably more challenging settings.

2.4 Scaling tests

Since the publication of our code paper [5], we have invested a significant amount of time in the optimisation of GRCHOMBO and have achieved considerable improvements in performance. In this section, we present the latest scaling tests of GRCHOMBO and demonstrate that it can run efficiently on large supercomputing systems. Furthermore, we analyse the impact of various parameters on the runtime in order to give guidelines on the optimal choice of parameters in GRCHOMBO.

There are two related but different concepts that capture how a program benefits from the use of more resources: *strong scaling* and *weak scaling*. Strong scaling refers to how much faster the same setup runs when more resources are used. For example, for an ideal program, the runtime should be halved as the number of cores is doubled. In practice, this can only be achieved to some extent: as we keep increasing the number of cores, parallel sections of the program run faster and faster while the runtime of serial sections remains unchanged so that they eventually dominate the runtime. However, strong scaling can be spoilt before this happens if the work in parallel regions cannot be divided enough to supply all cores with work.

Weak scaling refers to the ability to simulate a more expensive problem in the same amount of time by using more resources. For example, for an ideal program we should be able to double the number of grid points in the computational domain but keep the runtime unchanged by doubling the number of cores too. In general, weak scaling is easier to achieve than strong scaling. The main reason for this is that the runtime of parallel sections in a program remain unchanged in a weak scaling test. As a result, serial portions are not a problem as long as they do not become more expensive as the size of the problem is increased. Furthermore, in a weak scaling test we are unlikely to run out of work for all cores since the problem size is increased at the same rate as the computational resources.

Whether strong scaling or weak scaling is more important depends on the particular application. In numerical relativity, it is hard to find situations which only require weak scaling. While increasing the resolution seems like a weak scaling problem as it increases the problem size, it also requires good strong scaling in numerical relativity. The reason for this is that increasing the resolution also requires decreasing the size of the time step due to the CFL condition (2.1). This means that more time steps are required to reach the end of the simulation. Since time steps have to be done one after the other, doing more steps in the same amount of time requires good strong scaling.

When performing scaling tests, it is important not to lose track of the main goal: making the code run faster. Since it is often much easier to get code that runs slowly to scale well, we must only test the scaling once we have ensured that we use the available resources efficiently. For this reason, we investigate the impact of various parameters such as the maximum box size, and we choose the optimal configuration for each core count. Furthermore, we investigate the intra-node scaling by testing different numbers of MPI processes per node and different numbers of threads per process. Using only one MPI process per node would give the best strong scaling, but as we will see, the threading in GRCHOMBO is not good enough yet for this to be the fastest configuration in most cases.

The scaling and performance tests in this section were performed on two of the largest and newest supercomputers in the world: MareNostrum4 and Stampede2. MareNostrum4 at the Barcelona Supercomputing Centre is comprised of 3456 nodes, each with two Xeon Platinum 8160 “Skylake” processors (see Tab. 2.1), giving the system 165,888 cores in total. The nodes we used all have 96GB of DRAM (dynamic random access memory) and are connected using Intel’s Omni-Path fabric in a full fat-tree topology.

Stampede2 at the Texas Advanced Computing Centre hosts 4,200 Intel Xeon Phi 7250 “Knights Landing” processors (see Tab. 2.1) with a total core count of 285,600. Stampede2 also includes 1,736 Skylake nodes, but we did not use them in our tests. Each Knights Landing node has 96GB of DRAM and 16GB of fast Multi-Channel DRAM, which can be used as DRAM, L3 cache, or a hybrid between the two. In the tests presented in this chapter, we use the processors in cache quadrant mode. The nodes are connected using Intel’s Omni-Path network in fat-tree topology.

2.4.1 Results

As the main benchmark problem for our strong scaling test, we use a binary black hole simulation. The black holes both have mass $0.5M$, are separated by $6M$ in the x -direction

initially, and have momenta $\pm 0.1M$ in the y -direction. The size of the computational domain is $192M$. For the strong scaling test, we use six refinement levels with a refinement ratio of 2. The coarsest level has 256 points in all directions, so that the coarsest resolution is $\Delta x = 0.75M$ and the finest is $\Delta x = 0.023M$. As tagging criterion we use (2.4) with a threshold of $\sigma_\chi = 0.03$. We set the minimum box size to 8 and the maximum box size to 32. As shown in the appendix, this is the best configuration. We take two complete time steps on the coarsest level, including all subcycling steps on finer levels, and report the average time per step. Averaging over more steps does not change the results noticeably so that two full steps are sufficient.

The measurements include all necessary ghost communication and interpolation, and full regridding and load balancing operations at every step of the coarsest three levels. However, we have excluded the initial data calculation as it takes at most one minute and is only done once in a simulation with a wall-clock time of several days. Furthermore, we have excluded the writing of checkpoint files, as this is only done every few hours and does not take more than a few minutes.

Fig. 2.4 shows the results on MareNostrum4 for three different numbers of MPI processes per socket. The number of threads per process is fixed so that every core is always assigned one thread. We found that this is the most efficient configuration with GRCHOMBO on both Skylake and Knights Landing. The results demonstrate that GRCHOMBO has excellent strong scaling until there are not enough boxes for all the MPI processes. For one process per socket this happens at around 20,000 cores, so that we get useful speedup until about 10,000 cores. Using more processes per socket leads to worse strong scaling as it means that we run out of boxes earlier. However, for low core counts where there are enough boxes to distribute to all MPI processes, our MPI parallelism is more efficient than our threading within a box so that is is best to use two to four processes per socket.

Aside from the number of MPI processes per node, an important parameter for the performance of GRCHOMBO is the maximum box size. For low core counts, larger boxes are more efficient since they have a better ratio of valid cells to ghosts cells and therefore incur less communication cost and use less memory. At high core counts, enforcing a smaller box size improves the scaling since there are more boxes to distribute among the MPI processes. This is taken into account in Fig. 2.4: all runs were done with the optimal box size for the given core count. Plots with strong scaling for different box sizes can be found in the appendix to this chapter.

Since good strong scaling continues until we have more MPI processes than boxes, the number of boxes GRCHOMBO can strong-scale to depends very much on the size of the

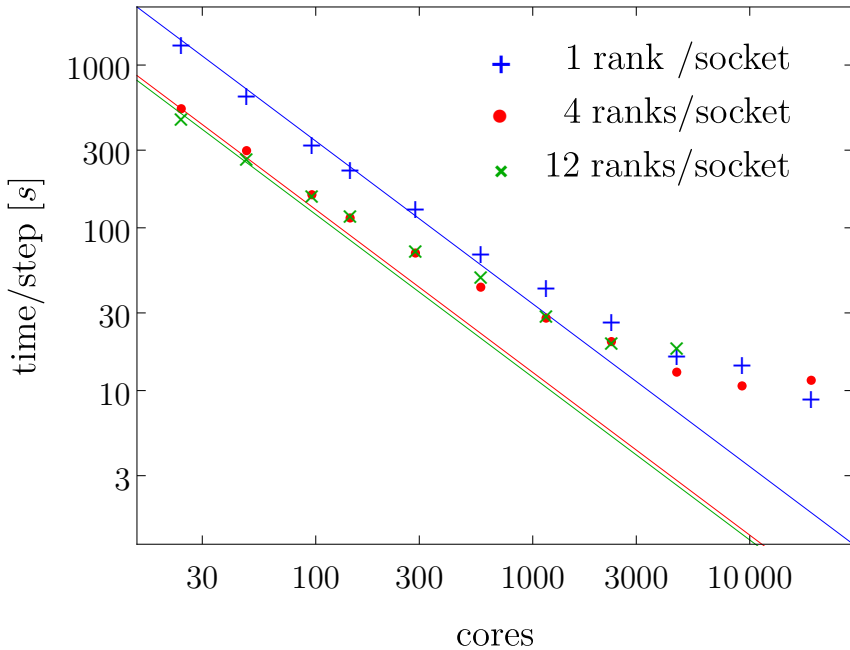


Fig. 2.4 Strong scaling behaviour of GRCHOMBO for a binary black hole simulation on Skylake processors at MareNostrum4 for three different numbers of MPI processes per socket. The straight lines represent perfect strong scaling for each of the three configurations.

problem. We chose the binary black hole simulation outlined above as the main benchmark problem since it is the standard test in the field. Furthermore, it has low enough memory requirements to fit on a single Skylake processor so that we can study strong scaling starting at one processor. However, many of the problems in this thesis, especially the simulations of instabilities of very thin rings, can be much more expensive than the binary black hole simulation we use for scaling tests. As a result, they can be strong-scaled to considerably more cores. We show an example of this in the appendix to this chapter.

To test the weak scaling of GRCHOMBO, we use the same binary black hole configuration as for the strong scaling test on 24 nodes as a starting point, but as we decrease and increase the node count, we adjust the resolution to keep the number of cells per node fixed. We achieve this by increasing the coarsest resolution and decreasing the refinement threshold σ_χ with the cube root of the node count. This increases the resolution of the grid while keeping the shape of refinement regions the same. For very small node counts, it is not possible to keep the shape of refinement regions exactly the same due to the requirement to keep a buffer between refinement boundaries. For this reason, we stop the weak scaling test at 3 nodes. The results in Fig. 2.5 show near-perfect weak scaling in the whole regime we could test (up to 19,200 cores): a 130-fold increase in the core count only leads to a 20% increase in runtime. Furthermore, this small increase only starts to manifest itself above 10,000 cores.

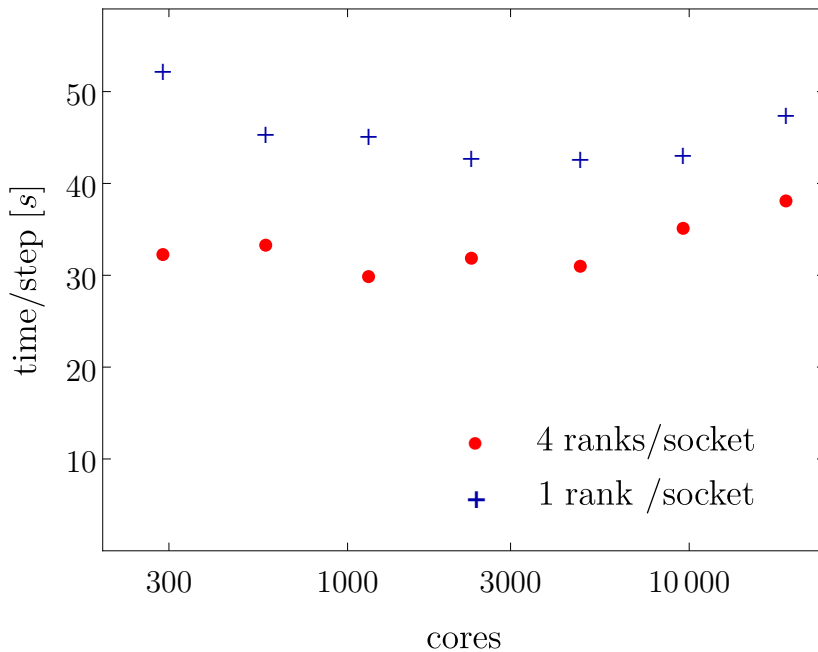


Fig. 2.5 Weak scaling behaviour of GRCHOMBO on Skylake processors at MareNostrum4 for two different numbers of MPI processes per socket.

2.4.2 Results on Knights Landing

Significant work was required to get GRCHOMBO to run efficiently on Intel Knights Landing. As can be seen in Tab. 2.1, Knights Landing has a much lower clock frequency than the other processors. In order to achieve a reasonable performance, we had to improve the vectorisation and threading of GRCHOMBO considerably. However, this was not the only difficulty. Many details of the code which made no difference whatsoever on other CPUs such as Skylake had a significant impact on the performance of GRCHOMBO on Knights Landing: branch mispredictions, divisions, memory allocations that are not aligned with huge page boundaries, etc. Furthermore, disabling all internal checks in CHOMBO sped up simulations by almost a factor of two.

Fig. 2.6 (left) shows the strong scaling results on Knights Landing processors at Stampede2 for three different numbers of MPI processes per node. The tests were done with the same setup as in the previous section and each data point was obtained with the optimal box size for the given number of cores. Fig. 2.6 (right) shows a performance comparison with Skylake in a plot of runtime versus TDP (see section 2.1.1). The latter was obtained by multiplying the TDP of a single processor with the number of processors that were used for the simulation. This gives a crude way of comparing the performance per watt of GRCHOMBO on Knights Landing and Skylake. The results shows that KNL achieves roughly the same performance

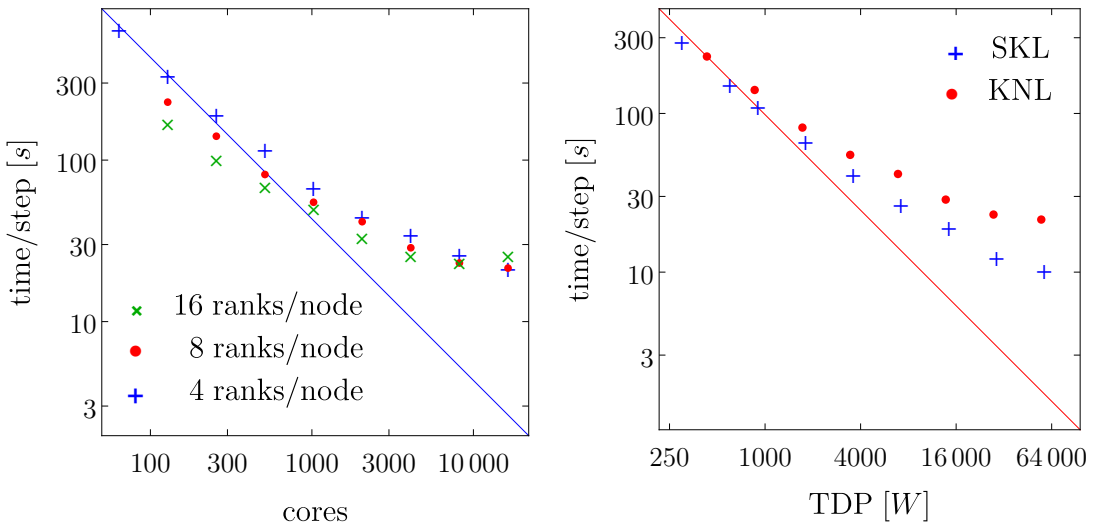


Fig. 2.6 *Left*: Strong scaling behaviour of GRCHOMBO on Knights Landing processors at Stampede2 for three different numbers of MPI processes per node. *Right*: Performance comparison between GRCHOMBO on Knights Landing and Skylake. The wall-clock time per step is plotted against the TDP (obtained by scaling the TDP of one processor by the number of processors used). We use this as a crude way of comparing the performance per watt.

per watt as Skylake up to approximately 32 KNL nodes (2,176 cores). For higher node counts, it performs slightly worse than Skylake since it exhibits worse strong scaling.

2.4.3 Performance summary and outlook

In summary, we find that GRCHOMBO exhibits excellent strong scaling until there are not enough boxes for all MPI processes. In the optimal configuration on Skylake, this happens at a few thousand cores for a standard binary black hole merger (Fig. 2.4) and at around 20,000 cores for a simulation of a thin black ring (Fig. 2.8). Furthermore, GRCHOMBO has excellent weak scaling up to at least 20,000 cores. Results on Knights Landing follow a similar pattern with a similar performance per watt than on Skylake.

As the efficiency of a simulation depends mostly on the number of boxes per MPI process, GRCHOMBO outputs the number of boxes per process at every time step, even on the lowest verbosity setting. Users should ensure that this number always stays between 2 and 10 and never becomes 0 for any MPI process. A number larger than 10 implies that GRCHOMBO is still in a regime of very good strong scaling so that one can use more nodes to get to the results faster without a significant loss of efficiency. Furthermore, the number of MPI processes per socket should be increased for a more efficient use of the resources within a socket. A

number smaller than 2 suggests that the simulation is inefficient and that, if possible, the number of MPI processes per socket should be decreased. Failing that, the user can decrease the number of nodes without a significant loss of speed. On Skylake and Knights Landing, a minimum box size of 8 should be chosen. The maximum box size should be 16 if there are fewer than 10 boxes per process, but it must be increased to 32 for more boxes to avoid a significant performance degradation.

Let us now turn to recommendations for future optimisations in GRCHOMBO. Currently, the runtime is completely dominated by CHOMBO library calls. This is not too surprising given the amount of time we have invested in optimising the GRCHOMBO right hand side calculation and the fact that the CHOMBO portions, such as the ghost cell interpolation, are significantly harder to optimise. Thus, the only way to improve the performance of GRCHOMBO is to optimise CHOMBO. We have already improved the threading of several CHOMBO calls significantly to get to this stage and we are continuing with this work.

Currently, we thread either the z and y loops over cells (the x loop is used for vectorisation) or the loop over evolution variables. The former leads to 64 chunks of work for a box size of 8^3 , the latter to only 25. It is therefore not surprising that the scaling with OpenMP threads tapers off completely at roughly 20 threads. This means that we have to use several MPI processes per node, which in turn decreases the number of nodes we can strong-scale to before running out of boxes. Thus, improving the threading of GRCHOMBO is one of the main targets for optimisation. The obvious, albeit highly non-trivial, first step is to collapse the loops over cells and evolution variables. In theory, this should be possible for all ghost interpolation and for the derivative calculation in the right hand side.

2.5 Design of GRCHOMBO

In this section, we give a brief overview of the design of GRCHOMBO. This has changed substantially between the publication of our code paper [5] and the public release of the code in 2018. This redesign was driven partly by a need for better maintainability and easier reuse of code between projects and partly by a desire for significant performance improvements. In its current form, GRCHOMBO is implemented entirely in C++, making heavy use of C++14 features. However, some parts of the CHOMBO library still use Fortran.

Fig. 2.7 shows a sketch of the most important classes in the core of GRCHOMBO. On top of this, there are many classes relating to evolution and constraint equations, and data analysis, which we will cover later. At the top of the hierarchy is GRAMR. It stores a list of pointers

to all refinement levels and orchestrates a simulation with adaptive mesh refinement. In particular, at the beginning of the simulation, GRAMR iterates through all levels and calls their appropriate functions to initialise the grid and calculate the initial data. Thereafter, it calls the advance functions of all levels in the appropriate order so that they evolve forwards in time. At user-defined intervals, it asks levels to provide the set of tagged cells where the resolution is not high enough and reshapes levels with higher resolution accordingly. This process is called regridding. Furthermore, it creates checkpoint files at user-defined intervals and requests all levels to write their data into these files. It is important to stress that GRAMR only orchestrates the runs by calling appropriate functions on all levels. It has no information about how these functions are implemented.

Apart from orchestrating the time-stepping, regridding, and checkpointing, GRAMR is involved in all tasks that require information about the whole level hierarchy. Examples of this include the horizon finder or the wave extraction, which have to be connected to GRAMR so that they have access to the data on all levels.

The concept of a refinement level in GRCHOMBO is represented by the abstract class `GRAMRLevel`, which defines all functions which are called by GRAMR during a run. Functions that we expect all general relativity simulations to share, for example the regridding or checkpointing, are implemented directly in `GRAMRLevel` but can be overridden when necessary. Functions which differ from problem to problem, such as the initial data calculation, are pure virtual and must be defined in a derived class. By default, `GRAMRLevel` takes time steps with Runge-Kutta-4 using a pure virtual function as right hand side, whose implementation must be provided by the user in a derived class. When writing a new application with GRCHOMBO, the most important step is to create a new derived class from `GRAMRLevel` and implement the necessary virtual functions. For example, in the binary black hole example that comes with GRCHOMBO, this is done in the class `BinaryBHLevel`.

Within a level, the data is organised into many boxes, which are distributed among MPI processes for parallelism. A box is represented by the CHOMBO class `FArrayBox`. The class `GRLevelData` organises the layout of these boxes and provides a unified interface for operations which should be carried out on all boxes. Finally, GRCHOMBO implements the class template `Cell` which collects all the pointers that are necessary for being able to access data at one grid cell in an `FarrayBox`.

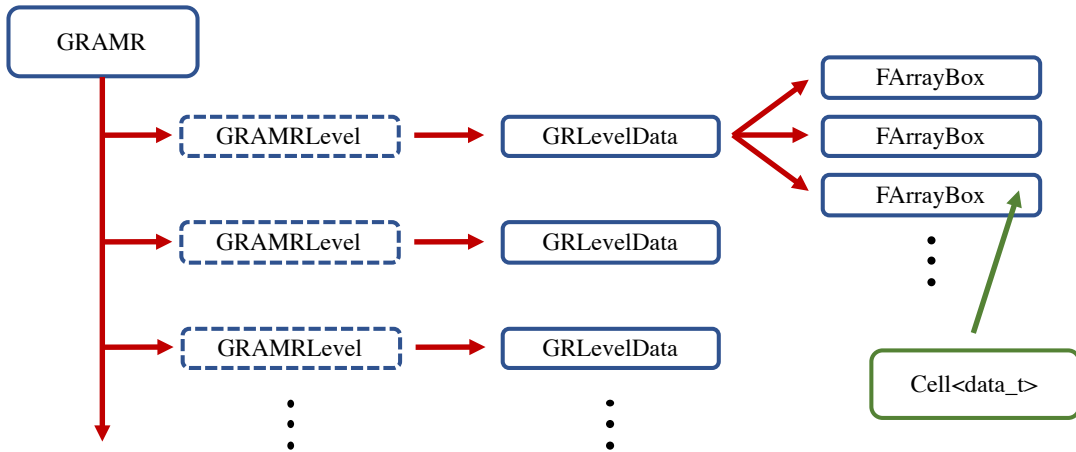


Fig. 2.7 Class structure of GRCHOMBO. A dashed frame indicates a pure virtual class. GRAMR contains and organises a vector of GRAMRLevel. The latter store their data using the class GRLevelData, which organises the data on a level into boxes that are represented by the class FArrayBox. The Cell class can be used to access the data in a grid cell inside a box.

2.5.1 Looping over cells

In numerical relativity, the most time-consuming operations all have to be repeated for all grid cells: calculating the right hand side, enforcing \tilde{A}_{ij} to be trace-free, calculating constraints, etc. Since looping over all grid cells to perform a task is so common, it is important that this loop is implemented efficiently. This is not easy if we want to use all available parallelism: first we have to iterate over all boxes on the MPI rank, then we have to use OpenMP to thread the loop over the z and y coordinates of the boxes. Finally, we have to break up the x -direction into chunks of size given by the SIMD width on the architecture we plan to run the executable on and loop over these chunks. Since this procedure is rather complex, we hide it from the user in GRChombo by providing functions which loop through all cells of a level and perform a user-specified task. This also allows us to tweak the way the loop is performed in the future, without breaking any existing code and therefore makes GRCHOMBO significantly more future-proof.

The task that a loop should carry out is specified using what we call a *compute class*, a class that implements a function template `compute<typename data_t>(Cell<data_t> current_cell)` or a function `compute(Cell<double> current_cell)`.³ The reason why this function can be templated is to allow vectorisation of the right hand side and will be

³The choice to name the function `compute` rather than simply `operator()` was taken for readability reasons even if it means that we cannot pass lambda expressions as `compute` functions.

discussed in detail in the next section. As an example, let us consider one of the simplest tasks already implemented in GRCHOMBO: enforcing \tilde{A}_{ij} to be trace-free. We first have to implement a compute class that loads the current values from the numerical grid, removes the trace from \tilde{A}_{ij} , and stores the values back to the grid. To save memory, GRCHOMBO only stores the upper diagonal part of symmetric tensors on the numerical grid. However, the whole tensor is restored for convenience as we load the data from the current cell into the compute class.

```
class TraceARemoval {
    template <class data_t>
    using Vars = ADMConformalVars::VarsNoGauge<data_t>;

public:
    template <typename data_t>
    void compute(Cell<data_t> current_cell) const {
        auto vars = current_cell.template load_vars<Vars>();

        const auto h_UU = TensorAlgebra::compute_inverse_sym(vars.h);
        TensorAlgebra::make_trace_free(vars.A, vars.h, h_UU);

        current_cell.store_vars(vars);
    }
}
```

As can be seen above, GRCHOMBO includes implementations of most of the standard tensor manipulations. The above compute class can then be passed to one of GRCHOMBO's loop functions in the BoxLoops namespace to remove the trace of \tilde{A}_{ij} for all cells on a level (represented by a GRLevelData):

```
loop(TraceARemoval(), level_data, level_data, INCLUDE_GHOST_CELLS);
```

where the value INCLUDE_GHOST_CELLS signals to GRCHOMBO that the operation can also be carried out for ghost cells as we do not need to calculate derivatives.

One potential problem with the above method is that it encourages the use of distinct loops for several little tasks. From a computational point of view, it is much better to do all the tasks at once in one loop. To address this problem, we provide functionality to pack up compute classes and pass them to a loop at once. We then use template meta-programming to iterate through all the compute classes and call their compute functions. For example, the following line enforces \tilde{A}_{ij} to be trace-free and ensures that the CCZ4 variables χ and α are positive in the same loop.

```
loop(make_compute_pack(TraceARemoval(), PositiveChiAndAlpha()),
      a_soln, a_soln, INCLUDE_GHOST_CELLS);
```

2.5.2 Vectorisation

Due to the increase in SIMD width in processors in recent years (c.f. Tab. 2.1), it has become crucial to ensure that the code makes use of SIMD instructions wherever possible. This process is called vectorisation as it involves converting scalar code to vector code which can then utilise SIMD instructions to operate on the whole vector at once. Unfortunately, compilers struggle to vectorise the calculation of the CCZ4 right hand side in GRCHOMBO automatically due to its complexity and the large number of short nested loops. As a solution to this, we vectorise the code manually by packing up several cells and then using so called vector intrinsics to force the compiler to generate SIMD instructions. While this leads to well-vectorised code, we must ensure that GRCHOMBO users do not have to worry about vectorisation and vector intrinsics and that they can write and debug their code as usual. To achieve this, we hide the SIMD implementation from the user inside a class template `simd<typename>`. This section explains the usage and implementation of this class template.

As explained in the previous section, loops over cells in GRCHOMBO are done using a compute class which specifies which task should be done for each cell by providing a function called `compute`. The only step a user has to take in order to ensure that GRCHOMBO vectorises the loop over cells is to template this function so that it works for arbitrary data types

```
template <class data_t >
void compute(Cell<data_t> current_cell) const {...}
```

As GRCHOMBO loops over cells, it will pack up cells in the x -direction wherever possible and call the `compute` function with a data type called `simd<double>`. Inside a compute class, the user can write code as usual as long as they ensure that they use the template type everywhere. For example, they should write

```
data_t rhs_lapse = - 2 * lapse * (K - 2 * Theta);
```

instead of

```
double rhs_lapse = - 2 * lapse * (K - 2 * Theta);
```

GRCHOMBO implements all overloaded operators and functions which are necessary to ensure that the user can write code as usual, including arithmetic operators and transcendental functions, for various architectures. For example, on an architecture that supports AVX512 instructions, such as Knights Landing or Skylake, the multiplication of one `simd<double>` variable by another is implemented as

```
simd& operator*=(const simd& a) {
    m_value = _mm512_mul_pd(m_value, a.m_value);
```

```
    return *this;
}
```

Furthermore, to aid debugging, GRCHOMBO allows the user to output a variable of type `simd<typename>` in the usual way. The only operations that become more involved are comparisons and the conditional operator. For example, as explained in section 1.3.1, to calculate the advection derivatives in CCZ4 one needs to take a stencil that is lopsided in the direction in which the shift points. In GRCHOMBO, this is achieved by calculating both the upwind and downwind derivative and using a mask to select which one should be used

```
auto shift_positive = simd_compare_gt(shift, 0.);
return simd_conditional(shift_positive, upwind, downwind);
```

The design outlined above makes it highly likely that every loop over grid cells will be vectorised well. Should there be any instruction in a compute class that cannot be vectorised, it leads to a compilation error. The disadvantage of this design is the introduction of a template parameter to many of the functions in GRCHOMBO. While this may not seem like a big problem, it has knock-on effects; for example, it makes it impossible to declare these functions virtual.

2.5.3 Tensor algebra and expression templates

One property that all numerical relativity formalisms share is that they are written in terms of tensors or tensor densities. In GRCHOMBO, these quantities are represented by the class template `Tensor<size_t Rank, typename T, size_t Size>`, where `T` is the type of tensor components. It would be very convenient to be able to use operations on tensors directly rather than having to loop over components and perform the operations component-wise. Unfortunately, in C++ this is not a trivial task at all. The reason is that with naive operator overloading, combining several operations together results in many unnecessary temporaries and repeated loops. For example, if `A, ..., D` are tensors, the code `A = B + C + D` will most likely be equivalent to [150]

```
auto temp = B + C;
auto temp1 = temp + D;
A = temp1;
```

This implementation is very inefficient as it creates two unnecessary temporary tensors and performs three consecutive loops over all components. Instead, we would like the code to involve only one loop over all components in which the operation is performed component-wise and no temporary tensor is created. This can be achieved by using expression templates

[151, 150], a trick that allows us to delay evaluation until the full expression is known. The full expression can then be evaluated component-wise without the need of temporary tensors. In GRCHOMBO, we have a full implementation of expression templates for a tensor in numerical relativity. However, there are several major disadvantages of this technique: it requires heavily templated code that is hard to maintain, can lead to compilation errors that are hard to interpret, and the performance relies heavily on how well the compiler optimises the code. We are currently testing whether the simplifications it introduces outweigh the disadvantages. In the meantime, the current version of GRCHOMBO forces users to write expressions component-wise with explicit loops and provides macros to simplify the most common loops over components.

2.6 Conclusion

In this chapter, we presented GRCHOMBO, a new open-source, multi-purpose general relativity code. The GRCHOMBO code was first released in 2015 in Ref. [5] and was made public in 2018. In the last three years, it was used in nine publications [3, 2, 5, 48–53]. GRCHOMBO includes BSSN, CCZ4, and GHCs and is designed to be as flexible as possible so that it can be used for new applications of numerical relativity. Most importantly, GRCHOMBO provides fully adaptive mesh refinement which can increase the resolution automatically in regions of arbitrary shape and topology. This has been absolutely essential for simulations of black hole instabilities in higher dimensions, which often lead to the formation of new length scales in a turbulent cascade in regions that are not known a-priori and that have very exotic shapes and sometimes toroidal topology.

Despite its power, adaptive mesh refinement has to be treated with care. Interpolation at mesh boundaries can introduce significant errors, especially when refinement regions have very irregular shapes or the algorithm refines and unrefines very often. In these cases, it may be necessary to increase the dissipation coefficient, the damping parameters, or the size of refinement regions and the buffer between them.

We presented the latest performance characteristics and have demonstrated that even for a relatively cheap binary black hole simulation, GRCHOMBO runs efficiently on the latest Intel Xeon and Xeon Phi processors. It exhibits very good strongly scaling to several thousand cores for a standard binary black hole merger and has near-perfect weak scaling up to at least 20,000 cores. This is also the reason for why more expensive simulations, such as those of black rings, exhibit good strong scaling up to 20,000 cores. These results are substantially

better than those presented in our first code paper Ref. [5] and are certainly going to be superseded in the next few years as we improve the performance of GRCHOMBO further.

2.7 Appendix

2.7.1 Strong scaling for black rings

In the main text, we presented GRCHOMBO’s scaling for a standard benchmark problem, a binary black hole merger. To investigate the strong scaling for a typical simulation in this thesis, let us look at a black ring with thickness parameter $v = 0.15$ and radius $R = 1$. In a production setting, this simulation requires 11 levels to resolve the ring sufficiently. This makes it unfeasible to take a full step on the coarsest level in a scaling test. However, since the coarsest levels do not contribute to the overall run time (they are evolved much less often due to the CFL condition), we simply measure the time of two full steps of level 5. This level has a grid spacing of $\Delta x = 0.125R$ so that the finest level has a grid spacing of approximately $\Delta x = 0.002R$. We use the tagging criterion (2.4) with threshold $\sigma_\chi = 0.3$. As above, we include all ghost communication and regridding in the timings. While thin rings require higher resolution than fat rings, we carry out the test immediately after the initial data calculation where the instability has not created new scales that need to be resolved yet. Thus, this ring setup should give a fairly representative estimate of how expensive the simulations in chapter 4 are.

Fig. 2.8 shows the results. For this more expensive setup, useful strong scaling continues up to 20,000 cores and this core count is still so low that using four MPI processes per socket is best.

2.7.2 Strong scaling with different box sizes

In this section, we present scaling tests for two values of the maximum box size. The minimum box size has little to no impact on the runtime as long as it is selected between 4 and 16. The results in Fig. 2.9 show that the maximum box size has a significant impact: for low core counts, a large value such as 32 is most efficient. For high core counts, a small value such as 16 improves the strong scaling of GRCHOMBO since there are more boxes to be distributed among the MPI processes.

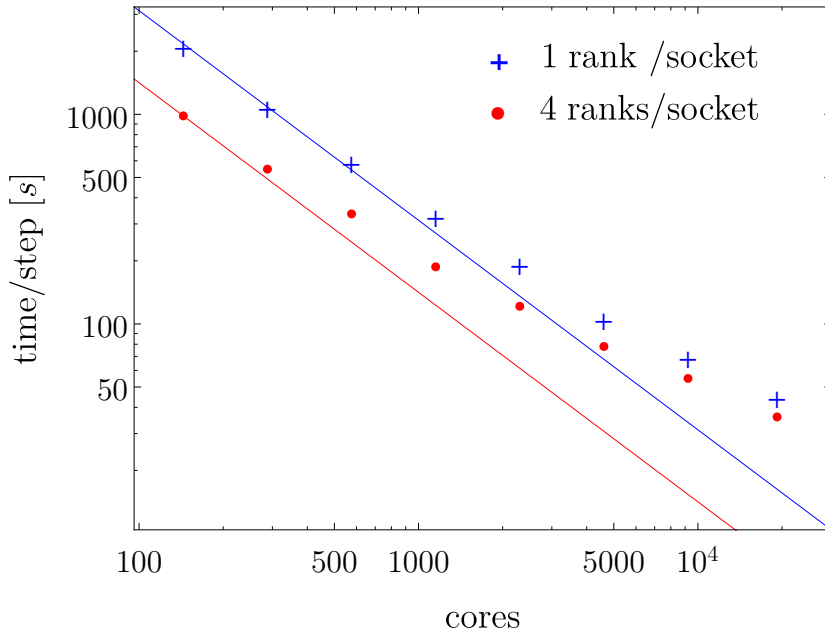


Fig. 2.8 Strong scaling behaviour of a black ring simulation with GRCHOMBO on Skylake processors at MareNostrum4.

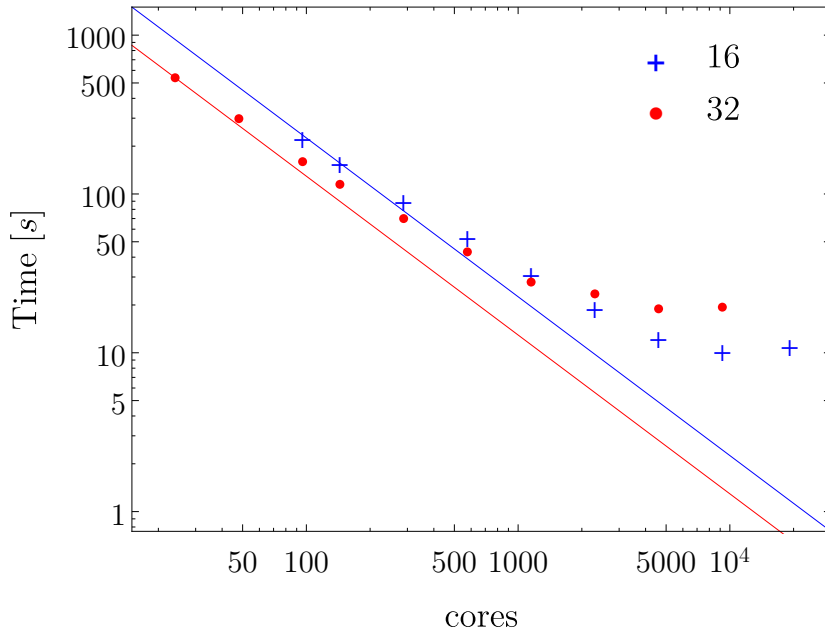


Fig. 2.9 Strong scaling behaviour on MareNostrum4 for several different maximum box sizes. With maximum box size 16, a single dual-socket Skylake node does not have enough memory to run the test.

Chapter 3

Numerical methods for higher dimensions

This chapter presents advances and adjustments we had to make to current numerical relativity methods in order to simulate higher dimensional spacetimes stably and efficiently. It includes gauge conditions that are optimised for higher dimensional black holes, a new singularity treatment, and a thorough analysis of how the modified Cartoon method, which was originally proposed in Ref. [152] for GHGs in axisymmetry, is best applied to CCZ4 with general $SO(N)$ symmetry.

Sections 3.2 and 3.3 are based on the co-authored publications [2, 3] and their supplemental material. These two sections are my own work. P. Figueras and S. Tunyasuvunakool provided helpful comments and G. Wells pointed out the literature on shock capturing in fluid dynamics, which motivated the diffusion term. Section 3.4 is based on the co-authored publication Ref. [153]. The analysis of $SO(2)$ is my own work; for $SO(N > 2)$, I performed an independent verification of the calculations for BSSN and obtained the necessary additional terms for CCZ4. I also performed an independent calculation of the regularisation terms (Appendix B). The latter are not unique and my results differ from those in Ref. [153].

3.1 Introduction

Most of the currently available numerical relativity techniques were originally devised for astrophysical settings. Simulations beyond astrophysics pose completely new challenges. They are often plagued by numerical instabilities and problems with the gauge conditions

[154, 155, 26, 153], which render the traditional methods at least partially unsuitable. Simulations in higher dimensions are particularly challenging. One reason is that they are very computationally expensive, even on the latest supercomputers. Currently, the only way to make them feasible is to use dimensional reduction techniques.

In this chapter, we summarise the three most important steps we had to take to make the simulations presented in chapters 4 and 5 possible. In section 3.2, we present adapted gauge conditions, which make it possible to simulate rapidly rotating black holes in higher dimensions. In section 3.3, we present a new singularity treatment for BSSN/CCZ4, which was necessary to stabilise the numerical evolution of higher dimensional black holes with puncture gauge. Finally, we present a detailed analysis of our dimensional reduction techniques, which are based on Ref. [152].

3.2 Gauge conditions

In this section, we describe modifications to the standard gauge evolution equations that were necessary for simulating rapidly rotating black holes in higher dimensions. The problem is that in general the initial data for rapidly rotating black holes is far from conformally flat, even in quasi-isotropic coordinates. As a result, the initial values of the conformal connection functions $\hat{\Gamma}^i$ are very large inside the horizon. In its standard form, the Gamma-Driver (1.31) freezes these initial values: it causes the gauge to adapt such that the conformal connection functions remain at their large initial values, even when the black hole has moved elsewhere. For example, for black rings we found that contours of the conformal connection functions kept their initial ring shape, even when the black hole collapses to a black hole of spherical topology. In theory, this is only a gauge effect and does not affect the physical results. In practice, forcing a region that is no longer covered by the horizon to retain very large conformal connection functions requires very extreme values in the other evolution variables. This in turn reduces the numerical accuracy and leads to significant constraint violations.

The freezing behaviour of the Gamma-Driver (1.31) can be understood by considering it in its integrated form, making sure to include all integration constants

$$\partial_t \beta^i - (\partial_t \beta^i)_{t=0} = F(\hat{\Gamma}^i - \hat{\Gamma}_{t=0}^i) - \eta(\beta^i - \beta_{t=0}^i). \quad (3.1)$$

The gauge parameters η and F are fixed by the requirement that the Gamma-Driver counters slice stretching effectively. With the required choice of parameters, the time scale over which the shift settles down to an approximately steady state is much faster than the time scale of

the evolution. If $\hat{\Gamma}_{t=0}^i$ is very large compared to $(\partial_t \beta^i)_{t=0}$ and $\beta_{t=0}^i$ inside the black hole, this steady state requires that $\hat{\Gamma}^i$ remains close to its initial value. One solution would be to cancel the offending integration constant $\hat{\Gamma}_{t=0}^i$ using the initial value for β^i or $\partial_t \beta^i$. However, this causes unacceptably fast gauge adjustment at early times.

Instead, we evolve the shift using

$$\partial_t \beta^i = F(\hat{\Gamma}^i - f(t, x^i) \hat{\Gamma}_{t=0}^i) - \eta(\beta^i - \beta_{t=0}^i) + \beta^k \partial_k \beta^i, \quad (3.2)$$

where $f(t, x^i)$ is an arbitrary function that is equal to one initially and then decays to zero. This gently unfreezes the conformal connection functions and allows them to tend to a value close to zero when the Gamma-Driver reaches its steady state. We typically choose $f(t, x^i)$ to be

$$f(t, x^i) = \exp(-\phi(x^i) t^2), \quad (3.3)$$

with a space-dependent function ϕ that controls the speed of gauge adjustment. For example, for a black hole of spherical topology, a good choice would be

$$\phi(x^i) = \delta_1 \frac{r_H^2}{r^2} + \delta_2, \quad (3.4)$$

where r is the coordinate radius, r_H is the location of the horizon, and δ_1 and δ_2 are positive parameters. With this choice of $\phi(x^i)$, the gauge adjustment outside the horizon is slower than inside, where the initial values of the conformal connection functions are larger and constraint violations resulting from rapid gauge adjustment cannot affect the exterior of the black hole. The modified Gamma-Driver (3.2) steers the gauge towards a quasi-stationary state in which $\hat{\Gamma}^i = 0$. In our simulations, we have found this to be a very stable condition.

Unlike the standard Gamma-Driver, the CCZ4 version of the standard $1 + \log$ slicing condition (1.30) also works well for higher dimensions and rapidly rotating black holes. We found the most stable results with a slightly reduced coefficient and with advection term

$$\partial_t \alpha = -\eta_\alpha (K - 2\Theta) + \beta^i \partial_i \alpha, \quad (3.5)$$

where η_α is a parameter which we typically choose between 1.3 and 2.0.

Since we write the initial data in isotropic-type coordinates for most of our simulations, we choose a pre-collapsed lapse (1.36). For rapidly rotating black holes, we also found it helpful

to modify the initial shift so that it has a similar profile by starting the simulation with

$$\alpha_0 = \chi^{\frac{D-3}{2}} \quad \text{and} \quad \beta_0^i = \chi \beta_{\text{an.}}^i, \quad (3.6)$$

where $\beta_{\text{an.}}^i$ is the analytic shift. An unintended but unavoidable side effect of not using analytic gauge initially is that the coordinates no longer co-rotate with the black hole as would usually be the case when using analytic initial conditions for stationary black holes. As a result, non-axisymmetric evolution variables such as off-diagonal metric components rotate on the numerical grid. The choice (3.6) keeps this rotation to a minimum so that it does not cause any problems as long as the Courant factor is small enough.

3.3 Singularity diffusion

Numerical relativity techniques turn out to be considerably less stable in non-standard settings such as higher dimensions, at high spins, or at ultra-relativistic speeds. For example, to improve the numerical stability of simulations of high-energy collisions in 4D, Ref. [156] had to lower the Courant factor substantially. In higher dimensions, gauge parameters had to be finely tuned and a very low Courant factor had to be chosen in Refs. [154, 155, 153], and excision had to be used in conjunction with the standard puncture method in Ref. [26]. There are several reasons for this: firstly, rapidly spinning and highly boosted black holes in higher dimensions often exhibit very steep gradients inside the horizon, which arise because the metric is far from conformally flat so that the BSSN/CCZ4 variables are not as well behaved as they are for astrophysical black holes with moderate boost and spin parameters.

Secondly, some higher dimensional black holes, such as black strings and black rings, have an extended coordinate singularity when written in isotropic-type coordinates, in contrast to spherical black holes for which this singularity is point-like. This makes it impossible to absorb the coordinate singularity in the conformal factor χ and makes numerical instabilities much more likely. A similar problem can be present even for black holes which, written in isotropic-type coordinates, only exhibit a point-like coordinate singularity, such as Myers-Perry black holes: if the horizon is highly flattened by the rotation, the region of high constraint violation inside the black hole is stretched out significantly in the rotational plane, making it harder to treat it in a stable fashion.

Thirdly, in higher dimensions or with high boost velocities or high spins, black holes can be defined by several very different length scales. An example of this are black rings, whose thickness can be much smaller than the radius. This makes it harder to find gauge parameters

that stabilise the interior of the black hole while keeping the overall shape of the horizon intact.

What all the problems above have in common is that they lead to the formation of numerical instabilities inside the black hole horizon: high frequency modes which grow so rapidly that they quickly cause floating point calculations to overflow. While physically no information can escape the horizon, floating point overflows quickly spread over the entire domain due to the finite difference stencils. A solution to this problem does not have to eliminate errors inside the horizon, it only has to stabilise the evolution sufficiently to prevent floating point overflow and to keep the causal structure intact.

An obvious solution would be to excise the regions inside the black hole which are expected to cause trouble. However, excision is not easy, especially when the black hole horizon takes on a very complicated shape. Furthermore, it requires finding the apparent horizon very frequently, which can be expensive and unreliable in cases where the apparent horizon finder has convergence problems. In this section, we outline a simple new method for dealing with the stability problems arising in non-astrophysical applications of numerical relativity. The idea is to add diffusion terms to Einstein's equations that are triggered automatically deep inside the horizon and only affect high frequency features.

We found that the only problematic quantity is the conformal metric $\tilde{\gamma}_{ij}$ as it appears with second derivatives in the equations of motion. While steep gradients arise in the extrinsic curvature and evolved conformal connection functions, they never caused problems in our simulations. Therefore, inspired by artificial viscosity terms [157–159]¹ in computational fluid dynamics, we add a term of the form

$$\Delta x^2 g(\chi, |\partial \tilde{\gamma}_{ij}|) (\nabla^2 \tilde{\gamma}_{ij})^{\text{TF}} \quad (3.7)$$

to the evolution equation of $\tilde{\gamma}_{ij}$ (1.19), where Δx is the grid spacing and $g(\chi, |\partial \tilde{\gamma}_{ij}|)$ is a sensing function which ensures that the diffusion term is only added sufficiently inside the horizon and only when the gradients in $\tilde{\gamma}_{ij}$ become large. This can easily be checked a posteriori with the apparent horizon data. We enforce the diffusion term to be trace-free to ensure that the constraint $\det \tilde{\gamma} = 1$ remains satisfied.

¹We are very grateful to Garth Wells for suggesting this to us.

The diffusion term (3.7) causes highly localised features to spread out and to decay in amplitude. For a Fourier mode of wavelength λ , the decay time is given approximately by

$$\tau \approx \frac{1}{8\pi g(\chi, |\partial \tilde{\gamma}_{ij}|)} \left(\frac{\lambda}{\Delta x} \right)^2. \quad (3.8)$$

This explains why the inclusion of a diffusion term of the form (3.7) mostly affects small wavelength features whilst keeping the physical results unchanged: due to the dependence of the decay time on $(\lambda/\Delta x)^2$, it mostly affects small length-scale features. Furthermore, due to the inclusion of Δx^2 in (3.7), the decay time automatically adapts when the grid resolution is changed. With a correctly calibrated sensing function g , it is therefore possible to only diffuse modes that could not be resolved by the grid. This is particularly nice with adaptive mesh refinement: the resolution is increased wherever it is physically necessary, thus preventing the diffusion term from being triggered. However, it is unfeasible to keep adding new refinement levels only to stabilise the evolution inside the black hole. Once the maximum number of refinement levels has been reached and the resolution is no longer increased, the diffusion term becomes important, but only affects modes that could not have been resolved accurately anyway.

One cause for concern is that the diffusion equation requires a stricter Courant condition than (2.1). For explicit time stepping schemes, a diffusion equation of the form $\partial_t Q = c_D \partial_x^2 Q$ leads to the CFL condition

$$\Delta t < \mu_{\text{CFL}} \frac{\Delta x^2}{c_D}, \quad (3.9)$$

where μ_{CFL} is a Courant factor that depends on the integration scheme. However, for our diffusion term (3.7) $c_D \propto \Delta x^2$, so that the Courant condition does not have worse scaling with Δx than (2.1).

While the inclusion of the diffusion term was inspired by shock capturing techniques in fluid dynamics, this analogy should not be taken too far. In particular, in fluid dynamics the aim of the diffusion term is to smear out shocks so that their properties can be accurately captured. In numerical relativity, we only want to smear out features, but have no hope of capturing any aspect of the singularity inside the black hole accurately.

The choice of the trigger function $g(\chi, |\partial \tilde{\gamma}_{ij}|)$ has to strike a fine balance between ensuring that the equations do not get modified outside the horizon and that the diffusion term is not

triggered too late to save the simulation. In our simulations, we use

$$g(\chi, |\partial \tilde{\gamma}_{ij}|) = c_L H(\chi_c - \chi) \sqrt{\frac{2}{D(D-1)} \sum_{i,j,k} (\partial_k \tilde{\gamma}_{ij})^2}, \quad (3.10)$$

where H is the Heaviside step function, c_L is an arbitrary coefficient which we typically chose between 0.01 and 0.2, and χ_c is a critical value for the conformal factor above which diffusion is switched off completely. The term under the square root makes sure that the diffusion term is only large in regions with large gradients. Since χ is approximately constant on the horizon, the Heaviside step function in (3.10) can be used to ensure that the diffusion term is switched off outside the horizon. We typically choose χ_c to be 10 to 100 times smaller than the approximate value of χ on the horizon. This cut-off is not strictly necessary for accurate simulations since the diffusion term only affects high frequency modes in regions of strong gradients. However, it makes it easier to guarantee that the results are not affected by ensuring that the diffusion term is only triggered deep down inside the horizon. We will present specific tests for this for black rings in chapter 4.

If the initial data already contain very steep gradients or very large values, the diffusion term might not be enough to stabilise the evolution. Therefore, a natural starting point for evolution with diffusion terms is *turduckened* initial data (1.38). For our purposes, 0th order turduckening in a very small region around the coordinate singularity is enough to lead to stable evolution with diffusion.

3.4 Modified Cartoon Method

3.4.1 Introduction

One of the key challenges of numerical relativity is that simulations are very expensive. This is not going to change in the foreseeable future since the complexity of our simulations increases at least as fast the computational power at our disposal. One of the ways in which simulations can be made feasible is by using symmetries to reduce the dimensionality of the problem. There are several reasons why simulations are more expensive for a higher number of dimensions:

Number of grid points. For an explicit time stepping scheme and a simple grid setup with N points in every direction, the number of grid points scales as $N^{D-1} = N^d$ and the

computational cost of a simulation as N^D .² For adaptive mesh codes, it is more complicated to estimate how the computational cost changes as D is increased. A good estimate can be obtained by only considering the finest level since this level requires the most time steps. Typically, the finest level has $N \approx 100$, so that increasing the number of dimensions by 1 increases the computational cost roughly by a factor of 100.

Tensor components. As the number of dimensions is increased, tensors have more components. This increases the number of variables that have to be evolved: in $D = 4$, CCZ4 with a second order Gamma-Driver shift condition requires 25 evolution variables; in $D = 8$, it requires 100. Furthermore, the calculation of the CCZ4 right hand side involves numerous loops over all tensor components. As the length of these loops is increased, the calculation of the right hand side becomes more and more costly.

Strong scaling. A rather subtle way in which a higher number of dimensions can affect the performance is due to worse strong scaling. GRCHOMBO, like most finite difference numerical relativity codes, achieves most of its parallelism by splitting up the domain into boxes and distributing them among MPI processes. The optimal run time one can achieve with this method is the time it takes one MPI process to operate on one box. Given a minimum box size n_{\min} this time is proportional to n_{\min}^d . To make matters worse, n_{\min} increases as the number of dimensions is increased, since the ratio of ghost cells to valid cells gets worse.³ Thus, the minimum runtime one can achieve with box parallelism increases faster than exponentially with D . This problem can be alleviated by using multiple layers of parallelism, but it cannot be completely eliminated and explains why simulating higher dimensional spacetimes is not just a matter of using a bigger supercomputer.

Due to the substantial saving in computational cost that comes with a decrease of the dimensionality of the problem, dimensional reduction techniques are crucial in numerical relativity. In $D = 4$, they allow more accurate simulations of phenomena that require very high resolution and they make it possible to perform parameter exploration and code tests much faster than would otherwise be possible. For example, to prepare a binary black hole inspiral simulation, one might first run tests of head-on collisions in axisymmetry at significantly reduced cost. In $D > 4$, dimensional reduction techniques are indispensable, as these simulations are currently unfeasible in full generality.

There are several ways in which symmetries can be used to reduce the dimensionality of the simulations. Most straight-forwardly, one can choose a coordinate system that makes

²The reason for the extra factor of N in the computational cost is that due to the Courant condition the size of the time step scales with the resolution, so that $O(N)$ steps are required to reach the end of the simulation.

³For example, for a fourth-order accurate code, which requires three layers of ghost cells, a box size of $n = 8$ leads to a ratio of ghost cells to valid cells of 2.1 in $d = 2$ and 4.4 in $d = 3$.

the symmetries manifest and leads to a simplified line element. For example, for spherical symmetry, the line element in spherical polar coordinates can be reduced to two functions of r and t

$$ds^2 = -\alpha(r,t)dt^2 + a(r,t)^2dr^2 + r^2d\Omega^2. \quad (3.11)$$

Einstein's equations yield evolution equations for $\alpha(r,t)$ and $a(r,t)$. This approach works well for reduction to a $1+1$ evolution system and has been widely used, for example in Ref. [40] to study critical collapse of a scalar field. The disadvantage is that the coordinates which make the symmetries manifest often exhibit a coordinate singularity, which makes numerical evolution more challenging. Furthermore, it becomes impractical beyond $1+1$ simulations, since every direction has to be treated differently and stable evolution is usually not possible with a gauge that is fixed a-priori.

Another class of symmetry reduction methods is based on the Geroch decomposition [160] which uses the symmetries to reduce the D dimensional vacuum Einstein equations to Einstein's equations in a lower dimensional space with auxiliary matter fields. This approach has been widely used and studied in various symmetry settings [161]. It is comparatively straight-forward to implement since existing numerical relativity codes can easily be adapted to include the auxiliary matter terms.

The cartoon method [162] is the only approach that requires no modification of the equations of motion. Instead, the computational domain is extended by ghost cells, which are filled using the symmetry condition. Let us illustrate this process for the case of axisymmetry in the $x - y$ plane in $D = 4$. Due to the symmetry, it is sufficient to solve the equations in the $x - z$ plane. To calculate y -derivatives, we add a thin layer of ghost cells in the y -direction, just enough to be able to calculate derivatives at $y = 0$. At every step, these ghost cells are filled by rotating values from the $y = 0$ plane, using the appropriate rotation matrices for tensorial quantities. This requires an interpolation step since grid points in the $x - z$ plane do not have the same cylindrical radius as the ghost points. The advantage of this method is that it allows symmetry reduction in Cartesian coordinates without any modifications to the evolution equations. The disadvantage is that the interpolation step can cause problems with the stability and accuracy of the code.

In our work, we use the *modified cartoon* method [152, 130, 4]. It is similar to the Cartoon method, but instead of adding ghost cells for calculating derivatives in the reduced directions, these derivatives are calculated analytically from the condition that the Lie derivative in the

symmetry directions vanishes

$$\mathcal{L}_{\xi_{\hat{a}}} T = 0, \quad (3.12)$$

where $\xi_{\hat{a}}$ are the Killing vectors that generate the symmetry group and T is any tensor obeying the symmetry. This has the significant advantage that no interpolation and no additional ghost cells are required.

3.4.2 Modified cartoon method for $SO(2)$ symmetry

There is a subtle difference between $SO(2)$ symmetry and $SO(N)$ symmetry with $N > 2$, which completely changes the way the modified Cartoon method should be implemented. The symmetry condition (3.12) implies that vector fields, V , must commute with all Killing vectors

$$[\xi_{\hat{a}}, V] = 0 \quad \forall \hat{a} \in \{1, \dots, N(N-1)/2\}. \quad (3.13)$$

For $N = 2$, there is only one independent Killing vector field: the one associated with the angular direction, ∂_{ϕ} . In this case, the symmetry condition (3.13) can be satisfied by a vector with non-zero ϕ -component. For $N > 2$, the situation is very different: as we will see in section 3.4.3, it is impossible to find vector fields V which commute with all Killing vectors and have non-trivial components in the symmetry directions. Fig. 3.1 shows a pictorial argument for why introducing another symmetry direction changes the setup so dramatically. Due to the substantial difference in how $SO(2)$ symmetry and $SO(N > 2)$ symmetry should be implemented, we consider them separately in the next two sections, starting with $SO(2)$.

Let us choose Cartesian coordinates (t, \hat{x}^i, z, w) such that the $SO(2)$ symmetry acts in the $z - w$ plane. In this section, indices $I, J, \dots \in \{1, \dots, D-2\}$ run over all the simulated spatial dimensions, indices $\hat{i}, \hat{j}, \dots \in \{1, \dots, D-3\}$ run over all simulated spatial dimensions except z , and indices $i, j, \dots \in \{1, \dots, D-1\}$ run over all spatial dimensions as usual. Furthermore, let ϕ be the polar angle in the $z - w$ plane.

The $SO(2)$ symmetry is generated by only one Killing vector

$$\partial_{\phi} = z \partial_w - w \partial_z. \quad (3.14)$$

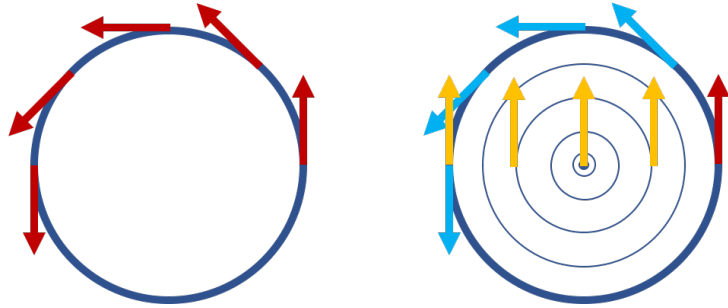


Fig. 3.1 Pictorial comparison between $SO(2)$ (left) and $SO(3)$ (right) symmetry. The former allows a vector field that is parallel to ∂_ϕ (red arrows). For the latter, we get incompatible requirements: the vector field must remain unchanged around both lines of constant latitude (blue arrows) and constant longitude (orange arrows).

Thus, for a scalar Q , the condition (3.12) implies

$$\partial_w Q = \frac{w}{z} \partial_z Q. \quad (3.15)$$

From which we can deduce the necessary w -derivatives in the $w = 0$ hyperplane

$$\partial_w Q = 0 \quad \text{and} \quad \partial_i \partial_w Q = \delta_i^w \frac{\partial_z Q}{z}. \quad (3.16)$$

For vectors, V , the condition (3.12) reduces to $[\partial_\phi, V] = 0$. In Cartesian coordinates this implies

$$z \partial_w V^i = w \partial_z V^i + V^z \delta_w^i - V^w \delta_z^i. \quad (3.17)$$

This allows us to calculate the first derivatives with respect to w in the $w = 0$ hyperplane,

$$\partial_w V^i = \frac{1}{z} (V^z \delta_w^i - V^w \delta_z^i), \quad (3.18)$$

and the second derivatives

$$\partial_j \partial_w V^i = \frac{1}{z} (\delta_j^w \partial_z V^i - \delta_j^z \partial_w V^i + \delta_w^i \partial_j V^z - \delta_z^i \partial_j V^w). \quad (3.19)$$

For rank-2 tensors, (3.12) implies

$$\partial_w T_{ij} = \frac{1}{z} (w \partial_z T_{ij} + T_{iw} \delta_j^z - T_{iz} \delta_j^w + T_{wj} \delta_i^z - T_{zj} \delta_i^w). \quad (3.20)$$

Thus, first and second derivatives involving w in the $w = 0$ hyperplane become

$$\partial_w T_{ij} = \frac{1}{z} \left(T_{iw} \delta_j^z - T_{iz} \delta_j^w + T_{wj} \delta_i^z - T_{zj} \delta_i^w \right) \quad (3.21)$$

and

$$\partial_k \partial_w T_{ij} = \frac{1}{z} \left(\delta_k^w \partial_z T_{ij} - \delta_k^z \partial_w T_{ij} + \partial_k T_{iw} \delta_j^z - \partial_k T_{iz} \delta_j^w + \partial_k T_{wj} \delta_i^z - \partial_k T_{zj} \delta_i^w \right). \quad (3.22)$$

While it is of course possible to eliminate the ∂_w derivatives in (3.19) and (3.22) using (3.18) and (3.21), this is not necessary and only makes the code more complicated: one can simply calculate $\partial_w V^i$ and $\partial_w T_{ij}$ first and then use these values in (3.19) and (3.22).

The modified cartoon method with $SO(2)$ symmetry allows us to model a D -dimensional spacetime on a $D - 2$ dimensional spatial grid corresponding to the $w = 0$ hyperplane. On this grid, we store all variables including all tensor components involving w indices such as V^w . As we will see in the next section, this is where the special case of $SO(2)$ differs substantially from $SO(N)$ with $N > 2$. In order to evolve the system by one timestep, we need to compute derivatives with respect to all coordinates. Derivatives with respect to x^I can be calculated on the grid using standard methods, e.g. finite difference stencils. Derivatives with respect to w , on the other hand, can be calculated using the expressions derived from (3.12). For example, for a vector in $D = 5$ with $SO(2)$ symmetry in the $w - z$ plane, the procedure for finding first derivatives is

$$V^i_{,j} = \left(\begin{array}{c|c} \text{calculate on} & \begin{array}{c} 0 \\ 0 \\ -V^w/z \\ V^z/z \end{array} \\ \text{the grid} & \end{array} \right). \quad (3.23)$$

Once all derivatives have been calculated, we can use the standard D -dimensional CCZ4 equations without the need for any extra terms. Thus, an $SO(2)$ symmetry reduction can be applied very easily to an existing numerical relativity code. It can even be combined with other symmetry reduction methods. For example, in chapter 5 we consider rapidly rotating black holes in $6D$. To make the simulations feasible, we enforce an $SO(3)$ symmetry in the transverse direction and combine it with an $SO(2)$ symmetry in the rotational plane. This reduces the equations to a system of PDEs in $2 + 1$ dimensions, leading to a significant reduction in computational cost and allowing us to study the instabilities of the black hole in great detail.

3.4.3 Modified cartoon method for $SO(N > 2)$ symmetry

Let us choose Cartesian coordinates $(t, x^{\hat{i}}, z, w^1, \dots, w^{N-1})$ similar to the ones used in the previous section with the only difference that now the $SO(N)$ symmetry acts in a space with several coordinates (z, w^1, \dots, w^{N-1}) . Indices $I, J, \dots \in \{1, \dots, D-N\}$ run over all the simulated spatial dimensions, indices $\hat{i}, \hat{j}, \dots \in \{1, \dots, D-N-1\}$ run over all simulated spatial dimensions except z , and indices $i, j, \dots \in \{1, \dots, D-1\}$ run over all spatial dimensions as usual. Furthermore, let us define indices $A, B, \dots \in D-N, \dots, D-1$, which run over all the coordinates w^1, \dots, w^{N-1} . The $SO(N)$ symmetry allows us to restrict our simulation to the semi-infinite subspace defined by $z > 0$ and $w^A = 0$ for all A : given information in this subspace, we can reconstruct the whole space using appropriate rotations.

As mentioned above, $SO(N > 2)$ symmetry requires some tensor components to vanish. Algebraically, we can deduce these restrictions from the symmetry condition $\mathcal{L}_{\xi_A} T = 0$ as follows: we pick two arbitrary directions A and B with coordinates w^A and w^B . The $SO(N)$ symmetry implies that there is a rotational symmetry in the (w^A, w^B) plane with Killing vector $\xi_{AB} = w^A \partial_B - w^B \partial_A$. For vectors this requires that

$$\mathcal{L}_{\xi_{AB}} V^A = w^A \partial_B V^A - w^B \partial_A V^A + V^B = 0. \quad (3.24)$$

We restrict our simulation to the subspace defined by $w^A = 0$ for all A , where the above condition simply becomes

$$V^A = 0 \quad \forall A. \quad (3.25)$$

Proceeding similarly for components of rank-2 tensors T , we find that in the $w^A = 0$ subspace

$$\mathcal{L}_{\xi_{AB}} T_{IA} = T_{IB} = 0, \quad (3.26)$$

$$\mathcal{L}_{\xi_{AB}} T_{AB} = T_{BB} - T_{AA} = 0, \quad (3.27)$$

$$\mathcal{L}_{\xi_{AB}} T_{BB} = T_{AB} = 0. \quad (3.28)$$

Thus, for vectors, none of the V^A components have to be simulated, while for tensors only one quantity is required, which we call T_{ww} . For the CCZ4 evolution system, only two additional evolution variables are necessary, $\tilde{\gamma}_{ww}$ and \tilde{A}_{ww} . For large N , this allows substantial savings in computational cost and memory. Unfortunately, trying to capitalise on these savings comes at a price: it means that we cannot just reuse non-dimensionally reduced code by filling in missing derivatives as we did for the $SO(2)$ case. Instead, we have to evaluate the extra symmetry terms by hand and add them to the CCZ4 right hand side. For example, the

term $T^{ij}T_{ij}$ has to be rewritten in terms of evolution variables as $T^{IJ}T_{IJ} + (N - 1)T_{ww}^2/\gamma_{ww}^2$, where we have used that $\gamma^{ww} = 1/\gamma_{ww}$ since (3.26) and (3.28) imply that γ_{ij} is diagonal in the cartoon components.

In the remainder of this section, we will present the cartoon terms for the CCZ4 system. To do this, we first have to express derivatives with respect to w^A . The method is similar to the previous section but we now have to take into account that there are several cartoon directions. We present the calculation of the most complicated cartoon expressions, derivatives of T_{IC} , as an example below and list all other necessary cartoon derivatives in the appendix to this chapter.

Symmetry in the (z, w^A) plane implies

$$\mathcal{L}_{\xi_{zA}} T_{IC} = z\partial_A T_{IC} - w^A \partial_z T_{IC} - T_{Iz} \delta_{AC} + T_{AC} \delta_{zI} = 0, \quad (3.29)$$

$$\mathcal{L}_{\xi_{zA}} T_{CD} = z\partial_A T_{CD} - w^A \partial_z T_{CD} + T_{zD} \delta_{AC} - T_{Cz} \delta_{AD} = 0. \quad (3.30)$$

As an immediate consequence we can deduce that in the subspace $w^A = 0 \forall A$

$$\partial_A T_{IC} = \frac{1}{z} (T_{Iz} \delta_{AC} - T_{AC} \delta_{zI}) = \delta_{AC} \frac{1}{z} (T_{Iz} - T_{ww} \delta_{Iz}), \quad (3.31)$$

$$\partial_A T_{CD} = \frac{1}{z} (T_{zD} \delta_{AC} - T_{Cz} \delta_{AD}) = 0, \quad (3.32)$$

where we have used equations (3.26) and (3.28) for the last equalities. Taking a partial derivative of (3.29) and (3.30) with respect to w^B and substituting in the above expression for $\partial_A T_{IC}$ and $\partial_A T_{CD}$, we find that in the subspace $w^A = 0 \forall A$

$$\partial_A \partial_B T_{IC} = 0, \quad (3.33)$$

$$\partial_A \partial_B T_{CD} = (\delta_{AC} \delta_{BD} + \delta_{AD} \delta_{BC}) \frac{T_{zz} - T_{ww}}{z^2} + \delta_{AB} \delta_{CD} \frac{\partial_z T_{ww}}{z}. \quad (3.34)$$

We proceed similarly for all other cartoon derivatives. The results are summarised in Appendix A to this chapter. With a significant amount of algebra, we can use these Cartoon expressions for derivatives to derive the CCZ4 equations with $SO(N > 2)$ symmetry reduction. They are given in Box 3. To simplify the expressions, we have defined $n = N - 1$ and $d = D - 1$. As explained in section 1.3.1, the terms $\mathcal{D}_i Z_j$ are never evaluated independently, but are used in the Ricci tensor to cancel derivatives of $\tilde{\Gamma}$ in favour of $\hat{\Gamma}^i$.

Box 3: CCZ4 with $SO(N)$ symmetry reduction for $N > 2$.

$$\partial_t \chi = \frac{2\chi}{d} \left(\alpha K - \partial_I \beta^I - n \frac{\beta^z}{z} \right) + \beta^I \partial_I \chi, \quad (3.35)$$

$$\partial_t \tilde{\gamma}_{IJ} = -2\alpha \tilde{A}_{IJ} + 2\tilde{\gamma}_{L(I} \partial_{J)} \beta^L - \frac{2}{d} \tilde{\gamma}_{IJ} \left(\partial_L \beta^L + n \frac{\beta^z}{z} \right) + \beta^L \partial_L \tilde{\gamma}_{IJ}, \quad (3.36)$$

$$\partial_t \tilde{\gamma}_{ww} = -2\alpha \tilde{A}_{ww} - \frac{2}{d} \tilde{\gamma}_{ww} \left(\partial_L \beta^L - (d-n) \frac{\beta^z}{z} \right) + \beta^L \partial_L \tilde{\gamma}_{ww}, \quad (3.37)$$

$$\begin{aligned} \partial_t \tilde{A}_{IJ} = \chi & \left[-\mathcal{D}_I \mathcal{D}_J \alpha + \alpha (\mathcal{R}_{IJ} + 2\mathcal{D}_{(I} Z_{J)} - 8\pi \alpha S_{IJ}) \right]^{\text{TF}} + \alpha \tilde{A}_{IJ} (K - 2\Theta) \\ & - 2\alpha \tilde{A}_{IL} \tilde{A}^L_J + 2\tilde{A}_{K(I} \partial_{J)} \beta^K - \frac{2}{d} \tilde{A}_{IJ} \left(\partial_K \beta^K + n \frac{\beta^z}{z} \right) + \beta^L \partial_L \tilde{A}_{IJ}, \end{aligned} \quad (3.38)$$

$$\begin{aligned} \partial_t \tilde{A}_{ww} = \chi & \left[-\mathcal{D}_w \mathcal{D}_w \alpha + \alpha ([\mathcal{R} + 2\mathcal{D}Z]_{ww} - 8\pi \alpha S_{ww}) \right]^{\text{TF}} + \alpha \tilde{A}_{ww} (K - 2\Theta) \\ & - 2\alpha \tilde{A}_{ww}^2 \tilde{\gamma}^{ww} - \frac{2}{d} \tilde{A}_{IJ} \left(\partial_K \beta^K - (d-n) \frac{\beta^z}{z} \right) + \beta^L \partial_L \tilde{A}_{IJ}, \end{aligned} \quad (3.39)$$

$$\begin{aligned} \partial_t \Theta = \frac{1}{2} \alpha & \left(\text{Tr} [\mathcal{R}_{ij} + 2\mathcal{D}_i Z_j] - \tilde{A}_{IJ} \tilde{A}^{IJ} - n \tilde{A}_{ww}^2 \tilde{\gamma}^{ww2} + \frac{d-1}{d} K^2 - 2\Theta K \right) - Z^I \partial_I \alpha \\ & + \beta^L \partial_L \Theta - \frac{1}{2} \alpha \kappa_1 (D + (d-1) \kappa_2) \Theta - 8\pi \alpha \rho, \end{aligned} \quad (3.40)$$

$$\begin{aligned} \partial_t K = 2(\partial_t \Theta - \beta^L \partial_L \Theta) + \alpha & \left(\tilde{A}_{IJ} \tilde{A}^{IJ} + n \tilde{A}_{ww}^2 \tilde{\gamma}^{ww2} + \frac{1}{d} K^2 \right) - \mathcal{D}^I \mathcal{D}_I \alpha \\ & - n \tilde{\gamma}^{ww} \mathcal{D}_w \mathcal{D}_w \alpha + \kappa_1 \alpha (1 - \kappa_2) \Theta + 2Z^I \partial_I \alpha + \beta^L \partial_L K + 4\pi \alpha (S + \rho), \end{aligned} \quad (3.41)$$

$$\begin{aligned} \partial_t \hat{\Gamma}^I = -2\tilde{A}^{IJ} \partial_J \alpha + 2\alpha & \left(\tilde{\Gamma}_{JL}^I \tilde{A}^{JL} + n \tilde{\Gamma}_{ww}^I \tilde{A}_{ww} \tilde{\gamma}^{ww2} - \frac{d-1}{d} \tilde{\gamma}^{IJ} \partial_J K - \frac{d}{2} \tilde{A}^{IJ} \frac{\partial_J \chi}{\chi} \right) \\ & + \frac{d-2}{d} \left(\tilde{\gamma}^{IJ} \partial_J \partial_L \beta^L + n \tilde{\gamma}^{IL} \frac{\partial_L \beta^z}{z} - n \tilde{\gamma}^{Jz} \frac{\beta^z}{z^2} \right) + \frac{2}{d} \tilde{\Gamma}^I \left(\partial_L \beta^L + n \frac{\beta^z}{z} \right) \\ & - \tilde{\Gamma}^L \partial_L \beta^I + 2\kappa_3 \left(\frac{2}{d} \tilde{\gamma}^{IJ} Z_J \left[\partial_L \beta^L + n \frac{\beta^z}{z} \right] - \tilde{\gamma}^{JL} Z_J \partial_L \beta^I \right) \\ & + \tilde{\gamma}^{JL} \partial_J \partial_L \beta^I + n \tilde{\gamma}^{ww} \left(\frac{\partial_z \beta^I}{z} - \delta_z^I \frac{\beta^z}{z^2} \right) + \beta^L \partial_L \hat{\Gamma}^I \\ & + 2\tilde{\gamma}^{IJ} \left(\alpha \partial_J \Theta - \Theta \partial_J \alpha - \frac{2}{d} \alpha K Z_J \right) - 2\alpha \kappa_1 \tilde{\gamma}^{IJ} Z_J - 16\pi \alpha \tilde{\gamma}^{IJ} j_J. \end{aligned} \quad (3.42)$$

The Hamiltonian and momentum constraints are

$$\mathcal{H} = 0 = \mathcal{R}_L^L + n\chi \tilde{\gamma}^{ww} \mathcal{R}_{ww} + \frac{d-1}{d} K^2 - \tilde{A}_{IJ} \tilde{A}^{IJ} - n \tilde{A}_{ww}^2 \tilde{\gamma}^{ww2} - 16\pi \rho, \quad (3.43)$$

$$\begin{aligned} \mathcal{M}_I = 0 = \tilde{\gamma}^{IL} \partial_J \tilde{A}_{LI} + n \tilde{\gamma}^{ww} & \frac{\tilde{A}^{Iz} - \delta_{iz} \tilde{A}_{ww}}{z} - \tilde{\Gamma}^L \tilde{A}_{LI} - n \tilde{\gamma}^{ww} \tilde{\Gamma}_{ww}^L \tilde{A}_{LI} - \tilde{\gamma}^{JL} \tilde{\Gamma}_{IJ}^M \tilde{A}_{ML} \\ & - \frac{1}{2} \tilde{\gamma}^{ww} \tilde{A}_{ww} \partial_I \tilde{\gamma}_{ww} - \frac{d-1}{d} \partial_I K - \frac{d}{2} \frac{\partial_J \chi}{\chi} \tilde{A}^J_I - 8\pi j_I. \end{aligned} \quad (3.44)$$

Box 3: continued ...

The Ricci tensor is calculated as $\mathcal{R}_{ij} = \mathcal{R}_{ij}^\chi + \tilde{\mathcal{R}}_{ij}$ with

$$\begin{aligned} \mathcal{R}_{IJ}^\chi &= \frac{1}{2\chi} \tilde{\gamma}_{IJ} \left[\tilde{\gamma}^{MN} \tilde{D}_M \tilde{D}_N \chi + n \left(\frac{1}{2} \tilde{\gamma}^{ww} \tilde{\gamma}^{MN} \partial_N \tilde{\gamma}_{ww} + \frac{\tilde{\gamma}^{Mz}}{z} \right) \partial_M \chi \right. \\ &\quad \left. - \frac{D-1}{2\chi} \tilde{\gamma}^{MN} \partial_M \chi \partial_N \chi \right] + \frac{D-3}{2\chi} \left(\tilde{D}_I \tilde{D}_J \chi - \frac{1}{2\chi} \partial_I \chi \partial_J \chi \right) \end{aligned} \quad (3.45)$$

$$\begin{aligned} \mathcal{R}_{ww}^\chi &= \frac{\tilde{\gamma}_{ww}}{2\chi} \left[\tilde{\gamma}^{MN} \tilde{D}_M \tilde{D}_N \chi + (D+n-3) \left(\frac{1}{2} \tilde{\gamma}^{ww} \tilde{\gamma}^{MN} \partial_N \tilde{\gamma}_{ww} + \frac{\tilde{\gamma}^{Mz}}{z} \right) \partial_M \chi \right. \\ &\quad \left. - \frac{D-1}{2\chi} \tilde{\gamma}^{MN} \partial_M \chi \partial_N \chi \right], \end{aligned} \quad (3.46)$$

$$\begin{aligned} \tilde{\mathcal{R}}_{IJ} &= n \tilde{\gamma}^{ww} \left[-\frac{1}{2} \frac{\partial_z \tilde{\gamma}_{IJ}}{z} + \frac{\delta_{z(I} \tilde{\gamma}_{J)z} - \delta_{Iz} \delta_{Jz} \tilde{\gamma}_{ww}}{z^2} + \frac{\tilde{\gamma}^{ww} \tilde{\gamma}_{z(J} - \delta_{z(J} \partial_{I)} \tilde{\gamma}_{ww}}{z} \right. \\ &\quad \left. - \frac{1}{4} \tilde{\gamma}^{ww} \partial_I \tilde{\gamma}_{ww} \partial_J \tilde{\gamma}_{ww} \right] - \frac{1}{2} \tilde{\gamma}^{MN} \partial_M \partial_N \tilde{\gamma}_{IJ} + \tilde{\gamma}_{M(I} \partial_{J)} \tilde{\Gamma}^M \\ &\quad + \tilde{\Gamma}^M \tilde{\Gamma}_{(IJ)M} + \tilde{\gamma}^{MN} \left[2 \tilde{\Gamma}_{M(I}^K \tilde{\Gamma}_{J)KN} + \tilde{\Gamma}_{IM}^K \tilde{\Gamma}_{KJN} \right], \end{aligned} \quad (3.47)$$

$$\begin{aligned} \tilde{\mathcal{R}}_{ww} &= -\frac{1}{2} \tilde{\gamma}^{MN} \partial_M \partial_N \tilde{\gamma}_{ww} + \frac{1}{2} \tilde{\gamma}^{ww} \tilde{\gamma}^{MN} \partial_M \tilde{\gamma}_{ww} \partial_N \tilde{\gamma}_{ww} - \frac{n}{2} \tilde{\gamma}^{ww} \frac{\partial_z \tilde{\gamma}_{ww}}{z} + \tilde{\gamma}_{ww} \frac{\tilde{\Gamma}^z}{z} \\ &\quad + \frac{1}{2} \tilde{\Gamma}^M \partial_M \tilde{\gamma}_{ww} + \frac{\tilde{\gamma}^{zz} \tilde{\gamma}_{ww} - 1}{z^2}. \end{aligned} \quad (3.48)$$

Furthermore, we need the auxiliary quantity

$$D_w D_w \alpha = \left(\frac{1}{2} \tilde{\gamma}^{MN} \partial_N \tilde{\gamma}_{ww} + \frac{\tilde{\gamma}^{z\bar{M}}}{z} \tilde{\gamma}_{ww} \right) \partial_M \alpha - \frac{1}{2\chi} \tilde{\gamma}_{ww} \tilde{\gamma}^{MN} \partial_M \chi \partial_N \alpha. \quad (3.49)$$

3.4.4 Boundary conditions and regularisation

Since in the modified cartoon method the simulation is restricted to the semi-infinite subspace $z > 0$ and $w^A = 0$, we have to find the correct boundary conditions at $z = 0$. Furthermore, due to the ubiquitous divisions by z in the cartoon terms, we cannot evaluate the equations at $z = 0$ without regularising them explicitly. Regularisation is only necessary for node-centred codes, which have grid points at $z = 0$. For cell-centred codes, the smallest value of z that will be encountered is $\Delta z / 2$, where Δz is the grid spacing in the z -direction, so that no regularisation is required.

The key observation we need to make in order to be able to regularise the cartoon terms is that in restricting the simulation to the semi-infinite subspace defined by $z > 0$ and w^A , we have given z the role of the radial coordinate in the subspace in which the $SO(N)$ symmetry acts. As a result, regularity at the origin requires that tensor components that contain an even number of z indices are even in z , whereas tensor components with an odd number of z indices are odd. For example, the series expansions of components of the shift are

$$\beta^{\hat{i}} = b_0^{\hat{i}} + b_2^{\hat{i}} z^2 + O(z^4) \quad \text{and} \quad \beta^z = b_1^z z + b_3^z z^3 + O(z^5). \quad (3.50)$$

Among others, this implies that we can write the following cartoon term arising in (3.42) in a manifestly regular form

$$\lim_{z \rightarrow 0} \left(\frac{\partial_z \beta^I}{z} - \delta_z^I \frac{\beta^z}{z^2} \right) = \begin{cases} \partial_z \partial_z \beta^{\hat{i}} & \text{if } I = \hat{i} \\ 0 & \text{if } I = z \end{cases}. \quad (3.51)$$

The regularisation of the remaining cartoon terms can be done in a similar fashion and is shown in the appendix to this chapter. The results are not unique since several terms allow multiple regularisations. In Ref. [4], we presented the regularisation terms whose stability had been tested most thoroughly in our code. In Appendix B to this chapter, we show a different approach for some terms, which simplifies the algebra and the resulting regularisation terms slightly.

Independently of whether the code is cell-centred or not, we have to impose boundary conditions at $z = 0$ in order to be able to take derivatives in the z direction at the lower edge of the numerical grid. The regularity conditions above imply that we should fix the parity of the evolution variables: those with an even number of z indices are enforced to be even, those with an odd number of indices are enforced to be odd. This can be achieved either by selecting derivative stencils which have the parity built in in the vicinity of $z = 0$, or by filling the ghost cells outside the computational domain by an odd or even extrapolation as appropriate. In GRChombo, we use the latter approach, as it is easier to implement and avoids inefficient branching instructions in the evolution code.

3.5 Appendix A: Tensor components for $SO(N > 2)$

For scalars and vectors with $SO(N > 2)$ symmetry, we find

$$0 = \partial_A Q = \partial_I \partial_A Q, \quad (3.52)$$

$$\partial_A \partial_B Q = \delta_{AB} \frac{\partial_z Q}{z}, \quad (3.53)$$

$$0 = V^A = \partial_I V^A = \partial_A V^I = \partial_A \partial_B V^C, \quad (3.54)$$

$$\partial_A V^B = \delta_A^B \frac{V^z}{z}, \quad (3.55)$$

$$\partial_I \partial_A V^B = \delta_A^B \left(\frac{\partial_I V^z}{z} - \delta_{Iz} \frac{V^z}{z^2} \right), \quad (3.56)$$

$$\partial_A \partial_B V^I = \delta_{AB} \left(\frac{\partial_z V^I}{z} - \delta_z^I \frac{V^z}{z^2} \right). \quad (3.57)$$

For rank-2 tensors, $SO(N > 2)$ symmetry implies

$$0 = T_{IA} = \partial_A T_{BC} = \partial_I \partial_A T_{BC} = \partial_A \partial_B T_{IC} = \partial_A T_{IJ} = \partial_I \partial_A T_{JL}, \quad (3.58)$$

$$T_{AB} = \delta_{AB} T_{ww}, \quad (3.59)$$

$$\partial_A \partial_B T_{CD} = (\delta_{AC} \delta_{BD} + \delta_{AD} \delta_{BC}) \frac{T_{zz} - T_{ww}}{z^2} + \delta_{AB} \delta_{CD} \frac{\partial_z T_{ww}}{z}, \quad (3.60)$$

$$\partial_A T_{IB} = \delta_{AB} \frac{T_{Iz} - \delta_{Iz} T_{ww}}{z}, \quad (3.61)$$

$$\partial_I \partial_A T_{JB} = \delta_{AB} \left(\frac{\partial_I T_{Jz} - \delta_{Jz} \partial_I T_{ww}}{z} - \delta_{Iz} \frac{T_{Jz} - \delta_{Jz} T_{ww}}{z^2} \right), \quad (3.62)$$

$$\partial_A \partial_B T_{IJ} = \delta_{AB} \left(\frac{\partial_z T_{IJ}}{z} - \frac{\delta_{Iz} T_{Jz} + \delta_{Jz} T_{Iz} - 2 \delta_{Iz} \delta_{Jz} T_{ww}}{z^2} \right). \quad (3.63)$$

3.6 Appendix B: Regularisation terms

In this appendix, we present the regularisation terms that are necessary for evaluating the evolution equations in Box 3 at $z = 0$. We use the same indices as in the main text and the same enumeration of the types of cartoon expressions as in Ref. [4]. Regularisation terms are not unique and our treatment of the terms 2, 5, and 9 differs from Ref. [4], where we presented the regularisation terms that we had used most in practice. While the terms below have not been tested as thoroughly, there is no reason to suspect that they should be any less stable.

In equations (3.35) to (3.48) many of the cartoon terms look hard to regularise. However, this is not because regularisation is inherently complicated; it is a result of us having simplified the cartoon expressions to a point where regularisation is not obvious anymore. Indeed, the regularisation of the cartoon derivatives in the previous section is straightforward. As a result, by keeping track of where a simplified term originated from, we can avoid having to employ more complicated regularisation techniques.

Type 1. Since terms involving an odd number of z indices are odd, we obtain

$$\lim_{z \rightarrow 0} \frac{\beta^z}{z} = \partial_z \beta^z \quad \text{and} \quad \lim_{z \rightarrow 0} \frac{\partial_z \alpha}{z} = \partial_z \partial_z \alpha. \quad (3.64)$$

Terms $\partial_z \chi/z$, $\partial_z \tilde{\gamma}_{ww}/z$ are treated in exactly the same way.

Type 2. For any rank-2 tensor T obeying the symmetry $T_{zz} - T_{ww} = O(z^2)$. This is a direct consequence of requiring $\partial_w^2 T_{zz}$ (3.63) to be regular at $z = 0$. Using $\tilde{\gamma}_{zz} - \tilde{\gamma}_{ww} = O(z^2)$ and the fact that $\tilde{\gamma}_{\hat{j}z}$ is odd we get

$$\lim_{z \rightarrow 0} \frac{\delta_z^I - \tilde{\gamma}^{zI} \tilde{\gamma}_{ww}}{z} = \lim_{z \rightarrow 0} \tilde{\gamma}^{IJ} \frac{\tilde{\gamma}_{Jz} - \delta_J^z \tilde{\gamma}_{ww}}{z} = \tilde{\gamma}^{I\hat{j}} \partial_z \tilde{\gamma}_{\hat{j}z}. \quad (3.65)$$

Type 3. We already described the regularisation procedure of this type of term in the main text,

$$\lim_{z \rightarrow 0} \left(\frac{\partial_z \beta^I}{z} - \delta_z^I \frac{\beta^z}{z^2} \right) = \begin{cases} \partial_z \partial_z \beta^{\hat{i}} & \text{if } I = \hat{i} \\ 0 & \text{if } I = z \end{cases}. \quad (3.66)$$

Type 4. Using the fact that β^z is odd we find

$$\lim_{z \rightarrow 0} \frac{\tilde{\gamma}^{IJ} \partial_J \beta^z}{z} - \tilde{\gamma}^{Iz} \frac{\beta^z}{z} = \lim_{z \rightarrow 0} \tilde{\gamma}^{IJ} \left(\frac{\partial_J \beta^z}{z} - \delta_J^z \frac{\beta^z}{z^2} \right) = \tilde{\gamma}^{I\hat{j}} \partial_{\hat{j}} \partial_z \beta^z. \quad (3.67)$$

Type 5. For the regularisation of this type of term it is helpful to keep in mind that it arose from the cancellation of several cartoon expressions

$$\begin{aligned} \lim_{z \rightarrow 0} \frac{\tilde{\gamma}^{zI}}{z} \partial_I \alpha &= \lim_{z \rightarrow 0} \tilde{\gamma}^{ww} \left(-\tilde{\gamma}^{IJ} \frac{\tilde{\gamma}_{Jz} - \delta_J^z \tilde{\gamma}_{ww}}{z} \partial_I \alpha + \frac{\partial_z \alpha}{z} \right) \\ &= \tilde{\gamma}^{ww} \left(-\tilde{\gamma}^{I\hat{j}} \partial_z \tilde{\gamma}_{\hat{j}z} \partial_I \alpha + \partial_z \partial_z \alpha \right) \end{aligned} \quad (3.68)$$

Type 6. Since $A_{\hat{i}z}$ is odd and $A_{zz} - A_{ww} = O(z^2)$, we have

$$\lim_{z \rightarrow 0} \frac{\tilde{A}_{Iz} - \delta_{Iz}\tilde{A}_{ww}}{z} = \begin{cases} \partial_z \tilde{A}_{\hat{i}z} & \text{if } I = \hat{i} \\ 0 & \text{if } I = z \end{cases}. \quad (3.69)$$

Type 7. Using $\tilde{\gamma}_{zz} - \tilde{\gamma}_{ww} = O(z^2)$ and the fact that $\partial_z \tilde{\gamma}_{IJ}$ is odd, we find

$$\lim_{z \rightarrow 0} -\frac{1}{2} \frac{\partial_z \tilde{\gamma}_{IJ}}{z} + \frac{\delta_{z(I}\tilde{\gamma}_{J)z} - \delta_{Iz}\delta_{Jz}\tilde{\gamma}_{ww}}{z^2} = \begin{cases} -\frac{1}{2} \partial_z \partial_z \tilde{\gamma}_{\hat{i}\hat{j}} & \text{if } I = \hat{i}, J = \hat{j} \\ -\frac{1}{2} \partial_z \partial_z \tilde{\gamma}_{ww} & \text{if } I = J = z \\ 0 & \text{otherwise} \end{cases}. \quad (3.70)$$

Type 8. Using $\tilde{\gamma}^{ww}\tilde{\gamma}_{zz} - 1 = \tilde{\gamma}^{ww}(\tilde{\gamma}_{zz} - \tilde{\gamma}_{ww}) = \tilde{\gamma}^{ww}O(z^2)$ and the fact that $\tilde{\gamma}_{z\hat{i}}$ is odd, we find

$$\frac{\tilde{\gamma}^{ww}\tilde{\gamma}_{z(J} - \delta_{z(J}\tilde{\gamma}_{I)w}}{z} \partial_{I)} \tilde{\gamma}_{ww} = \begin{cases} \tilde{\gamma}^{ww} \partial_z \tilde{\gamma}_{z(\hat{j}} \partial_{\hat{i})} \tilde{\gamma}_{ww} & \text{if } I = \hat{i}, J = \hat{j} \\ 0 & \text{otherwise} \end{cases}. \quad (3.71)$$

Type 9. This term appears complicated to regularise at first sight, but after breaking it up into its original constituents, it can be regularised easily using $\tilde{\gamma}_{zz} - \tilde{\gamma}_{ww} = O(z^2)$ and the fact that $\partial_z \tilde{\gamma}_{IJ}$ is odd

$$\begin{aligned} \lim_{z \rightarrow 0} \frac{1}{z^2} (\tilde{\gamma}^{zz}\tilde{\gamma}_{ww} - 1) &= \lim_{z \rightarrow 0} \tilde{\gamma}^{ww} \left(\frac{\tilde{\gamma}_{zz} - \delta_{zz}\tilde{\gamma}_{ww}}{z} \frac{\tilde{\gamma}_{zz} - \delta_{zz}\tilde{\gamma}_{ww}}{z} \tilde{\gamma}^{IJ} - \frac{\tilde{\gamma}_{zz} - \tilde{\gamma}_{ww}}{z^2} \right) \\ &= \tilde{\gamma}^{ww} \left(\tilde{\gamma}^{\hat{i}\hat{j}} \partial_z \tilde{\gamma}_{\hat{i}z} \partial_z \tilde{\gamma}_{\hat{j}z} - \frac{1}{2} \partial_z^2 \tilde{\gamma}_{zz} + \frac{1}{2} \partial_z^2 \tilde{\gamma}_{ww} \right). \end{aligned} \quad (3.72)$$

Chapter 4

End point of black ring instabilities

This chapter presents the results of fully non-linear numerical simulations of black ring instabilities with the GRCHOMBO code. For a wide range of thin and fat rings, we follow the evolution of various instabilities of black rings, identify which one dominates, and find its end point. In this process, we discover a previously unknown instability of black rings which stretches and deforms the ring. We analyse the geometry of the apparent horizon throughout the evolution and present evidence that the GL instability causes very thin rings to pinch off.

This chapter is based on the co-authored publication Ref. [3]. Furthermore, it contains unpublished results on fat rings, the approach to pinch-off in the instability of very thin black rings, and the $m = 1$ mode of the GL instability of thin rings. Some of the results presented in this chapter were also included in the PhD thesis [163] of my co-author S. Tunyasuvunakool. I implemented the black ring code with symmetry reduction in GRCHOMBO. Furthermore, I was responsible for finding the gauge conditions and the diffusion term that stabilised the evolution of black rings and carried out roughly half the simulations presented in this chapter. The analysis of the gravitational wave data and the numerical tests in Appendix B were entirely my own work. The apparent horizon finder was implemented by S. Tunyasuvunakool and therefore the discussion of it is kept to the necessary minimum in this thesis. The interested reader is referred to Ref. [163] for details.

4.1 Introduction

As already outlined in the introduction to this thesis, one of the most interesting aspects of general relativity in higher dimensions is that black holes may have non-spherical topology.

The first explicit example of this was the $5D$ black ring spacetime [55, 164], which has horizon topology $S^1 \times S^2$. Amazingly, this solution was found analytically and can be written in a remarkably simple form [165]

$$ds^2 = -\frac{F(\eta)}{F(\xi)} \left(dt - C(v, \lambda) R \frac{1+\eta}{F(\eta)} d\psi \right)^2 + \frac{R^2}{(\xi - \eta)^2} F(\xi) \left[-\frac{G(\eta)}{F(\eta)} d\psi^2 - \frac{d\eta^2}{G(\eta)} + \frac{d\xi^2}{G(\xi)} + \frac{G(\xi)}{F(\xi)} d\phi^2 \right], \quad (4.1)$$

where

$$F(x) = 1 + \lambda x, \quad G(x) = (1 - x^2)(1 + vx), \quad \text{and} \quad C = \sqrt{\lambda(\lambda - v) \frac{1 + \lambda}{1 - \lambda}}. \quad (4.2)$$

As can be seen in the above metric, the ring rotates in the direction given by the angle ψ and has a $U(1)$ symmetry in both the rotational plane and the transverse direction given by the angle ϕ . The ring coordinates ξ and η have ranges $-1 \leq \xi \leq 1$ and $-\infty < \eta \leq -1$, where the horizon lies at $\eta = -\frac{1}{v}$ and spatial infinity is approached as both ξ and η tend to -1 . Requiring the absence of conical singularities in the spacetime fixes the parameter λ and the periodicity of ϕ and ψ

$$\lambda = \frac{2v}{1 + v^2} \quad \text{and} \quad \Delta\phi = \Delta\psi = \frac{2\pi}{\sqrt{1 + v^2}}. \quad (4.3)$$

This leaves only two free parameters: the radius parameter of the ring, $R \in (0, \infty)$, and the thickness parameter, $v \in (0, 1)$.

To get some intuition as to why the black ring solution exists, one can imagine connecting the ends of a black string to form a ring and boosting it to counter the forces due to tension [166]. Indeed, the relation (4.3) can be interpreted as the requirement that centrifugal force and tension must be exactly balanced. However, while this intuition is correct in the limit of infinitely thin rings, it fails to describe the behaviour of fatter rings as we will see presently.

Fig. 4.1 shows the phase diagram of all known stationary, asymptotically flat, single black hole solutions rotating in a single plane in $5D$. The mass is fixed, and used to rescale the horizon area and angular momentum such that they become dimensionless as proposed in Ref. [167]. The solid blue line shows the $5D$ Myers-Perry black hole [96], which will be investigated in more detail in the next chapter. The black ring metric (4.1) forms two distinct branches, which meet at a cusp with thickness parameter $v = 0.5$: the “fat” branch, which ranges from the cusp to a naked singularity with $v = 1$, and the “thin” branch, which extends

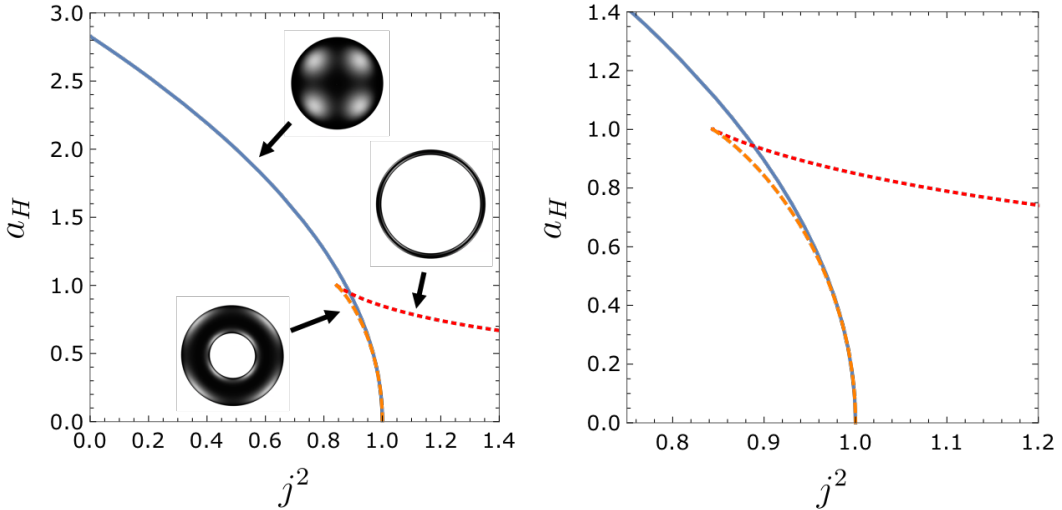


Fig. 4.1 *Left*: Phase diagram of all known stationary, asymptotically flat, singly-spinning, single black hole solutions in 5D. The mass is fixed and used to rescale the angular momentum and horizon area to make them dimensionless as proposed in [167]. *Right*: Zoom of the phase diagram that highlights the region in which black holes are not uniquely identified by their mass and angular momentum.

from the cusp to arbitrarily large angular momentum. The aforementioned intuition that black rings can be thought of as boosted black strings with their ends connected only holds in the limit of very thin black rings. Very fat black rings, on the other hand, behave more like Myers-Perry black holes with a hole drilled through them.

In addition to the single black hole solutions in Fig. 4.1, there are multi-black hole solutions such as the black Saturn [91], a combination of a black ring and a central Myers-Perry black hole, di-rings [92, 93], and orthogonal di-rings [94]. Furthermore, 5D Myers-Perry black holes can rotate it up to two planes [96], and black rings can be doubly-spinning [168].

The most striking feature of the phase diagram in Fig. 4.1 is that in the range $\frac{27}{32} < j^2 < 1$ there are three different black hole solution for the same mass and angular momentum. Hence, black ring spacetimes not only show that in higher dimensions restrictions on black hole topology become less stringent, they also demonstrate that in higher dimensions black holes are not uniquely described by their mass and angular momentum.

Prior to our work, two instabilities of black rings were known: a radial instability for fat rings, i.e. an instability which preserves the $U(1)$ symmetry in the rotational plane, and a GL-like instability for thin rings. Ref. [28] presented evidence for the existence of the radial instability by considering off-shell perturbations, singular deformations of the black ring spacetime that mimic the action of a small external force on the ring. They found that

fat rings were unstable to this off-shell perturbation and thin rings were stable. Ref. [29] confirmed the existence of this radial instability rigorously by constructing perturbations of fat black rings which violate a local Penrose inequality. In essence, this means that the authors constructed perturbed fat rings which cannot possibly settle down to a fat ring due to the restriction that entropy can only increase, mass can only decrease due to the emission of gravitational waves, and angular momentum cannot be radiated due to the $U(1)$ symmetry.

For thin rings, Refs. [30, 31] found a GL-like instability that creates ripples along the ring, which break the $U(1)$ symmetry. The presence of this instability is intuitive for very thin rings due to their similarity to boosted black strings. However, Ref. [30] found that the instability covers the whole thin branch and might even extend slightly into the fat branch. Put together, the two instabilities cover the whole parameter range of black rings. As a result, if one restricts to asymptotically flat, stationary black hole solutions that are stable, the $4D$ restrictions on black hole uniqueness and topology are recovered.

One important question that could not be addressed in previous work is what the end point of these instabilities is. Based on their entropies (see Fig. 4.1), fat black rings could settle down to a Myers-Perry black hole or a thin ring. The former would demonstrate that an asymptotically flat black hole with a connected horizon can undergo a smooth change of topology. Similar to the evolution of black strings [33], the GL instability of black rings could lead to the black hole pinching off. This could have significant implications for the Weak Cosmic Censorship Conjecture in asymptotically flat spacetimes.

The remainder of this chapter is organised as follows: in section 4.2, we present the numerical methods including the initial data, our gauge conditions, and our singularity treatment. In section 4.3, we present the methods we used to draw gauge-independent conclusions from our data. The results are presented in 4.4. In section 4.5, we discuss the limitations of our results and identify questions relating to black rings that are still unsolved. Finally, we present preliminary results for the $m = 1$ mode of the GL instability of black rings in Appendix A and detailed numerical tests in Appendix B.

4.2 Numerical methods

We perform fully non-linear numerical evolution of singly-spinning black rings in five dimensions and follow the instabilities to their end point. Adaptive mesh refinement is completely indispensable in order to be able to resolve all scales including any new features that may form as the instabilities progress. Furthermore, the adaptive mesh-refinement must

be able to refine regions of non-spherical topology. The GRCHOMBO code is ideal for this task; indeed, it was written with black rings in mind. Even with adaptive mesh refinement, simulations of black ring instabilities are very expensive. The production runs presented in this chapter took between one and two months using 500 Sandy Bridge Xeon processor cores.

We employ the CCZ4 formalism presented in section 1.3.1, with the redefinition $\kappa_1 \rightarrow \kappa_1/\alpha$, which allows us to make the covariant choice $\kappa_3 = 1$. Furthermore, we choose $\kappa_1 = 0.1$ and $\kappa_2 = 0$. Experiments with other values led to no improvement in the accuracy of the simulations and the physical results did not change.

We use adaptive mesh refinement with 8 to 13 levels with a resolution of between $0.3\tilde{R}$ and $0.5\tilde{R}$ in the wave extraction zone, where \tilde{R} is the radius of the black ring in our coordinates. The resolution on the finest level is chosen such that the interior of the horizon is always covered by at least 50 grid points after gauge adjustment. We use fourth-order finite differencing stencils and perform time steps using the fourth-order Runge-Kutta method. Similar to other work on higher dimensional black holes [153, 25, 26, 155], we had to choose very small Courant factors $0.1 \leq dt/dx \leq 0.3$ and often had to reduce the Courant factor further in the highly dynamic stages of the evolution. However, we found that the Courant factor only affects the numerical stability of the simulations: once it is small enough for stability, any further reduction does not change the physical results.

For the spatial directions, we choose a Cartesian coordinates system (x, y, z, w) such that the ring rotates in the $x - y$ plane and is centred at the origin. In order to make the simulations feasible numerically, we have to exploit the $U(1)$ symmetry in the transverse direction, i.e. in the $z-w$ plane corresponding to the angular direction ϕ in the metric (4.1). This is done using the modified Cartoon method (chapter 3) to restrict the simulation to the $w = 0$ hyperplane. We do not expect that breaking the $U(1)$ symmetry in the transverse plane would affect the conclusions of our work, as no known instability of black rings breaks this transverse direction in the linear regime. Furthermore, transverse perturbations have been found to be stable for boosted black strings [169]. However, we cannot exploit the symmetry in the rotational plane present in (4.1), since this symmetry is broken by the GL instability. Thus, we are left with a 3 + 1-dimensional evolution system.

As required by the modified Cartoon method, we actively enforce even or odd boundary conditions for our evolution variables at the $z = 0$ boundary. At the other boundaries, we impose periodic boundary conditions. While this is not correct analytically, we move these boundaries so far away that they are never in causal contact with the black hole or the wave

extraction zone during the evolution. Due to the adaptive mesh refinement and our deep mesh hierarchy, this is possible without incurring a noticeable performance penalty.

Our choice of CCZ4 as evolution system enables us to use the puncture gauge so that we avoid having to excise the interior of the black hole. For black rings, this is a considerable advantage as excision would be very challenging due to the complicated excision regions that would be required. Furthermore, excision requires finding the apparent horizon very often, which is very tricky for the extreme horizon shapes we encountered during the evolution of black rings.

4.2.1 Initial data

Ideally, we should start puncture gauge evolution with initial data that contain no physical singularities. To this end, we write the metric (4.1) in the coordinates introduced in Ref. [29], which are ideal for numerical evolution: they render the metric manifestly asymptotically flat and cover two copies of the exterior of the horizon so that the computational domain contains only a coordinate singularity, not a physical one.

Here, we will give a derivation of these coordinates that highlights their similarity to isotropic coordinates for the 4D Schwarzschild black hole. Let us start from the coordinate

$$Y = -\frac{\tilde{R}}{1+\eta} \quad \text{with} \quad \tilde{R} = R \sqrt{\frac{1-v}{1+v^2}}. \quad (4.4)$$

The use of \tilde{R} instead of R will be convenient later, when we have to use \tilde{R} to obtain a manifestly asymptotically flat metric in Cartesian coordinates [164]. The coordinate Y is a dimensionful quantity in the range $(0, \infty)$, where 0 corresponds to the ring singularity, the apparent horizon is located at constant $Y = Y_H$, where

$$Y_H = \frac{\tilde{R}v}{1-v}, \quad (4.5)$$

and ∞ corresponds to spatial infinity on the outside of the ring and the centre of the ring on the inside. Close to the black ring, Y can be thought of as the radial coordinate of the 4D black hole that results from taking a constant- ψ slice of the ring. Hence, we will treat Y as the equivalent to the radial coordinate for the Schwarzschild black hole and perform the

standard transformation to an isotropic coordinate \tilde{Y} given by

$$Y = \tilde{Y} \left(1 + \frac{1}{4} \frac{\tilde{Y}_H}{\tilde{Y}} \right)^2. \quad (4.6)$$

We have used the $4D$ version of the transformation, since that is the dimension of a constant- ψ slice of the ring. The isotropic coordinate \tilde{Y} ranges from 0 to ∞ and covers two copies of the region outside the horizon, which is now located at $\tilde{Y}_H = Y_H/4$. It will feature very heavily in this chapter due to its interpretation as isotropic coordinate radius of a constant- ψ slice through the ring. We will use it whenever there is a need to restrict any action, such as a modification in the gauge condition or the initial perturbation, to the region inside or close to the horizon.

For our numerical simulations, we have to express the initial data in terms of Cartesian coordinates. This is most easily done via the ring coordinate related to \tilde{Y} through $\tilde{\eta} = -1 - \tilde{R}/\tilde{Y}$, i.e. the inverse transformation of (4.4). In terms of Cartesians [164], the resulting coordinates are given by

$$\begin{aligned} \tilde{\eta} = -\frac{\tilde{R}^2 + r^2}{\Sigma} &\Rightarrow \tilde{Y} = \frac{\tilde{R}\Sigma}{\tilde{R}^2 + r^2 - \Sigma}, \\ \xi = \frac{\tilde{R}^2 - r^2}{\Sigma}, \quad \text{and} \quad \psi &= \tan^{-1}(y/x), \end{aligned} \quad (4.7)$$

with

$$\Sigma = \sqrt{(\tilde{R}^2 + r^2)^2 - 4\tilde{R}^2(x^2 + y^2)} \quad \text{and} \quad r = \sqrt{x^2 + y^2 + z^2}, \quad (4.8)$$

where we have used the $U(1)$ symmetry in the transverse direction to restrict to the $w = 0$ plane. After the series of coordinate transformations outlined above, the metric (4.1) takes exactly the same form as in Ref. [29]. In particular, it covers two copies of the outside of the horizon and is manifestly asymptotically flat.

In our initial data, we vary v to investigate different thicknesses, but we fix $\tilde{R} = 1$ so that the initial coordinate radius of the ring is the same for all simulations. This means that the mass of the ring changes as we vary v , with fatter rings having substantially higher mass than thinner ones in our simulations. We initialise the gauge evolution with a pre-collapsed lapse $\alpha = \chi$ and an initial shift of χ times the analytic shift. As argued in section 3.2 this minimises initial gauge adjustment.

At the beginning of the evolution, we introduce a small perturbation which has two maxima and two minima around the ring in the rotational plane and, therefore, corresponds to an

$m = 2$ perturbation when expanded in terms of Fourier modes $\cos(m\psi)$. This perturbation is applied to the conformal factor as

$$\chi = \chi_0 \left[1 + \frac{A}{(1 + (\tilde{Y}/\tilde{Y}_H)^2)^{\frac{3}{2}}} \frac{x^2 - y^2}{\Sigma} \right], \quad (4.9)$$

where χ_0 is the unperturbed conformal factor and A is the amplitude of the perturbation. As explained above, \tilde{Y} can be thought of as an isotropic radial coordinate of a constant- ψ cross-section of the ring. Thus, the fraction involving \tilde{Y} in (4.9) ensures that the perturbation decays quickly away from the horizon and does not modify the mass or angular momentum of the spacetime.

We choose the perturbation amplitude in the range $10^{-6} \leq A \leq 0.002$. For studying the end point of the instability alone, much larger values such as $A \sim 0.05$ would have been completely sufficient and much cheaper computationally. However, our small choice allowed us to study the evolution in the linear regime in a lot of detail and to compare the frequency and growth rate of the instability with the values in the literature.

The perturbation (4.9) introduces small violations in the Hamiltonian and the momentum constraints. However, due to the constraint damping properties of CCZ4, these constraint violations decay away very quickly, long before any other significant evolution takes place. Indeed, in this short initial phase, CCZ4 acts like an initial data solver. As the perturbation amplitude is decreased from 0.002 to 10^{-6} , the results in the linear regime remain unchanged up to rescaling by the amplitude. This strongly suggests that constraint violations in our initial perturbation do not affect the results.

4.2.2 Gauge conditions and singularity treatment

As gauge evolution equations, we use 1 + log slicing (3.5) with an advection term and slightly decreased coefficient $\eta_\alpha = 1.5$. To avoid freezing in large initial values of $\hat{\Gamma}$, we use our adapted Gamma-driver shift condition (3.2) with an advection term, $F = 2/3$, $\eta = \tilde{R}^{-1}$, and

$$f(t, x^i) = \exp \left[- \left(\delta_1 \left(\frac{Y_H}{Y} \right)^2 + \delta_2 \right) t^2 / M \right]. \quad (4.10)$$

For the two dimensionless constants δ_1 and δ_2 , we typically choose values 0.25 and 0.1 respectively. As described in section 3.2, our modified Gamma-driver causes the gauge to adjust such that the large initial values of $\hat{\Gamma}$ decay. The purpose of the first term in the

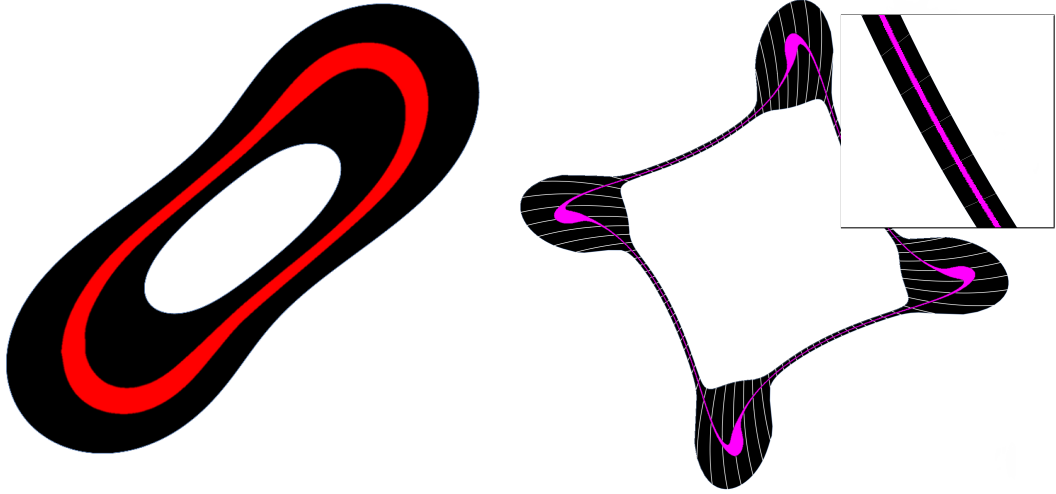


Fig. 4.2 Region of non-zero diffusion (red/pink) shown on top of the apparent horizon for $v = 0.3$ (left) and $v = 0.15$ (right). The diffusion region covers much less than 50% of the horizon's interior, even in the highly non-linear regime and at the thin necks.

exponential in (4.10) is to speed up this gauge adjustment inside the horizon where initial values of $\hat{\Gamma}$ are larger and constraint violations resulting from rapid gauge adjustment do not matter. To tame high frequency modes arising in the simulation, we use Kreiss-Oliger numerical dissipation with factor $\sigma = 0.3$.

Even with puncture gauge, dissipation, and initial data that contain no physical singularity, the simulations develop large, high frequency features inside the horizon. These numerical instabilities ultimately lead to floating point overflow inside the horizon, which propagates outwards, spoiling the whole simulation. To solve this problem, we use the singularity diffusion outlined in section 3.3 with $0.015 \leq \chi_c \leq 0.03$. As outlined in section 3.3, diffusion is most naturally started with turduckened initial data, which we achieve by manually enforcing $\Sigma \geq \varepsilon^2$ in (4.7). Typically, we choose $0.2 \leq \varepsilon \leq 0.5$ depending on the thickness of the ring. We ensure that the turduckened region and the region in which diffusion is applied are always restricted to less than 50% of the apparent horizon (see Fig. 4.2 for an example). The upper limit of 50% is only attained in the short time before gauge adjustment; afterwards, the diffusion region occupies a much smaller fraction of the horizon. Since no information can escape the horizon and we have plenty of points across the apparent horizon, turduckening and diffusion do not affect the results. We present explicit evidence for this in Appendix B in this chapter.

4.3 Analysis methods

4.3.1 Wave analysis

To estimate frequencies and growth rates of the instabilities, we monitor the gravitational waves far away from the black ring, as they provide a very clear and more gauge-independent signal. Following Ref. [25], we extract the $+$ -mode of gravitational waves using the quantity

$$h_+ = \frac{\tilde{\gamma}_{xx} - \tilde{\gamma}_{yy}}{2} \left(\frac{z}{\tilde{R}} \right)^{\frac{3}{2}} \quad (4.11)$$

on the z -axis, where $\tilde{\gamma}_{ij}$ is the conformally rescaled spatial metric.

Since numerical relativity is an inherently non-linear tool, finding good estimates for frequency and growth rate from the gravitational wave signal is tricky, especially when there are several competing modes. In particular, extracting a long linear signal requires selecting a tiny amplitude for the initial perturbation. However, due to grid noise we could only obtain meaningful results for large enough initial amplitudes, $A \gtrsim 10^{-6}$ in (4.9). With these initial amplitudes, the modes we aim to investigate become nonlinear after only a few periods. This is enough for a Fourier analysis to pick up the dominant frequency with reasonable accuracy, but not enough to detect any sub-dominant modes. We therefore use the procedure described below, which allows us to determine the frequency and growth rate and their associated errors accurately, even for a sub-dominant mode. The procedure performed well in our tests on fabricated data that resemble our measured signal but consist of several known exponentially growing modes superposed with Gaussian noise.

Our method is based upon a fit to the two-mode ansatz

$$A_1 \sin(\Re \omega_1 t + \varphi_1) e^{\Im \omega_1 t} + A_2 \sin(\Re \omega_2 t + \varphi_2) e^{\Im \omega_2 t}. \quad (4.12)$$

Of course, the same procedure could be used for an ansatz with a different number of modes, but our results suggest that exactly two distinct black ring instabilities exist in the $m = 2$ sector.

We first fit the entire wave signal in the linear regime to the ansatz (4.12) to obtain a rough estimate for the parameters. This estimate is then used to rescale the wave signal and fitting function (4.12) by $\exp(\Im \omega_{\max} t)$, where $\Im \omega_{\max}$ is the larger of the two growth rates, so that the amplitude of the signal stays roughly constant. The effect of this is that subsequent least-squares fits will not minimise the absolute errors but the errors measured as fraction of

the amplitude at the time. This greatly improves the accuracy of the extracted frequency and growth rate.

Finally, we fit the rescaled data in a time window of size roughly $10\sqrt{\tilde{R}}$ as the window slides across the whole signal. We use the mean of the resulting fit parameters as our best estimate for the frequency and growth rate, and the standard deviation as an estimate for the accuracy. This estimate not only measures the uncertainty of the fit, but also the uncertainty due to the fact that our results are obtained from a non-linear simulation, with contamination from constraint violating modes towards the beginning and non-linearities towards the end. Fig. 4.11 shows an example of results obtained by this procedure. The uncertainty in the frequency is much lower than the uncertainty in the growth rate. The reason for this is that while (4.12) fixes the frequency exactly, there is a slight degeneracy between the growth rates and the initial amplitudes when performing the fit. The latter are unknown to us since we do not know how the amplitude of the constraint-violating initial perturbation (4.9) translates into initial amplitudes of the various modes.

4.3.2 Apparent horizons

In order to study the geometry of the black rings as they undergo the instability, we find the apparent horizon at regular intervals during the simulation. For the black holes of spherical topology arising in some of our simulations, this can be done using the standard methods [110]: we use polar coordinates (r, θ, ϕ) with respect to a point inside the black hole and find the function $R(\theta, \phi)$ such that the surface defined by the zero contour of $r - R(\theta, \phi)$ has zero expansion.

For the toroidal horizons of black rings, the same method can be used if one switches to ring coordinates (4.7). The apparent horizon is then given by the function $H(\xi, \psi)$ for which the zero contour

$$\tilde{\eta} - H(\xi, \psi) \equiv 0 \quad (4.13)$$

has zero expansion. In practice, $\tilde{\eta}$ is not very convenient due to its range. Instead, we usually used $\tanh^{-1}(-1/\eta)$, although the coordinate \tilde{Y} defined in (4.6) would likely have been an equally good alternative.

The parametrisation $H(\xi, \psi)$, with coordinate transformation (4.7), assumes that the circle $x^2 + y^2 = \tilde{R}^2$ on the $z = 0$ plane lies inside the apparent horizon. Unfortunately, this is not the case in later stages of the evolution since the ring stretches significantly in the rotation

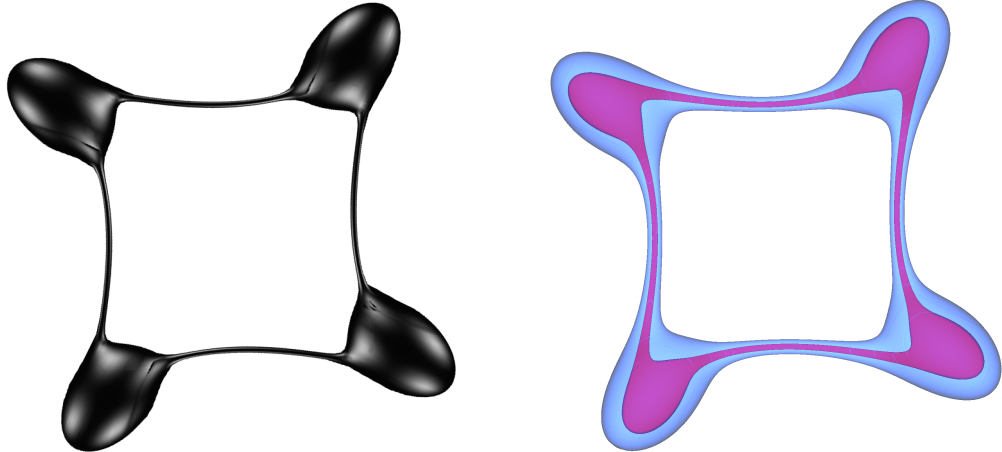


Fig. 4.3 *Left*: The most extreme apparent horizon we could find for the evolution of a very thin ring with $v = 0.15$. *Right*: The $\chi = 0.2$ (pink) and $\chi = 0.4$ (light blue) contours for the same snapshot. The $\chi = 0.2$ contour approximates the apparent horizon well along the thin necks, while the $\chi = 0.4$ contour approximates the big bulges.

plane (see Fig. 4.7). We solved this problem by allowing \tilde{R} in the coordinate transformation (4.7) to vary with ψ . A suitable function $\tilde{R}(\psi)$ can be obtained by taking a very small-valued contour of the conformal factor χ , which tends to zero inside the black hole. This allowed us to find apparent horizons for almost all shapes we encountered.

Allowing \tilde{R} to vary is not enough for very extreme stages of the evolution for which the position of the ring can no longer be defined as a single-valued function $\tilde{R}(\psi)$. However, with our gauge choice, our experience showed that contours of the conformal factor χ share the symmetries of the apparent horizon: if the apparent horizon settles down to a spherically symmetric shape, the conformal factor will be approximately constant on the apparent horizon. If it takes on the shape of a black string with translational symmetry, the conformal factor will be constant along the string. An example of this is shown in Fig. 4.3. This also implies that we can use contours of the conformal factor to get a qualitative understanding of the behaviour of the apparent horizon: if the apparent horizon has some approximate symmetry and we know which χ -contour the apparent horizon corresponds to, then if χ subsequently develops features, it is highly likely that the apparent horizon developed similar features too. We will use this method to gain some intuition for the short periods where our apparent horizon finder fails.

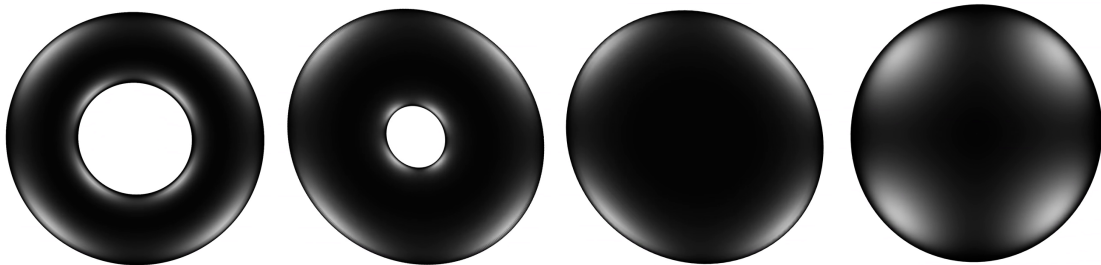


Fig. 4.4 Snapshots of the apparent horizon taken from the evolution of a fat ring with $v = 0.7$.

4.4 Results

In this section, we present the results of our simulations, starting with fat rings and moving to progressively thinner ones. Our simulations showed that there are three different regimes: very fat rings with $v \gtrsim 0.6$, intermediate rings with $0.2 \lesssim v \lesssim 0.6$, and very thin rings with $v \lesssim 0.2$. It is unexpected that the intermediate regime covers both thin and fat rings and that we find no significant difference in the dynamical behaviour of thin and fat rings in this regime.

4.4.1 Very fat rings

Rings in the regime $v \gtrsim 0.6$, like all fat rings, are known to be unstable to radial perturbations [28, 29]. Since axisymmetric modes cannot cause angular momentum to be radiated and the horizon area must increase, the phase diagram in Fig. 4.1 suggests that the instability should end in either a Myers-Perry black hole or a thin ring.

Fig. 4.4 shows our results for $v = 0.7$. They confirm the existence of a radial mode and show that the radial mode leads to very quick collapse to a Myers-Perry black hole. Thus, the black hole changes its topology from toroidal to spherical, with the spacetime remaining smooth throughout. This is the first concrete example of an asymptotically flat black hole with a connected horizon smoothly changing its horizon topology. Despite trying many different initial conditions, including ones that make the horizon thinner, we could not find evidence of the evolution ever approaching a thin ring as metastable state or endpoint. This conclusion did not change even when we imposed axisymmetry, which suppresses all known instabilities of thin rings.

We find that the apparent horizon does not transition continuously from toroidal to spherical topology. The spherical apparent horizon seen in the third snapshot in 4.4 appears very

suddenly: the two middle snapshots are only separated by one coarse time step with $\delta t = 0.004t/\tilde{R}$. This is not unexpected, as the apparent horizon, the outermost trapped surface, is not required to move continuously. The event horizon, on the other hand, must move continuously and since it must always lie outside the apparent horizon, it must have changed topology by merging in the centre at some point before the third snapshot in Fig. 4.4.

Even though the radial mode does not break axisymmetry, we did not impose this symmetry in our simulations. Very unexpectedly, we found a noticeable breaking of axisymmetry in our simulations, also visible in Fig. 4.4, even in the regime $v \gtrsim 0.6$. These deviations from axisymmetry are only small, and it was impossible for us to isolate their cause due to the fast growth of the radial instability. However, we will see below that they are not a numerical artefact or a non-linear effect, but rather the precursor of a previously undiscovered axisymmetry-breaking instability.

4.4.2 Intermediate rings

For rings in the regime $0.2 \lesssim v \lesssim 0.6$, Ref. [30] showed the presence of the GL mode, which should get progressively weaker as the thickness increases. For $0.5 \leq v \lesssim 0.6$, the fat rings in this regime, the radial instability identified in Refs. [28, 29] is still present. Figs. 4.5, 4.6, and 4.7 show three representative examples of the results of our numerical evolution in this regime¹. As expected, we find that the evolution is characterised by strong breaking of $U(1)$ symmetry. Interestingly, however, the thickness variations along the ring expected for the GL mode are only prominent for the thinner rings in this regime. The evolution with $v = 0.5$ (Fig. 4.5) shows no measurable signs of thickness variations. Instead, the rings get very noticeably stretched. Most strikingly, though, all intermediate black rings always collapse to a Myers-Perry black hole before the thickness variations can grow large enough to cause the ring to pinch off like the black strings in Ref. [33].

Let us make these qualitative observations more rigorous and more gauge-independent by examining geometric quantities on the apparent horizon. Fig. 4.8 shows the minimum and maximum areal radius of the S^2 of the apparent horizon. This is a good measure of the thickness variations along the ring. The results for $v = 0.3$ show that the minimum ring thickness never decreases substantially. Furthermore, the strong increase in the maximum thickness only happens very late and is only a non-linear effect due to the black ring collapsing to a Myers-Perry black hole. For $v = 0.2$, the thickness variations are more pronounced with

¹Videos for most simulations presented in this chapter can be found at www.grchombo.org.

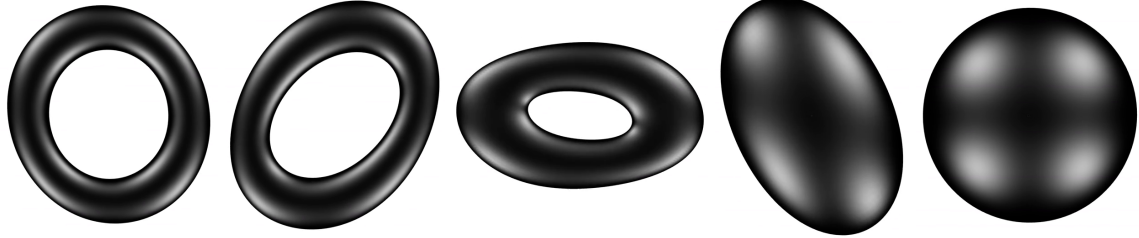


Fig. 4.5 Snapshots of the apparent horizon taken from the evolution of a black ring with $v = 0.5$.

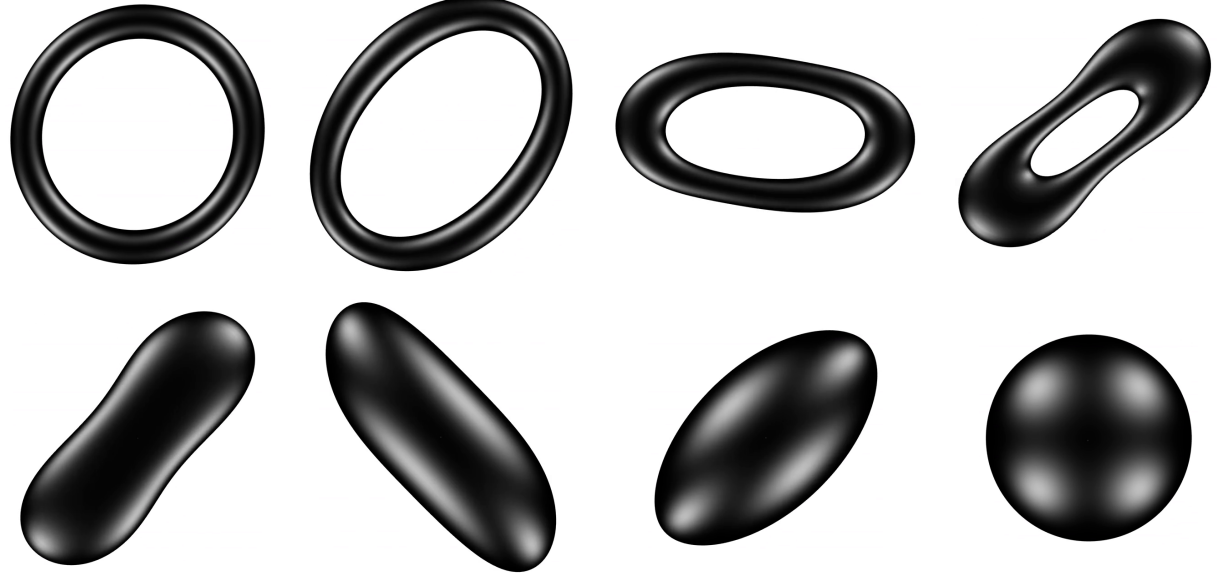


Fig. 4.6 Snapshots of the apparent horizon taken from the evolution of a thin ring with $v = 0.3$.

a clear decrease in the minimum thickness. Still, by the time an apparent horizon of spherical topology appears, the minimum thickness has only roughly halved.

Fig. 4.9 shows the minimum and maximum length of spacelike geodesics from the centre of the ring to the inner edge of the apparent horizon on a constant-time slice. This is a measure of the variation of the radius of the S^1 of the ring. The results show a very clear and growing divergence between the minimal and maximal S^1 radius, confirming our observation that the ring is physically stretching. There is a sharp decrease of the minimal S^1 radius as the ring collapses, but the spherical apparent horizon forms before the S^1 radius has shrunk to zero size, showing that the evolution of the apparent horizon is not continuous at this point.

The results above demonstrate the presence of the GL mode (the thickness variations) and show that there is a strong stretching effect which ultimately causes the black ring to collapse.

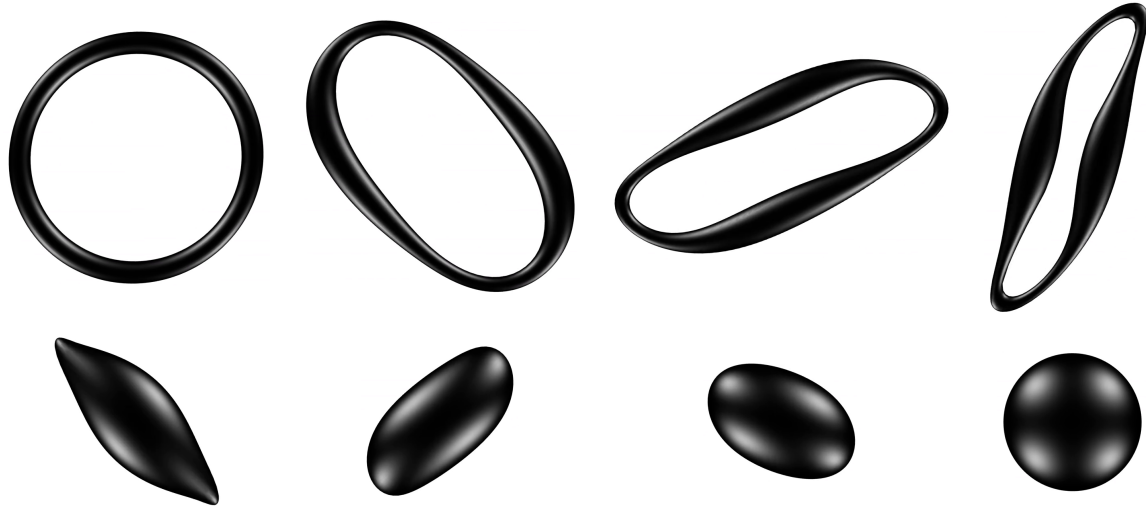


Fig. 4.7 Snapshots of the apparent horizon taken from the evolution of a thin ring with $v = 0.2$.

They cannot tell us whether the stretching is a non-linear effect of the GL instability or is a result of a previously unknown additional instability in the $m = 2$ sector. To address this question, we extract and analyse the gravitational wave signal calculated using (4.11) on the z -axis, far away from the black hole. In the linear regime, the results (see Fig. 4.10 for an example) show the mixing of several modes very clearly. Subsequently, one mode dominates and becomes non-linear. This causes the black ring to collapse and ring down to a Myers-Perry black hole. To disentangle the competing modes in the linear regime, we fit a two-mode ansatz (4.12) using the procedure outlined in section 4.3.1. Fig. 4.10 (bottom) shows an example of the results together with the fit. A one-mode ansatz would clearly be insufficient, but the quality of the two-mode fit indicates that no other $m = 2$ modes are relevant. We therefore conclude that intermediate black rings have two linear instabilities: the known GL instability and a previously undiscovered instability which stretches and deforms the ring without changing its thickness. In analogy with blackfolds [170], we term it an *elastic* mode. Even though the initial perturbation (4.9) was selected with the GL instability in mind, the analysis with a two-mode fit shows that it excites both instabilities with roughly equal amplitude.

Fig. 4.11 shows the frequency and growth rates obtained from our fitting procedure for a range of thin rings. Our results for the GL mode agree very well with the values obtained in Ref. [30]. For $v \gtrsim 0.2$, however, the GL mode is dwarfed by the faster growing elastic instability, so that it becomes impossible for us to isolate it in our generic, non-linear evolution. For $v = 0.2$, the growth rates of the two modes are roughly equal. This explains the complex

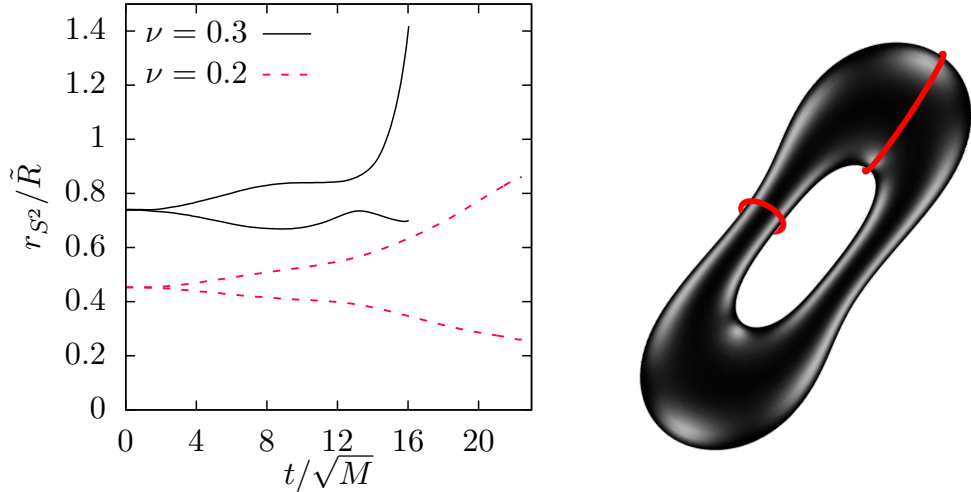


Fig. 4.8 *Left*: maximum and minimum areal radius of the S^2 of the ring. *Right*: Illustration of how this areal radius is measured.

behaviour in the apparent horizon geometry we found earlier and the evolution shown in Fig. 4.7. The GL instability leads to the formation of two large bulges connected by very thin necks while the elastic mode significantly stretches the ring. However, even though the GL mode is very significant for $\nu = 0.2$, the ring still collapses to a black hole of spherical topology.

In summary, we find that generically, thin rings in the regime $0.2 \lesssim \nu \lesssim 0.6$ collapse to a Myers-Perry black hole due to the new elastic instability. It is instructive to display this range of black holes on the phase diagram we showed at the beginning of the chapter. Fig. 4.12 highlights the relevant range and gives an example of a start and end point of the evolution. Most black rings in this range have higher entropy than the corresponding Myers-Perry black hole with equal angular momentum and for a large portion the angular momentum is even above the upper bound for which Myers-Perry black holes exist. However, the very strong breaking of $U(1)$ symmetry resulting from the elastic mode allows the black ring to radiate angular momentum very efficiently, so that it collapses to a solution with much lower angular momentum and considerably higher entropy.

4.4.3 Very thin rings

Our results for the growth rates obtained from the wave data in the linear regime (Fig. 4.11) show that for rings with $\nu \lesssim 0.15$ the GL mode grows fastest. Therefore, there is a large chance that it will also dominate the non-linear regime. It turns out that in this regime the $m = 4$ modes grows significantly faster than the $m = 2$ modes for both the GL and the elastic

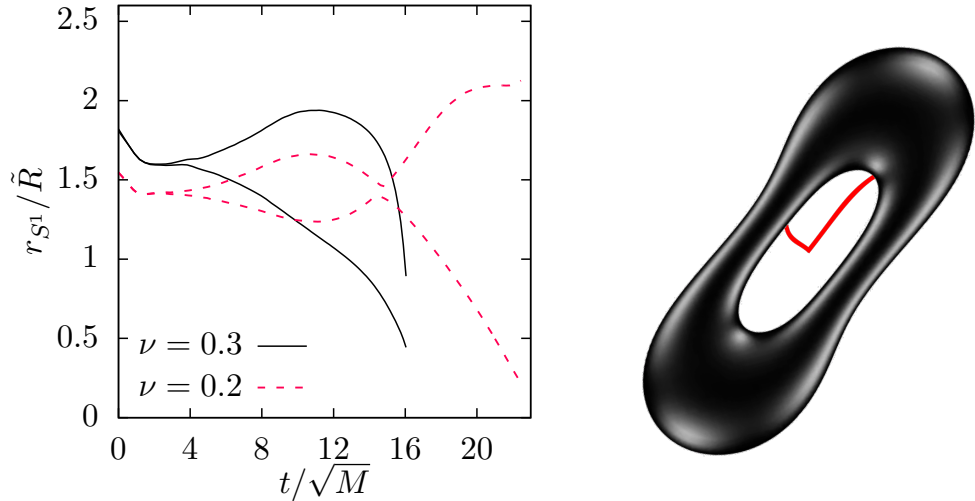


Fig. 4.9 *Left*: maximum and minimum geodesic distance from the centre of the ring to the inner edge. This shows variations of the radius of the S^1 of the ring. *Right*: Illustration of how this geodesic distance is measured.

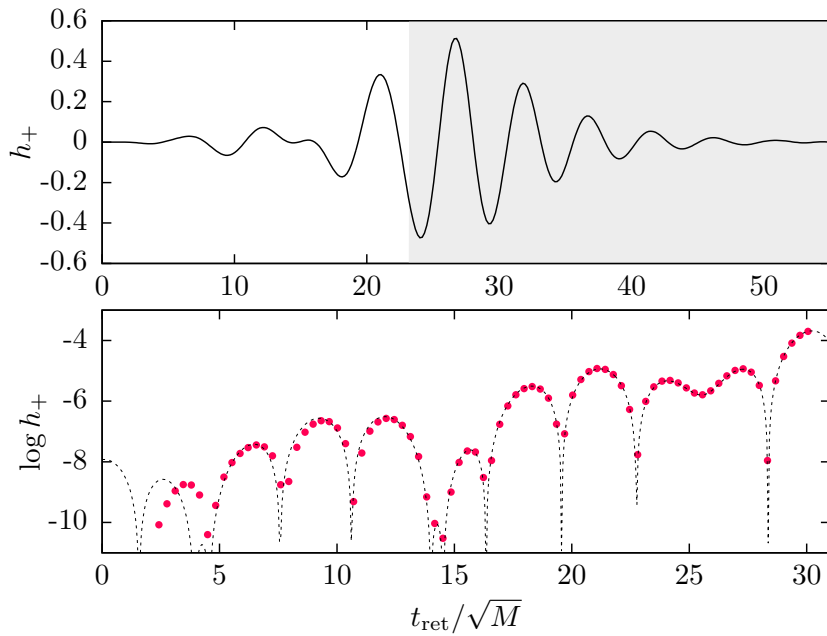


Fig. 4.10 *Top*: complete gravitational waveform for the evolution of the $\nu = 0.25$ ring perturbed with an $m = 2$ mode with amplitude $A = 5 \times 10^{-4}$. The shaded part corresponds to the portion of the evolution where the outermost apparent horizon has spherical topology. *Bottom*: fit (4.12) of the data in the linear regime (red dots) for a perturbation with amplitude $A = 10^{-5}$. At the early stages of the evolution, there is contamination from constraint violating modes.

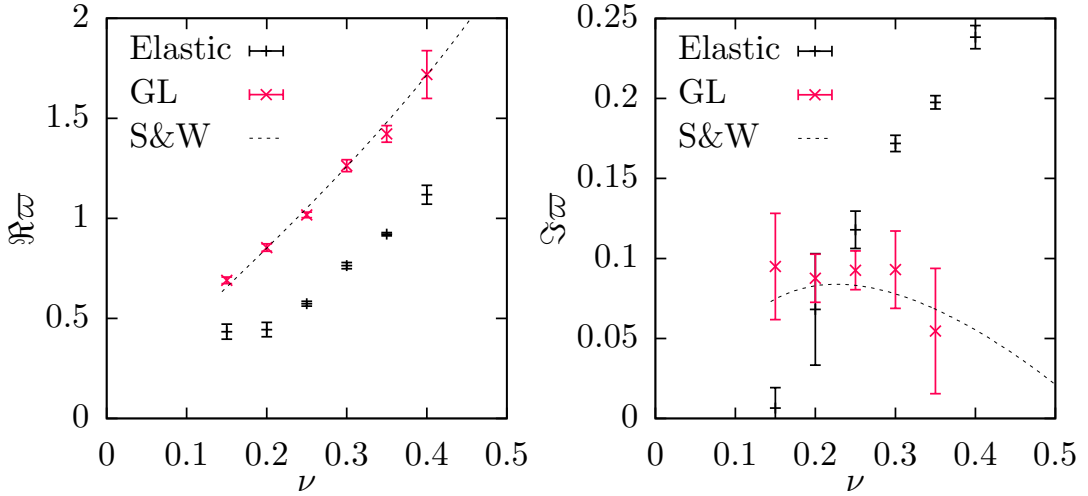


Fig. 4.11 Real (left) and imaginary (right) parts of the frequency, $\omega \equiv \omega/(2\pi T)$, of the gravitational waves in the linear regime. We rescale by the temperature, T , of the unperturbed ring so that we can compare to the results of Ref. [30], which are shown by the dashed line. The errors in the growth rate are larger than those in the frequency. The reason is that there is a slight degeneracy between the growth rate and the amplitude of the perturbation, which we do not know precisely since we use a constraint violating perturbation. For $\nu = 0.4$, we could not reliably extract the growth rate of the GL mode; the error bars would have exceeded the range of the plot.

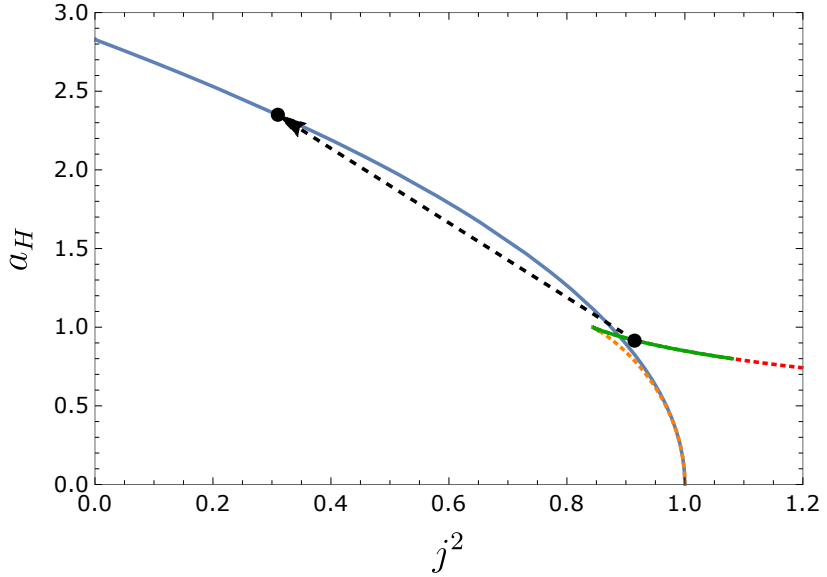


Fig. 4.12 Intermediate range $0.2 \lesssim \nu \lesssim 0.6$ (solid green line) displayed in a phase diagram. This range extends into the fat branch, but in such a small region of phase space that it is impossible to see in the plot. The black rings in this range collapse to Myers-Perry black holes due to the elastic instability. The arrow shows the start and end point of the evolution of $\nu = 0.3$ (displayed in Fig. 4.6).

instability. This is not unexpected given what we know about black strings: Ref. [169] found that for a black string of transverse radius r_H , every mode has a maximum unstable value of kr_H , where k is the wave number, above which the mode becomes stable. Let us denote this with $(kr_H)_{\max}$. For a black string with a compact flat direction with period $2\pi R$, the periodicity constrains the wave number to discrete values $k = n/R$, where n is a positive integer. Thus, modes are only unstable if

$$kr_H = \frac{nr_H}{R} < (kr_H)_{\max}(n) \quad \Rightarrow \quad n < \frac{R(kr_H)_{\max}(n)}{r_H}, \quad (4.14)$$

demonstrating that for fixed R as the string gets thinner and thinner, more and more modes switch on. Furthermore, according to the results of [169], for sufficiently thin strings, modes with larger wave number will always grow faster. Since thin black rings behave similarly to boosted black strings, this explains why the $m = 4$ starts to dominate over the $m = 2$ mode as the ring thickness is decreased

The presence and rapid growth of higher m modes for very thin rings means that it is impossible to restrict to the $m = 2$ mode in generic non-linear evolution. Instead, we either have to look at an $m = 4$ mode, or a superposition of $m = 2$ and $m = 4$. Fig. 4.13 shows the results for the $m = 4$ mode. Now, four bulges are created along the ring and the elastic mode gives the ring a star shape. More importantly, however, in stark contrast to the intermediate rings considered in the previous section, the GL mode now dominates completely, forming four very large bulges connected by four very thin black strings. This can be seen very clearly in the plots of the maximum and minimum areal radius of the S^2 of the ring in Fig. 4.14 (left). Towards the end of our simulation, the maximum and minimum radius differ by a factor of 80.

Due to this vast separation of scales, the black string sections evolve on a much faster timescale than the rest of the black ring. As a result, we can be confident that the string sections will undergo the GL instability exactly as Ref. [33] found: they will give rise to further generations of bulges connected by ever thinner black strings and pinch off in finite asymptotic time, long before the overall ring has had time to evolve significantly. Furthermore, Fig. 4.14 (right) shows that our data are compatible with the scaling law that was found in Ref. [33], $r_{S^2} \propto (t_c - t)$, where $t_c/R = 33.0 \pm 0.5$ is the estimated pinch-off time. However, this statement has to be interpreted with great care since we could not follow up the instability very far. We will be able to analyse the scaling law behaviour in much more detail for Myers-Perry black holes in the next chapter.

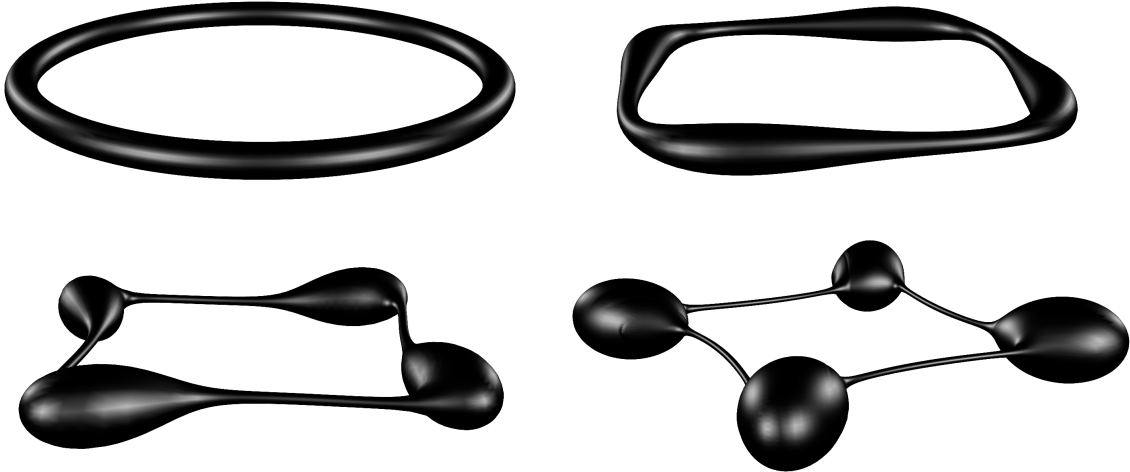


Fig. 4.13 Snapshots of the apparent horizon taken from the evolution of a very thin ring with $v = 0.15$ that was perturbed with a pure $m = 4$ mode.

Unfortunately, simulations of black rings are considerably more computationally expensive than those of black strings since they require simulating one more dimension. Therefore, for the pure $m = 4$ mode our computational resources were not sufficient for simulating the onset of another generation of bulges accurately enough. The situation is different for a mixture between the $m = 2$ and $m = 4$ mode (Fig. 4.15): the $m = 2$ mode stretches two of the string sections, causing the GL instability to progress much faster. As a result, we were able to find evidence for the onset of a second generation of bulges in a regime where we could still afford high enough resolution to simulate the evolution accurately. This suggests that for very thin rings the GL instability dominates and leads to a fractal structure of bulges connected by ever thinner black strings as found in Ref. [33]. Due to this self-similar structure, the thinnest neck should reach zero size in finite asymptotic time. Thus, we have concrete evidence that instabilities can cause black holes to pinch off in higher dimensions, even in asymptotically flat spacetimes.

4.5 Discussion and outlook

We have studied the non-linear dynamics of both thin and fat black rings under generic non-axisymmetric perturbations and identified the end point of their instabilities. Very fat rings ($v \gtrsim 0.6$) rapidly collapse to Myers-Perry black holes due to the radial instability identified in Refs. [28, 29], showing that an asymptotically flat black hole with a connected horizon can smoothly undergo a change of horizon topology. Intermediate rings ($0.2 \lesssim v \lesssim 0.6$) also collapse to Myers-Perry black holes due to a new linear instability, an elastic instability which

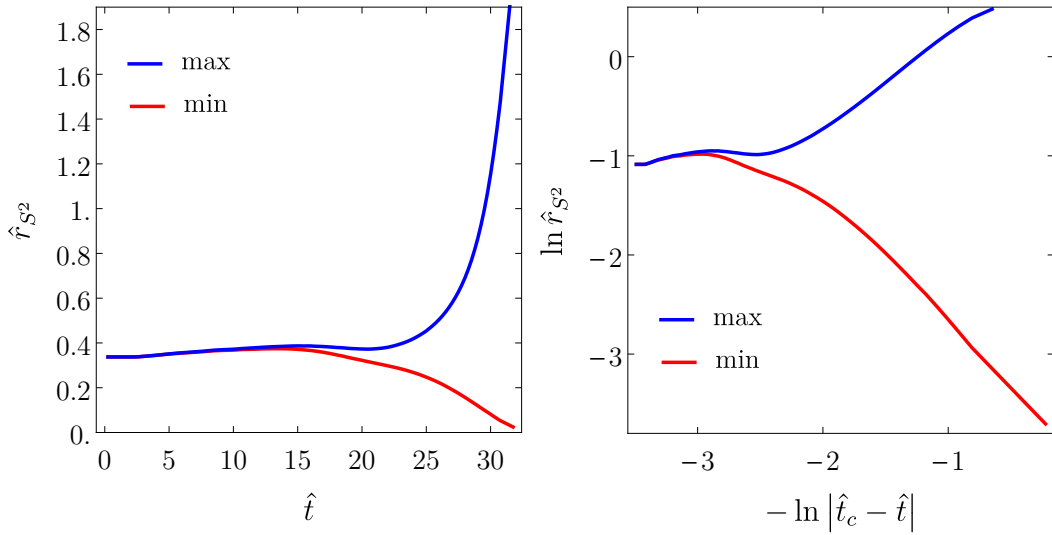


Fig. 4.14 *Left*: Maximum and minimum areal radius of the S^2 of the ring during the evolution of a $v = 0.15$ black ring with a pure $m = 4$ perturbation. Hatted quantities have been rescaled by \tilde{R} to make them dimensionless. *Right*: The same data in a plot of $\ln \hat{r}_{S^2}$ versus $-\ln |\hat{t}_c - \hat{t}|$, where $\hat{t}_c = 33.0 \pm 0.5$ is the estimated pinch-off time.

causes the ring to stretch without changing its thickness significantly. This instability had not been anticipated and was not seen in Refs. [30, 31], although its presence was later confirmed by Ref. [32] using the large D limit of general relativity. For very thin rings ($v \lesssim 0.15$), the GL instability dominates the evolution. It leads to the formation of a fractal structure of bulges connected by ever thinner black string sections and ultimately causes the ring to pinch off. Since black hole horizons cannot smoothly bifurcate, this indicates that a singularity is formed on or outside the horizon. As we will discuss in chapter 6, this is the first concrete evidence that generic initial data can give rise to arbitrarily large curvature scalars outside of black hole regions in higher dimensions, even in asymptotically flat spacetimes.

A possible caveat to our conclusion is that while our initial data and evolution are completely generic, we still have to impose a $U(1)$ symmetry in the transverse direction in order to make the simulations feasible. It is unlikely, however, that this influences the results, since modes in the transverse direction are expected to be stable just as for black strings [169]. Furthermore, our black ring simulations have less restrictive symmetry assumptions than the black string simulations in Ref. [33]: we impose a $SO(2)$ rather than an $SO(3)$ symmetry. Despite this, we reach exactly the same conclusion for string portions of the black ring. As a result, it is unlikely that relaxing the symmetry assumptions further would have any impact.

Even though we have only considered the asymptotically flat 5D case, our results should extend to even higher dimensions. Furthermore, black rings also exist in asymptotically AdS

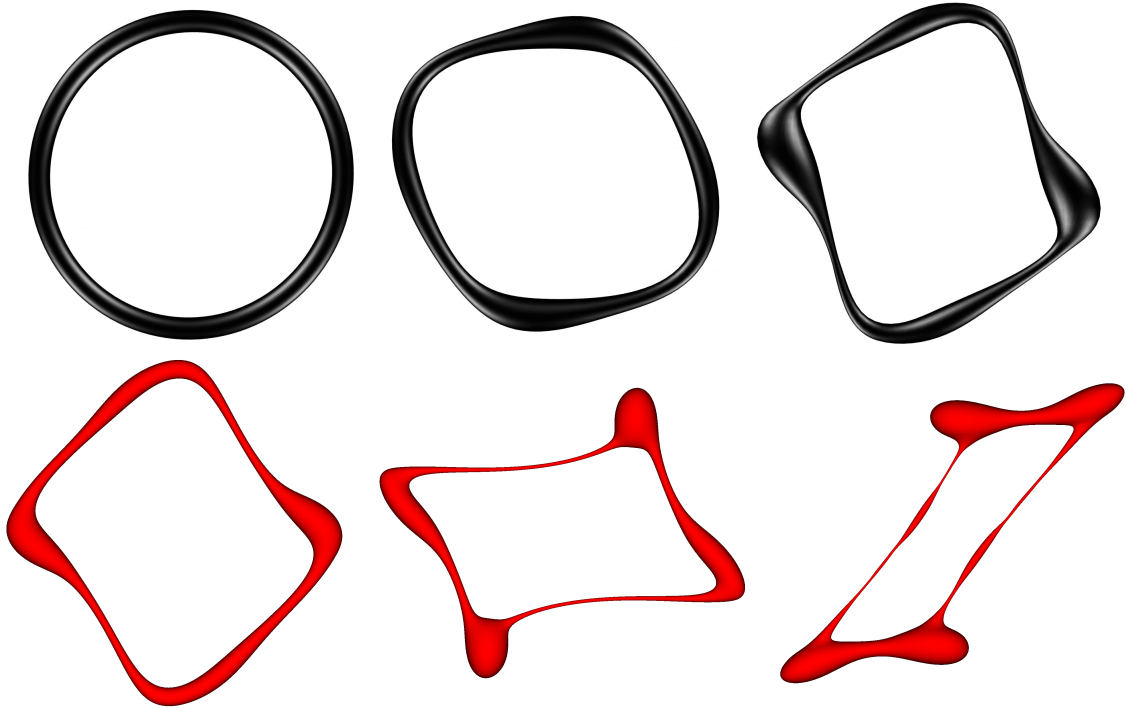


Fig. 4.15 Snapshots taken from the evolution of a very thin ring with $v = 0.15$ that was perturbed with a mixed $m = 2$ and $m = 4$ mode. The first three snapshots show the apparent horizon. For the snapshots in the bottom row, we could not find the apparent horizon since $\tilde{R}(\psi)$ is no longer a single-valued function (see section 4.3). Instead, we plot the $\chi = 0.2$ contour, which is a good qualitative estimate for the location of the apparent horizon along the thin necks.

spacetimes [171]. Since the GL instability is only local, it is highly likely that for black rings that are sufficiently small compared to the AdS length, our results would still hold.

In this work, we have focused largely on the $m = 2$ and $m = 4$ mode of the elastic and GL instabilities. However, other modes are unstable too. It would be very interesting to do a detailed analysis of these modes, their growth rates, and their dynamics. We present preliminary results for the $m = 1$ mode of the GL instability in Appendix A. This mode is of particular interest, since it leads to one-sided gravitational wave emission, giving the black ring a kick.

Finally, it would be very interesting to do a detailed analysis of the mass and angular momentum that is lost as the black rings collapse to Myers-Perry black holes. Our results indicate that the highly complicated dynamics of intermediate black rings lead to a very significant fraction (up to 17%) of the mass being radiated as they collapse. However,

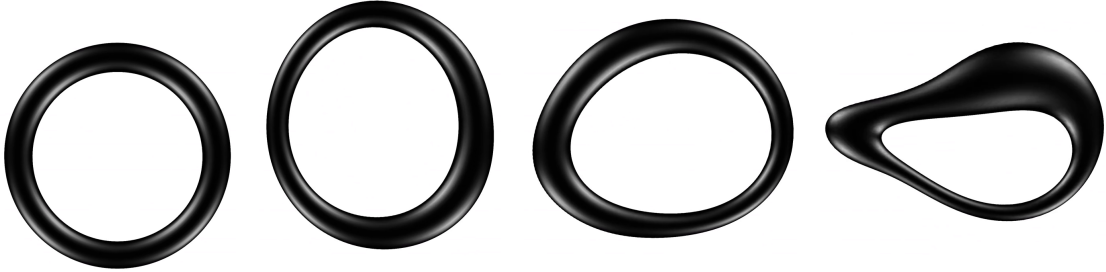


Fig. 4.16 Snapshots of the apparent horizon taken from the evolution of a thin ring ($\nu = 0.3$) that was perturbed with an $m = 1$ mode.

quantifying this amount reliably would require a more detailed analysis of the gravitational waves.

4.6 Appendix A: Behaviour of the $m = 1$ mode

In this section we present preliminary results for the $m = 1$ mode. Fig. 4.16 shows the evolution of a thin black ring ($\nu = 0.3$) that has been perturbed with an $m = 1$ mode. For the GL instability, the $m = 1$ should exist in analogy to boosted black strings [169]. Indeed, the horizon develops one large bulge connected by a thin neck. Using the horizon data alone, it is not possible to ascertain whether other instabilities exist in the $m = 1$ sector. An analysis of the gravitational waves should help answer this question soon. Since the $m = 1$ mode causes one-sided gravitational wave emission, the black hole does not remain in its position and is given a kick by the perturbation and instability. We are currently investigating the details of this. The end point is a Myers-Perry black hole.

4.7 Appendix B: Numerical tests

In this section, we present several numerical test to demonstrate the correctness of our results. First, we present convergence tests for representative samples of the wave and horizon data presented in Figs. 4.10, 4.9, and 4.8. Fig. 4.17 (*top*) shows the wave data for $\nu = 0.2$ and $\nu = 0.3$ for three different resolutions. Since the case $\nu = 0.2$ is very computationally expensive, the resolution is slightly lower than for $\nu = 0.3$ and we restrict the convergence test to the relevant regime before collapse to a spherical black hole. The results clearly converge. Furthermore, the errors in frequency and growth rate due to the finite resolution

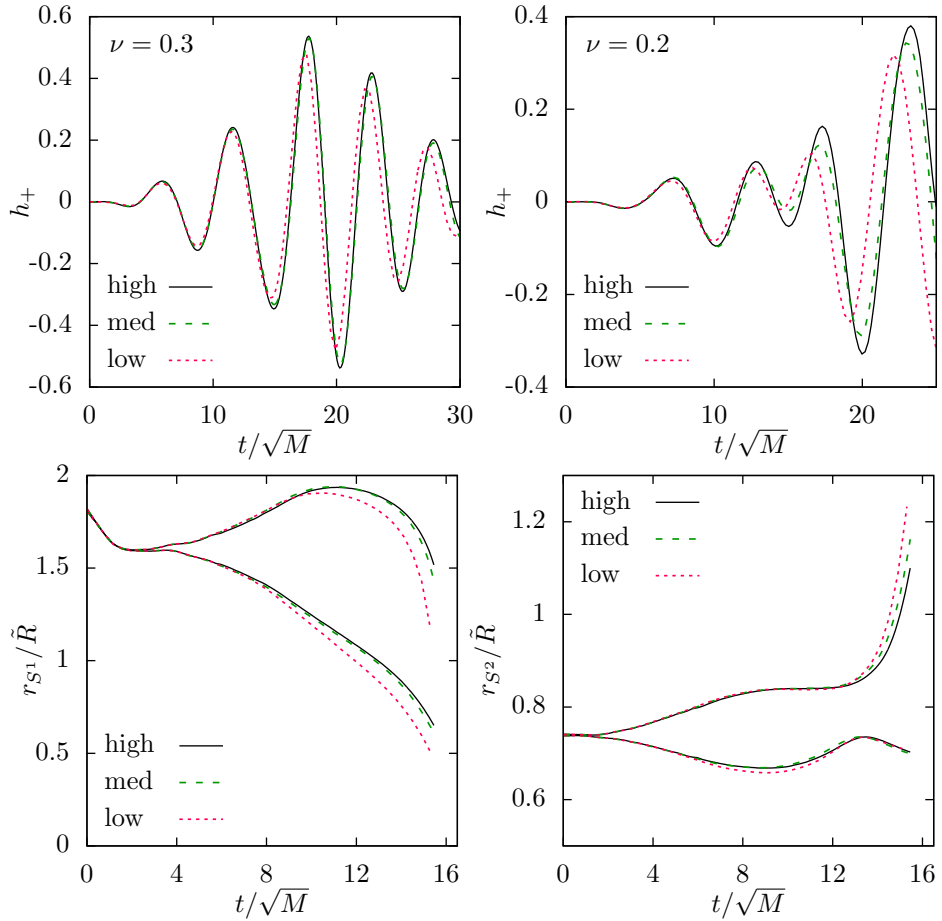


Fig. 4.17 *Top*: Convergence tests for the wave data. The runs for $\nu = 0.2$ are very expensive computationally and were restricted to the regime before collapse to a spherical black hole. *Bottom*: Convergence tests for the maximum and minimum radius of the S^1 (left) and S^2 (right) for $\nu = 0.3$. For all data there is a factor of 1.3 between different resolutions. The highest resolution as measured on the finest refinement level is $\Delta x = 0.003\tilde{R}$ for $\nu = 0.3$ and $\Delta x = 0.002\tilde{R}$ for $\nu = 0.2$.

are much smaller than the errors due to the fit. Fig. 4.17 (*bottom*) shows the minimum and maximum S^1 and S^2 radius for $\nu = 0.3$ for three different resolutions. Again, the results clearly show convergence. All the runs presented in the paper have resolution at least as high as the medium resolution runs in Fig. 4.17, both in terms of number of points covering the horizon and resolution in the wave zone.

Let us now turn to tests of the singularity diffusion inside the horizon. The convergence tests above are also strong indicators that the diffusion term does not affect the physical results. The reasons for this are twofold: firstly, as the resolution is increased the number of points between the apparent horizon and the region where diffusion is applied increases. Secondly,

Growth:					
χ_c	0.05	0.03	0.018	$\Delta(0.05, 0.018)$	$\Delta(0.03, 0.018)$
$\Re\omega_{el}$	0.736	0.764	0.751	2.0%	1.7%
$\Im\omega_{el}$	0.162	0.172	0.169	4.2%	1.6%
$\Re\omega_{GL}$	1.21	1.26	1.24	2.6%	2.0%
$\Im\omega_{GL}$	0.083	0.093	0.092	9.2%	1.4%

Ring-down:					
χ_c	0.05	0.03	0.018	$\Delta(0.05, 0.018)$	$\Delta(0.03, 0.018)$
$\Re\omega$	1.19	1.22	1.21	1.6%	1.2%
$\Im\omega$	-0.1657	-0.1681	-0.1679	1.3%	0.11%

Table 4.1 Results for frequency ($\Re\omega$) and growth rate ($\Im\omega$) for different χ_c for the initial growth of the instability and the final ring-down to a Myers-Perry black hole for a $v = 0.3$ ring. For the growth $\omega = \omega/(2\pi T)$, where T is the temperature of the unperturbed ring and for the ring-down $\omega = \omega\sqrt{M_{MP}}$, where M_{MP} is the mass of the final Myers-Perry black hole. The modulus of the difference between the results for two different values of χ_c is denoted by $\Delta(\chi_c^1, \chi_c^2)$.

the diffusion term (3.7) is scaled with Δx^2 and therefore vanishes in the continuum limit. As a final test, we change the size of the diffusion region by varying the cutoff χ_c and monitor changes in the wave signal. We expect the wave signal to converge as χ_c is reduced. Table 4.1 shows the results for frequency and growth rate of the initial stage of the instability and the final ring-down after the ring has collapsed to a spherical black hole. The results clearly show convergence and indicate that for the values of χ_c used for this paper ($0.015 < \chi_c < 0.03$) the effect of the diffusion term is negligible.

For simulations in which the ring collapses into a spherical black hole, we can compute the area of the apparent horizon and the circumference on the rotation plane of the final black hole. This allows us to estimate the mass and angular momentum of the resulting Myers-Perry black hole. By extracting the quasinormal modes from the wave signal, we can compare with existing results in the literature [27], and we find good agreement.

Chapter 5

End point of Myers-Perry instabilities

This chapter presents the results of fully non-linear numerical evolution of Myers-Perry black holes in $5D$ and $6D$. We perform a thorough analysis of the axisymmetric ultraspinning instability, which causes the black hole to be torn apart by its rotation. Furthermore, we present recent results on the non-linear stability of Myers-Perry black holes in $5D$ and non-axisymmetric instabilities in $6D$.

Chapter 5 contains material that was presented in the co-authored publication Ref. [2] together with a significant amount of unpublished results on non-axisymmetric instabilities, which were obtained in collaboration with H. Bantilan, P. Figueras, and R. Panosso Macedo. I implemented all the time-evolution code, the initial data, and the symmetry reduction for this chapter. Furthermore, I was responsible for finding gauge conditions, damping and dissipation parameters, and a diffusion term that stabilised the simulations, and performed roughly half of the simulations presented in this chapter. The horizon finder code was developed by S. Tunyasuvunakool and therefore the discussion of it is kept to the necessary minimum. The interested reader is referred to Ref. [163] for details. Apart from the scripts for calculating Komar mass and angular momentum, all the tools for analysing the geometry of the apparent horizon, the growth rate of the perturbations, the approach to pinch-off, the cylindrical radial velocity of light rays on the apparent horizon, and the analysis of the wave data for non-axisymmetric instabilities are my own work. Furthermore, I carried out the numerical tests in the appendix to the chapter.

5.1 Introduction

As was already mentioned in the introduction, the higher dimensional analogue of the Kerr solution [14] is called the Myers-Perry black hole, after the two authors of Ref. [96]. The metric for a singly spinning Myers-Perry black hole in D dimensions is

$$ds^2 = -dt^2 + \frac{\mu}{r^{D-5}\Sigma}(dt - a \sin^2 \theta d\phi)^2 + \frac{\Sigma}{\Delta}dr^2 + \Sigma d\theta^2 + (r^2 + a^2) \sin^2 \theta d\phi^2 + r^2 \cos^2 \theta d\Omega_{(D-4)}^2, \quad (5.1)$$

where μ and a are the mass and rotation parameter respectively,

$$\Sigma = r^2 + a^2 \cos^2 \theta, \quad \text{and} \quad \Delta = r^2 + a^2 - \frac{\mu}{r^{D-5}}. \quad (5.2)$$

As the number of dimensions is increased beyond $D = 5$, the behaviour of Myers-Perry black holes changes substantially. In particular, for $D \leq 5$ there is an upper bound on the angular momentum parameter of the black hole, while in $D \geq 6$ singly spinning Myers-Perry black holes can rotate arbitrarily fast. To see this, we consider the location of the event horizon, which can be found by solving $g_{rr}^{-1} = 0$. It lies at $r = r_H$ with

$$\Delta(r_H) = r_H^2 + a^2 - \frac{\mu}{r_H^{D-5}} = 0. \quad (5.3)$$

In $D \leq 5$, this is a quadratic equation in r_H , which only has real roots if a is sufficiently small. This imposes an upper bound on the angular momentum a Myers-Perry black hole can have: the Kerr bound $a \leq \mu/2$ in $4D$, and $a < \sqrt{\mu}$ in $5D$. In $D \geq 6$, on the other hand, $\Delta(r) \rightarrow \infty$ as $r \rightarrow \infty$ and $\Delta(r) \rightarrow -\infty$ as $r \rightarrow 0$ so that (5.3) always has a solution. Thus, for $D \geq 6$ there is no upper bound on the rotation parameter of singly spinning Myers-Perry black holes. This change of behaviour as the number of dimensions is increased is not unexpected: for larger D , the gravitational attraction drops faster, but the strength of the centrifugal barrier, which only acts in one plane, remains unchanged.

In higher dimensions, rotations in more than one plane are allowed, and the metric (5.1) can be generalised to $\lfloor (D-1)/2 \rfloor$ independent planes of rotation [96, 99]. If all spin parameters are non-zero, Myers-Perry black holes can no longer rotate arbitrarily fast, even for $D \geq 6$. Fig. 5.1 shows the region of parameters space for which Myers-Perry black holes exist in $D = 5$ (left) and $D = 6$ (right). It shows that in $6D$ arbitrarily large spin in one plane is possible, but only if the spin in the other rotation plane is zero. However, for every value of one of the spin parameters, there is an open set of spin parameters in the second rotation

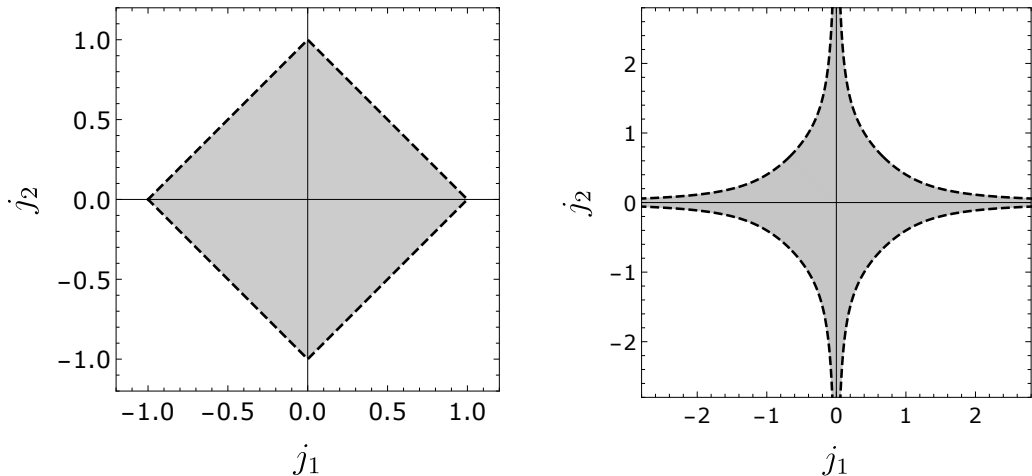


Fig. 5.1 Regions in phase space for which Myers-Perry black holes exist in 5D (left) and 6D (right) [99]. In 6D, singly spinning black holes can rotate arbitrarily fast.

plane for which black holes exist. In this sense, Myers-Perry black holes with arbitrarily large angular momentum in one rotation plane can be considered generic. However, as we will see in the next section, there is a dynamic upper bound on the angular momentum parameter, above which the black hole becomes unstable.

5.1.1 (In-)stability of Myers-Perry black holes

In 5D, there are conflicting results for the stability of Myers-Perry black holes. Ref. [25] found an axisymmetry-breaking instability for spin parameters $a \geq 0.88\sqrt{\mu}$ in their non-linear numerical relativity simulations. However, four years later, Ref. [27] performed a linear stability analysis that showed no evidence for an instability in 5D. This is particularly puzzling because the authors of Ref. [25] also used exactly the same code and methodology in $D \geq 6$ [26], and in this setting the linear results in Ref. [27] were in good agreement. Therefore, Ref. [27] suggested that the instability in 5D may only be a non-linear effect.

In $D \geq 6$, Ref. [26] found an axisymmetry-breaking instability, the *bar-mode* instability, for sufficiently rapidly rotating black holes. Their simulations showed that the bar-mode instability causes the black hole to become more and more elongated in the rotation plane. This causes it to radiate angular momentum until it rotates slowly enough to be stable. Thus, in the regime that was simulated in Ref. [26], the end point is another Myers-Perry black hole albeit with a much smaller angular momentum parameter. This instability can be interpreted as a dynamical upper bound on the angular momentum parameter: no stable Myers-Perry

black holes exist above the angular momentum parameter at which the bar mode instability sets in. These findings were confirmed and studied in detail in the linear regime in Ref. [27].

In addition to the bar-mode instability, there is an axisymmetric instability in $D \geq 6$, called the ultraspinning instability [23, 172]. The existence of the ultraspinning instability was already conjectured in Ref. [23] for the following reason: as argued above, Myers-Perry black holes can rotate arbitrarily fast in $D \geq 6$. As the rotation parameter is increased, they become increasingly flattened. To see this, note that for large a and fixed mass the horizon radius is given by

$$r_H \approx \left(\frac{\mu}{a^2} \right)^{\frac{1}{D-5}} \ll a. \quad (5.4)$$

The thickness of the black hole can be measured using the areal radius of the transverse sphere, $r_{(D-4)}^\perp$. Ref. [23] characterises the extent of the black hole in the rotation plane using the areal radius of the horizon at a fixed point in the transverse sphere, $r_{(2)}^\parallel$. Using (5.4) and the metric (5.1), we find

$$r_{(D-4)}^\perp = r_H \ll r_{(2)}^\parallel = \sqrt{r_H^2 + a^2} \approx a. \quad (5.5)$$

Thus, at high rotation parameters the black hole becomes increasingly stretched in the rotation plane but flattened in the transverse direction. Ref. [23] shows that close to the axis of rotation, the geometry of this highly flattened black hole approaches that of a black membrane. This led the authors to conjecture that ultraspinning Myers-Perry black holes undergo the GL instability just like black membranes. This intuition was confirmed in Ref. [172] using a numerical linear perturbation analysis. Due to its similarity to the GL instability of black membranes, it is possible that the ultraspinning instability leads to the pinch-off of the black hole.

In this chapter, we present fully non-linear numerical evolution of rapidly rotating Myers-Perry black holes in $5D$ and $6D$. In $D = 5$, we present our results for the dynamics up to $a = 0.89\sqrt{\mu}$, which is comfortably in the regime where Refs. [25, 27] reported potentially conflicting results. While many of the black rings in $5D$ we considered in the previous chapter collapsed to a Myers-Perry black hole, the angular momentum was never high enough to be in the relevant regime.

In $D = 6$, we present a detailed study of the ultraspinning instability in the range $1.5 \leq a/\mu^{\frac{1}{3}} \leq 2.0$. The first (ring-shaped) unstable mode sets in at $a/\mu^{\frac{1}{3}} = 1.572$ and the second (Saturn-shaped) mode sets in at $a/\mu^{\frac{1}{3}} = 1.849$ [24]. Thus, our simulations comfortably cover the regime in which both ring- and Saturn-shaped modes are present. Since the ultraspinning

instability is axisymmetric, simulations of it can be reduced to a system of PDEs in $2 + 1$ dimensions. This makes them much cheaper computationally than the simulations of black rings in the previous chapter and allows us to study the horizon geometry and dynamics in great detail. Finally, we report intriguing early results of ongoing work for non-axisymmetric instabilities in $6D$ with angular momentum up to $a = 1.5\mu^{\frac{1}{3}}$. This is larger than the range of angular momenta considered in Ref. [26] ($a \lesssim 1.1\mu^{\frac{1}{3}}$), and leads to a very surprising new behaviour.

5.1.2 $6D$ phase diagram and bumpy black holes

We have already considered the phase diagram of $5D$ black hole solutions in the previous chapter in Fig. 4.1. Let us now do the same for $D = 6$. Fig. 5.2 displays a sketch of the phase diagram of all known asymptotically flat, stationary single black hole solutions rotating in a single rotational plane in $6D$. As argued above, $6D$ Myers-Perry black holes can rotate arbitrarily fast (red curve in Fig. 5.2) and therefore extend to infinite angular momentum in the phase diagram, with ever decreasing horizon area. Just like in $5D$, there are two branches of black ring solutions in $6D$ [97], thin and fat rings. A few selected multi-black hole solutions are added for reference (dotted lines). The solutions that were included are special in that they are in thermodynamic equilibrium. This is the case if the horizon temperature and angular velocity are the same for all parts of the horizon. Without this requirement, multi-black hole solutions such as black Satellites cover the strip $a_H < a_H^{\text{Schw.}}$, where $a_H^{\text{Schw.}}$ is the dimensionless area parameter of the Schwarzschild-Tangherlini black hole.

The onset of the ultraspinning instability is related to the emergence of new branches of stationary black hole solutions, called bumpy black holes. Bumpy black holes were constructed numerically in Refs. [173, 174]. They come in several families of two branches, $(+)_i$ and $(-)_i$, where i determines how many zeros the deformation has in the radial direction of the rotational plane. For example, $(+)_1$ bumpy black holes (orange curve in Fig. 5.2) have one central dent, $(-)_1$ (black curve) one central bulge, $(+)_2$ one central bulge and one ring-shaped dent, $(-)_2$ one central dent and a ring-shaped bulge, etc. The $(-)_i$ branches all have lower entropy than the corresponding Myers-Perry black hole of the same mass and angular momentum and end in a singular solution, presumably without connecting to any other stationary black hole solution [173, 174]. The $(+)_i$ branches have very interesting behaviour: their entropy is initially higher than that of the corresponding Myers-Perry black hole but only in a very small region of the parameter space. Thereafter, the curve turns around in a cusp and connects to the fat branch of black rings for $i = 1$, and corresponding equilibrium multi-black hole solutions for higher modes. The fact that the $(+)_i$ families of

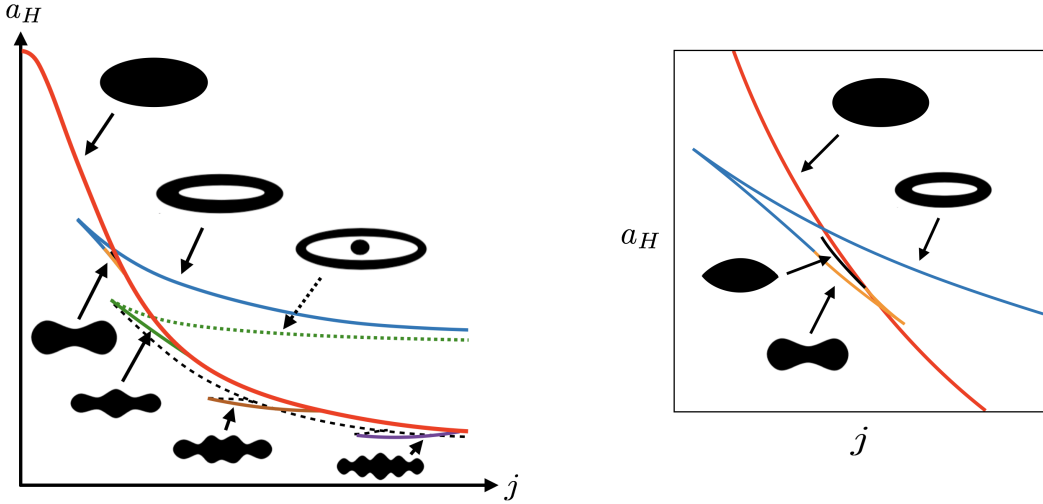


Fig. 5.2 *Left*: Sketch of the phase diagram of singly-spinning 6D black hole solutions that are in thermal equilibrium. This is only a sketch and heavily exaggerates some of the important features, which would otherwise be hard to see in one plot. Plots with numerical data can be found in Refs. [173, 174]. The sketch was taken partly from Fig. 6 in Ref. [167], but has been updated with the most recent insights obtained in Refs. [173, 174]. *Right*: Zoom of the region where the $(+)_1$ (orange) and the $(-)_1$ (black) bumpy black holes branch off the Myers-Perry solution.

bumpy black holes have higher entropy when they branch off from the curve of Myers-Perry solutions indicates that the latter must develop an instability at these points: the ultraspinning instability.

5.2 Stability in 5D

As outlined in the introduction, there are conflicting results on the stability of Myers-Perry black holes to axisymmetry-breaking perturbations in 5D. In this section, we present fully non-linear numerical evolutions of Myers-Perry black holes in $D = 5$. We present these results separately from those in 6D in the next section since we changed our numerical methods in 5D to follow Ref. [25], which reported an instability for $a \geq 0.88\sqrt{\mu}$, more closely. The only major difference is that we use CCZ4 whereas Ref. [25] used BSSN.

5.2.1 Numerical methods

We solve the vacuum CCZ4 equations with damping parameters $\kappa_1 = 0.1$, $\kappa_2 = 0$, and the redefinition $\kappa_1 \rightarrow \kappa_1/\alpha$, which enables us to choose $\kappa_3 = 1$. To make the evolution feasible, we impose a $U(1)$ symmetry in the transverse plane using the modified Cartoon method. Ref. [25] used precisely the same symmetry reduction. As gauge evolution equations, we choose 1 + log slicing (3.5) with coefficient $\eta_\alpha = 1.5$ and the standard second-order Gamma-driver shift condition (1.31) with parameters $\eta = \mu^{-\frac{1}{2}}$ and $F = 1/3$ and no advection terms. We use a Cartesian grid with fourth order finite difference stencils and a fourth order Runge-Kutta integration scheme with Courant factor 0.4. The resolution in the wave extraction zone is $0.7\sqrt{\mu}$ and we add 8 levels with refinement ratio 2 : 1 to ensure that the horizon is covered by at least 60 points throughout the evolution. To suppress high frequency modes in the simulation, we add Kreiss-Oliger dissipation with coefficient $\sigma = 0.1$.

As initial data, we use the metric (5.1) with a change to quasi-isotropic radial coordinates defined by

$$r = \rho + \frac{r_H^2}{4\rho}. \quad (5.6)$$

We try to excite a non-axisymmetric instability by perturbing the conformal factor with an $m = 2$ mode

$$\chi = \chi_0 \left(1 + A \frac{x^2 - y^2}{\mu} \exp \left[-\frac{\rho^2}{\rho_H^2} \right] \right), \quad (5.7)$$

where χ_0 is the value of the unperturbed conformal factor and A is a parameter controlling the amplitude of the perturbation. To observe the behaviour of the modes that are excited by (5.7), we follow Ref. [25] and extract gravitational waves by monitoring the quantity

$$h_+ = \frac{\tilde{\gamma}_{xx} - \tilde{\gamma}_{yy}}{2} \left(\frac{z}{\sqrt{\mu}} \right)^{\frac{3}{2}} \quad (5.8)$$

on the z -axis, similarly to (4.11) for black rings in the previous chapter. As reported by Ref. [25], the perturbation (5.7) should lead to an instability that is visible in the quantity h_+ for Myers-Perry black holes with spin parameter $a \geq 0.88\sqrt{\mu}$.

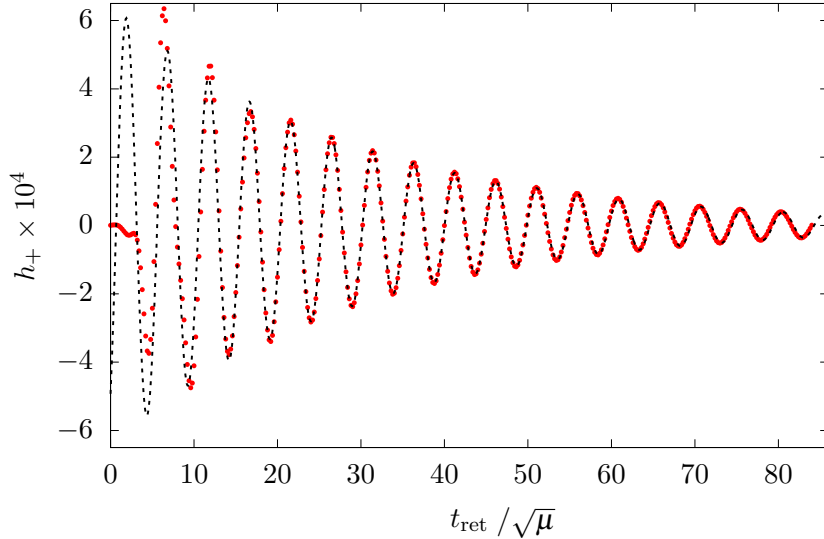


Fig. 5.3 Results (red dots) for the gravitational wave signal h_+ for a 5D Myers-Perry black hole with $a = 1.89\sqrt{\mu}$ and a bar-mode perturbation. The black dotted line shows a fit with parameters (5.9). Here $t_{\text{ret}} = t - r$, where r is the extraction radius.

5.2.2 Results

For the entire range of spin parameters we could investigate, $a \leq 0.89\sqrt{\mu}$, we find that Myers-Perry black holes are stable. Fig. 5.3 shows the wave data for $a = 0.89\sqrt{\mu}$ with perturbation amplitude $A = 0.2$. It exhibits a perfect exponential ring down with frequency and growth rate

$$\Re(\omega)r_H = 0.58 \pm 0.02 \quad \text{and} \quad \Im(\omega)r_H = -0.0159 \pm 0.0011, \quad (5.9)$$

which is in good agreement with the results of Ref. [27]. We find no evidence for a non-linear instability in this regime.

Since the branch of 5D Myers-Perry black holes ends in a naked singularity for $a = \sqrt{\mu}$ (see the phase diagram in Fig. 4.1), it is not unreasonable to speculate that there might be an instability as this naked singularity is approached. However, Ref. [27] considered spins up to $a = 0.97\sqrt{\mu}$ and found no evidence for a linear instability. Our results indicate that, contrary to the results of Ref. [25], Myers-Perry black holes for $a \leq 0.89\sqrt{\mu}$ remain stable even if non-linear effects are taken into account. This still leaves the possibility of linear instabilities for $a > 0.97\sqrt{\mu}$ or non-linear instabilities for $a > 0.89\sqrt{\mu}$. However, very different methods will be required to study this regime.

5.3 Instabilities in 6D

In this section, we report on numerical simulations of 6D Myers-Perry black holes. We present a comprehensive study of the ultraspinning instability, and preliminary results for axisymmetry-breaking instabilities.

5.3.1 Numerical methods

We use the GRChombo code to study the instabilities of rapidly rotating Myers-Perry black holes in 6D by performing fully non-linear numerical evolutions. Both the bar-mode and the ultraspinning instability lead to the creation of new, smaller length scales in regions that are hard to predict a-priori, but GRCHOMBO’s adaptive mesh refinement allows us to resolve these features accurately.

We use Cartesian coordinates such that the singly-spinning black hole rotates in the $x - y$ plane. To make the simulations computationally feasible, we impose an $SO(3)$ symmetry in the transverse directions using the modified Cartoon method. Furthermore, for the study of the ultraspinning instability, which is axisymmetric, we also impose a $U(1)$ symmetry in the rotation plane. The implications of these symmetry assumptions on the genericity of our results are discussed in section 5.3.5. As required by the modified Cartoon method, we impose even or odd boundary conditions at $z = 0$. In addition, for the study of the ultraspinning instability with $U(1)$ symmetry even or odd boundary conditions are also imposed at $x = 0$. Our domain is periodic in all other directions, but so large that the boundary never comes into causal contact with the black hole during the evolution.

We discretise the equations on a rectangular mesh, calculate spatial derivatives using fourth-order finite difference stencils, and integrate in time using the explicit fourth order Runge-Kutta scheme. The resolution on the coarsest level is $0.35\mu^{\frac{1}{3}}$ and we keep adding new refinement levels so that the apparent horizon is covered by at least 57 points at all times. To reach the final frame in Fig. 5.7, we needed 22 levels in total. Due to this very deep mesh hierarchy, it is no longer enough to write checkpoint files at every coarse time step. We therefore checkpoint at intermediate steps, storing time interpolation coefficients as described in section 2.2.1. The convergence tests presented in the appendix to this chapter indicate that our results converge with third order. This is not unexpected, since we use fourth order discretisation but the interpolation at mesh boundaries reduces the convergence order of the code slightly.

We use the CCZ4 evolution equations with damping parameters $\kappa_1 = 0.5$ and $\kappa_2 = 0$. This large choice of the damping parameters (compared to $\kappa_1 = 0.1$ used for rings in the previous chapter) was necessary to keep the black hole parameters constant throughout the evolution. With less aggressive constraint damping, we found that constraint violating modes increased the mass of the black hole by a few percent over the course of the evolution. This would have made a quantitative analysis of the horizon geometry impossible and could even have changed the qualitative behaviour in extreme cases.

We evolve the lapse using the $1 + \log$ slicing condition (3.5) with advection terms and coefficient $\eta_\alpha = 1.5$. Due to the very large values of $\hat{\Gamma}^i$ in our initial data, we use the modified Gamma-driver shift condition (3.2) with advection terms, $F = 0.6$, $\eta = \mu^{-\frac{1}{3}}$, and

$$f(t, x^i) = \exp \left[- \left(\delta_1 \frac{r_H^2}{r^2} + \delta_2 \right) \frac{t^2}{\mu^{\frac{2}{D-3}}} \right], \quad (5.10)$$

where r_H is the location of the horizon, and δ_1 and δ_2 are two dimensionless parameters that we chose to be 0.2 and 0.075 respectively. As discussed in section 3.2, this shift condition drives the system to a gauge that is much more suitable for numerical evolution and for adding the perturbation. The purpose of the first term in the exponential in (5.10) is to speed up the gauge adjustment deep inside the apparent horizon, where the initial values of $\hat{\Gamma}^i$ are large and constraint violations resulting from violent gauge adjustment do not matter. Since GRCHOMBO is cell-centered, (5.10) is never evaluated at $r = 0$, so that there are no problems with division by zero. To select initial conditions for the gauge evolution, we follow the discussion in section 3.2 and choose $\alpha = \chi$ and $\beta^i = \chi \beta_{\text{MP}}^i$, where β_{MP}^i is the analytic shift obtained from (5.1) and χ denotes the conformal factor.

Similar to the simulations of black rings in the previous chapter, puncture gauge is not sufficient to keep the numerical evolution inside the horizon stable. We, therefore, add a diffusion term to our equations as described in section 3.3 with $0.01 \leq \chi_c \leq 0.02$, and use the turduckening method [133, 134] to regularise the coordinate singularity in our initial data inside a region of coordinate radius of 5% of the horizon radius.

Initial data

To use the singly-spinning Myers-Perry metric in the form (5.1) as initial condition of puncture evolution, we first have to transform to coordinates in which constant-time slices contain no physical singularity. We achieve this by defining a new quasi-radial coordinate, ρ ,

through

$$r = \rho \left(1 + \frac{1}{4} \left[\frac{r_H}{\rho} \right]^{D-3} \right)^{\frac{2}{D-3}}, \quad (5.11)$$

where r_H is the horizon radius. The transformation (5.11) is the standard change to isotropic coordinates for the Schwarzschild-Tangherlini black hole. For Myers-Perry, it no longer leads to isotropic coordinates, but this does not cause any problems for numerical evolution. What matters is that constant-time slices of the metric (5.1) written in the coordinate ρ contain no physical singularities, only a coordinate singularity at $\rho = 0$. They are smooth on the horizon, which is located at $\rho_H = r_H/4^{1/(D-3)}$.

Even with the coordinate transformation above, the metric (5.1) is not ideal as a starting point for numerical evolution, as it uses a heavily skewed coordinate system. In particular, the horizon lies at constant $\rho = \rho_H$ even though Myers-Perry black holes are highly flattened by their rotation. This is bad from a numerical point of view, as it leads to strong gradients in some regions and smaller gradients in others, requiring complicated regions of higher refinement. Furthermore, the discrepancy between the shape of the horizon on the numerical grid and its physical shape makes it harder to implement a perturbation which excites the ultraspinning instability. To solve this problem, we use our modified Gamma-Driver to drive the system to a more suitable gauge first, and only perturb the black hole after gauge adjustment. We outline the details of this procedure below.

We start the evolution from the metric (5.1) with quasi-radial coordinate (5.11) and evolve the unperturbed black hole until the gauge has settled down completely. The timescale over which this happens depends on the choice of δ_1 and δ_2 in (5.10), but was never larger than $10\mu^{\frac{1}{3}}$. Our shift condition (3.2) drives the system towards coordinates for which $\hat{\Gamma}^i = 0$. In this gauge, the shape of the horizon roughly matches its physical shape: the black hole becomes highly flattened in the rotational plane. For every simulation, we verify that there was no physical evolution during the short gauge adjustment phase by monitoring the properties of the black hole, most importantly, its mass, horizon area, and thickness.

Once the gauge evolution has settled, we trigger the ultraspinning instability by perturbing the conformal factor via

$$\chi = \chi_0 \left\{ 1 + A J_0 \left[j_{0,k} \sin \left(\frac{\pi}{2} \sigma \right) \right] \exp \left[- \left(\frac{\chi_0}{\chi_H} - \frac{\chi_H}{\chi_0} \right)^2 \right] \right\}, \quad (5.12)$$

where A is the amplitude of the perturbation, χ_0 is the unperturbed conformal factor, χ_H is the value of the unperturbed conformal factor on the horizon, J_0 is the Bessel function of

the first kind, $j_{0,k}$ is the k^{th} zero of J_0 , and $\sigma = \min\left(\sqrt{x^2 + y^2}/\tilde{R}, 1\right)$ with a parameter \tilde{R} that determines the extent of the deformation in the plane of rotation. Since χ is roughly constant on the flat portion of the horizon, the exponential term in (5.12) ensures that the perturbation is localised on the horizon. While (5.12) does not explicitly decay to zero at infinity since χ only asymptotes to one, it very quickly decays to a value that is too small to have any influence on the numerical evolution or the numerical results for the mass of the spacetime. The term involving the Bessel function gives the perturbation the correct shape close to the axis of rotation, where J_0 captures the unstable mode reasonably accurately [23]. The index k (5.12) determines the shape of the perturbation: $k = 1$ gives the perturbation a ring shape, $k = 2$ a Saturn shape, etc.

Our perturbation of χ introduces constraint violations, but they are small and depend linearly on the perturbation amplitude. Furthermore, they decay rapidly due to the CCZ4 constraint damping terms. Once the system has been brought back onto the constraint surface, we check that the black hole parameters differ by less than 1% from those of the unperturbed black hole.

5.3.2 Analysis methods

Apparent horizon

To study the geometry of the Myers-Perry black hole as it undergoes the ultraspinning instability, we monitor the apparent horizon. Most traditional methods for finding apparent horizons assume that it can be defined as the level set of a function (see Ref. [175]). For a black hole of spherical topology, one would typically specify the apparent horizon location as $r = R(\theta)$ (assuming axisymmetry). However, this method is unsuitable for the ultraspinning instability since $R(\theta)$ fails to be a single-valued function (Fig. 5.7). An alternative approach would be to specify the apparent horizon location in terms of the Cartesian coordinate z as a function of the cylindrical radius, $z = Z(r_{S^1})$. However, since the radial extent of the black hole in the rotation plane is not fixed, it is hard to specify appropriate boundary conditions at the outer edge of the apparent horizon.

To solve this problem, we consider the apparent horizon as a general parametric surface $(r_{S^1}(u), z(u))$, where u is the parameter and we are still assuming axisymmetry. To be able to construct a well-posed system, we have to specify a gauge condition for the parameter u . We found that generalised harmonic gauge with respect to the induced metric on the apparent horizon works well. This gauge condition, together with the equation that is obtained by

setting the expansion of the surface to zero, forms a system of elliptic PDEs, which we can solve for $z(u)$ and $r_{S^1}(u)$. The technical details of this approach can be found in Ref. [163]. In theory, this method can be extended to allow non-axisymmetric shapes by introducing another parameter. This would enable us to find the very complicated horizon shapes we will encounter for axisymmetry-breaking instabilities towards the end of this chapter. However, we have not yet been able to find a method that converges reliably in these settings. This is work in progress.

Embedding diagrams

To visualise the shape of the apparent horizon as it undergoes the ultraspinning instability, we follow Refs. [174, 28] and embed constant- ϕ slices of the apparent horizon into four-dimensional Euclidean space with metric

$$ds_{\mathbb{E}^4}^2 = dU^2 + dZ^2 + Z^2 d\Omega_{(2)}^2. \quad (5.13)$$

By our symmetry assumptions, the metric on the $\phi = 0$ slice of the apparent horizon is

$$ds_{\phi=0}^2 = (g_{xx} + 2g_{xz}z'(x) + g_{zz}z'(x)^2) dx^2 + z(x)^2 g_{ww} d\Omega_{(2)}^2, \quad (5.14)$$

where $z(x)$ defines the location of the apparent horizon. Embedding this $\phi = 0$ slice of the horizon into \mathbb{E}^4 requires finding a parametrised surface $(U(x), Z(x))$ in Euclidean space which has metric (5.14). By comparing coefficients of $d\Omega_{(2)}^2$, we immediately see that

$$Z = \sqrt{g_{ww} z^2}, \quad (5.15)$$

which by comparing dx^2 terms implies that

$$\left(\frac{dU}{dx} \right)^2 = g_{xx} + 2g_{xz}z' + g_{zz}z'^2 - z'^2 g_{ww} - z z' g'_{ww} - z^2 \frac{g'^2_{ww}}{g_{ww}}. \quad (5.16)$$

In our simulations, we found that the right-hand-side of the above equation was always positive so that we could take the square root and integrate it numerically to find $U(x)$. Fig. 5.4 shows the embedding diagram for an unperturbed Myers-Perry black hole with $a = 1.7\mu^{\frac{1}{3}}$. This very clearly shows how flattened the horizon is due to the rotation.

It is important to bear in mind that the embedding above is done for a constant- ϕ slice and, therefore, loses all information about the length in the ϕ direction. This means that U is not a good measure for the physical radius of the S^1 in the plane of rotation, which is given

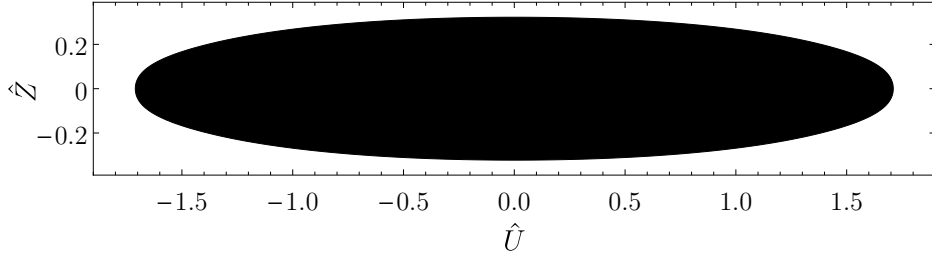


Fig. 5.4 Embedding of a constant- ϕ slice of the apparent horizon into \mathbb{E}^4 for a 6D Myers-Perry black hole with $a = 1.7\mu^{\frac{1}{3}}$. Hatted quantities have been rescaled by $\mu^{\frac{1}{3}}$.

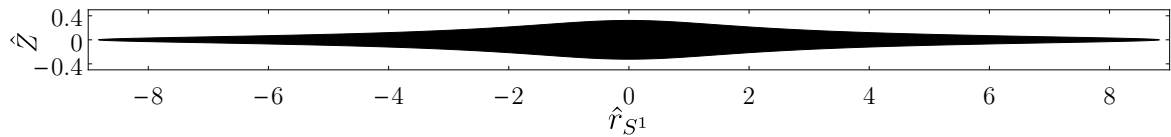


Fig. 5.5 Plot of the areal radius of the transverse sphere versus the S^1 radius for a 6D Myers-Perry black hole with $a = 1.7\mu^{\frac{1}{3}}$. Hatted quantities have been rescaled by $\mu^{\frac{1}{3}}$.

by $\sqrt{x^2 g_{yy}}$. Fig. 5.5 shows the same black hole as above but now as a plot of S^2 radius, $Z = \sqrt{z^2 g_{ww}}$, versus the S^1 radius. The resulting picture looks much more extreme, but lacks all information about the arc length along the apparent horizon. We will use the S^1 radius to check whether the black rings that arise during the ultraspinning instability are balanced. In particular, for a given mass and S^1 radius, there is a precise value for the angular momentum for which the ring can be in equilibrium.

Physical quantities

To monitor the mass and angular momentum of the black hole throughout the evolution, we measure the Komar mass and angular momentum. The former is defined for spacetimes with a timelike Killing vector field, the latter for all spacetimes with a rotational symmetry. Since we only work with vacuum spacetimes, we may calculate them as integrals on the horizon, \mathcal{H} ,

$$M = \frac{1}{12\pi G} \int_{\mathcal{H}} *d\xi \quad \text{and} \quad J = -\frac{1}{16\pi G} \int_{\mathcal{H}} *\omega, \quad (5.17)$$

where ξ and ω are the one forms dual to the timelike and the rotational killing vector field respectively. While we explicitly preserve the symmetry in the rotation plane, we never have exact time-translation symmetry. In theory, this prevents us from using the Komar mass. In practice, our evolution has quasi-stationary regimes during which the time-dependence is very slow compared to the length scale associated to the horizon. We find that in these

regimes the Komar mass settles down to an approximately stationary value, which we use as an estimate for the mass of the black hole.

It is very useful that Komar mass and angular momentum can be calculated as integrals on the horizon: it allows us to estimate the contributions of various parts of the black hole to the overall mass or angular momentum. In particular, the ultraspinning instability leads to the separation of the black hole into distinct quasi-stationary parts. An example of this can be seen in Fig. 5.7, which shows the black hole breaking into several black rings. Since these black rings are almost stationary, we can estimate not only their angular momentum but also their mass using (5.17).

Any two quantities out of mass, angular momentum, S^1 radius, and horizon area define a Myers-Perry black hole uniquely. In the case of black rings, they either define a unique solution or a unique pair of a thin and a fat ring. Thus, if all these quantities agree with the values for the Myers-Perry metric or the black ring, we can be confident that the evolution has indeed settled down to one of these solutions.

5.3.3 Results: Ultraspinning instability

Fig. 5.7 displays several snapshots¹ from the evolution of the ultraspinning instability for $a = 1.7\mu^{\frac{1}{3}}$. They show an embedding of a constant- ϕ slice of the apparent horizon into \mathbb{E}^4 . At this value of the spin parameter, only the “ring-shaped” mode is present. Indeed, a very large ring forms quickly at the outermost edge of the horizon, connected by a thin membrane section in the middle. Over the whole range of angular momentum parameters we have investigated ($1.5 \leq a/\mu^{\frac{1}{3}} \leq 2.0$), we did not find any strong qualitative difference in the evolution of the ultraspinning instability. In particular, even though the second mode, which is “Saturn-shaped”, sets in at $a = 1.849\mu^{\frac{1}{3}}$, the ring mode grows fastest and completely dominates the non-linear evolution. This is the case, even if we perturb with a “Saturn-shaped” perturbation by setting $k = 2$ in (5.12).

Since the growth rates of the ultraspinning instability are not currently available in the literature, we estimate them by fitting the thickness of the black hole at the centre with an exponentially growing perturbation of the form

$$Z(x = 0, t) = Z_0 \left(1 - B e^{\Im \sigma t} \right), \quad (5.18)$$

¹Videos can be found at <http://www.grchombo.org>.

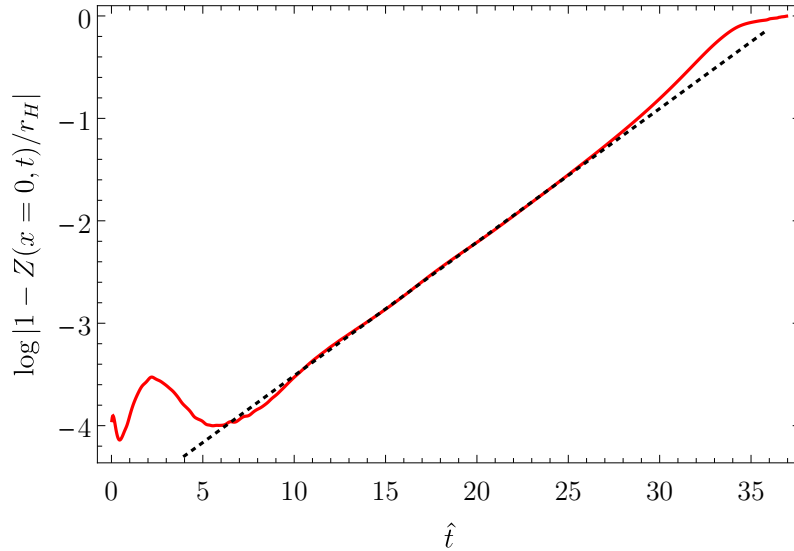


Fig. 5.6 Growth of the “ring-shaped” perturbation of an ultraspinning Myers-Perry black hole with $a = 1.7\mu^{\frac{1}{3}}$. Here $\hat{t} = t/\mu^{\frac{1}{3}}$. The dotted black line shows a fit with the parameters $Z_0 = 0.33\mu^{\frac{1}{3}}$, $\Im\omega = 0.13\mu^{-\frac{1}{3}}$, and $B = 0.0081$.

$a/\mu^{\frac{1}{3}}$	1.6	1.7	1.8	1.9	2.0
$\Im\omega \mu^{\frac{1}{3}}$	0.020	0.130	0.213	0.262	0.299

Table 5.1 Growth rates of the first unstable mode. Error ranges are $\pm 3\%$ for $a/\mu^{\frac{1}{3}} \geq 1.7$. For $a/\mu^{\frac{1}{3}} = 1.6$, the growth rate is much smaller and therefore has a much larger fractional error (around $\pm 25\%$) associated with it.

where Z_0 , B , and $\Im\omega$ are the quantities to be determined. We could have set $Z_0 = r_H$ a priori, but the constraint violating perturbation can change r_H by up to 1% so that re-fitting Z_0 increases the accuracy of the measured growth rate slightly. Fig. 5.6 shows an example of this fit for $a = 1.7\mu^{\frac{1}{3}}$. Towards the beginning of the evolution, the logarithmic scale highlights how the constraint violating perturbation affects the thickness at the centre and how the CCZ4 constraint damping terms take the system back onto the constraint surface. Thereafter, there is a long phase of exponential growth in the linear regime until non-linearities become important towards the end of the evolution. The results for the growth rate obtained from this fitting procedure are displayed in Tab. 5.1.

In our simulations, the outermost ring very quickly settles down to an almost stationary state. However, in the final snapshot of Fig. 5.7 it is still rigidly expanding outwards in the plane of rotation. Compared with the balanced black rings constructed numerically in Refs. [97, 173], the radius and area of the outermost ring are still 7% below their target values, while the

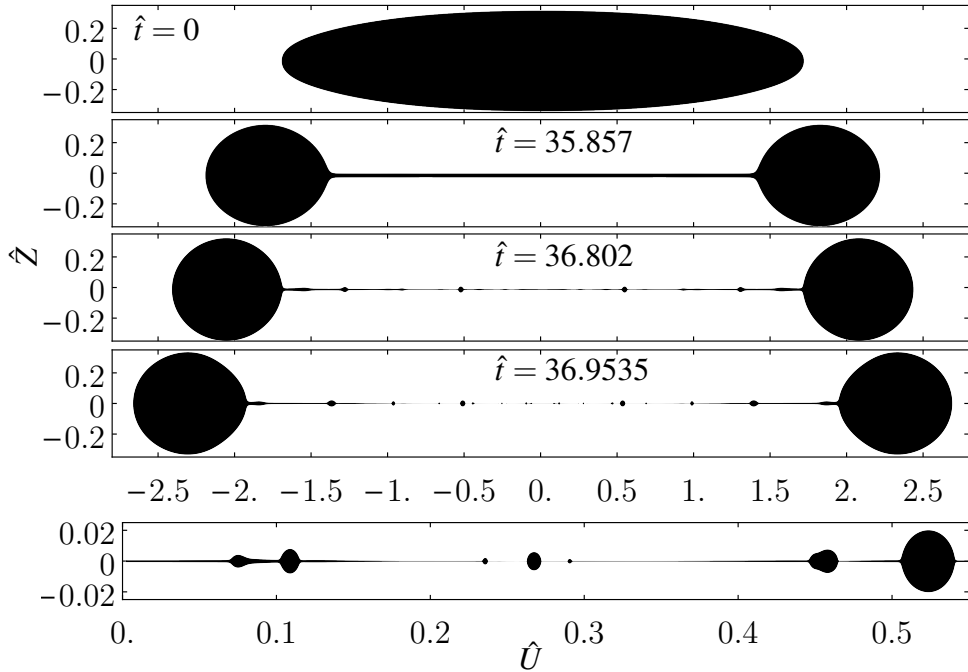


Fig. 5.7 *Top*: Embedding diagrams of the apparent horizon at different stages of the evolution of the ultraspinning instability of a Myers-Perry black hole with $a/\mu^{\frac{1}{3}} = 1.7$. Hatted quantities have been rescaled by $\mu^{\frac{1}{3}}$. The structure of rings that form on the membrane in the middle depends sensitively on the grid setting and is not convergent.

angular velocity is 15% above its target value. These results are consistent with conservation of angular momentum: since for a thin ring the angular momentum scales as ΩR^2 , where Ω and R are the angular velocity and the S^1 radius of the ring respectively, Ω has to decrease by roughly 15% to keep the angular momentum constant despite a 7% increase in R .

To estimate how much mass and angular momentum are contained within the outermost ring, we calculate the corresponding Komar integrals (5.17) on the apparent horizon. As discussed in section 5.3.2, the Komar mass is only meaningful once the system has settled down to a steady state. However, towards the end of our simulation the calculated Komar mass changes by less than 1%, indicating that the majority of the apparent horizon has settled down sufficiently. For the entire range of spin parameters we have investigated, the outermost ring accounts for 98–99% of the total mass and more than 99.99% of the angular momentum. During the evolution of the ultraspinning instability, only a small amount of mass is radiated (less than 2%). Angular momentum cannot be radiated due to our symmetry assumptions.

After the outermost large ring has formed, the region on the rotational plane inside the ring remains connected by a black membrane that is 50 times thinner than the original black hole. This black membrane is rotating and, therefore, locally boosted in the ϕ -direction. However,

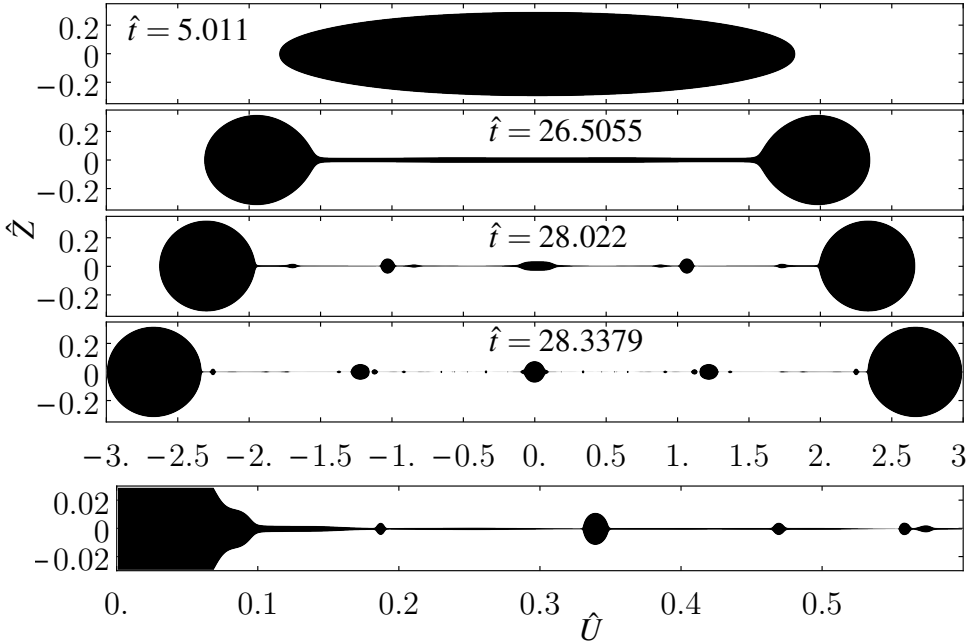


Fig. 5.8 Embedding diagrams of the apparent horizon at different stages of the evolution of the ultraspinning instability of a Myers-Perry black hole with $a/\mu^{\frac{1}{3}} = 1.8$. Hatted quantities have been rescaled by $\mu^{\frac{1}{3}}$.

since the evolution of the ultraspinning instability takes place in the radial direction, this orthogonal local boost does not affect the timescale of the instability. Furthermore, since the transverse direction is flat, the evolution should be similar to the GL dynamics of a black string in 5D. The portion of the apparent horizon that resembles a black membrane is long and thin enough to be GL unstable and can accommodate many unstable modes. Similarly to black strings, its subsequent evolution leads to a fractal structure of ever thinner rings connected by ever thinner black membrane sections, which themselves undergo the GL instability. In many cases, a black hole of spherical topology also forms in the centre.

While it is tempting to attribute the emergence of the central black hole to the presence of the ‘‘Saturn’’ mode, we find no evidence that the two are related. In particular, initial data with $a < 1.849\mu^{\frac{1}{3}}$ can also give rise to a central bulge as can be seen in Fig. 5.8. Instead, the structure of bulges that form on the membrane in the middle depends sensitively on the grid setting and is not convergent. In particular, while we demonstrate convergence for properties of the entire black hole, the first generation and the minimum membrane thickness in the appendix to this chapter, the position of higher generation rings and the size of the central bulge do not converge. Exactly the same behaviour was observed for black strings in Ref. [33, 75]. The reason for this is that in the dispersion relation of the black string, two different modes have the same growth rate, making the evolution very sensitive to small changes in the

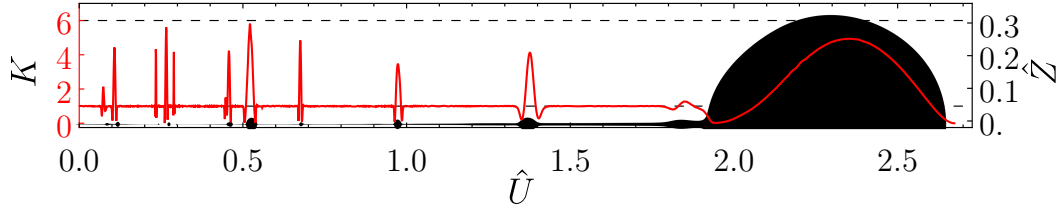


Fig. 5.9 Normalized spacetime Kretschmann invariant pulled back onto the apparent horizon.

initial data and the grid setting. We expect the membrane sections arising in our simulations to behave similarly, especially since starting from the second generation, the membrane is always thin enough to accommodate many unstable modes.

As evidence that the horizon has the geometry of concentric rings connected by membrane sections, we evaluate the normalised spacetime Kretschmann invariant

$$K = R_{abcd}R^{abcd}Z^4/12, \quad (5.19)$$

on the apparent horizon, where Z is the areal radius of the transverse sphere. The normalization is such that $K = 1$ for a black membrane and $K = 6$ for a 6D black string. The results (Fig. 5.9) are in close agreement with $K = 1$ on the membrane sections and approach $K = 6$ on most of the fully formed rings, suggesting that they are well-approximated by stationary black strings.

Higher generation rings differ from the outermost ring in that they are not balanced by their rotation. Fig. 5.10 shows a plot of the angular velocity of zero angular momentum geodesics on the apparent horizon versus the S^1 radius. For all fully formed rings, including the outermost one, the angular velocity is constant on the apparent horizon in agreement with our claim that they are approximately stationary. For a thin ring to be balanced, it has to have angular velocity [167]

$$\Omega = \frac{1}{\sqrt{D-3}} \frac{1}{R} + O\left(\left(\frac{Z_{\text{AH}}}{R}\right)^2\right), \quad (5.20)$$

where R is the S^1 radius of the ring and Z_{AH} is the areal radius of the transverse sphere. Comparing this condition to the data in Fig. 5.10, we see that higher generation rings do not rotate fast enough to be balanced. In particular, rings that are closer to the axis of rotation rotate more slowly than the outermost ring rather than faster as (5.20) would suggest. Instead, higher generation rings are held in place by the tension of the surrounding membrane sections.

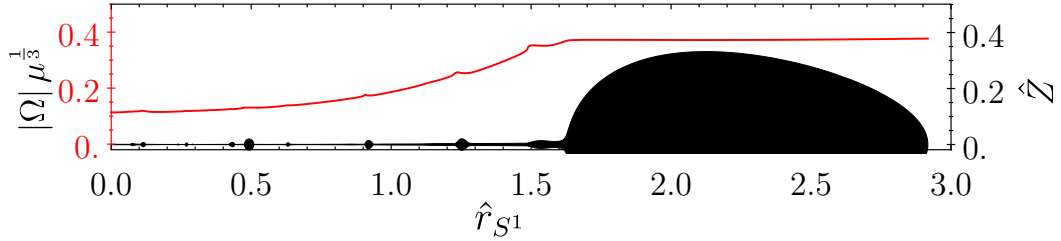


Fig. 5.10 Angular velocity of zero angular momentum geodesics on the apparent horizon.

The membrane that forms during the evolution of the ultraspinning instability lacks the translational symmetry an unperturbed black string has. There are three reasons for this: firstly, Myers-Perry black holes have compact horizons that do not wrap any topological direction in spacetime. Thus, any self-similarity is broken near the edges of the black hole. Secondly, in the early stages of the instability the radial extent of the black membrane sections is of the same order of magnitude as their distance from the axis of rotation. As a result, the inner and outer edge of the membrane sections have very different extent in the ϕ -direction, breaking translation symmetry. Thirdly, Myers-Perry black holes are rotating. The resulting centrifugal forces redistribute angular momentum outwards, so that the black membrane has a non-uniform thickness from the outset (e.g. in the third snapshot in Fig. 5.7).

One of the pieces of evidence Ref. [33] used to show that black strings pinch off in finite asymptotic time is that the time it takes to form a new generation decreases with a constant factor. This analysis turns out to be much harder for Myers-Perry black holes. For one, the aforementioned lack of translational symmetry causes different membrane sections to evolve at different timescales, so that a specific generation occurs at different times along the membrane. Furthermore, as argued above we cannot expect the structure and formation times of higher generations to be a convergent feature of the simulations. This problem should also be present for black strings, but as we will see below the ultraspinning instability gives rise to membrane sections that are much thinner compared to their length so that they can fit many more unstable modes. This makes the appearance of new generations more chaotic.

Having mentioned these two caveats, let us look at the formation times of new generations close to the membrane section with minimal thickness. Tab. 5.2 lists the results for the simulation displayed in Fig. 5.7 with spin parameter $a = 1.7\mu^{1/3}$. The data should be viewed as a representative example of the evolution rather than the “correct” result since the formation of new generations is chaotic. The table also includes the ratio between the radial extent of the black membrane section, L_i , and its thickness, Z_i , after the formation of the i^{th} generation. The data indicate that the evolution of the ultraspinning instability is only qualitatively

Gen.	1	2	3	4	5
$t_i/\mu^{\frac{1}{3}}$	31.8	36.45	36.78	36.916	36.952
$L_i/Z_{\text{AH},i}$	540	530	370	510	> 370

Table 5.2 Properties of the generations. The ratio of length to thickness of the i^{th} generation membrane was measured just before the formation of the $(i+1)^{\text{th}}$ generation. The time it takes to form the next generation decreases with factors 0.07, 0.41 and 0.26.

self-similar: while newly-formed membrane sections all undergo the GL instability, the time between the formation of successive generations does not decrease with a universal factor, even for later generations. Instead, for $a/\mu^{\frac{1}{3}} = 1.7$ we observe factors, X_i , which depend on the generation and lie between 0.07 and 0.41. Since for all the resolutions we used the largest factor we observed was $X_{\text{max}} \ll 1$, we can bound the pinch-off time by a geometric series

$$t_c < t_0 + (t_1 - t_0) \sum_i X_i < t_0 + (t_1 - t_0)/(1 - X_{\text{max}}). \quad (5.21)$$

While this upper bound is not sharp, it provides evidence that the black hole pinches off in finite asymptotic time.

The data in Tab. 5.2 suggest that the ultraspinning instability approaches pinch-off much faster than would be expected from the simulations of 5D black strings [33]. This is partly due to the quick drop in formation times between generations at the beginning and partly due to the membranes in higher generations being much thinner: the typical ratio $L_i/Z_{\text{AH},i}$ between the length and the thickness of a membrane section varies between 300 and 600. For the GL instability of black strings, this ratio is approximately 100 across all generations [33]. Therefore, the membranes that form in the evolution of the ultraspinning instability are more unstable, leading to a faster pinch-off time. Furthermore, they fit more unstable modes so that the formation of new bulges is more chaotic.

Throughout the evolution of the ultraspinning instability, the small concentric rings that form after the first generation move around significantly. This stretches some membrane sections making them much thinner and more GL unstable. To quantify and explain this movement, we calculate the cylindrical radial velocity dr/dt of null rays which co-rotate with the black hole and track the movement of the apparent horizon in the z -direction. The results (Fig. 5.11) paint a very consistent picture: the radial velocity on the horizon of the outermost ring is constant, in agreement with our earlier observation that it is still rigidly expanding. Near each ring, the radial velocity decreases or reverses completely, leading to a build-up of mass. This explains the numerous sign changes around the thinnest point of the

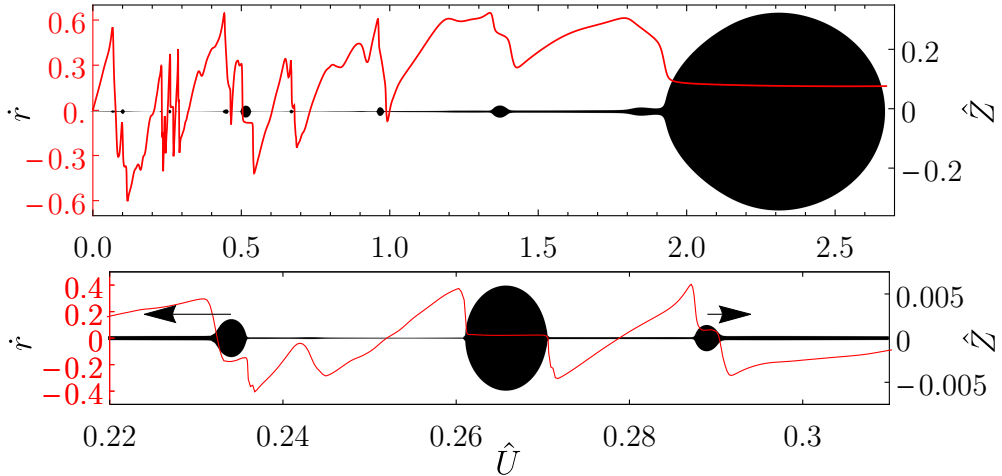


Fig. 5.11 *Top*: Cylindrical radial velocity $\dot{r} \equiv dr/dt$ of a null ray moving with the apparent horizon. *Bottom*: Zoom of the thinnest region. The arrows indicate the direction of the local velocity of the rings and highlight that they are pulled towards the thicker membrane sections.

membrane, where many higher generation rings are present. Indeed, the radial velocity can be used as an early indication of where the next ring is going to form: for example, in the zoomed frame in Fig. 5.11 a new generation is forming near $U = 0.24\mu^{\frac{1}{3}}$.

At late times, Fig. 5.11 shows that the flow in the $U < 1$ region is unaffected by the pull from the outermost ring. Instead, it is dominated by membrane tension and the gravitational attraction to higher generation rings. As we discussed earlier, these higher generation rings are not balanced by their rotation but held in place by the tension of the surrounding membrane sections. For the 6D black membranes in our simulations, the tension in the radial direction scales linearly with the thickness of the membrane at a fixed radius [167]. This means that higher generation rings always develop a radial velocity towards the thicker membrane section, further stretching the thinner membrane. This effect is clearly visible in Fig. 5.11 (bottom), and is large enough to change the width of a membrane section during the development of a new generation by a significant fraction, causing it to undergo the GL instability faster.

Since the radial extent of the black membrane sections becomes shorter and shorter compared to their distance from the rotation axis as the instability progresses, it is tempting to expect that approximate translational symmetry may be restored along this small membrane section. This in turn could imply that the ultraspinning instability may approach a precisely self-similar pattern as the instability progresses. However, our data indicate that this is not the case: since the speed at which the GL instability takes place depends on the thickness of the membrane, differences in thickness along the membrane are amplified not reduced.

Furthermore, as we saw above, the small concentric rings that form after the first generation are always pulled towards the thicker membrane section, stretching the thinner ones. Thus, we do not expect the ultraspinning instability to approach a precisely self-similar pattern, even at late times.

To obtain a precise value for the pinch-off time, we track the global minimum thickness of the membrane, a robust convergent feature of our simulations (as we demonstrate in the appendix to this chapter). Even though the dynamics of higher generation rings prevents the formation of new generations from being self-similar, our results (Fig. 5.12) show that the minimum thickness closely follows the scaling law

$$Z_{\text{AH}} = \kappa(t_c - t), \quad (5.22)$$

similar to black strings [33, 75] and the Rayleigh-Plateau instability of fluid columns. By performing a 2-parameter fit with (5.22) in Fig. 5.12, we can obtain values for the pinch-off time t_c and the dimensionless constant κ . The value for the latter, $\kappa = (9.9 \pm 0.2) \times 10^{-3}$, is universal in that it is the same for all of our runs and is independent of the rotation parameter and initial data. While Fig. 5.12 shows the fit for the global minimum thickness, all local minima exhibit the same scaling law behaviour, albeit with different pinch-off time.

The fact that the minimum thickness closely follows the scaling law (5.22) over almost three orders of magnitude strongly supports our earlier conclusion that the black hole will pinch off in finite asymptotic time, t_c , giving rise to a naked singularity. Furthermore, we saw earlier that $K = 1$ on membrane sections, with K defined as in (5.19). Thus, as the thickness decreases, the Kretschmann scalar diverges as

$$R_{abcd}R^{abcd} \propto \frac{1}{(t_c - t)^4} \quad (5.23)$$

so that the spacetime just outside the horizon develops arbitrarily large curvature within finite asymptotic time.

Let us finally speculate about the end point of the evolution. There are two ways to motivate this question: firstly, we can restrict to classical general relativity and ask which configuration the system is evolving towards, even though it may not be possible to reach this end point within classical general relativity. Secondly, we can allow quantum gravity effects and assume that they provide a mechanism for the black hole to pinch off without affecting the rest of the black hole substantially. This is not an unreasonable assumption since the evolution enters the quantum gravity regime only in a very small region of spacetime that contains very little mass. It would also be analogous to the Rayleigh-Plateau instability in

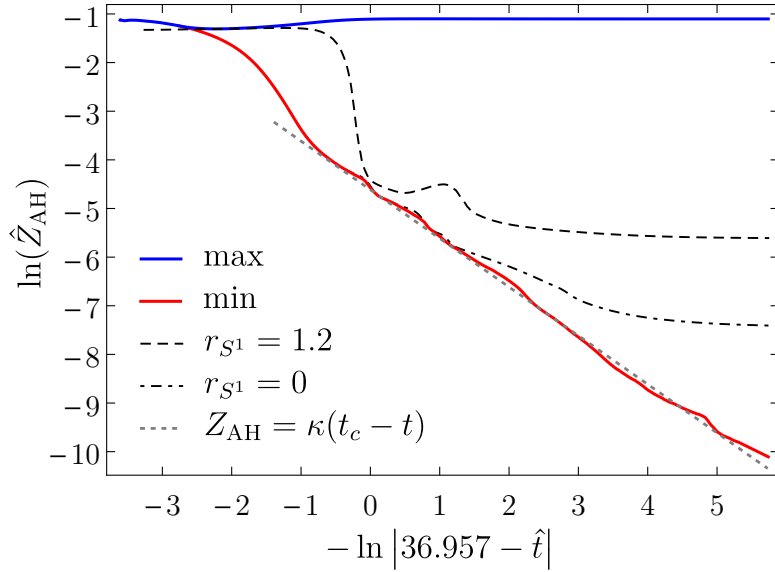


Fig. 5.12 Evolution of the thickness of the apparent horizon at several representative locations for $a/\mu^{\frac{1}{3}} = 1.7$.

fluid dynamics, for which molecular effects allow the pinch-off of the fluid column without affecting the macroscopic behaviour.

The plot of radial velocities (Fig. 5.11) suggests that after pinch-off the outermost ring will settle down to its balanced configuration, absorbing the nearby ($U \gtrsim 1$) membrane section. As discussed earlier, the angular velocity in the central region of the membrane is too low to allow rings to be balanced. Thus, rings and membrane sections closer to the centre will collapse into a spherical black hole with negligible angular momentum. Therefore, in our axisymmetric setting the end point will be a black Saturn in 6D. However, it will not be the Saturn that maximizes the entropy for a given final mass and angular momentum: the latter would consist of a central black hole carrying all the mass surrounded by a thin ring that accounts for all the angular momentum [176]. We find that as $a/\mu^{\frac{1}{3}}$ is increased, the outermost ring contains a slightly lower fraction of the overall mass. This raises the possibility that the maximum entropy configuration is approached for very high spins. However, over the range of spin parameters we could investigate, the differences in the fraction of mass contained in the outermost ring were too small to substantiate this claim.

5.3.4 Results: Non-axisymmetric instabilities

In this section, we present early results of an ongoing project to investigate axisymmetry-breaking instabilities of Myers-Perry black holes in 6D. The range $a \lesssim 1.1\mu^{\frac{1}{3}}$ has already

been investigated with fully non-linear simulations in Ref. [26], and a linearised analysis in Ref. [27]. The numerical evolution indicated that the black holes become unstable to a bar-mode instability at $a = 0.74\mu^{\frac{1}{3}}$, and that the end point of this instability is a Myers-Perry black hole with much lower angular momentum. Our goal is to extend these simulations to spin parameters above $1.6\mu^{\frac{1}{3}}$ where the ultraspinning instability becomes important.

We use exactly the same numerical methods as we used for the ultraspinning instability in the previous section. However, we do not impose the $U(1)$ symmetry in the rotation plane and we add a small bar-mode perturbation to the conformal factor using

$$\chi = \chi_0 \left(1 + A \frac{x^2 - y^2}{\mu^{\frac{2}{3}}} \exp \left[-\frac{\rho^2}{\rho_H^2} \right] \right), \quad (5.24)$$

where χ_0 is the unperturbed conformal factor, A is the perturbation amplitude, and ρ is the isotropic radial coordinate defined in (5.11). To measure the growth rate of the $m = 2$ mode of the instability, we extract the gravitational wave signal by monitoring the quantity h_+ (5.8), rescaled by $\mu^{\frac{1}{3}}$ rather than $\sqrt{\mu}$.

Fig. 5.13 shows the evolution of the apparent horizon for $a = 1.3\mu^{\frac{1}{3}}$. The black hole becomes extremely elongated and thin. This strong breaking of axisymmetry allows it to radiate angular momentum efficiently, until it has reached a regime where Myers-Perry black holes are stable so that it can settle down. The same behaviour can be seen in the gravitational wave data (Fig. 5.14), which exhibits exponential growth initially and a very slow quasi-normal ring-down towards the end. Fitting the gravitational wave data with exponentially growing and exponentially decaying sinusoids, we obtain the following results for the frequency and growth rate

$$\text{Growth: } \Re \omega r_H = 0.445 \pm 0.005, \quad \Im \omega r_H = 0.120 \pm 0.015, \quad (5.25)$$

$$\text{Decay: } \Re \omega r_H = 0.90 \pm 0.05, \quad \Im \omega r_H = -0.04 \pm 0.01. \quad (5.26)$$

The errors in the decay parameters are significantly larger, since we do not only have to perform the fit, but also have to estimate the final value of r_H from the horizon data. Since $a = 1.3\mu^{\frac{1}{3}}$ is beyond the range considered in Refs. [26, 27], we cannot compare the results for the initial growth. However, the results for the decay are in good agreement with Ref. [27].

The extreme horizon shapes that arise during the evolution of the bar-mode instability for $a = 1.3\mu^{\frac{1}{3}}$ suggest that the black hole could become so elongated that it becomes GL unstable. This was already postulated in Ref. [26], in which the authors estimate that for $a \gtrsim 1.6\mu^{\frac{1}{3}}$

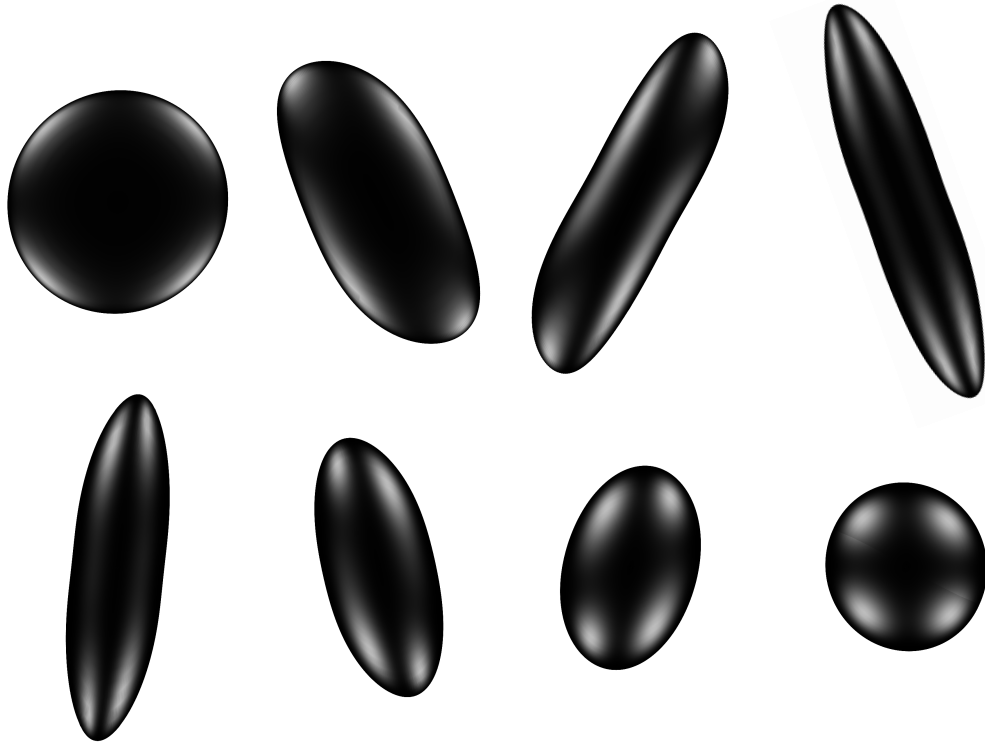


Fig. 5.13 Snapshots of the apparent horizon taken from the evolution of a 6D Myers-Perry black hole with $a = 1.3\mu^{\frac{1}{3}}$. The black hole is undergoing the bar-mode instability.

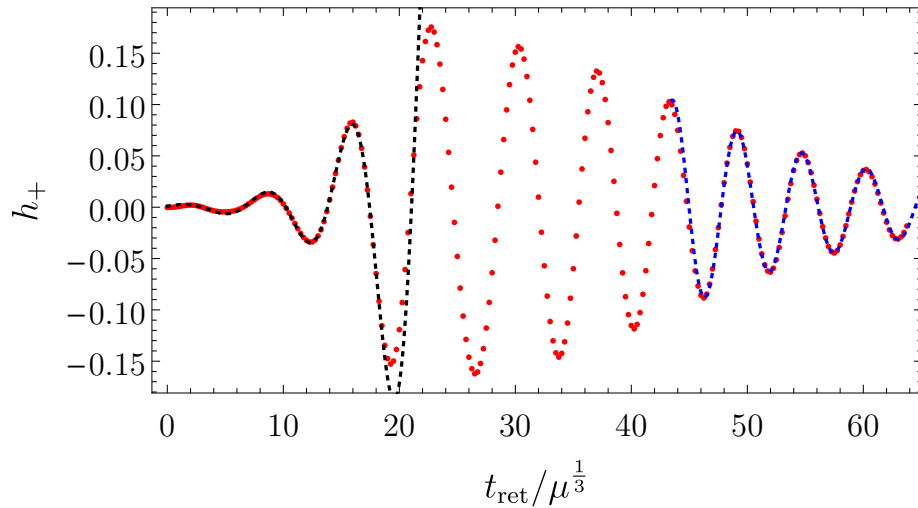


Fig. 5.14 Gravitational wave signal h_+ for a Myers-Perry black hole with $a = 1.3\mu^{\frac{1}{3}}$ undergoing the bar-mode instability. The dashed black line shows an exponentially growing sinusoid with fitted parameters (5.25); the dashed blue line shows a decay with fitted parameters (5.26).

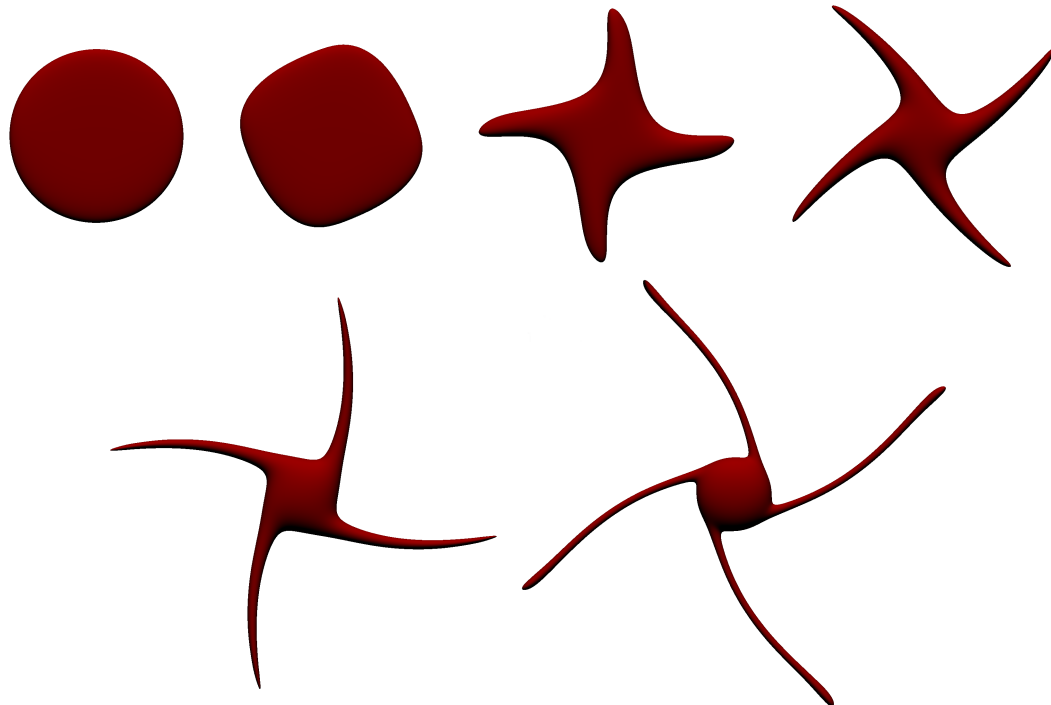


Fig. 5.15 Snapshots of the $\chi = 0.2$ contour taken from the evolution of a 6D Myers-Perry black hole with $a = 1.5\mu^{\frac{1}{3}}$. The black hole undergoes an elastic instability with $m = 4$.

gravitational wave emission is not strong enough to stop the growth of the bar-mode before it causes the black hole to pinch off. However, we find that before a reaches this regime, higher m modes start to dominate. Fig. 5.15 shows the instability of a Myers-Perry black hole with $a = 1.5\mu^{\frac{1}{3}}$. It only shows χ -contours since our apparent horizon finder is currently not general enough to find the complicated shapes that arise during the instability. However, as argued in the previous chapter, χ -contours capture the qualitative behaviour of the apparent horizon very well.

Even though we perturb the black hole with an $m = 2$ mode (5.24) initially, the evolution in Fig. 5.15 is clearly dominated by an $m = 4$ mode. This behaviour is very similar to what we found for black rings in 5D, for which higher m modes start to dominate as the thickness is decreased. The $m = 4$ mode gives the black hole the shape of a star whose tips are so far away from the centre that the gravitational attraction to the centre can no longer balance the centrifugal force. As a result, while the central portion settles down to a Myers-Perry black hole with lower angular momentum, the tips keep expanding outwards, becoming more and more elongated.

We have not yet been able to simulate the spacetime beyond the final frame of Fig. 5.15 with sufficiently high resolution, but this frame contains enough information to be able to predict

the subsequent behaviour. The black string portions that have formed on all four tips will be stretched further and further outwards, until they become GL unstable and detach from the central black hole in finite asymptotic time. We are currently working on simulations that investigate this process in detail and an apparent horizon finder that can capture the very complicated shapes that arise during the instability.

5.3.5 Discussion

We have studied the ultraspinning instability of rapidly rotating Myers-Perry black holes in $6D$ with spin parameters in the range $1.5 \leq a/\mu^{\frac{1}{3}} \leq 2.0$. We find that the ultraspinning instability causes the black hole to tear apart into multiple concentric rings. Unlike the evolution of black strings in Ref. [33], our results do not show a quantitative self-similarity: while the membrane forms a repeated structure of rings connected by ever thinner membrane sections, the times between generations do not decrease with a constant factor. However, similarly to black strings, the minimum membrane thickness very closely follows a scaling law (5.22), with a universal constant κ . Thus, we conclude that this scaling law fundamentally underlies the approach to pinch-off in a GL-type instability.

The imposition of the $U(1)$ symmetry made it possible for us to study the approach to pinch-off in detail but it also made our findings less generic since Myers-Perry black holes are unstable to non-axisymmetric modes in $D \geq 6$ [26, 27]. For this reason, we have recently extended our study to non-axisymmetric settings. We find that for $a \lesssim 1.3\mu^{\frac{1}{3}}$ the $m = 2$ mode dominates: the black hole becomes very elongated and radiates angular momentum until it has reached a stable configuration. For $a \gtrsim 1.5$, higher m modes dominate and give the black hole m spikes, which stretch outwards and eventually detach from the central black hole in a GL-type instability.

We find that for $a \gtrsim 1.5$, all known instabilities of Myers-Perry black holes lead to the black hole pinching off in finite asymptotic time in a GL-type process. However, exactly as for black rings and black strings, there is a chance that the curvature singularity is formed on the horizon and stays on the horizon so that future null infinity is still complete. This will be discussed in more detail in the next chapter. However, our detailed study of the approach to the pinch-off in the ultraspinning instability strongly suggests that the Kretschmann scalar just outside the horizon becomes arbitrarily large. This is an indication that quantum gravity effects may become important in the causal past of future null infinity.

Even though the non-axisymmetric instabilities of Myers-Perry black holes have larger growth rate than the ultraspinning instability, at least in the regime which we could study

in our work ($a \lesssim 2.0\mu^{\frac{1}{3}}$), the latter is not completely irrelevant. For sufficiently suppressed axisymmetry breaking modes in the initial data, the ultraspinning instability should have enough time to form the outermost ring. At this point, the membrane inside becomes thinner by a factor of 50 so that the axisymmetric instability of the membrane should be an order of magnitude faster than the axisymmetry-breaking instability of the outermost ring.

A potential caveat to the genericity of our conclusion is that Myers-Perry black holes can rotate in more than one rotation plane and that for rotation in several planes the spin parameters can no longer be arbitrarily large. However, for each angular momentum parameter j_1 in one rotation plane, there is an open set of values for the other spin parameters such that a black hole exists (see Fig. 5.1). In this sense, the results presented in this chapter should be generic.

Our results indicate that the factor κ in the scaling law (5.22) is universal in that it does not depend on the spin of the black hole or the initial perturbation. Furthermore, the results for rings in Fig. 4.14 are consistent with exactly the same value for κ . While this is intriguing, it has to be interpreted with care since κ is slicing-dependent. It would be very interesting to formulate a slicing-independent statement so that our results can be compared to those of Ref. [33], which uses GHGs. It might even be possible to make analytic predictions of the value of κ : for the Rayleigh-Plateau instability of fluid columns, Ref. [177, 178] could derive the scaling law (5.22) analytically. It would be very interesting to investigate whether a similar calculation is possible for GL-type instabilities of black holes.

5.4 Appendix: Numerical tests

To test convergence, we produce the output presented in the main text at four different grid resolutions. The highest resolution run had a coarsest grid spacing of $0.25\mu^{\frac{1}{3}}$. During the evolution, levels with refinement ratio 2 : 1 were added to ensure that the apparent horizon was always covered by a minimum of 80 points. For the study of the ultraspinning instability we needed to add up to 22 levels. For the lower resolutions, we increase the grid spacing by factors of $\sqrt{2}$ and correspondingly decrease the minimum number of points across the apparent horizon. Fig. 5.16 shows the area of the apparent horizon for each resolution. Since the area is sensitive to the overall structure of the horizon, this gives an indication of the accuracy with which we can determine the properties of the outermost ring. The results clearly show convergence; even the lowest resolution run is in the convergent regime. However, since the errors for the lowest two resolutions are still rather high, all results in this chapter were obtained at the second highest resolution (solid curve in the plot).

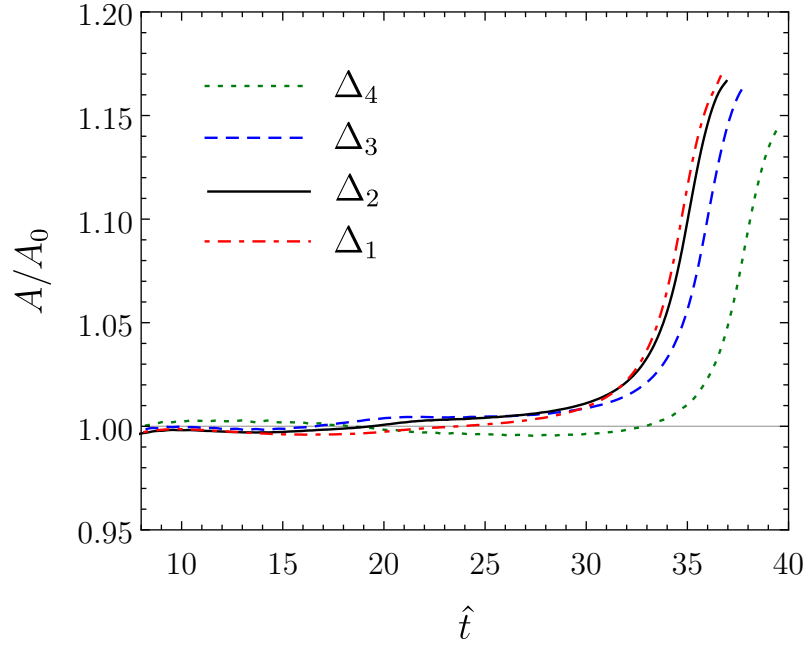


Fig. 5.16 Convergence test for the apparent horizon area. The highest resolution run had a resolution of $\Delta_1 = 0.25\mu^{\frac{1}{3}}$ on the coarsest level. For the other runs, the resolution was lowered by factors of $\sqrt{2}$. For all simulations presented in this chapter, we use resolution Δ_2 (solid black curve).

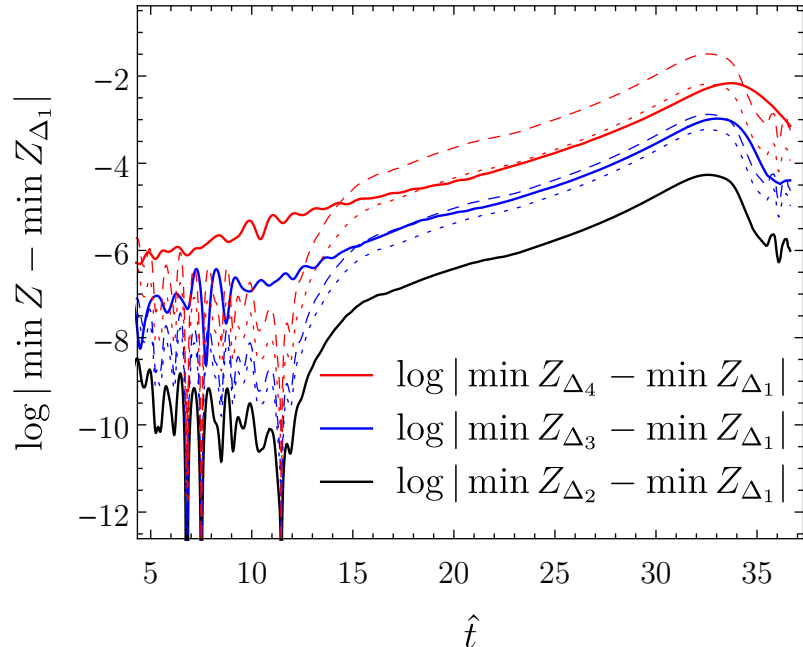


Fig. 5.17 Convergence test for the global minimum membrane thickness. Dotted and dashed lines correspond to third and fourth order convergence respectively. The resolutions Δ_i are the same as in Fig. 5.16.

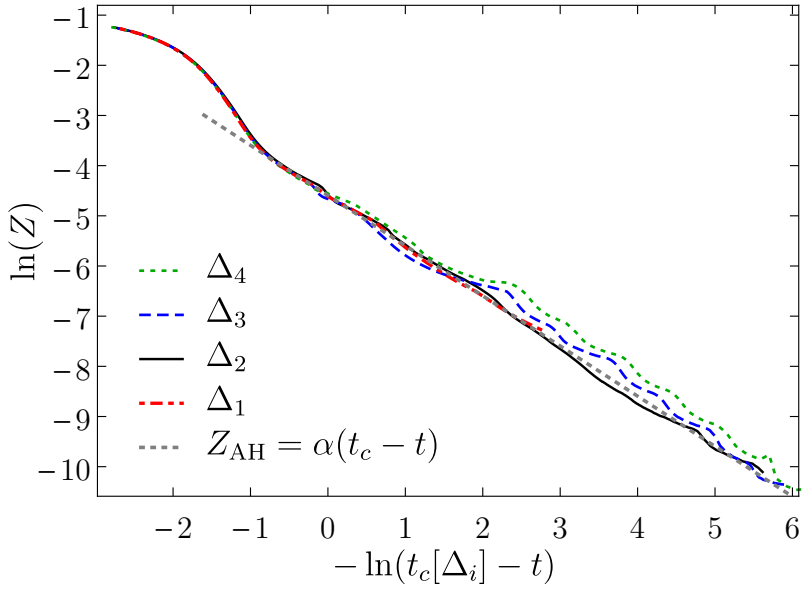


Fig. 5.18 Convergence test for the results presented in Fig. 5.12. The resolutions Δ_i are the same as in Fig. 5.16. The highest resolution run had to be terminated earlier than the others as it became unfeasible. Note that the pinch-off time, t_c , varies slightly with the resolution (it converges with 3rd order). To be able to compare the approach to pinch-off, each run was plotted with its specific value for t_c .

Fig. 5.17 shows a convergence plot for the minimum thickness of the membrane. Before the first minimum appears, we simply plot the thickness in the middle as the middle becomes the first minimum. This is representative of the accuracy with which we can track the growth rate of the instability and the subsequent evolution of the membrane. The results converge at a rate between third and fourth order throughout the whole evolution. This is consistent with the fact that we use a fourth order scheme but that the order is reduced due to the interpolation at mesh boundaries.

One of our key findings is that the global minimum thickness very closely follows the scaling law $Z_{AH} = \kappa(t_c - t)$ (Fig. 5.12). Fig. 5.18 presents the same plot for four different resolutions. Our results converge and follow the scaling law increasingly more precisely as the resolution is increased.

It is important to stress that, despite the convergence results presented above, not all features in the simulation are convergent. In particular, while we find convergence for properties of the entire black hole, the first generation and the minimum membrane thickness, the position of higher generation rings does not converge. Most prominently, as discussed in the main text, the appearance of a central bulge is not a robust feature, but depends on the initial data, the perturbation, and the grid setup.

Chapter 6

Implications for Weak Cosmic Censorship

In the previous two chapters, we have presented numerical evidence that higher dimensional, asymptotically flat black holes can pinch off. However, Ref. [88] showed that black holes cannot smoothly bifurcate. Indeed, our results suggest that the spacetime becomes singular, at least on the horizon. This does not necessarily imply that future null infinity is incomplete. As Fig. 6.1 illustrates, it is possible to capture all known results on the GL instability of black strings, black rings, and Myers-Perry black holes in a Penrose diagram that does not violate Weak Cosmic Censorship. In particular, the spacetime depicted in Fig. 6.1 is strongly asymptotically predictable, the singularity is not naked, and future null infinity is complete. It is important to stress that this is only an illustration that this is possible; even for the simplest setting, a pinching black string, the diagram would have to be more complicated since we could not neglect the compact direction of the black string, whose translational symmetry is broken by the GL instability. Unfortunately, our numerical study could not determine whether future null infinity is complete since the latter was not part of the numerical domain and since we could not evolve past the time when constant- t slices intersect the physical singularity that forms on the horizon. Further work with very different numerical or analytic methods will be required to answer this question.

The above argument shows that it is plausible that the GL instability does not cause future null infinity to be incomplete. As a result, to the best of our knowledge, no confirmed candidates for counterexamples to the Weak Cosmic Censorship Conjecture in its mathematical form [59–61] have been found, not even in higher dimensions, with compact extra dimensions, or in AdS spacetimes. Unfortunately, the literature on potential violations of the Weak Cosmic

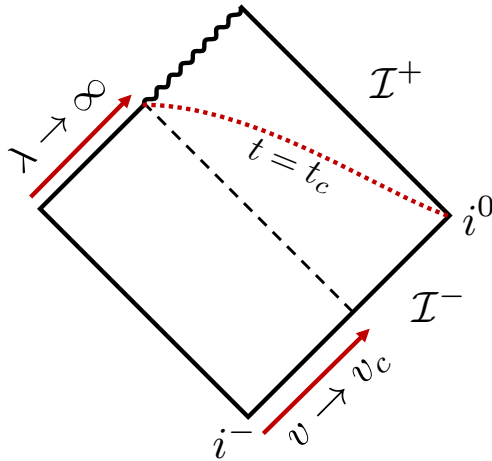


Fig. 6.1 Example of a spacetime that exhibits a behaviour compatible with the results for the GL instability: a singularity forms on the horizon after infinite affine parameter on the horizon [100], but at finite asymptotic time [74, 103, 33]. Future null infinity is complete so that the Weak Cosmic Censorship Conjecture is not violated. The line $t = t_c$ represents the last constant-time slice our numerical simulations would be able to reach for this spacetime. This is only an illustration: for the black string, the compact direction cannot be neglected since the translational symmetry is broken by the GL instability.

Censorship Conjecture [33, 75, 3, 2, 63, 64] is not very clear on the distinction between counterexamples to the conjecture and situations where quantum gravity effects generically arise outside of black holes.¹ This is undesirable since imprecise statements that the Weak Cosmic Censorship Conjecture may be violated cloud the truly remarkable fact that despite intense efforts, no clear counterexample has been found to date.

Having said this, situations in which quantum gravity effects arise outside of black holes should not be dismissed only because future null infinity may remain complete: if general relativity no longer applies, its predictions on the completeness of future null infinity are physically irrelevant. Our detailed study of the approach to pinch-off in the previous chapter shows that the Kretschmann scalar just outside the horizon becomes arbitrarily large as black rings or Myers-Perry black holes pinch off due to their instabilities. This is an indication that in a generic setting quantum gravity effects can become important outside of black holes in higher dimensions, even in asymptotically flat spacetimes. While there is evidence that the same can happen in 4D AdS spacetimes [63, 64], to the best of our knowledge no situation in 4D asymptotically flat spacetimes is known in which quantum gravity effects become important outside of black holes without any need for fine-tuning.

¹This includes the author's own work.

An interesting question that should be explored further is what the precise meaning of the word “generic” in the Weak Cosmic Censorship Conjecture should be. All the results presented in this thesis should hold in an open set of initial data, but they all consider perturbations around an unstable black hole spacetime. It is currently unclear whether these black holes can form from the gravitational collapse of initial data that contain no trapped surfaces. If they cannot, it could be argued that they are not “generic”. We are currently working on numerical simulations that address this issue. In AdS, it is likely that the Weak Cosmic Censorship Conjecture will have to be augmented with restrictions that ensure that the boundary conditions are “generic” and “reasonable”, although at this point it is unclear what these restrictions should be.

In conclusion, given the evidence that is currently available to us, it is conceivable that the Weak Cosmic Censorship Conjecture holds, even in higher dimensions, and that in $4D$ asymptotically flat spacetimes (but not in $D > 4$ or AdS) it may be possible to formulate a stronger conjecture which posits that quantum gravity effects cannot generically arise outside of black holes. Both would be truly remarkable properties of our theory of gravity.

6.1 Bifurcation process

Even though describing the bifurcation process of a black hole would likely require a theory of quantum gravity, we can make a few concrete speculations about it based on our results. Currently, the only known mechanism by which black holes can bifurcate is the GL instability. Even in settings where no GL-type instability is present in the unperturbed black hole, such as $6D$ Myers-Perry black holes with $a = 1.5\mu^{\frac{1}{3}}$, the pinch-off happens due to a secondary GL instability that is made possible by the extreme horizon shapes caused by the primary instability. Independently of the initial conditions, we find that the pinch-off of the horizon is approached with the same scaling law that was found for black strings [33, 75],

$$r_{\text{AH}} = \kappa(t_c - t), \quad (6.1)$$

where r_{AH} is the thickness of the apparent horizon, t_c is the pinch-off time, and κ is a constant, which unfortunately is not slicing-independent. Therefore, our results indicate that the pinch-off is an attractor solution and always happens in exactly the same way.

Since the quantum gravity regime would only enter in a tiny region and with a completely negligible energy, it is unlikely to affect the overall evolution of the spacetime. This behaviour would be similar to the Rayleigh-Plateau instability of fluid columns [177, 178]: the process

of a fluid column pinching off can only be described by molecular dynamics, but the details of how this happens do not affect the large-scale behaviour. If this speculation is true, then an observation of a pinching black hole may not provide much information about the details of quantum gravity.

Chapter 7

Numerical simulations in AdS

This chapter presents our numerical results on non-axisymmetric scalar field collapse in AdS space and outlines recent work to allow the simulation of asymptotically AdS spacetimes with GRCHOMBO.

This chapter is based on the co-authored publication [1]. Furthermore, it reports on unpublished work to simulate asymptotically AdS spacetimes with GRCHOMBO. I worked mainly on implementing and stabilising AdS evolution in GRCHOMBO, in collaboration with P. Figueras. Due to the difficulties with GRCHOMBO being cell-centred, this took slightly longer than expected and therefore the simulations we presented in Ref. [1] (section 7.4) were all carried out by H. Bantilan using the code he developed in Refs. [135, 136]. I helped with the data analysis, most importantly with the calculation of the energy density on the boundary, and the comparison between collapse and thermalisation time.

7.1 Introduction

In the last decade, there has been a growing interest in the numerical evolution of Einstein's equations (1.1) with negative cosmological constant. In this setting, the maximally symmetric solution is anti-de Sitter space (AdS) with metric

$$ds^2 = - \left(1 + \frac{r^2}{L^2} \right) dt^2 + \frac{dr^2}{1 + \frac{r^2}{L^2}} + r^2 d\Omega_{(D-2)}^2, \quad (7.1)$$

where the AdS length L is related to the cosmological constant by

$$L = \sqrt{\frac{(D-1)(D-2)}{2|\Lambda|}}. \quad (7.2)$$

There are two main motivations for simulations of asymptotically AdS spacetimes: firstly, numerical simulations may help elucidate mathematical questions such as the stability of AdS and other solutions with AdS asymptotics, or the weak cosmic censorship conjecture in AdS. Secondly, the AdS/CFT correspondence relates the dynamics of certain strongly coupled conformal field theories in D dimensions to the dynamics of classical gravity in $(D+1)$ -dimensional asymptotically AdS space [37–39]. Thus, the study of gravitational dynamics in AdS may help us understand the behaviour of strongly coupled quantum field theories, at least qualitatively. Currently, this is the only known way to access the far-from-equilibrium regime of quantum field theories. It could also provide a promising route to understanding phenomena such as superconductivity or fluid and superfluid turbulence [179, 180].

Evolving AdS space numerically is highly non-trivial due to its causal structure. AdS space is very different from Minkowski and de Sitter space in that it has a timelike boundary, which in the coordinates in (7.1) lies at $r = \infty$. This boundary is in causal contact with the bulk: a null ray travelling radially inwards from $r = \infty$ reaches $r = 0$ after a time $t = L\pi/2$. Thus, solving Einstein’s equations in asymptotically AdS space constitutes an initial boundary value problem; it requires not only data on the initial time slice but also boundary conditions at $r = \infty$. Imposing these boundary conditions in a numerically stable fashion is very challenging.

In this chapter, we will present the technical implementation of AdS evolution with GRCHOMBO, which is complicated by the fact that GRCHOMBO uses cell-centred grids. Furthermore, we present the results of numerical simulations of massless scalar fields, and investigate how breaking spherical symmetry affects the collapse to a black hole. These results were not obtained with GRCHOMBO, but with a code based on the one used for Refs. [135, 136].

7.1.1 Stability of AdS

The stability of AdS space has attracted intense interest recently, partly because of the AdS/CFT correspondence and partly because as the maximally symmetric solution of Einstein’s equations (1.1) with a negative cosmological constant ($\Lambda < 0$), AdS is mathematically as fundamental as Minkowski ($\Lambda = 0$) or de Sitter space ($\Lambda > 0$). The latter two have been

rigorously proven to be stable in Ref. [34] and Refs. [35, 36] respectively. Since the boundary of AdS is in causal contact with the bulk, the stability of AdS also depends on the boundary conditions. With the reflective conditions that are most commonly used in the AdS/CFT literature, Refs. [44, 45] conjectured that AdS would be non-linearly unstable to the formation of black holes.

Numerically, the stability of AdS has been investigated by studying Einstein's equations coupled to a scalar field. This makes it easy to restrict to spherical symmetry while still obtaining non-trivial dynamics. For $D \geq 4$, groundbreaking numerical results published in Ref. [41] showed that in AdS, black hole formation can occur for arbitrarily small initial amplitude of the scalar field. This is in stark contrast to the asymptotically flat setting, where there is a minimum required amplitude below which the scalar field just disperses [67, 68, 40]. In AdS, if the amplitude is not large enough for gravitational collapse to take place within one light-crossing time, the scalar field gets reflected off the boundary repeatedly and gets focused into an ever smaller region with every bounce. Eventually, after a time that is inversely proportional to the square of the initial amplitude, the scalar field collapses to a black hole.

A very remarkable pair of papers [46, 47] recently proved the instability of AdS with Einstein-null dust and an inner mirror. In this proof, the author analysed how the energy in beams of null dust increases as they get reflected off the boundary and the inner mirror repeatedly. Eventually, the energy is high enough to lead to the formation of a black hole.

Even though all the evidence outlined above indicates that AdS generically exhibits a turbulent instability that leads to the formation of black holes, there are open sets of initial perturbations away from AdS, which do not lead to an instability [181–183]. It should also be mentioned that there are several other asymptotically AdS solutions whose stability is currently under investigation, for example Schwarzschild-AdS, and more generally Kerr-AdS.

Beyond spherical symmetry, little is known about the non-linear instability of AdS. The studies to date [184–188] have been perturbative, and therefore could not address the nonlinear regime of the instability and in particular the formation of black holes. In this chapter, we present the first fully non-linear study of gravitational collapse in AdS beyond spherical symmetry. In particular, we use numerical relativity to investigate whether breaking spherical symmetry facilitates or impedes gravitational collapse.

7.2 Numerical methods in AdS

There are currently two competing methods for time evolution in asymptotically AdS spacetimes, the characteristic formulation and GHGs (section 1.3.4). The first-ever evolutions in AdS were achieved with the characteristic formulation [189, 190]. In this approach, a metric ansatz is made which slices the spacetime into ingoing null hypersurfaces. Einstein's equations can then be reduced to evolution equations along ingoing null slices, which can be integrated inwards starting from the AdS boundary and using the boundary data as initial conditions. If done correctly, this step only involves the integration of several ordinary differential equations and is therefore rather cheap computationally. A very detailed explanation of this procedure is presented in Ref. [191].

The other method of evolving AdS that is currently available is based on the GHC formalism with constraint damping (section 1.3.4). Stable evolution of asymptotically AdS spacetimes with GHGs was first achieved in Ref. [135]. Since this is the method which we use for our work, we present it in a little more detail here. Ref. [135] writes the metric of AdS space in the form (7.1) but with a compactified AdS radial coordinate ρ defined through

$$r = \frac{\rho}{1 - \rho/L}. \quad (7.3)$$

This brings the boundary of AdS to finite radius $\rho = L$, so that it can be part of the numerical domain. Ref. [135] proceeds by splitting the metric of an asymptotically AdS spacetime into a pure AdS background and a deviation as

$$g_{\mu\nu} = g_{\mu\nu}^{\text{AdS}} + h_{\mu\nu}, \quad (7.4)$$

where the deviation $h_{\mu\nu}$ need not be small but must vanish at the boundary. The boundary conditions on $h_{\mu\nu}$ can be obtained by requiring that the metric is asymptotically invariant under the symmetry group of AdS, i.e. that $\mathcal{L}_\xi g_{\mu\nu} = O(h_{\mu\nu})$, where ξ are the generators of the symmetry. Refs. [135, 192] show that this fixes the decay of $h_{\mu\nu}$ towards the boundary to be

$$h_{\mu\nu} = q^{p_{\mu\nu}} (1 + O(q)), \quad (7.5)$$

where $q = L - \rho$ and the exponents $p_{\mu\nu}$ are

$$p_{\rho\rho} = D - 3, \quad p_{\rho\mu \neq \rho} = D - 2, \quad \text{and} \quad p_{\mu \neq \rho \nu \neq \rho} = D - 3. \quad (7.6)$$

In Ref. [135], the authors enforce these fall-offs by defining a rescaled metric $\bar{h}_{\mu\nu} = q^{-p_{\mu\nu}+1}h_{\mu\nu}$ and enforcing the Dirichlet boundary conditions $\bar{h}_{\mu\nu} = 0$ at the AdS boundary. This suppresses all terms whose order is lower than $O(q)$ close to the boundary so that when the rescaling is undone, $h_{\mu\nu}$ satisfies (7.5). An analogous approach can be used to ensure regularity at the origin, $\rho = 0$, by factoring out appropriate powers of ρ .

To form a consistent evolution system, it is essential that the GHC source functions H^μ are compatible with the fall-off of metric components. Substituting (7.5) into the definition of the source functions (1.40), we find the necessary fall-offs for H^μ . Similarly to the boundary conditions for metric components, these are enforced by imposing Dirichlet conditions for the rescaled source functions.

So far, the majority of numerical work in AdS has used the characteristic evolution scheme due to its simplicity and the natural way in which the AdS boundary conditions are incorporated in the evolution. However, it has several downsides compared to GHCs: firstly, the characteristic formulation cannot handle pure, global AdS since it would lead to caustics at the origin. More concretely, the characteristic evolution scheme proposed in Refs. [189, 190] requires a horizon on the infrared side of the ingoing null hypersurfaces. With GHCs, there are no such restrictions so that it is possible to simulate global AdS. As we will see in section 7.4, one can even avoid problems with the coordinate singularity at the origin by choosing Cartesian coordinates.

Secondly, the experience from asymptotically flat spacetimes shows that characteristic slicing is prone to the formation of caustics when simulating binary black hole spacetimes. In the numerical work so far this has not been a major issue [191], but it may become more problematic in more general settings, for example for simulations of black hole collisions in AdS and when symmetry assumptions are relaxed. Finally, while the simplicity of the equations makes it easy to use spectral methods, which can give higher accuracy than finite difference stencils at lower computational cost, the integration along ingoing null slices is hard to parallelise. As a result, it is much harder to run the characteristic formulation for AdS on supercomputers at large scale.

To date, no stable evolution of asymptotically AdS spacetimes has been achieved with algorithms based on BSSN. However, there is no a-priori reason for why it should not be possible to achieve stable evolution with CCZ4 by replicating the steps that were necessary for GHCs. Since singularity-avoiding gauges are known for CCZ4, this would greatly simplify black hole simulations by eliminating the need for excision.

	$-\frac{9}{2}\Delta x$	$-\frac{7}{2}\Delta x$	$-\frac{5}{2}\Delta x$	$-\frac{3}{2}\Delta x$	$-\frac{1}{2}\Delta x$	Boundary
$-\frac{1}{2}\Delta x$		$-\frac{1}{21}$	$\frac{3}{10}$	-1	$-\frac{1}{6}$	$\frac{32}{35}$
$-\frac{3}{2}\Delta x$		$\frac{1}{14}$	$-\frac{3}{5}$	$-\frac{1}{6}$	1	$-\frac{32}{105}$
$-\frac{5}{2}\Delta x$	$\frac{1}{12}$	$-\frac{2}{3}$	0	$\frac{2}{3}$	$-\frac{1}{12}$	

Table 7.1 Fourth order first derivative stencils with Dirichlet boundary condition for a cell-centred code. The leftmost column shows the evaluation location, the columns are labelled by the distance to the boundary at which the weight is applied.

7.3 Asymptotically AdS spacetimes in GRCHOMBO

For studies of turbulent behaviour in asymptotically AdS spacetimes, the flexible adaptive mesh refinement offered by GRCHOMBO would be very beneficial. For this reason, we have started implementing AdS evolutions in GRCHOMBO. So far, we have implemented the GHC-based method outlined in the previous section. This is not entirely trivial since GRCHOMBO is cell-centred so that there is no grid point at the boundary. In this section, we briefly sketch how the Dirichlet conditions required at the AdS boundary can be enforced stably in a cell-centred code.

In a cell-centred code, no grid point lies at the AdS boundary. In this setting, an easy way of enforcing a Dirichlet boundary condition is to use adapted stencils close to the boundary which have an inhomogeneous step size and include the boundary value. Tab. 7.1 shows an example for the derivative stencils which can be used to enforce a Dirichlet boundary condition. GRCHOMBO is written in a way which makes the process of choosing different stencils for specific regions of the domain simple and efficient.

In order to stabilise the evolution close to the boundary, it is essential to add sufficient Kreiss-Oliger dissipation. This is not trivial: the standard choice of a second order sixth derivative stencil fails to damp high frequency modes close to the boundary. Even worse, it can be shown [193, 194] that the resulting dissipation operator is positive definite, and therefore causes numerical errors to grow exponentially. To solve this problem, we follow the calculation in Refs. [193–195] in order to construct positive definite boundary stencils. Unfortunately, to achieve non-zero dissipation at the grid point closest to the boundary, the order of the derivative approximation at this grid point has to be decreased. This is not necessarily a problem as the error at this grid point will likely only dominate at a much higher resolution than we need for accurate simulations.

With the method of enforcing boundary conditions above and the correct dissipation stencils, GRCHOMBO is able to reproduce the results for numerical evolution of a black brane in asymptotically AdS_4 . We are currently working on extending it to more general settings. In the future, we also hope to be able to adapt the CCZ4 formalism to AdS , so that no excision is required for black hole simulations. This would greatly simplify the simulation of black hole collisions in asymptotically AdS spacetimes, which are a good qualitative model for heavy ion collisions according to the gauge/gravity duality.

7.4 Non-spherically symmetric collapse

In this section, we present our results on scalar field collapse in AdS without the imposition of spherical symmetry, which be published in Ref. [1]. This allows us to elucidate how moving away from spherical symmetry affects the time it takes for the turbulent instability of AdS to form black holes.

7.4.1 Numerical Scheme

To evolve asymptotically AdS spacetimes in axisymmetry, we use the GHC evolution scheme as proposed in Ref. [135, 196] and described in the introduction to this chapter. However, instead of (7.3), we use

$$r = \frac{2\rho}{1 - \rho^2/L^2}. \quad (7.7)$$

In polar coordinates, the grid spacing decreases significantly close to the origin at $\rho = 0$. Due to the CFL condition, this would require us to take unacceptably small time steps. To avoid this problem, we perform all our simulations in Cartesian coordinates. This makes the treatment of the AdS boundary more complicated since $\rho = L$ does not necessarily lie on a grid point. However, this problem can be solved by enforcing the boundary conditions on the grid points closest to $\rho = L$ and filling the grid points immediately to the interior of the boundary points by interpolation. Since we only use second order discretisation, we can use the standard second-order finite difference stencils for all other grid points.

In $5D$, with Cartesian coordinates $x = \rho \cos \chi$ and $y = \rho \sin \chi$, and the redefinition (7.7), the AdS metric (7.1) becomes

$$ds^2 = \frac{1}{(1-\rho^2)^2} \left[-((1-\rho^2)^2 + 4\rho^2) dt^2 + 4 \left(dx^2 + dy^2 + y^2 d\Omega_{(2)}^2 \right) \right], \quad (7.8)$$

where we have set $L = 1$. In our simulations, we break spherical symmetry, but preserve the $SO(3)$ symmetry that acts in the direction of the 2-sphere represented by $d\Omega_{(2)}^2$. Our gauge source functions are chosen so that they evolve towards target source functions which are consistent with the decay of the metric components near the boundary (7.5) and decay to zero in the bulk.

To construct initial data, we specify the initial scalar field profile and solve the Hamiltonian constraint. The momentum constraint is satisfied automatically since our initial data are time-symmetric. As initial scalar field profiles, we choose bubbles with a tunable symmetry breaking term

$$\varphi(\rho, \chi) = A(1-h(\rho)) + 4Bh(\rho)(1-h(\rho)) \cos \chi, \quad (7.9)$$

where

$$h(\rho) = \begin{cases} 1 & , \rho \geq \rho_d \\ 1 - R^3(6R^2 - 15R + 10) & , \rho_d \geq \rho \geq \rho_c \\ 0 & , \text{otherwise} \end{cases}, \quad (7.10)$$

with $R(\rho) = (\rho_d - \rho)/(\rho_d - \rho_c)$ and arbitrary parameters ρ_c and ρ_d , which we typically choose to be 0.4 and 0.8 respectively. This choice of $h(\rho)$ ensures that the spatial gradients of the scalar field are only non-vanishing in the annulus $\rho_c < \rho < \rho_d$. However, our results are not sensitive to the specific choice of $f(\rho)$ and $g(\rho)$. The leftmost snapshot Fig. 7.1 (bottom) shows an example of an initial scalar field profile with $\rho_c = 0.4$, $\rho_d = 0.8$, $A = 0$, and $B = 0.0087$.

We solve Einstein's equations coupled to a massless real scalar field using the PAMR/AMRD libraries [197]. The spatial directions are discretised using second order finite difference stencils and we integrate in time using an iterative Newton-Gauss-Seidel relaxation procedure with a typical Courant factor of 0.2. Even though PAMR has AMR capabilities, we use a unigrid setup which covers the region $x \in [-1, 1]$ and $y \in [0, 1]$ with a typical number of grid points of $N_x = 1025$ and $N_y = 513$ respectively. To avoid physical singularities in the computational domain, we excise a small region inside the apparent horizon of black holes. Close to the boundary of the excision region, we use one-sided stencils, so that no boundary conditions are required at the excision boundary. While unigrid simulations do not suffer from

constraint violations that would arise at the refinement boundaries, high-frequency constraint violating modes still arise, especially close to the point where the AdS boundary intersects the $y = 0$ axis. To suppress these unphysical modes, we use Kreiss-Oliger dissipation [145] with a typical dissipation parameter of $\sigma = 0.35$.

7.4.2 Results

As expected from the results in spherical symmetry, the time evolution of the initial scalar field distribution (7.9) always leads to gravitational collapse either directly if the amplitude is large enough or after several reflections off the AdS boundary. The number of bounces and reflections that are required depends on the values of both A and B . For the spherically symmetric case ($B = 0$), the scalar field eventually collapses to a Schwarzschild black hole at the origin $\rho = 0$, in agreement with the simulations in Ref. [41]. When spherical symmetry is broken with an $l = 1$ mode, i.e. for $B > 0$, we observe the formation of two black holes at antipodal points on the x -axis. An example of this behaviour is shown in Fig. 7.1. The snapshots on the top show the normalised difference $K/K_{AdS} - 1$ between the Kretschmann scalar $K = R_{\alpha\beta\rho\sigma}R^{\alpha\beta\rho\sigma}$ and its pure AdS value. The bottom row shows the evolution of the scalar field over time. In this example, the two black holes form at $x = \pm 0.12L$. Aside from the last snapshot, which corresponds to a time shortly before collapse at $t = 9.04L$, the snapshots are taken after each bounce to emphasize the quasi-periodic nature of the evolution. With every bounce, the spatial gradients become sharper and both the scalar field amplitude and the curvature of spacetime increase.

Across the whole parameter range, we find that for a fixed total mass and radial compactness of the initial scalar field distribution, configurations that are further away from spherical symmetry require fewer bounces to collapse to black holes. We visualise this behaviour in two ways: firstly, we plot how the collapse time varies as the initial data are moved further away from spherical symmetry by increasing B (Fig. 7.2 left). In this process, A is fixed by requiring the total mass of the spacetime to remain constant. We display points for two different values for the total mass, $M = 0.021$ and $M = 0.030$. Other values of the mass show the same qualitative behaviour. The left-most points in the plot correspond to spherical symmetry, for which the scalar field collapses to a Schwarzschild black hole as found in Ref. [41]. As B is increased, the collapse time gradually decreases as fewer bounces are required for gravitational collapse. The fastest collapse time is reached for a maximal spherical symmetry breaking, i.e. $A = 0$. Furthermore, for sufficiently large B , the gravitational collapse leads to two distinct black holes first, whose distance increases as B is increased.

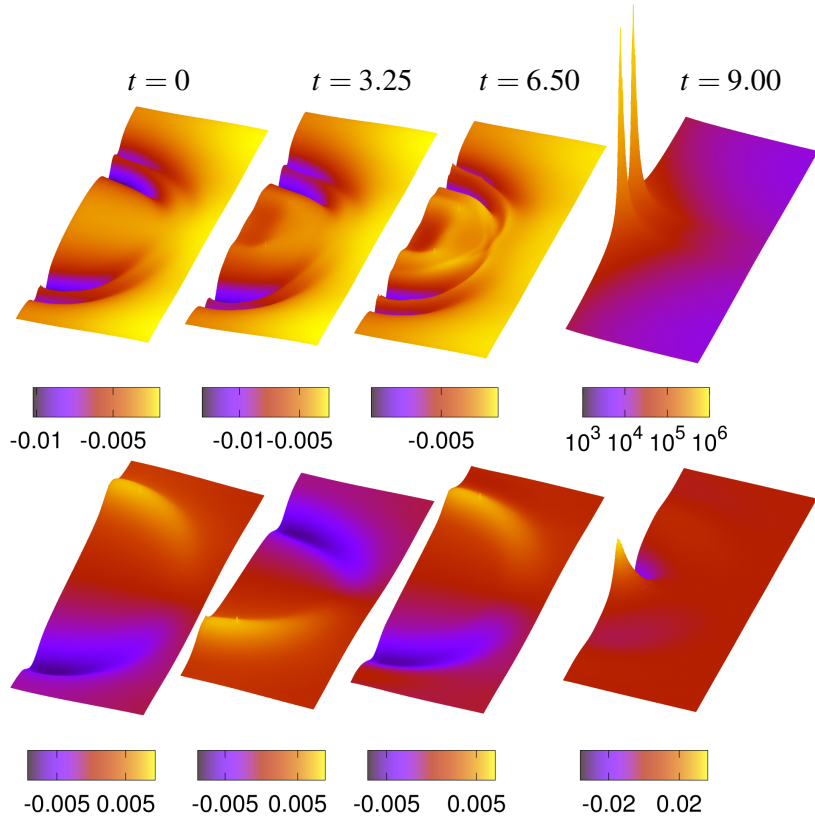


Fig. 7.1 *Top*: Snapshots of $K/K_{AdS} - 1$ from the evolution of a non-spherically symmetric scalar field collapse with multiple bounces. The initial amplitudes were $A = 0$ and $B = 0.0087$, and the total mass was $M = 0.021$ in units of L^2 . An apparent horizon forms at $t = 9.04L$. *Bottom*: Snapshots of the scalar field profile for the same evolution.

Secondly, for a given deformation B away from spherical symmetry, we plot the maximum total mass the spacetime can have while still taking a fixed number of bounces to collapse. If the mass were increased beyond this maximum value, gravitational collapse would happen with one fewer bounce. In practice, we determine this value by fixing A and increasing B , and thus the total mass, until the collapse time decreases by πL . Our results show that as B is increased, less mass is required for collapse to occur in a given time implying that perturbations away from spherical symmetry facilitate gravitational collapse.

For asymptotically flat spacetimes with spherical symmetry, Ref. [68] derived a condition on the strength of curvature deformation, which guarantees that the scalar field will collapse to a black hole. This condition can be generalised to AdS [198], where it can be used to give an indication for when black hole formation will occur without further bounces. The condition

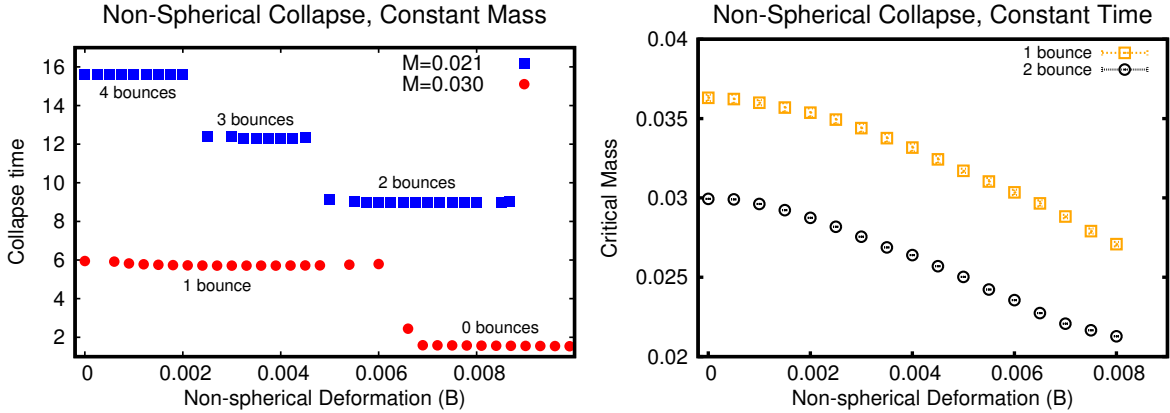


Fig. 7.2 *Left*: Collapse time versus deformation amplitude B away from spherical symmetry at constant total mass $M = 0.021$ (blue squares) and $M = 0.030$ (red circles). Configurations with stronger symmetry breaking undergo gravitational collapse faster. The collapse time is a decreasing, discontinuous function of the deformation amplitude. *Right*: Maximum mass for which a black hole is formed after one bounce (yellow squares) and two bounces (black circles) versus the deformation amplitude B . Configurations that are further away from spherical symmetry require less total mass to collapse in a given number of bounces.

is based on the curvature deformation away from AdS per unit volume

$$\frac{\eta}{E} \equiv \frac{\int_{\mathcal{V}} d^4x \sqrt{\det \gamma} |K/K_{AdS} - 1|}{\int_{\mathcal{V}} d^4x \sqrt{\det \gamma}}, \quad (7.11)$$

where \mathcal{V} is defined as the region where $|K/K_{AdS} - 1| > \delta$, for an arbitrary cut-off value δ , on a given time slice with intrinsic metric γ . To test the condition in our setting, we plot the behaviour of the dimensionless number η/E over time for various representative cases with different collapse times. Fig. 7.3 shows the results. With every bounce of the scalar field, η/E undergoes an oscillation, but once η/E exceeds roughly unity, gravitational collapse happens within the next bounce. These results are robust under changes of δ , although the critical value of η/E above which collapse will take place within one bounce changes.

Let us now consider what non-spherical symmetric collapse of a scalar field implies for the dual CFT. Fig. 7.4 depicts the same evolution as in Fig. 7.1 but now in terms of the energy density of the dual CFT on the boundary S^3 . This was extracted using the procedure proposed in Ref. [199]. With every bounce, the energy density becomes more and more localised at the poles of the S^3 , corresponding to the formation of black holes on the x -axis. On the CFT side, the collapse of a scalar field to a black hole corresponds to the thermalisation of the CFT. In our non-spherically symmetric setting, the thermalisation is finished once the two black holes that form on the axis have merged into a single Schwarzschild-AdS black hole at

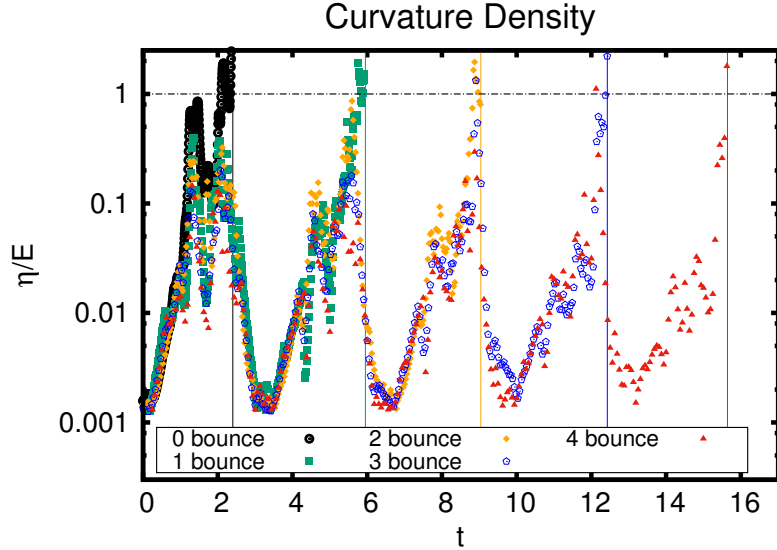


Fig. 7.3 The dimensionless ratio η/E defined in (7.11) for various representative cases that collapse after between zero and four bounces. The ratio η/E begins to exceed unity within a bounce prior to the formation of a trapped surface. The collapse time for each case is indicated by a vertical line.

the origin. However, the discrepancy between the thermalisation time and the collapse time cannot be large enough to change our conclusion that breaking spherical symmetry speeds up the collapse and the thermalisation. To show this, note that the time it takes for a particle in AdS to drop from rest at any point in the bulk to the origin is given by $L\pi/2$. Since the black holes that form from the collapse of the scalar field are well approximated by point particles in AdS (their radius is much smaller than L), this gives a good upper bound on the merger time. Any gravitational interaction between the two black holes can only speed up the merger and thus the thermalisation. Once the black holes have coalesced, the ring down to a Schwarzschild-AdS solution is exponentially fast and, therefore, negligible. Since the upper bound of $L\pi/2$ is only half the time of one bounce, the discrepancy between collapse time and thermalisation time is not large enough to affect the result in Fig. 7.1 significantly.

A potential caveat to the conclusion about the thermalisation of the CFT is that Schwarzschild-AdS has been conjectured to be dynamically unstable for generic perturbations in Ref. [200]¹. As a result, it is possible that the Schwarzschild-AdS black hole that forms from gravitational collapse is only a meta-stable state and that further evolution will take place, implying that the dual CFT may not thermalise at all.

¹However, Ref. [181] argued that Schwarzschild-AdS should remain stable for a long time for sufficiently regular perturbations.

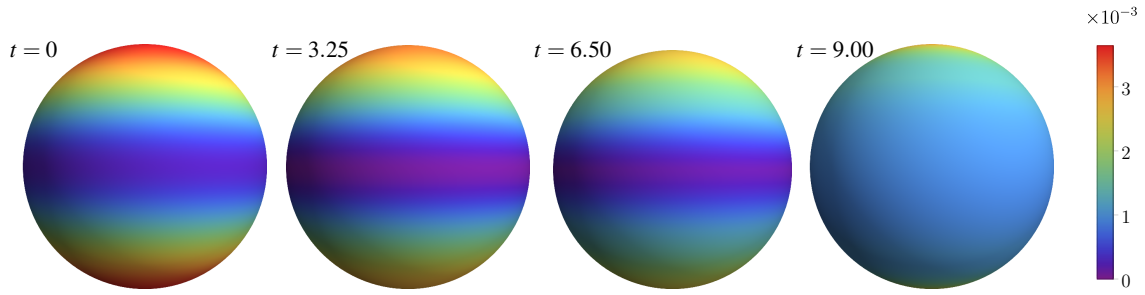


Fig. 7.4 Snapshots of the energy density on the boundary of global AdS at different global times t for the simulation shown in Fig. 7.1. Initially, the energy density is peaked at the poles. Subsequently, it oscillates back and forth between the poles and the equator in a quasi-periodic fashion. Gravitational collapse corresponds to a localisation of the energy density at the poles.

7.4.3 Discussion

We have presented the first study of gravitational collapse of a massless scalar field in AdS with inhomogeneous deformations away from spherical symmetry. Our results exhibit a similar behaviour as was observed for the first time in Ref. [41]: gravitational collapse takes place for arbitrarily small initial amplitudes of the scalar field through repeated reflections off the boundary, which gradually cause the scalar field to become more and more focused. We find that breaking the spherical symmetry *facilitates* the gravitational collapse: for a fixed total mass and radial compactness, breaking spherical symmetry reduces the number of bounces that are required for gravitational collapse to occur and therefore decreases the collapse time. Similarly, the more the spherical symmetry is broken, the less mass is required to achieve gravitational collapse in a given time.

This behaviour is intuitive, since for a fixed radial compactness and mass, breaking the spherical symmetry leads to stronger gradients. However, it was far from clear whether this intuition would remain correct in the non-linear regime after several reflections off the AdS boundary. Our results may also have consequences for the specific sets of asymptotically AdS initial data which are non-linearly stable [181–183]. Since breaking spherical symmetry facilitates gravitational collapse, it is likely that these “islands of stability” become smaller as the deviation away from spherical symmetry is increased.

In this initial study, we have broken spherical symmetry with an $l = 1$ mode while preserving an $SO(3)$ symmetry in five dimensions. In this setting, we found that two black holes form on the x -axis. If the restrictions on the symmetry and initial data were relaxed further, these black holes would generically form away from the axis and the number of black holes that form may change. We have begun to extend our results to higher harmonics and found

that under perturbations with higher harmonics the collapse happens faster. Further work in this direction is ongoing. A straightforward extension of our work would be to consider spacetimes with non-zero total angular momentum. This would entail solving the Momentum constraint alongside the Hamiltonian constraint to construct initial data, as the initial data would no longer be time-symmetric. Currently, there are conflicting results on the effect of angular momentum on the non-linear instability of AdS. Using perturbation theory, the authors of Ref. [188] argue that angular momentum enhances the instability, while Ref. [201] finds examples in which the inclusion of angular momentum delays the collapse of a scalar field.

As we noted in the previous section, it is not clear whether Schwarzschild-AdS, or more generally Kerr-AdS, are non-linearly stable. As a result, general perturbations away from AdS may not settle down to a black hole and the dual CFT may not thermalise. Considerably longer numerical evolutions, and ultimately a rigorous mathematical study will be required to address this question.

7.4.4 Appendix: Convergence tests

To ascertain whether our numerical results indeed converge with second order, the order of our finite difference stencils, we calculate the convergence factor

$$Q(t, x, y) = \frac{1}{\ln(2)} \ln \left(\frac{f_{4h}(t, x, y) - f_{2h}(t, x, y)}{f_{2h}(t, x, y) - f_h(t, x, y)} \right), \quad (7.12)$$

where f_h represents an evolution variable obtained at mesh spacing h . Fig. 7.5 (top) shows the L^2 norm of Q calculated for \bar{g}_{xx} . The results converge at second order with a small decrease in convergence rate in the most dynamical stages of the evolution.

To check whether our numerical simulation solves Einstein's equations in the continuum limit, we repeat the same process for the residual $f_h^E = G_{\mu\nu} + \Lambda g_{\mu\nu} - 8\pi T_{\mu\nu}$ calculated at grid spacing h . Fig. 7.5 (bottom) shows the results for the convergence factor

$$Q_{EFE}(t, x^i) = \frac{1}{\ln(2)} \ln \left(\frac{f_{2h}^E(t, x^i)}{f_h^E(t, x^i)} \right), \quad (7.13)$$

which checks second order convergence for a quantity that should be zero in the continuum limit.

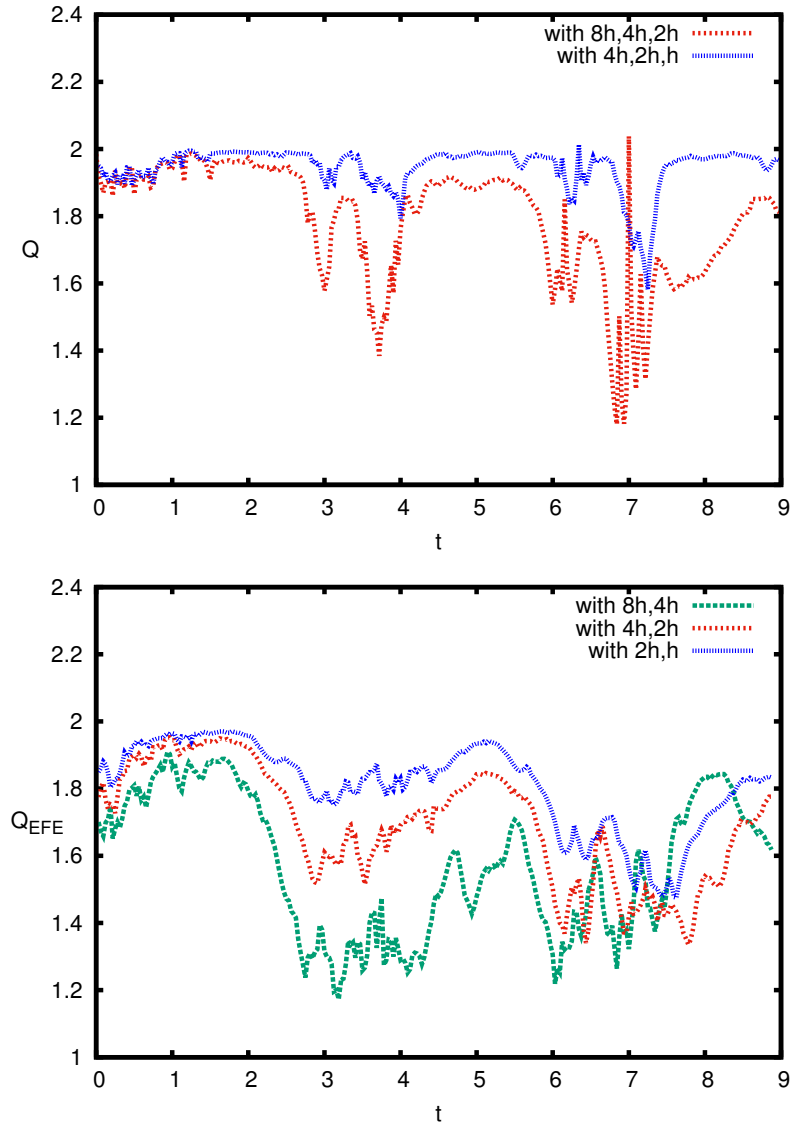


Fig. 7.5 *Top*: Convergence factors for \bar{g}_{xx} for the simulation shown in Fig. 7.1. *Bottom*: Convergence factors for the independent residual from the same simulation. In both cases, the L^2 norm of the convergence factors is taken over the entire grid.

Chapter 8

Summary

In this thesis, we used numerical relativity simulations to examine instabilities in general relativity in a fully non-linear setting. In $5D$ asymptotically flat spacetimes, we have simulated all known vacuum, singly-spinning, single black hole solutions. For very fat black rings [55], the previously known radial instability [28, 29] dominates the evolution and causes the black ring to collapse to a Myers-Perry black hole, changing its topology from toroidal to spherical, with the spacetime remaining smooth throughout. For intermediate rings, we have discovered a new axisymmetry-breaking instability, an elastic instability that stretches the ring and causes it to collapse to a Myers-Perry black hole. For very thin rings, the GL instability [72, 30] dominates and we have presented evidence that it causes the horizon of the black ring to pinch off into black holes of spherical topology. For Myers-Perry black holes [96] in $5D$, our results show no signs of a non-linear instability in the parameter range we investigated ($a \leq 0.89\sqrt{\mu}$), contrary to the findings of Ref. [25].

In six dimensions, we have conducted a fully non-linear numerical investigation of axisymmetric instabilities of Myers-Perry black holes with $a \leq 2.0\mu^{\frac{1}{3}}$ and non-axisymmetric instabilities in the range $a \leq 1.5\mu^{\frac{1}{3}}$. In the axisymmetric sector, the “ring-shaped” mode of the ultraspinning instability [23, 172] dominates in the entire parameter range we examined, even though a “Saturn-shaped” mode is also known to become unstable in this regime [172]. Our numerical results suggest that the black hole pinches off and that the minimum thickness, Z_{AH} , closely follows a scaling law $Z_{AH} \propto (t - t_c)$, where t_c is the pinch-off time. It would be very interesting to find a slicing-independent statement of this scaling law and to study it analytically using methods similar to those of Refs. [177, 178]. In the non-axisymmetric sector, the $m = 2$ “bar-mode” instability [26, 27] dominates for $a \lesssim 1.3\mu^{\frac{1}{3}}$. The black hole becomes very elongated, and radiates mass and angular momentum until it can settle down

again. For $a \gtrsim 1.5\mu^{\frac{1}{3}}$, higher m modes dominate and we have presented evidence that they cause the outer parts of the horizon to separate from the central portion of the black hole.

The results of our investigation of both $5D$ black rings and $6D$ Myers-Perry black holes suggest that in higher dimensions black holes can pinch off, even in a generic, asymptotically flat setting. In this process, curvature scalars in the causal past of future null infinity become arbitrarily large and quantum gravity effects may not be “censored” from far-away observers. In our work, we always started with initial data in the vicinity of an unstable black hole. For the genericity of our conclusions, it would be important to check whether at least some of these black holes can be formed from the gravitational collapse of initial data with no trapped surfaces. Work in this direction is underway. Since our numerical study could not determine whether future null infinity remains complete, we could not draw any conclusions about the Weak Cosmic Censorship Conjecture in its mathematical form [59–61]. Very different numerical techniques or analytic methods will be required to study this.

In asymptotically AdS spacetimes, we have investigated how breaking spherical symmetry affects the collapse of a scalar field. We found that scalar field profiles that are further away from spherical symmetry require fewer reflections off the AdS boundary to collapse. These results suggest that breaking spherical symmetry accelerates the instability of $5D$ AdS space.

To enable these simulations, and many others in related fields such as cosmology or astrophysics, we have developed the new open-source general relativity code GRCHOMBO. The very flexible adaptive mesh refinement of GRCHOMBO makes it ideal for simulations of instabilities, where new length scales can be created dynamically in regions of arbitrary shape and topology. In this thesis, we presented the design of GRCHOMBO in detail, demonstrated its accuracy, and analysed its strong and weak scaling on Intel Xeon and Intel Xeon Phi clusters.

Finally, we presented the changes we made to current numerical relativity methods to be able to simulate higher-dimensional black holes stably and efficiently. This includes adapted gauge conditions, a new singularity treatment, and the extension of the modified Cartoon method to CCZ4 with $SO(N)$ symmetry. One of the most important avenues for further research on numerical methods would be to try to find a new singularity treatment for GHGs that does not rely on excision. This would greatly reduce the complexity of numerical relativity codes.



References

- [1] H. Bantilan, P. Figueras, M. Kunesch, and P. Romatschke, *Phys. Rev. Lett.* **119**, 191103 (2017), 1706.04199.
- [2] P. Figueras, M. Kunesch, L. Lehner, and S. Tunyasuvunakool, *Phys. Rev. Lett.* **118**, 151103 (2017), 1702.01755.
- [3] P. Figueras, M. Kunesch, and S. Tunyasuvunakool, *Phys. Rev. Lett.* **116**, 071102 (2016), 1512.04532.
- [4] W. G. Cook, P. Figueras, M. Kunesch, U. Sperhake, and S. Tunyasuvunakool, *Int. J. Mod. Phys. D* **25**, 1641013 (2016), 1603.00362.
- [5] K. Clough *et al.*, *Class. Quant. Grav.* **32**, 245011 (2015), 1503.03436, [*Class. Quant. Grav.* **32**, 24 (2015)].
- [6] C. M. Will, *Living Rev. Rel.* **17**, 4 (2014), 1403.7377.
- [7] Virgo, LIGO Scientific, B. P. Abbott *et al.*, *Phys. Rev. Lett.* **116**, 061102 (2016), 1602.03837.
- [8] Virgo, LIGO Scientific, B. P. Abbott *et al.*, *Phys. Rev. Lett.* **116**, 241102 (2016), 1602.03840.
- [9] Virgo, LIGO Scientific, B. P. Abbott *et al.*, *Phys. Rev. Lett.* **116**, 241103 (2016), 1606.04855.
- [10] VIRGO, LIGO Scientific, B. P. Abbott *et al.*, *Phys. Rev. Lett.* **118**, 221101 (2017), 1706.01812.
- [11] Virgo, LIGO Scientific, B. P. Abbott *et al.*, *Phys. Rev. Lett.* **119**, 141101 (2017), 1709.09660.
- [12] Virgo, LIGO Scientific, B. Abbott *et al.*, *Phys. Rev. Lett.* **119**, 161101 (2017), 1710.05832.
- [13] Virgo, LIGO Scientific, B. P. Abbott *et al.*, *Astrophys. J.* **851**, L35 (2017), 1711.05578.
- [14] R. P. Kerr, *Phys. Rev. Lett.* **11**, 237 (1963).
- [15] B. F. Whiting, *J. Math. Phys.* **30**, 1301 (1989).

- [16] M. Dafermos and I. Rodnianski, (2010), 1010.5132.
- [17] M. Dafermos, I. Rodnianski, and Y. Shlapentokh-Rothman, (2014), 1402.7034.
- [18] M. Dafermos, I. Rodnianski, and Y. Shlapentokh-Rothman, (2014), 1412.8379.
- [19] S. Aretakis, Phys. Rev. **D87**, 084052 (2013), 1304.4616.
- [20] H. Yang, A. Zimmerman, and L. Lehner, Phys. Rev. Lett. **114**, 081101 (2015), 1402.4859.
- [21] S. E. Gralla, A. Zimmerman, and P. Zimmerman, Phys. Rev. **D94**, 084017 (2016), 1608.04739.
- [22] R. Gregory and R. Laflamme, Phys. Rev. Lett. **70**, 2837 (1993), hep-th/9301052.
- [23] R. Emparan and R. C. Myers, JHEP **09**, 025 (2003), hep-th/0308056.
- [24] O. J. C. Dias, P. Figueras, R. Monteiro, J. E. Santos, and R. Emparan, Phys. Rev. **D80**, 111701 (2009), 0907.2248.
- [25] M. Shibata and H. Yoshino, Phys. Rev. **D81**, 021501 (2010), 0912.3606.
- [26] M. Shibata and H. Yoshino, Phys. Rev. **D81**, 104035 (2010), 1004.4970.
- [27] O. J. C. Dias, G. S. Hartnett, and J. E. Santos, Class. Quant. Grav. **31**, 245011 (2014), 1402.7047.
- [28] H. Elvang, R. Emparan, and A. Virmani, JHEP **12**, 074 (2006), hep-th/0608076.
- [29] P. Figueras, K. Murata, and H. S. Reall, Class. Quant. Grav. **28**, 225030 (2011), 1107.5785.
- [30] J. E. Santos and B. Way, Phys. Rev. Lett. **114**, 221101 (2015), 1503.00721.
- [31] K. Tanabe, JHEP **02**, 151 (2016), 1510.02200.
- [32] K. Tanabe, (2016), 1605.08116.
- [33] L. Lehner and F. Pretorius, Phys. Rev. Lett. **105**, 101102 (2010), 1006.5960.
- [34] D. Christodoulou and S. Klainerman, The Global nonlinear stability of the Minkowski space, 1993.
- [35] H. Friedrich, Communications in Mathematical Physics **107**, 587 (1986).
- [36] H. Friedrich, Journal of Geometry and Physics **17**, 125 (1995).
- [37] J. M. Maldacena, Int. J. Theor. Phys. **38**, 1113 (1999), hep-th/9711200, [Adv. Theor. Math. Phys.2,231(1998)].
- [38] S. S. Gubser, I. R. Klebanov, and A. M. Polyakov, Phys. Lett. **B428**, 105 (1998), hep-th/9802109.

- [39] E. Witten, *Adv. Theor. Math. Phys.* **2**, 253 (1998), hep-th/9802150.
- [40] M. W. Choptuik, *Phys. Rev. Lett.* **70**, 9 (1993).
- [41] P. Bizon and A. Rostworowski, *Phys. Rev. Lett.* **107**, 031102 (2011), 1104.3702.
- [42] S. L. Liebling, *Phys. Rev.* **D87**, 081501 (2013), 1212.6970.
- [43] A. Buchel, L. Lehner, and S. L. Liebling, *Phys. Rev.* **D86**, 123011 (2012), 1210.0890.
- [44] M. Dafermos and G. Holzegel, unpublished (2006).
- [45] M. Dafermos, Newton Institute, Cambridge (2006).
- [46] G. Moschidis, (2017), 1704.08681.
- [47] G. Moschidis, (2017), 1704.08685.
- [48] K. Clough and E. A. Lim, (2016), 1602.02568.
- [49] K. Clough *et al.*, *JCAP* **1709**, 025 (2017), 1608.04408.
- [50] T. Helfer *et al.*, *JCAP* **1703**, 055 (2017), 1609.04724.
- [51] K. Clough, R. Flauger, and E. A. Lim, *JCAP* **1805**, 065 (2018), 1712.07352.
- [52] T. Helfer, E. A. Lim, M. A. G. Garcia, and M. A. Amin, (2018), 1802.06733.
- [53] T. Helfer, J. C. Aurrekoetxea, and E. A. Lim, (2018), 1808.06678.
- [54] GRChombo collaboration, www.grchombo.org, 2018.
- [55] R. Emparan and H. S. Reall, *Phys. Rev. Lett.* **88**, 101101 (2002), hep-th/0110260.
- [56] Y. Choquet-Bruhat, *Acta Math.* , 141–225 (1952).
- [57] Y. Choquet-Bruhat and R. P. Geroch, *Commun. Math. Phys.* **14**, 329 (1969).
- [58] J. Sbierski, *Annales Henri Poincaré* **17**, 301 (2016), 1309.7591.
- [59] R. Penrose, *Nuovo Cimento Rivista Serie* **1** (1969).
- [60] G. T. Horowitz, *General Relativity and Gravitation* **10**, 1057 (1979).
- [61] D. Christodoulou, *Classical and Quantum Gravity* **16**, A23 (1999).
- [62] R. M. Wald, Gravitational collapse and cosmic censorship, in *Black Holes, Gravitational Radiation and the Universe: Essays in Honor of C.V. Vishveshwara*, pp. 69–85, 1997, gr-qc/9710068.
- [63] T. Crisford and J. E. Santos, *Phys. Rev. Lett.* **118**, 181101 (2017), 1702.05490.
- [64] T. Crisford, G. T. Horowitz, and J. E. Santos, (2018), 1805.06469.
- [65] P. Diener, *Class. Quant. Grav.* **20**, 4901 (2003), gr-qc/0305039.

[66] M. I. Cohen, H. P. Pfeiffer, and M. A. Scheel, *Class. Quant. Grav.* **26**, 035005 (2009), 0809.2628.

[67] D. Christodoulou, *Commun. Math. Phys.* **109**, 613 (1987).

[68] D. Christodoulou, *Commun. Pure Appl. Math.* **44**, 339 (1991).

[69] D. Christodoulou, *Annals Math.* **140**, 607 (1994).

[70] N. Deppe, L. E. Kidder, M. A. Scheel, and S. A. Teukolsky, (2018), 1802.08682.

[71] D. Christodoulou, *Commun. Math. Phys.* **93**, 171 (1984).

[72] R. Gregory and R. Laflamme, *Nucl. Phys.* **B428**, 399 (1994), hep-th/9404071.

[73] M. W. Choptuik *et al.*, *Phys. Rev.* **D68**, 044001 (2003), gr-qc/0304085.

[74] D. Garfinkle, L. Lehner, and F. Pretorius, *Phys. Rev.* **D71**, 064009 (2005), gr-qc/0412014.

[75] L. Lehner and F. Pretorius, Final state of Gregory–Laflamme instability, in *Black holes in higher dimensions*, edited by G. T. Horowitz, pp. 44–68, 2012, 1106.5184.

[76] D. Christodoulou, *Annals of Mathematics-Second Series* **149**, 183 (1999).

[77] M. Dafermos, *Commun. Pure Appl. Math.* **58**, 0445 (2005), gr-qc/0307013.

[78] M. Dafermos and I. Rodnianski, *Invent. Math.* **162**, 381 (2005), gr-qc/0309115.

[79] J. Luk and J. Sbierski, (2015), 1512.08259.

[80] J. Luk and S.-J. Oh, *Duke Math. J.* **166**, 437 (2017), 1501.04598.

[81] Y. Angelopoulos, S. Aretakis, and D. Gajic, *Adv. Math.* **323**, 529 (2018), 1612.01566.

[82] J. Luk and S.-J. Oh, (2017), 1702.05715.

[83] J. Luk and S.-J. Oh, (2017), 1702.05716.

[84] M. Dafermos and J. Luk, (2017), 1710.01722.

[85] V. Cardoso, J. L. Costa, K. Destounis, P. Hintz, and A. Jansen, *Phys. Rev. Lett.* **120**, 031103 (2018), 1711.10502.

[86] T. Kaluza, *Sitzungsberichte der Königlich Preußischen Akademie der Wissenschaften (Berlin)*, Seite p. 966-972, 966 (1921).

[87] O. Klein, *Zeitschrift für Physik* **37**, 895 (1926).

[88] S. W. Hawking and G. F. R. Ellis, *The Large Scale Structure of Space-Time* Cambridge Monographs on Mathematical Physics (Cambridge University Press, 2011).

[89] G. J. Galloway and R. Schoen, *Commun. Math. Phys.* **266**, 571 (2006), gr-qc/0509107.

- [90] G. J. Galloway, (2006), gr-qc/0608118.
- [91] H. Elvang and P. Figueras, JHEP **05**, 050 (2007), hep-th/0701035.
- [92] H. Iguchi and T. Mishima, Phys. Rev. **D75**, 064018 (2007), hep-th/0701043, [Erratum: Phys. Rev. D78, 069903(2008)].
- [93] J. Evslin and C. Krishnan, Class. Quant. Grav. **26**, 125018 (2009), 0706.1231.
- [94] K. Izumi, Prog. Theor. Phys. **119**, 757 (2008), 0712.0902.
- [95] F. R. Tangherlini, Nuovo Cim. **27**, 636 (1963).
- [96] R. C. Myers and M. J. Perry, Annals Phys. **172**, 304 (1986).
- [97] B. Kleihaus, J. Kunz, and E. Radu, Phys. Lett. **B718**, 1073 (2013), 1205.5437.
- [98] B. Kleihaus, J. Kunz, and E. Radu, Black Rings in More Than Five Dimensions, in *Proceedings, 13th Marcel Grossmann Meeting on Recent Developments in Theoretical and Experimental General Relativity, Astrophysics, and Relativistic Field Theories (MG13): Stockholm, Sweden, July 1-7, 2012*, pp. 1321–1323, 2015.
- [99] R. Emparan and H. S. Reall, Living Rev. Rel. **11**, 6 (2008), 0801.3471.
- [100] G. T. Horowitz and K. Maeda, Phys. Rev. Lett. **87**, 131301 (2001), hep-th/0105111.
- [101] T. Wiseman, Class. Quant. Grav. **20**, 1137 (2003), hep-th/0209051.
- [102] S. S. Gubser, Class. Quant. Grav. **19**, 4825 (2002), hep-th/0110193.
- [103] D. Marolf, Phys. Rev. **D71**, 127504 (2005), hep-th/0504045.
- [104] V. Cardoso and O. J. C. Dias, Phys. Rev. Lett. **96**, 181601 (2006), hep-th/0602017.
- [105] U. Sperhake, Class. Quant. Grav. **32**, 124011 (2015), 1411.3997.
- [106] F. Pretorius, Phys. Rev. Lett. **95**, 121101 (2005), gr-qc/0507014.
- [107] A. D. Rendall, *Partial differential equations in general relativity* (Oxford University Press, 2008).
- [108] C. Gundlach and J. M. Martin-Garcia, Class. Quant. Grav. **23**, S387 (2006), gr-qc/0506037.
- [109] O. Sarbach and M. Tiglio, Living Rev. Rel. **15**, 9 (2012), 1203.6443.
- [110] M. Alcubierre, *Introduction to 3+1 numerical relativity* (Oxford University Press, 2008).
- [111] M. Headrick, S. Kitchen, and T. Wiseman, Class. Quant. Grav. **27**, 035002 (2010), 0905.1822.
- [112] P. Figueras, J. Lucietti, and T. Wiseman, Class. Quant. Grav. **28**, 215018 (2011), 1104.4489.

[113] A. Adam, S. Kitchen, and T. Wiseman, *Class. Quant. Grav.* **29**, 165002 (2012), 1105.6347.

[114] P. Figueras and T. Wiseman, *Phys. Rev. Lett.* **110**, 171602 (2013), 1212.4498.

[115] T. Wiseman, Numerical construction of static and stationary black holes, in *Black holes in higher dimensions*, edited by G. T. Horowitz, pp. 233–270, 2012, 1107.5513.

[116] P. Figueras and T. Wiseman, *Class. Quant. Grav.* **34**, 145007 (2017), 1610.06178.

[117] R. L. Arnowitt, S. Deser, and C. W. Misner, *Phys. Rev.* **116**, 1322 (1959).

[118] M. Shibata and T. Nakamura, *Phys. Rev.* **D52**, 5428 (1995).

[119] T. Nakamura, K. Oohara, and Y. Kojima, *Prog. Theor. Phys. Suppl.* **90**, 1 (1987).

[120] T. W. Baumgarte and S. L. Shapiro, *Phys. Rev.* **D59**, 024007 (1999), gr-qc/9810065.

[121] C. Bona, T. Ledvinka, C. Palenzuela, and M. Zacek, *Phys. Rev.* **D67**, 104005 (2003), gr-qc/0302083.

[122] C. Gundlach, J. M. Martin-Garcia, G. Calabrese, and I. Hinder, *Class. Quant. Grav.* **22**, 3767 (2005), gr-qc/0504114.

[123] D. Alic, C. Bona-Casas, C. Bona, L. Rezzolla, and C. Palenzuela, *Phys. Rev.* **D85**, 064040 (2012), 1106.2254.

[124] D. Alic, W. Kastaun, and L. Rezzolla, *Phys. Rev.* **D88**, 064049 (2013), 1307.7391.

[125] A. Lichnerowicz, *L'intégration des équations de la gravitation relativiste et le problème des n-corps* (Gauthier-Villars, 1944).

[126] M. Alcubierre, *Class. Quant. Grav.* **20**, 607 (2003), gr-qc/0210050.

[127] C. Bona, J. Masso, E. Seidel, and J. Stela, *Phys. Rev. Lett.* **75**, 600 (1995), gr-qc/9412071.

[128] M. Hannam, S. Husa, F. Ohme, B. Bruegmann, and N. O’Murchadha, *Phys. Rev.* **D78**, 064020 (2008), 0804.0628.

[129] M. Alcubierre *et al.*, *Phys. Rev.* **D67**, 084023 (2003), gr-qc/0206072.

[130] H. Yoshino and M. Shibata, *Phys. Rev.* **D80**, 084025 (2009), 0907.2760.

[131] J. G. Baker, J. Centrella, D.-I. Choi, M. Koppitz, and J. van Meter, *Phys. Rev. Lett.* **96**, 111102 (2006), gr-qc/0511103.

[132] M. Campanelli, C. O. Lousto, P. Marronetti, and Y. Zlochower, *Phys. Rev. Lett.* **96**, 111101 (2006), gr-qc/0511048.

[133] J. D. Brown *et al.*, *Phys. Rev.* **D76**, 081503 (2007), 0707.3101.

[134] J. D. Brown, P. Diener, O. Sarbach, E. Schnetter, and M. Tiglio, *Phys. Rev.* **D79**, 044023 (2009), 0809.3533.

- [135] H. Bantilan, F. Pretorius, and S. S. Gubser, Phys. Rev. **D85**, 084038 (2012), 1201.2132.
- [136] H. Bantilan, *Numerical Simulations of Asymptotically AdS Spacetimes*, PhD thesis, Princeton U., 2013.
- [137] H. P. Pfeiffer, L. E. Kidder, M. A. Scheel, and S. A. Teukolsky, Comput. Phys. Commun. **152**, 253 (2003), gr-qc/0202096.
- [138] A. H. Mroue *et al.*, Phys. Rev. Lett. **111**, 241104 (2013), 1304.6077.
- [139] F. Löffler *et al.*, Class. Quant. Grav. **29**, 115001 (2012), 1111.3344.
- [140] L. Barack *et al.*, (2018), 1806.05195.
- [141] M. Adams *et al.*, Lawrence Berkeley National Laboratory Report No. LBNL-6616E, 2015 (unpublished).
- [142] A. Danowitz, K. Kelley, J. Mao, J. P. Stevenson, and M. Horowitz, Communications of the ACM **55**, 55 (2012).
- [143] Intel Corporation, Processor specifications, 2018, <https://ark.intel.com>.
- [144] R. Courant, K. Friedrichs, and H. Lewy, Mathematische annalen **100**, 32 (1928).
- [145] H. Kreiss, H.-O. Kreiss, and J. Oliger, *Methods for the approximate solution of time dependent problems* (International Council of Scientific Unions, World Meteorological Organization, 1973).
- [146] M. Berger and I. Rigoutsos, IEEE Transactions on Systems, Man, and Cybernetics **21**, 1278 (1991).
- [147] M. J. Berger and P. Colella, Journal of Computational Physics **82**, 64 (1989).
- [148] The HDF Group, Hierarchical Data Format, version 5, 1997-NNNN, <http://www.hdfgroup.org/HDF5/>.
- [149] M. C. Babuic *et al.*, Class. Quant. Grav. **25**, 125012 (2008), 0709.3559.
- [150] D. Vandevoorde, N. Josuttis, and D. Gregor, *C++ Templates: The Complete Guide* (Pearson Education, 2017).
- [151] T. Veldhuizen, C++ Report **7**, 26 (1995).
- [152] F. Pretorius, Class. Quant. Grav. **22**, 425 (2005), gr-qc/0407110.
- [153] W. G. Cook, U. Sperhake, E. Berti, and V. Cardoso, Phys. Rev. **D96**, 124006 (2017), 1709.10514.
- [154] M. Zilhao *et al.*, Phys. Rev. **D81**, 084052 (2010), 1001.2302.
- [155] H. Witek, *Black hole dynamics in generic spacetimes*, PhD thesis, Lisbon, CFTP, 2013, 1307.1145.

- [156] U. Sperhake, E. Berti, V. Cardoso, and F. Pretorius, Phys. Rev. Lett. **111**, 041101 (2013), 1211.6114.
- [157] J. Donea and A. Huerta, *Finite Element Methods for Flow Problems*Finite Element Methods for Flow Problems (John Wiley & Sons, 2003).
- [158] A. Lapidus, Journal of Computational Physics **2**, 154 (1967).
- [159] J. Von Neumann and R. D. Richtmyer, Journal of Applied Physics **21**, 232 (1950).
- [160] R. P. Geroch, J. Math. Phys. **12**, 918 (1971).
- [161] M. Zilhao, *New frontiers in Numerical Relativity*, PhD thesis, Aveiro U., 2012, 1301.1509.
- [162] M. Alcubierre *et al.*, Int. J. Mod. Phys. **D10**, 273 (2001), gr-qc/9908012.
- [163] S. Tunyasuvunakool, *Applications of Numerical Relativity Beyond Astrophysics*, PhD thesis, Cambridge U., 2017.
- [164] R. Emparan and H. S. Reall, Class. Quant. Grav. **23**, R169 (2006), hep-th/0608012.
- [165] R. Emparan, JHEP **03**, 064 (2004), hep-th/0402149.
- [166] H. Kodama and A. Ishibashi, Prog. Theor. Phys. **110**, 701 (2003), hep-th/0305147.
- [167] R. Emparan, T. Harmark, V. Niarchos, N. A. Obers, and M. J. Rodriguez, JHEP **10**, 110 (2007), 0708.2181.
- [168] A. A. Pomeransky and R. A. Sen'kov, (2006), hep-th/0612005.
- [169] J. L. Hovdebo and R. C. Myers, Phys. Rev. **D73**, 084013 (2006), hep-th/0601079.
- [170] R. Emparan, T. Harmark, V. Niarchos, and N. A. Obers, JHEP **03**, 063 (2010), 0910.1601.
- [171] P. Figueras and S. Tunyasuvunakool, JHEP **03**, 149 (2015), 1412.5680, [JHEP03,149(2015)].
- [172] O. J. C. Dias, P. Figueras, R. Monteiro, and J. E. Santos, Phys. Rev. **D82**, 104025 (2010), 1006.1904.
- [173] O. J. C. Dias, J. E. Santos, and B. Way, JHEP **07**, 045 (2014), 1402.6345.
- [174] R. Emparan, P. Figueras, and M. Martinez, JHEP **12**, 072 (2014), 1410.4764.
- [175] J. Thornburg, Living Rev. Rel. **10**, 3 (2007), gr-qc/0512169.
- [176] H. Elvang, R. Emparan, and P. Figueras, JHEP **05**, 056 (2007), hep-th/0702111.
- [177] J. Eggers, Phys. Rev. Lett. **71**, 3458 (1993).
- [178] J. Eggers, Rev. Mod. Phys. **69**, 865 (1997).

- [179] A. Adams, P. M. Chesler, and H. Liu, *Science* **341**, 368 (2013), 1212.0281.
- [180] A. Adams, P. M. Chesler, and H. Liu, *Phys. Rev. Lett.* **112**, 151602 (2014), 1307.7267.
- [181] O. J. C. Dias, G. T. Horowitz, D. Marolf, and J. E. Santos, *Class. Quant. Grav.* **29**, 235019 (2012), 1208.5772.
- [182] M. Maliborski and A. Rostworowski, *Phys. Rev. Lett.* **111**, 051102 (2013), 1303.3186.
- [183] V. Balasubramanian, A. Buchel, S. R. Green, L. Lehner, and S. L. Liebling, *Phys. Rev. Lett.* **113**, 071601 (2014), 1403.6471.
- [184] G. T. Horowitz and J. E. Santos, *Surveys Diff. Geom.* **20**, 321 (2015), 1408.5906.
- [185] O. Dias and J. E. Santos, *Class. Quant. Grav.* **33**, 23LT01 (2016), 1602.03890.
- [186] A. Rostworowski, *Phys. Rev.* **D95**, 124043 (2017), 1701.07804.
- [187] G. Martinon, G. Fodor, P. Grandclément, and P. Forgàcs, *Class. Quant. Grav.* **34**, 125012 (2017), 1701.09100.
- [188] O. J. C. Dias and J. E. Santos, (2017), 1705.03065.
- [189] P. M. Chesler and L. G. Yaffe, *Phys. Rev. Lett.* **106**, 021601 (2011), 1011.3562.
- [190] P. M. Chesler and L. G. Yaffe, *JHEP* **07**, 086 (2014), 1309.1439.
- [191] W. van der Schee, *Gravitational collisions and the quark-gluon plasma*, PhD thesis, Utrecht U., 2014, 1407.1849.
- [192] M. Henneaux and C. Teitelboim, *Commun. Math. Phys.* **98**, 391 (1985).
- [193] K. Mattsson, M. Svärd, and J. Nordström, *Journal of Scientific Computing* **21**, 57 (2004).
- [194] K. Mattsson and J. Nordström, *Journal of Computational Physics* **199**, 503 (2004).
- [195] L. Lehner, O. Reula, and M. Tiglio, *Class. Quant. Grav.* **22**, 5283 (2005), gr-qc/0507004.
- [196] H. Bantilan and P. Romatschke, *Phys. Rev. Lett.* **114**, 081601 (2015), 1410.4799.
- [197] <http://laplace.physics.ubc.ca/Group/Software.html> .
- [198] P. Figueras, unpublished (2010).
- [199] V. Balasubramanian and P. Kraus, *Commun. Math. Phys.* **208**, 413 (1999), hep-th/9902121.
- [200] G. Holzegel and J. Smulevici, *Commun. Pure Appl. Math.* **66**, 1751 (2013), 1110.6794.
- [201] M. W. Choptuik, O. J. C. Dias, J. E. Santos, and B. Way, *Phys. Rev. Lett.* **119**, 191104 (2017), 1706.06101.
- [202] D. Gerosa and M. Vallisneri, *The Journal of Open Source Software* **2** (2017).